ISSN 1983-4195

IBRACON

IBRACON Structures and Materials Journal

Revista IBRACON de Estruturas e Materiais

Volume 14, Number 2

April 2021

ISSN 1983-4195
Volume 14, Number 2
April 2021

IBRACON Structures and Materials Journal
Revista IBRACON de Estruturas e Materiais

Contents

Cover: Parametric Tower

Courtesy: Marcela Noronha P. de O. e Sousa

IBRACON

Ibracon Structures and Materials Journal
is published bimonthly
(February, April, June, August, October, and December) by IBRACON.

IBRACON
Instituto Brasileiro do Concreto Founded in 1972

Av. Queiroz Filho, nº 1700 — sala 407/408
Torre D — Villa Lobos Office Park
CEP 05319-000 — São Paulo, SP — Brazil
Phone: +55 11 3735-0202
Fax: +55 11 3733-2190
E-mail: riem@ibracon.org.br
Website: http://www.ibracon.org.br

Cover design & Layout: Editora Cubo
www.editoracubo.com.br

Aims and Scope

Aims and Scope

The IBRACON Structures and Materials Journal (in Portuguese: Revista IBRACON de Estruturas e Materiais) is a technical and scientific divulgation vehicle of IBRACON (Brazilian Concrete Institute), published every two months. Each issue has 12 to 15 articles and, possibly, a technical note and/or a technical discussion regarding a previously published paper. All contributions are reviewed and approved by professionals with recognized scientific competence in the area. The IBRACON Structures and Materials Journal is an open access Journal, free of charges for authors and readers.

Objectives

The IBRACON Structures and Materials Journal´s main objectives are:

- Present current developments and advances in concrete structures and materials.
- Make possible the better understanding of structural concrete behavior, supplying subsidies for a continuous interaction among researchers, producers, and users.
- Stimulate the development of scientific and technological research in the areas of concrete structures and materials, through papers peer-reviewed by a qualified Editorial Board.
- Promote the interaction among researchers, constructors and users of concrete structures and materials and the development of Civil Construction.
- Provide a vehicle of communication of high technical level for researchers and designers in the areas of concrete structures and materials.

Submission Procedure

The procedure to submit and revise the contributions, as well as the formats, are detailed in the Journal Website (ismj.org).

The papers and the technical notes are revised by at least two reviewers indicated by the editors. Discussions and replies are accepted for publication after a review by the editors and at least one member of the Editorial Board. In case of disagreement between the reviewer and the authors, the contribution will be sent to a specialist in the area, not necessarily linked to the Editorial Board. Conflict of interests is carefully handled by the Editors.

Contribution Types

The Journal will publish original papers, short technical notes, and paper discussions. Original papers will be accepted if they are in accordance with the objectives of the Journal and present quality of information and presentation. A technical note is a brief manuscript. It may present a new feature of research, development, or technological application in the areas of Concrete Structures and Materials, and Civil Construction. This is an opportunity to be used by industries, companies, universities, institutions of research, researchers, and professionals willing to promote their works and products under development.

A discussion is received no later than 3 months after the publication of the paper or technical note. The discussion must be limited to the topic addressed in the published paper and must not be offensive. The right of reply is granted to the Authors. The discussions and the replies are published in the subsequent issues of the Journal.

The submission file should be in accordance with the paper template available at the Journal Website. It is recommended that the length of the papers does not exceed 25 pages. Where available, URLs for the references should be provided.

The IBRACON Structures and Materials Journal will conduct the review process for manuscripts submitted in English. Titles, abstracts, and keywords are presented in English, and in Portuguese or Spanish. Articles and technical notes are peer-reviewed and only published after approval of the reviewers and the Editorial Board.

Once accepted, an article is typeset according to the journal layout. The author will be required to review and approve the galleys before publishing. At this stage only typesetting errors will be considered.

Internet Access

The IBRACON Structures and Materials Journal Webpage is available at http://ismj.org.

Sponsors

The funds for the maintenance of the Journal are currently obtained from the IBRACON. The Journal is not supposed to be maintained with funds from private sponsorship, which could diminish the credit of the publications.

Photocopying

Photocopying in Brazil. Brazilian Copyright Law is applicable to users in Brazil. IBRACON holds the copyright of contributions in the journal unless stated otherwise at the bottom of the first page of any contribution. Where IBRACON holds the copyright, authorization to photocopy items for internal or personal use, or the internal or personal use of specific clients, is granted for libraries and other users registered at IBRACON.

Copyright

IBRACON

Av. Queiroz Filho, 1700 – sala 407/408 – Torre D
Villa Lobos Office Park
05319-000 – Vila Hamburguesa
São Paulo – SP
Phone: +55 (11) 3735-0202
E-mail: riem@ibracon.org.br

Disclaimer

Papers and other contributions and the statements made or opinions expressed therein are published on the understanding that the authors of the contribution are the only responsible for the opinions expressed in them and that their publication does not necessarily reflect the views of IBRACON or of the Journal Editorial Board.

Editorial Board

Rev. IBRACON Estrut. Mater., vol. 14, no. 2, e14201, 2021

IBRACON Structures and Materials Journal
Revista IBRACON de Estruturas e Materiais
ISSN 1983-4195 ismj.org

ORIGINAL ARTICLE

Experimental and numerical analysis of composite steel and concrete trusses

Análise Numérica e Experimental de Treliças Mistas de Aço e Concreto

Joel Donizete Martins[a]
Sineval Esteves Pereira Junior[b]
Ellen Martins Xavier[c]
Luiz Henrique de Almeida Neiva[c]
Arlene Maria Cunha Sarmanho[c]

[a]Instituto Federal Minas Gerais – IFMG, Campus Congonhas, Congonhas, MG, Brasil
[b]Universidade Federal de São Carlos – UFSCar, Programa de Pós-graduação em Engenharia Civil - PPGECiv, São Carlos, SP, Brasil
[c]Universidade Federal de Ouro Preto – UFOP, Programa de Pós-graduação em Engenharia Civil – PROPEC, Ouro Preto, MG, Brasil

Received 08 December 2017
Accepted 16 June 2020

Abstract: In the present work, two composite trusses formed by tubular shapes supporting a concrete slab were evaluated. Based on analytical formulation related to the problem, according to recommendations of standards, numerical analyses were performed, with models created using the software Ansys, and an experimental analysis with full-scale tests. Good agreement between the three analysis types was observed. A possible shear connection failure in one truss was observed. With a change in the second truss's connector length, an increase in the structure's strength and rigidity was achieved. In this study, because the shear connectors were directly welded on the upper chord wall, local effects with localized plastifications were evidenced.

Keywords: composite trusses, tubular connections.

Resumo: Neste trabalho foram avaliadas duas treliças mistas projetadas com perfis tubulares, associadas a uma laje maciça de concreto. Baseando-se em expressões analíticas relacionadas ao problema, seguindo as recomendações de normas, análises numéricas foram realizadas, com modelos criados utilizado o programa computacional Ansys e uma análise experimental, por meio de ensaios em laboratório com a estrutura em escala real. Houve boa aproximação dos resultados nas três análises, sendo observada a possibilidade de falha na conexão de cisalhamento em uma das treliças. Com uma mudança no comprimento do conector da segunda treliça, foi observado um aumento na resistência e na rigidez da estrutura. No estudo, ficaram evidentes os efeitos localizados da ligação entre os perfis em seção tubular e da fixação do conector de cisalhamento diretamente sobre a parede do banzo superior, que causaram plastificações também localizadas.

Palavras-chave: treliças mistas, ligações tubulares.

How to cite: J. D. Martins, S. E. Pereira Junior, E. M. Xavier, L. H. A. Neiva, and A. M. C. Sarmanho, "Experimental and numerical analysis of composite steel and concrete trusses," *Rev. IBRACON Estrut. Mater.*, vol. 14, no. 2, e14201, 2021, https://doi.org/10.1590/S1983-41952021000200001

INTRODUCTION

Lately, composite structures made of steel trusses and concrete slabs in bridge slabs and even buildings with large open spans have become more viable. The composite truss systems have proven to be very economical since they allow exploring each material's best characteristics. Due to the composite section bending, the greater compression values are concentrated in the slab, whereas the tension occurs in the lower chord. According to Wardenier et al. [1], in trusses designed without considering the composite section solution, 50% of the material weight used to fabricate the structure

Corresponding author: Arlene Maria Cunha Sarmanho. E-mail: arlene.sarmanho@gmail.com
Financial support: None.
Conflict of interest: Nothing to declare.

is concentrated in the compressed chord, 30% in the chord under tension, and 20% in the elements of the diagonals and vertical posts. Therefore, there can be a significant reduction in materials consumption when considering the composite section since the upper chord's dimensions can be reduced without influencing the structure capacity.

This study presents experimental and numerical analyses of composite trusses designed with tubular profiles associated with a concrete slab. The experimentally analyzed truss was donated to the *Universidade Federal de Ouro Preto* (UFOP). The analysis results are assessed to investigate the mechanisms used to ensure a better steel-concrete interaction, providing a behavior with most of the slab under compression. The steel is under tension, allowing a more efficient and secure composite section. Two truss models are numerically evaluated. For the first truss, numerical and experimental analyses were performed, and the results were compared to literature recommendations and standard code specifications. For the second truss, only numerical analyses were performed. The difference between Truss 1 and 2 is a change in the shear connection from Truss 1 to make the initially tested structure more efficient.

THEORETICAL FOUNDATION

Studies on composite trusses are still few, and most of them, including what is regulated by the Brazilian standards of steel and composite structures [2], were initially proposed in a publication of the 1980s (Chien and Ritchie [3]). According to these authors, composite trusses' design for the ultimate limit states is performed using a model considering sections plastification (Figure 1).

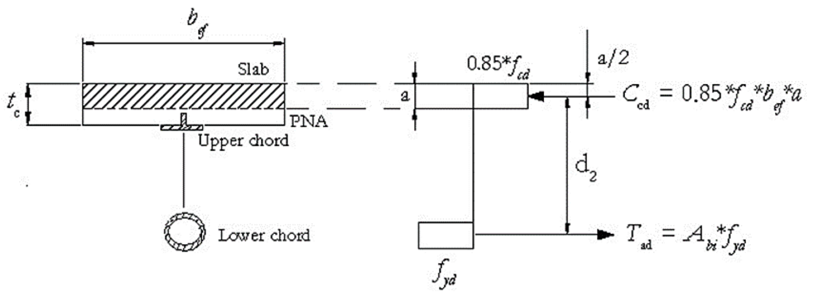

Figure 1. Model for global analysis of a composite truss under bending.

In this model, only the concrete slab and the lower chord are considered. The bending lever arm, d_2, formed between the concrete compression force and the tension force in the lower chord, is considered. The plastic neutral axis, PNA, must be positioned within the concrete slab in the Truss ultimate strength. Thus, the height of the plastic section (a) must be lower than the slab thickness (t_c). For a ductile rupture to occur, the lower chord section yielding stress (T_{ad}) must occur before concrete crushing (C_{cd}) and rupture of the shear connection (Q_{rd}), also ensuring the total or complete interaction regime.

Concerning the other truss members, the diagonals are dimensioned to resist the total vertical shear load, while the upper chord is only considered in the analyses performed before concrete curing. However, this is a fundamental member in the composite section, even with the slab presence. It directly influences the shear connection behavior, especially when it comes to stress redistribution [4]. That is impaired in composite trusses because of stress concentration in the connecting nodes region, as demonstrated in Machacek and Cudejko [5] and Bouchair et al. [6]. Eurocode [7] proposes a methodology considering a non-uniform elastic distribution of stresses among the connectors. Such procedure is used in composite trusses whenever the plastic analysis of the connection may not be safe, as in bridges under fatigue or when the connectors are not ductile.

For serviceability limit states, when evaluating vertical displacements, it is recommended to calculate the structure stiffness considering the moment of inertia of the composite section, I_{mist}. That is made turning the concrete slab effective area into an equivalent area of steel, neglecting the concrete and the upper chord in the tension zone. To consider the effect of shear deformations on diagonal members, the effective moment of inertia, I_{ef}, must be calculated as Equation 1. I_{met} is the cross section moment of inertia, considering only the truss steel members. This procedure is recommended by Chien and Ritchie [3] and is included in the Brazilian standard [2].

$$I_{ef} = I_{mist} - 0.15 I_{met} \tag{1}$$

This moment of inertia is calculated considering the total interaction between the slab and the truss. The Canadian standard [8] presents Equation 2 to calculate the effective moment of inertia. The factor "P" considers the degree of interaction between the slab and the truss. In the case of total interaction, this factor is considered equal to 1.0.

$$I_{ef} = 0.15 I_{met} + 0.85 P^{0.25} \left(I_{mist} - 0.15 I_{met} \right) \tag{2}$$

According to Murray et al. [9], the standard reduction of 15% in the moment of inertia of the steel section can lead to good results when the relationship between the span length and the truss height (L/h) has a value greater or equal to 15. Therefore, the author proposes to consider a reduction factor, C_r, dependent on the ratio (L/h) as shown in Equation 3 and to calculate the effective moment of inertia using Equation 4. From Murray et al. [9], this equation may lead to better results for $L/h < 15$, rather than to consider the standard decrease of 15%. In this case, the moment of inertia of the composite section, I_{mist}, must also be calculated to take the upper chord into account.

$$C_r = 0.9(1 - e^{-0.28(L/h)})^{2.8} \tag{3}$$

$$I_{ef} = \frac{1}{\frac{1 - C_r}{C_r \cdot I_{met}} + \frac{1}{I_{mist}}} \tag{4}$$

NUMERICAL ANALYSIS

Definition of prototypes

The trusses evaluated were designed to have an open span length of 10000 mm and its height equal to 1146 mm (Figure 2). Upright posts were used in the truss profiles with circular tubular hollow section on the diagonal members (CHS 101.6 x 6.4) and upright posts (CHS 60.2 x 6.4), and rectangular hollow section in the lower chord (RHS 150.0 x 120.0 x 6.4) and the upper chord (RHS 150.0 x 120.0 x 4.8). All these members were fabricated in VMB 300 steel (f_y = 300MPa). Due to the probability of the plastification occurring in the truss tubular connections, shell plates with a thickness of 12.5 mm were added at these points, as indicated in Figure 2b.

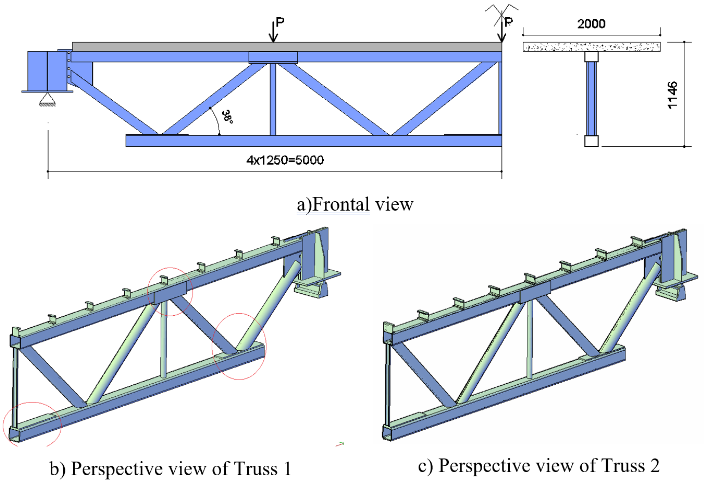

Figure 2. Configurations of the evaluated composite trusses.

The slab was designed to a length equal to 2000 mm, a thickness of 100 mm, and concrete compressive strength, f_{ck}, of 25 MPa. In order to connect the slab to the upper chord, shear connectors were designed in a hot rolled U-profile (Figure 2b) with length (l_{fcs}) equal to 80 mm, web thickness (t_{wcs}) equal to 4.32 mm, and flange thickness (t_{fcs}) equal to 6.9 mm, made of ASTM A36 steel. The connectors were arranged along the chord with a 625 mm spacing.

Table 1. Results of the materials testing.

Member	Yield strength (MPa)	Ultimate strength (MPa)	Compressive strength (MPa)
Chords	456	720	-
Diagonals	442	930	-
Upright posts	442	930	-
Shell plates	350	450	-
Slab concrete	-	-	25

After the trusses were fabricated, the yielding strengths were obtained by experimental tests for the steel used in the chords, diagonals, reinforcement plates, and upright posts, according to Table 1. No characterization tests were performed in the steel of the shear connectors and the steel reinforcing bars. Thus, nominal values of yielding strength equal to 250 MPa and 500 MPa, were considered in the analyses, respectively. The results showed that yield strength was higher than expected. Concerning the specific case of the chords' material, which is fundamental for determining the composite structure rupture limit, the tests showed a yield strength equal to 456 MPa, well above the expected 300 MPa. Thus, the ultimate limit turned out to be the shear connection rupture and not the lower chord yielding, as recommended in standards and predicted in the design. The composite truss would work in a partial interaction mode since the shear connection resistance ($\sum Q_r$) presented a value smaller (22%) than the tension axial load that causes the lower chord to yield by tension ($A_{bi} \cdot f_y$).

A possible solution to avoid such a loss of interaction would be to increase the concrete strength or modify the shear connectors. However, these changes would negatively impact the fidelity of the evaluated prototypes to the initially designed structure, which would impair the research conclusions. It was then decided to evaluate the composite truss as it was initially conceived and to also model a second structure, modifying only the shear connection. In the composite Truss 2, the shear connection was modified, using a connector of length (l_{fcs}) extended to the end of the chord, with a width of 150 mm, as shown in Figure 2c. This modification increases the connection resistance capacity because the connector is welded along the chord width, which will load the lateral side of the member, not only the top face when the connector is mobilized, providing more stiffness to its base.

Numerical models design

The numerical modeling was performed in the Ansys program using a three-dimensional analysis. For faster analysis, half of the truss was modeled due to its symmetry. The three-dimensional reinforced concrete finite element *SOLID65* (Figure 3a) was used [10]. Although the internal reinforcing bar could be considered diffuse in the element *SOLID65*, it was decided to use independent elements for the reinforcement, which was modeled using the finite element *LINK8* (Figure 3b). The slab mesh had nodes position coincided with the reinforcement nodes position, as shown in Figure 3c.

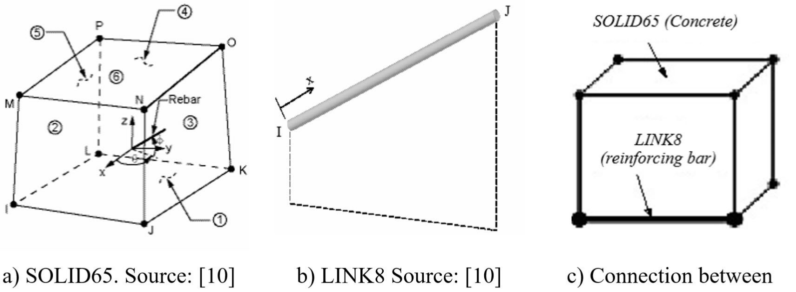

a) SOLID65. Source: [10] b) LINK8 Source: [10] c) Connection between elements

Figure 3. Finite elements used in slab modeling.

The modeling of the chords, diagonals, upright posts, and shear connectors was done using shell elements, *SHELL181* (Figure 4a), allowing to consider localized effects in the connection nodes of the tubular section members. These elements were used in other studies involving tubular profiles with good results [11]. The modeling of the shell elements was done considering the dimensions of the cross-section midline of the tubular profiles. The connection of the slab with the shear connectors was made so that there was also a coincidence of node position of the finite elements of the slab and the shear connector elements, subsequently coupling these nodes, making for a rigid connection between the two structural elements, as shown in Figure 4b. Figure 5 shows a complete view of the model used.

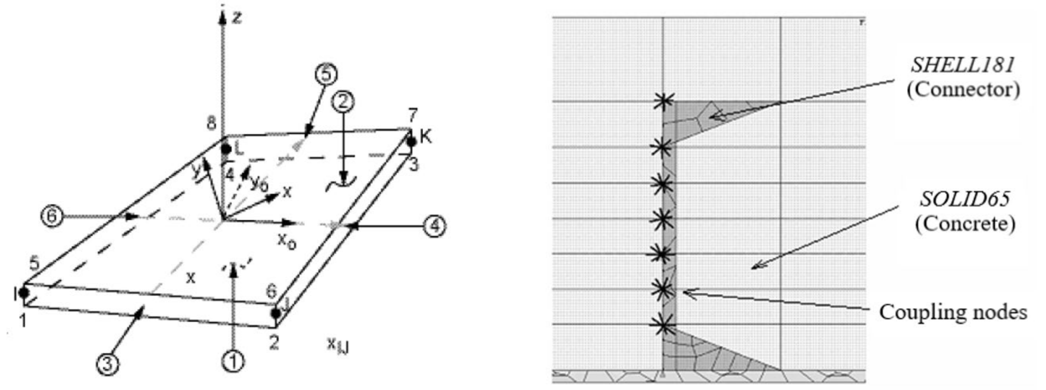

a) *SHELL181* Source: [10] b) Coupling of nodes of different elements

Figure 4. Details of finite element *SHELL181* and the coupling of nodes of slab elements and connectors.

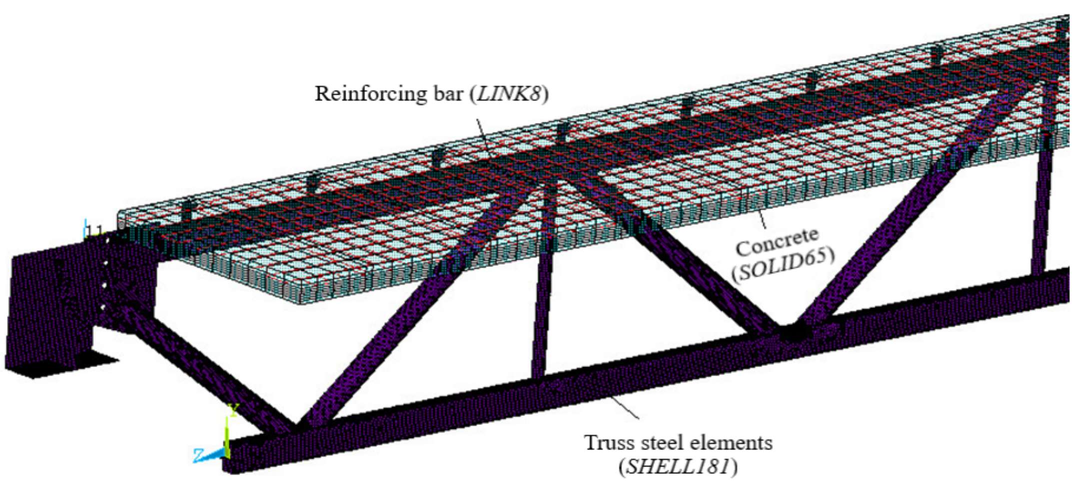

Figure 5. Overall view of the numerical model with members discretization.

A multilinear elastoplastic behavior with isotropic hardening was considered for the chords, upright posts, and diagonals to consider the materials mechanical properties extrapolating the elastic limit (Figure 6). For the truss steel members, stress versus strain curves considered the experimental data (Table 1) and a modulus of elasticity of 205 GPa. As for the concrete, the stress versus strain curve was defined according to the Brazilian Standard specification for reinforced concrete [12], using a parabolic curve defined with the expression shown in (Equation 5). Figure 6 shows the stress versus strain curves considered for the concrete chords and for the steel chord.

$$\sigma_c = f_{ck}\left[1-\left(1-\varepsilon_c / 0.002\right)^2\right] \quad (5)$$

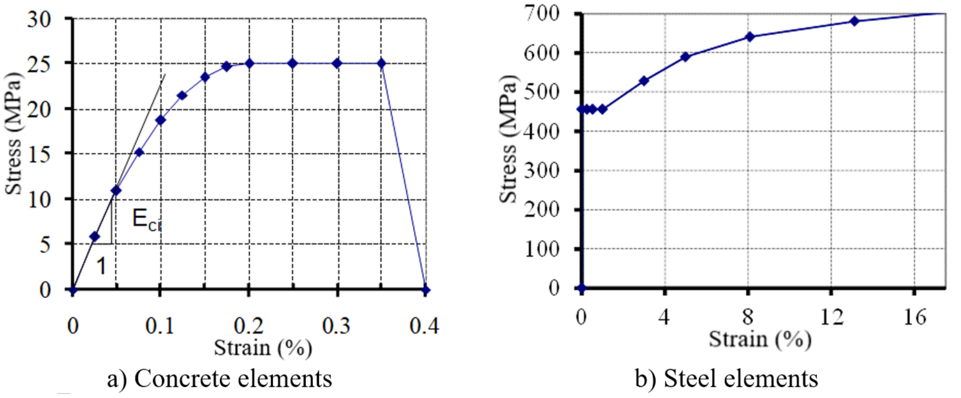

Figure 6. Stress versus strain curves used as materials properties.

The steel reinforcing bars were modeled considering a perfect elastoplastic behavior. The shear connectors steel was modeled considering a bilinear behavior with yielding strength equal to 250 MPa and the ultimate strength equal to 400 MPa.

The load was applied to nodes located on the concrete slab, allowing the Ansys program to control the load increase during the analyses automatically. Minimum and maximum increments limit were imposed equal to 1% and 10% of the total estimated load, respectively. A large-displacement analysis was adopted since it is an efficient method to solve non-linear equations, and the program automatically defines the convergence criteria.

EXPERIMENTAL PROGRAM

Test assembly

The tests with Truss 1 occurred in the Laboratory of Structures "*Professor Altamiro Tibiriçá Dias*" at the Department of Civil Engineering of the *Universidade Federal de Ouro Preto*. Figure 7 shows an overall image of the test assembly and loading scheme. Three reinforcing bars connected the specimen to the lateral containment frames to avoid tipping during the tests. The load application was performed using three hydraulic actuators with a load capacity of 500 kN. The actuators were fixed directly to the reaction frame and to a pinned load cell that guarantees verticality in the loading. Rectangular plates were placed below the load cell at the slab concrete to minimize the contact region compression stress, avoiding concrete local crushing.

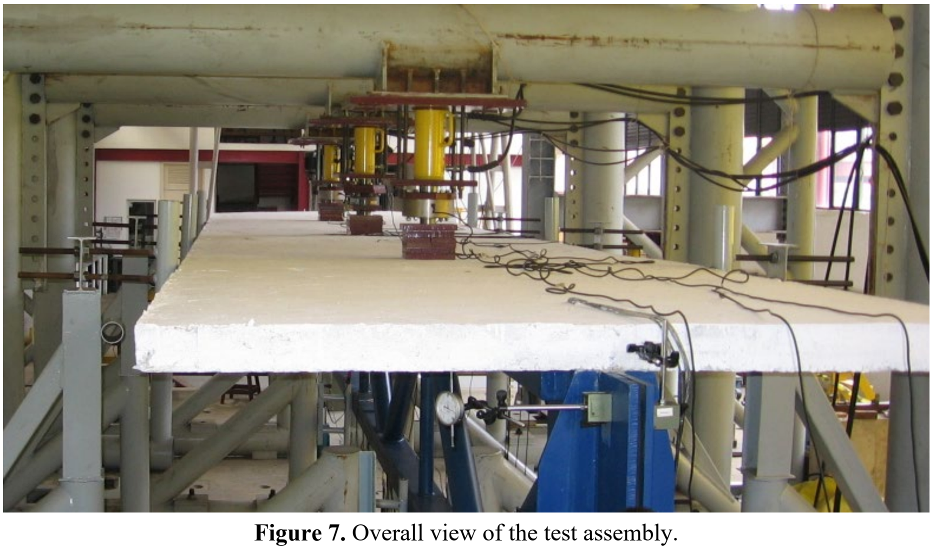

Figure 7. Overall view of the test assembly.

Strain gages were used to measure strains, with eighteen unidirectional strain gages for linear strain and four 45° rosettes strain gages. Displacements were measured with five LVDTs - “Linear Variable Displacement Transducers” and with seven analog deflectometers. The instrumentation positioning was defined based on the numerical analysis results. An automatized computer-controlled data acquisition and monitoring system was used.

RESULTS AND DISCUSSIONS

Load versus Displacement

Figure 8 illustrates the Load versus Displacement curves obtained in the vertical direction in the middle of the span, demonstrating a good correlation of the experimental and numerical results. The graph indicates load values that are, theoretically, the shear connection strength limit, the elastic limit (beginning of the yielding of the lower chord by tension), and the plastic limit (total yielding of the lower chord by tension). As previously reported, the results using formulations of standards and literature indicate the possibility of failure in the shear connection before the chord yielding. The maximum load reached, both in the numerical analysis and in the experiment (≈ 268.0 kN), was slightly higher than the connection load capacity limit (253.0 kN). For Truss 2, designed with the modification in the shear connection to guarantee a total interaction, the plastic limit load of 322.0 kN was reached.

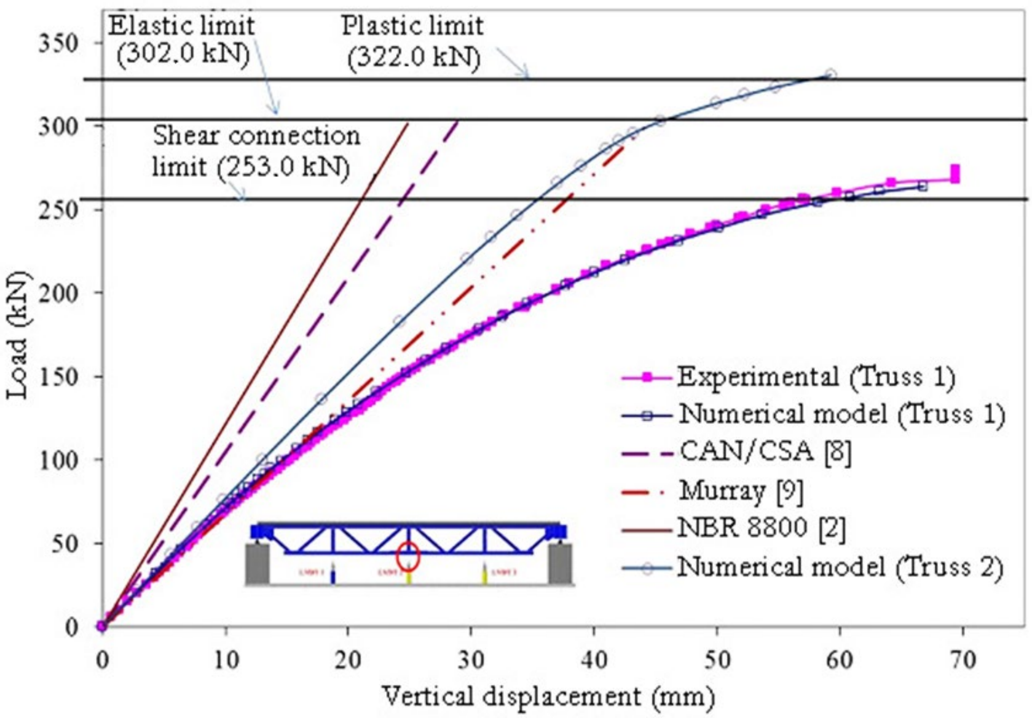

Figure 8. Comparison of load versus displacement curves.

The nonlinearity in the results from the initial loads is observed for Truss 1 due to excessive deformations in the connectors because of the upper chord wall great flexibility, where the connectors were welded (Figure 9). The top face wall has a thickness of 4.8 mm and a width of 150 mm, which are measures within limits for a compressed member ($b/t = 1,14\sqrt{E/f_y} < b/t\sqrt{E/f_y}_{lim}$) according to Brazilian standard [2]. Since the connector has a length of 80 mm, its stability depends entirely on the chord upper face stiffness. The modification in the shear connection in Truss 2 ensures greater stiffness and greater strength to the structure, as the numerical results indicate.

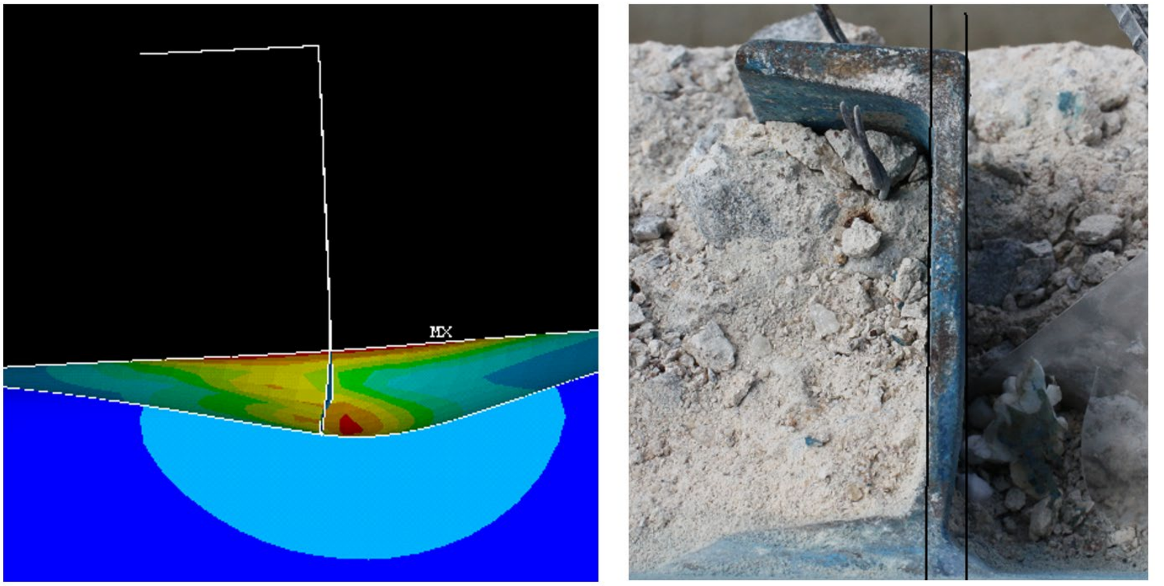

a) Numerical model b) Experimental test

Figure 9. Deformation of connector due to low stiffness of the top face of the chord.

The load limits from formulations of standards and literature, indicated in Figure 8, were obtained considering the effective moments of inertia calculated using Equations 1, 2, and 4 referring respectively to the specifications of the Brazilian Standard [2], Canadian Standard [8] and Murray et al. [9]. There was a more significant divergence with the experimental results when assessing the Brazilian standard [2] and a better approximation when considering the recommendations of Murray et al. [9]. Even in this last case, a good correlation was observed only for the initial loads of Truss 1. A better approximation of the effective moment of inertia values obtained using Equations 1 and 2 is possible whenever the relationship between the span length and the height of the truss (L/h) is greater than 15 and in the presence of more rigid shear connectors, as it observed in other similar studies [13], [14]. In such studies, the shear connection was designed with a "Perfobond" connector, considered more rigid. For the truss evaluated in this paper, the relation length-height is ($L/h = 10$), and the connector is more flexible. Thus, a better approximation of the results is obtained using Equation 4. The shear connection greater deformability influenced the results, increasing the relative horizontal sliding between the slab and the upper chord, measured experimentally by a displacement transducer. Numerical analyses also showed the relative displacement, as can be observed in Figure 10. This relative horizontal sliding indicates the loss of interaction between the upper chord and the slab, characterizing a partial interaction type.

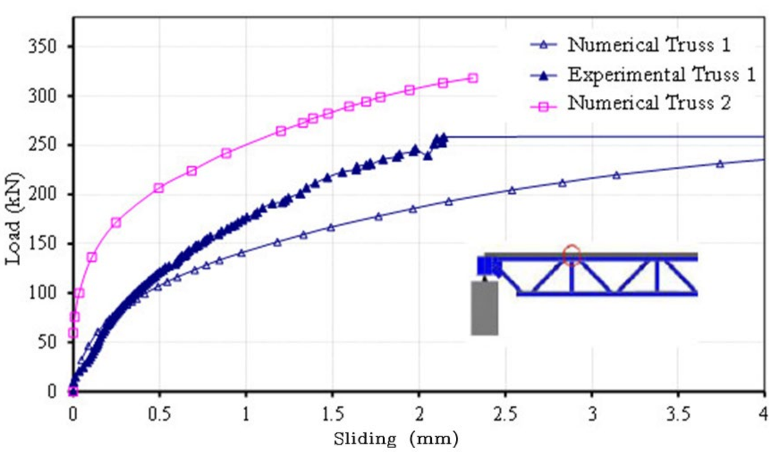

Figure 10. Horizontal sliding between the slab and the upper chord.

Load versus Deformation

The study compared the linear deformations observed in the lower face of the lower chord (Figure 11), von Mises deformations in the shear connector near the support (Figure 12), and the region of the truss inferior node without reinforcement (Figure 13). The numerical result concerning the lower chord presented a good approximation with the experimental results. In Truss 2, a linear behavior is observed up to the load corresponding to the chord yielding (indicated by the vertical line in the graphs and equal to 280 kN), which matches the analytically calculated elastic limit load shown in Figure 8.

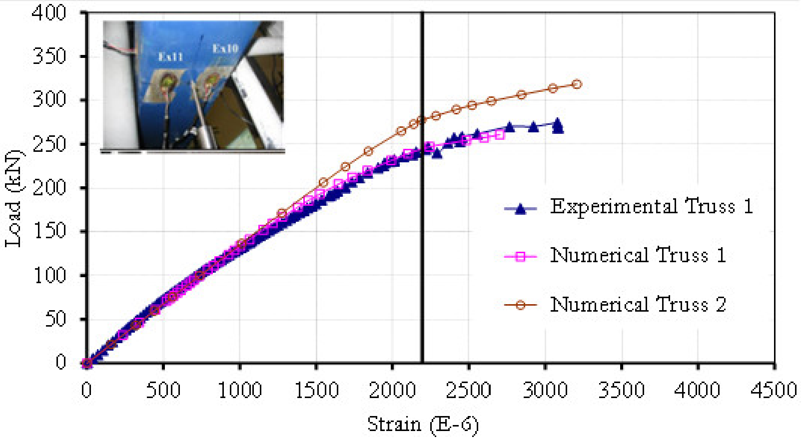

Figure 11. Strains in the lower face of the lower chord.

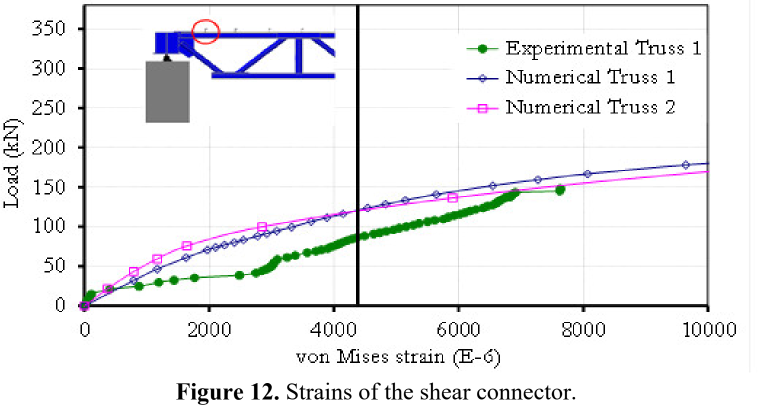

Figure 12. Strains of the shear connector.

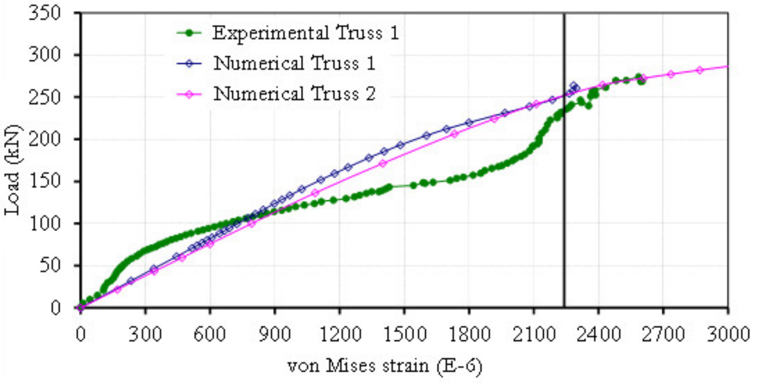

Figure 13. Strains in the region of one of the lower nodes.

As shown in Figure 11, the lower chord strains indicate that this member is under tension. In the experimental analyses performed, the upper chord strains were also measured (Figure 14). The strains in the upper chord indicate that this member is under compression.

For the shear connector (Figure 12), the curve obtained with the numerical results presented a slightly different shape from the experimental results, which may be explained due to localized effects. After the yielding limit (indicated by the vertical line), there was a better approximation of the results. The numerical results of Truss 2 are similar to the results obtained from Truss 1.

In the region where the diagonals are connected to the lower chord (Figure 13), in which there were no reinforcement plates, differences in numerical and experimental results are also observed, with an approximation of values for maximum loads.

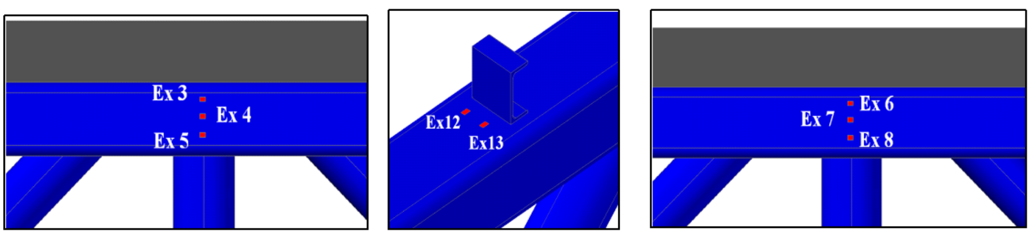

(a) Position of the strain gages

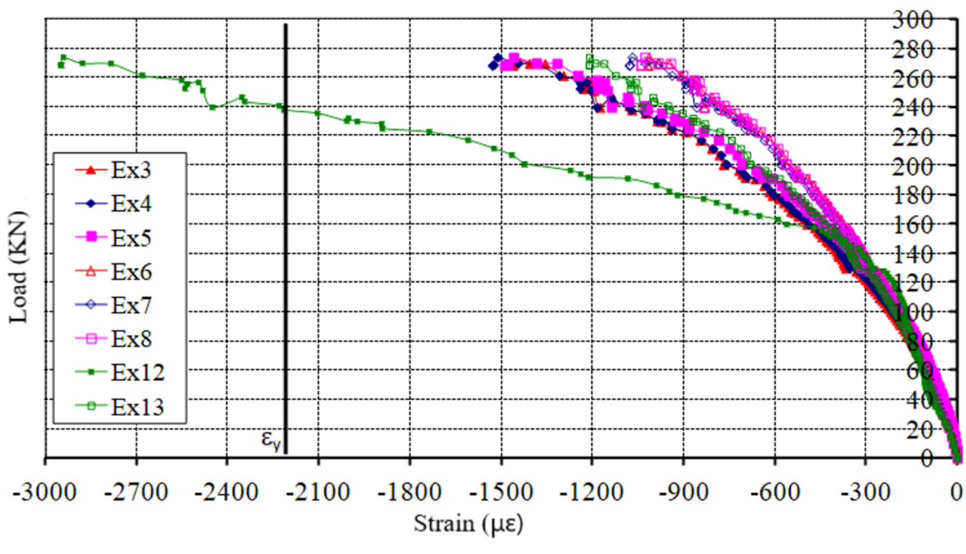

(b) Load versus strain curves for each strain gage

Figure 14. Strains measured in the upper chord.

Maximum stress observed in truss members.

Figure 15 and Figure 16 show the stress field (von Mises total stress) for the steel members, considering the analyses maximum load. In Truss 1 (Figure 15), the stresses with values higher than the material yield limit were concentrated along the upper chord in the regions where the shear connectors are attached. There was a plastification in the area around the chord connection, in the diagonal and in the upright posts in the central node region, which were added to the plastification in the connector. Thus, the plastification is more evident in this member region. Plastification can also be found in the regions at the most demanded diagonal members ends, in the lower chord, around the connecting node without reinforcement, and at the middle of the span along the lower face.

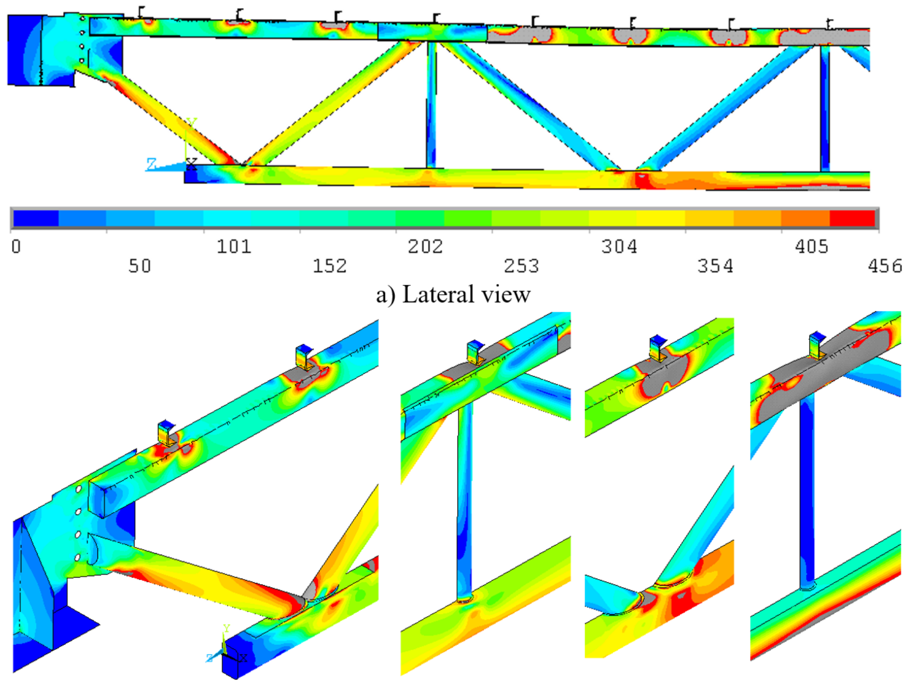

a) Lateral view

b) 3D view

Figure 15. von Mises stresses in MPa for the steel members of Truss 1.

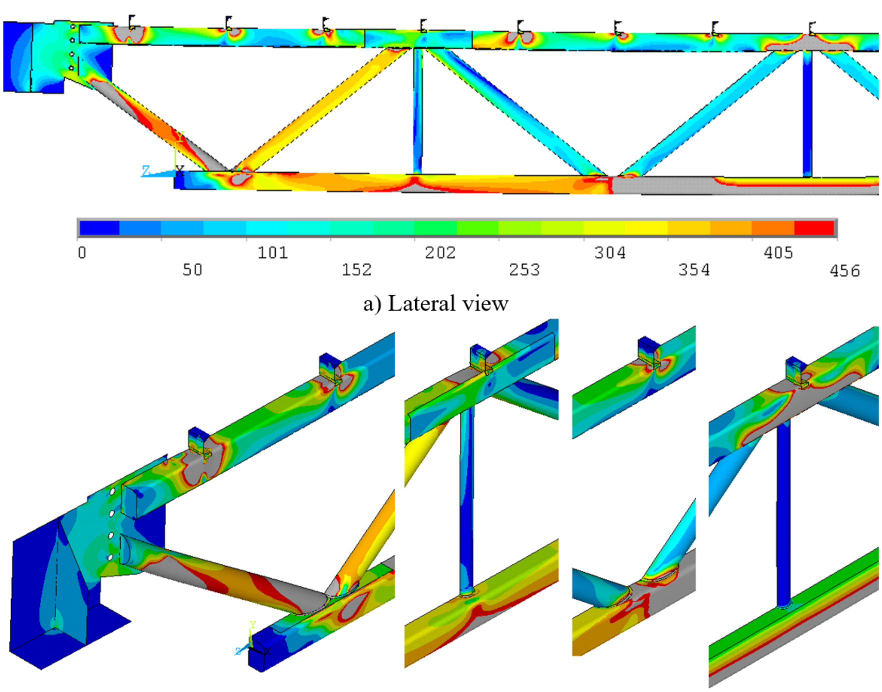

a) Lateral view

b) 3D view

Figure 16. von Mises stresses in MPa for the steel members of Truss 2.

For Truss 2 (Figure 16), the yield limit was exceeded in the lower chord along the entire central span section and concentrated in the nodes and in the connectors regions. This occurs with less intensity in Truss 1. Plastification is also observed at the ends of the most demanded diagonals and in the upper chord, in the region of the connecting nodes, in the middle of the span, and the at the support.

Along the lower chord and in the middle of the span, the deformations from the structure bending results the member under tension. In the connecting nodes region and in the ends of the diagonal members, the plastification is due to the localized effects of the connection between members in the tubular section. Those plastifications were considered in the analyses via the formulations of standards and literature, used to obtain the strength of tubular connections without reinforcement.

Figure 17 and Figure 18 display the transverse stresses measured along the top and lower slab faces for maximum loads. Because of the structure bending, compressive stress predominates on the top face, and tension stress can be seen on the lower face. More significant efforts were observed in the regions above the connecting nodes, among the upper chord, diagonals, and upright posts, indicating the existence of concentrated moment loads. These efforts, added to the global bending of the slab, caused stress concentration in the middle of the span. The shear connectors also caused stress concentration on the slab as it can be observed, mainly, along the lower face of the Truss 2 slab. For this case, there was a stress concentration in the region near to the top node, close to the support. Its value decreased as it moved away from the node. Truss 1, characterized by a partial interaction type, has more efforts developed, resulting from the global bending. Truss 2 has higher efforts and greater stresses were localized in the regions of connecting nodes and in the region where the connectors were positioned.

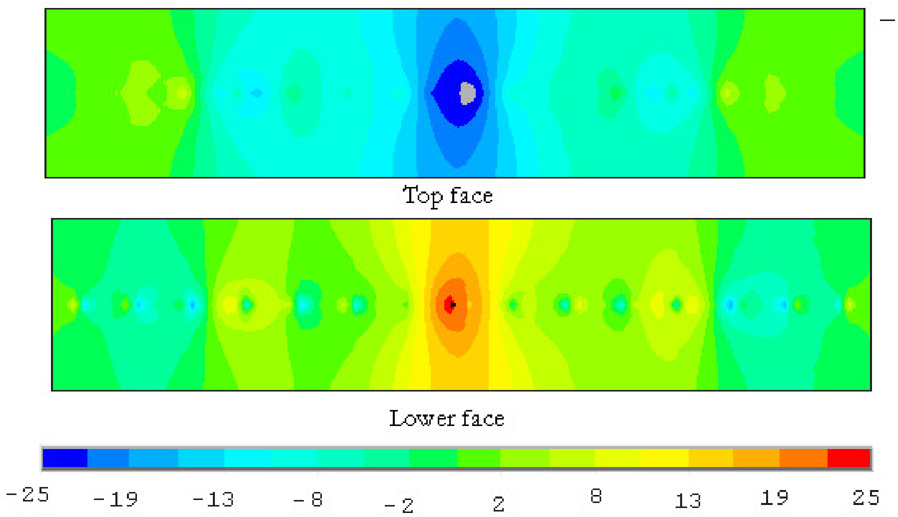

Figure 17. Transverse stresses in MPa measured in the slab faces of Truss 1.

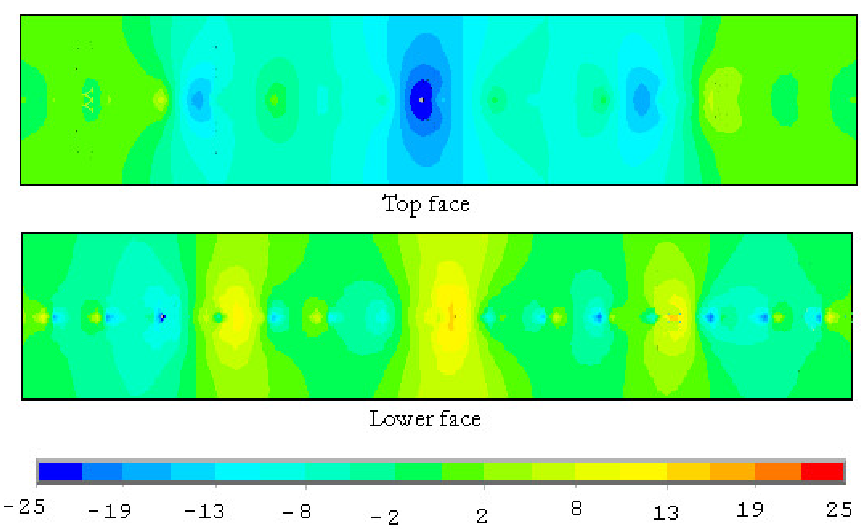

Figure 18. Transversal stresses in MPa measured in the slab faces of Truss 2.

In both trusses, the position of the neutral axis is inside the slab. The average strains in the slab height were measured from strain gage localized in the upper and lower slab faces and in the steel reinforcing bars. In Truss 1, the neutral axis was initially positioned 20 mm from the contact base between the upper chord and the slab (Figure 19). With the load increasing, it migrated to a 45 mm position from the base for the maximum load of 264 kN. In Truss 2, the neutral axis was positioned 35 mm from the base for the maximum load of 368 kN.

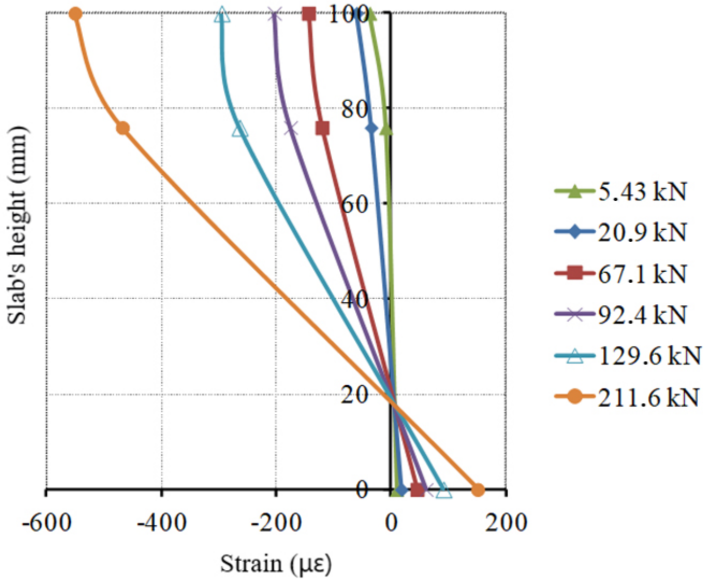

Figure 19. Strains in the slab height.

As shown in Figure 11 and Figure 14, the lower chord is under tension, and the upper chord is under compression, indicating the existence of a neutral axis in Truss 1. A second neutral axis is also observed in the slab, as shown in Figure 19. Two neutral axes characterize a steel-concrete partial interaction type, with sliding in the steel-concrete interface, supported by the shear connector that presents plastic deformation (Figure 9).

CONCLUSIONS

The study evaluated composite trusses from experimental and numerical analyses. Comparisons of these results with standards and literature analytical expressions were performed to verify the influence of the shear connection in the truss bending behavior.

Truss 1 allowed a good approximation between experimental and numerical results. Regarding the shear connection strength, the possibility of connection failure before the chord yielding was observed. The maximum loads obtained, both in the numerical and experimental analysis, were slightly higher than the load capacity limit calculated for the shear connection. With the modification in the shear connectors to guarantee the total interaction in Truss 2, a standard plastic limit load was achieved.

Experimental and numerical analyses indicate the influence of the upper chord wall flexibility on the deformability of the shear connection. This influence is more observed in Truss 1. Even with the shear connection change in Truss 2, a good correlation between the numerical results and those obtained according to the standard recommendations is still not possible. For the trusses evaluated, with the relationship between span length and height (L/h) equal to 10, better results were obtained according to Murray et al. [9], where the effective moment of inertia is calculated considering the L/h ratio.

The von Mises stresses on the steel members of Truss 1, shows a larger plastification in the upper chord region where the shear connectors were fixed, which made the structure very deformable. In Truss 2, the largest plastification occurred along the lower chord in the middle of the span, where there was total plastification of the member section, as recommended by the standards.

ACKNOWLEDGEMENTS

Special thanks to CAPES, CNPQ, and FAPEMIG, for the financial support in the preparation of this work; to Vallourec for the supply of the test prototypes, to the IFMG and, mainly to UFOP for the logistical and financial support in conducting this study; and finally, to the team of the UFOP Structures Laboratory for the availability and direct support in the execution of the experiments.

REFERENCES

[1] J. Wardenier, Y. Kurobane, J. A. Packer, D. Dutta, and N. Yeomans, *Design Guide for Circular Hollow Section (CHS) Joints Under Predominantly Static Loading*. Germany: Comité International pour le Développemente et l'Étude de la Construction Tubulaire, 1991.

[2] Associação Brasileira de Normas Técnicas, *Projeto de Estruturas de Aço e Estruturas Mistas de Aço e Concreto de Edifícios*, ABNT NBR 8800, 2008.

[3] E. Y. L. Chien and J. K. Ritchie, "Composite open web steel joints and trusses," in *Design and Construction of Composite Floor Systems*. Ontario: Canadian Institute of Steel Construction, 1984, ch. 5.

[4] ASCE – Task Committee on Design Criteria for Composite Structures in Steel and Concrete, "Proposed specification and commentary for composite joints and composite trusses," *J. Struct. Eng.*, vol. 122, no. 4, pp. 350–35, 1996.

[5] J. Machacek and M. Cudejko, "Composite steel and concrete bridge trusses," *J. Eng. Struct.*, vol. 33, no. 12, pp. 3136–3142, Dec 2011, http://dx.doi.org/10.1016/j.engstruct.2011.08.017.

[6] A. Bouchair, J. Bujnak, and P. Duratna, "Connection in steel-concrete composite truss," *Procedia Eng.*, vol. 40, pp. 96–101, 2012, http://dx.doi.org/10.1016/j.proeng.2012.07.062.

[7] European Committee for Standardization, *Eurocode 4 – Design of Composite Steel and Concrete Structures, Part 2: Composite Bridges*, DD ENV 1994-2:2001, 2001.

[8] Canadian Standard Association, *Limit States Design of Steel Structures*, CAN/CSA-S16-01, 2003.

[9] T. M. Murray, D. Allen, and E. Ungar, *Floor Vibrations Due to Human Activity* (Steel Design Guide Series 11). Chicago: American Institute of Stell Construction, 1997.

[10] Ansys, *User's Manual for Revision 11*. Houston, PA: Swanson Analysis Systems Inc., 2007.

[11] A. M. S. Freitas, F. C. Mendes, and S. Steves, "Numerical analysis of hollow section T joints with residual stresses," in *Proc. XXXIII Jorn. Sudam. Ing. Estruct.*, Santiago, Chile, 2008.

[12] Associação Brasileira de Normas Técnicas, *Projeto de Estruturas de Concreto – Procedimento*, ABNT NBR 6118, 2014.

[13] J. D. Martins and A. M. S. Freitas, "Participação da laje de concreto na resistência a esforços em composite trusses," in *An. 53° Cong. Bras. Concr.*, 2011.

[14] J. D. Martins, A. M. S. Freitas, "Análise em elementos finitos de composite trusses com conexões tubulares," in *XXV Jorn. Sulam. Eng. Estrut.*, Rio de Janeiro, 2012.

Author contributions: JDM: conceptualization, numerical model, formal analysis, data curation, writing; SEPJ: conceptualization, experimental model; EMX and LHAN: formal analysis, data curation, revision; AMCS: funding acquisition, supervision.

Editors: José Luiz Antunes de Oliveira e Sousa, Guilherme Aris Parsekian.

IBRACON Structures and Materials Journal
Revista IBRACON de Estruturas e Materiais
ISSN 1983-4195 ismj.org

ORIGINAL ARTICLE

MATLAB computational routines for moment-curvature relation of reinforced concrete cross sections

Rotinas computacionais em MATLAB para relação momento-curvatura de seções transversais de concreto armado

Gabriel Figueiredo de Melo[a]
André Jacomel Torii[b]
Eduardo Morais de Medeiros[a]
Aref Kalilo Lima Kzam[b]

[a]Universidade Federal da Paraíba – UFPB, Programa de Pós-graduação em Engenharia Civil e Ambiental, João Pessoa, PB, Brasil
[b]Universidade Federal da Integração Latino-Americana – UNILA, Instituto Latino-Americano de Tecnologia, Infraestrutura e Território, Foz do Iguaçu, PR, Brasil

Received 23 May 2019
Accepted 18 June 2020

Abstract: In this paper we present a set of MATLAB routines for evaluation of the moment-curvature relationship of reinforced concrete cross sections. This is a topic of major importance for both academic and practical design purposes in the context of structural engineering. The computational routines were developed to be simple, general and flexible. This allows wide practical application and future improvements and modifications. The well-known fibers approach is employed, but an alternative development of the method is also presented. This is interesting from the conceptual point of view. Finally, numerical comparisons are presented to validate the routines.

Keywords: reinforced concrete, moment-curvature, computational routines, non-linear analysis.

Resumo: Neste trabalho apresenta-se um conjunto de rotinas do MATLAB para calcular a relação momento-curvatura de seções transversais de concreto armado. Este é um assunto de grande importância para fins acadêmicos e práticos de projeto no contexto da engenharia estrutural. As rotinas computacionais foram desenvolvidas de forma a serem simples, gerais e flexíveis. Isso permite ampla aplicação prática e futuras melhorias e modificações. A conhecida abordagem das lamelas foi utilizada, no entanto também é apresentado um desenvolvimento alternativo do método, que é interessante do ponto de vista conceitual. Por fim, são apresentadas comparações numéricas para validação das rotinas.

Palavras-chave: concreto armado, momento-curvatura, rotinas computacionais, análise não linear.

How to cite: G. F. Melo, A. J. Torii, E. M. Medeiros, and A. K. L. Kzam, "MATLAB computational routines for moment-curvature relation of reinforced concrete cross sections," *Rev. IBRACON Estrut. Mater.*, vol. 14, no. 2, e14202, 2021, https://doi.org/10.1590/S1983-41952021000200002

1 INTRODUCTION

Evaluation of the moment-curvature relation of reinforced concrete cross sections is a problem of significant importance in structural engineering, with wide application to both scientific and design purposes. For this reason, it has been subject of intense investigation over the last decades. The main goal of this work is to present a set of simple, general and flexible computational routines for the problem at hand. The routines were developed in MATLAB programing language and are intended mainly for engineering education and academic purposes.

Corresponding author: Gabriel Figueiredo de Melo. E-mail: gabrielfmelo@hotmail.com
Financial support: None.
Conflict of interest: Nothing to declare.

Several approaches to obtain the moment-curvature relation have been proposed over the years. In general, the most significant difference between them concerns how integration of the stress field is made. Conceptually, evaluation of the moment-curvature relation requires integration of the stress field over the cross section to evaluate force and moment resultants. According to Papanikolaou [1], most approaches can be broadly classified into methods that employ: a) analytical integration; b) fiber integration and c) numerical integration. An interesting conceptual comparison between these approaches was presented by Papanikolaou [1]. Here we present only a brief account of works from the past three decades that are relevant to the present study. For an extensive review on the subject the reader may refer to Kwak and Kim [2]; Papanikolaou [1]; Vaz Rodrigues [3]; Simão et al. [4].

Tsao and Hsu [5] presented a general approach for building moment-curvature relations of reinforced concrete sections that was latter named the fiber approach (Spacone et al. [6]; Sfakianakis [7]). Fafitis [8] presented an approach based on Green's Theorem that only requires boundary integrals, evaluated with Gauss quadrature. The work by Kwak and Kim [9] employed moment-curvature relations for non-linear structural analysis of reinforced concrete beams, but no emphasis was given to how moment-curvature relations for arbitrary cross sections can be obtained. Bonet et al. [10] presented a general approach for building the moment curvature relation or reinforced concrete beams, employing Gaussian quadrature and integration cells. Papanikolaou [1] presented a general approach for arbitrary cross sections that employs an adaptive Gaussian quadrature scheme. A particularly good review on the subject was also presented in the work by Papanikolaou [1]. Vaz Rodrigues [3] adopted a novel technique based on computer graphics for subdivision of the cross-section domain together with Gaussian quadrature. The works by Kwak and Kim [2]; Simão et al. [4] also addressed the application of moment-curvature relations for structural analysis, but no emphasis was given to how moment-curvature relations can be obtained. Finally, even though Liew et al. [11] studied the moment-curvature relation for metal cross section, the work illustrates how these concepts are important in a wider sense in the context of structural engineering.

Unfortunately, analytical integration of the stress field is possible only in the case of very simple cross sections and simple constitutive laws. For this reason, approaches based on analytical integration are generally limited to simple cross sections and polynomial constitutive laws. Otherwise, some computational scheme is necessary.

In the case of the fiber approach [5]–[7], the cross section is divided into rectangles (fibers). Force and moment resultants are then evaluated considering the contribution of each fiber. The main advantage of this approach is its simplicity from both the conceptual and computational point of view, since it employs the intuitive notion of summation of the fiber's contribution instead of abstract numerical quadrature schemes. Consequently, it is also very flexible and general. However, some authors argue that the resulting computational routines may be slow [1], since a large number of fibers may be required to obtain sufficient accuracy in some cases.

To improve computational efficiency, later works focused on improved quadrature schemes, such as the works by Fafitis [8]; Bonet et al. [10]; Papanikolaou [1]; Vaz Rodrigues [3]. In this case, integration of the stress field is made using standard quadrature rules from numerical analysis (Atkinson [12]; Burden and Faires [13]). The resulting methods are generally more efficient than the fiber approach, but the use of standard quadrature rules leads to some issues. First, in several cases it is necessary to employ some subdivision of the cross section into integration cells, a procedure that increases the overall complexity of the computational routines. Besides, most available quadrature rules are inefficient for integration of discontinuous functions [12], [13]. Consequently, numerical quadrature schemes require a fine integration mesh when discontinuous constitutive laws are employed. In some cases, the resulting computational effort may be increased so much that no significant gain in efficiency is observed in comparison to fiber based approaches.

In this work we present a set of general, flexible, and simple computational routines for building the moment-curvature of reinforced concrete sections. The routines are intended for engineering education and academic purposes. Integration of the stress field is made using the fiber approach. An alternative development of the fibers approach is presented, that is interesting from the conceptual point of view. The resulting algorithm does not require meshing of the cross section into integration cells and has no issues with discontinuous constitutive laws. The results are compared to those obtained with the software Response 2000, that is described in detail by Bentz [14].

This paper is organized as follows. In Section 2 we present a brief review on the behavior of RC cross sections. The quadrature scheme used for evaluation of the axial and moment resultants is described in Section 3. A procedure for obtaining the moment-rotation diagram is described in Section 4. In Section 5 the constitutive laws employed are described. Numerical examples are presented in Section 6 to validate the routines developed. The conclusions are presented in Section 7. The computational routines developed are detailed in the Appendix A.

2 STRUCTURAL MODEL OF THE CROSS SECTION

We assume the z axis is aligned with the beam axis, the x axis is the direction of the applied bending moment and the y axis is that orthogonal to both x and y. In this case the cross section is defined in the xy plane, with bending moment applied on the direction of x. The axes are represented in Figure 1.

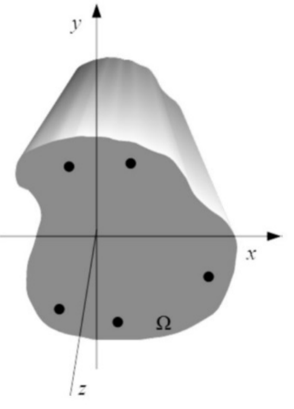

Figure 1. Axes.

If cross sections remain plane after deformation, the strain field on the cross section can be written as

$$\varepsilon(y,\theta,y_c) = (y - y_c)\tan\theta \tag{1}$$

where θ is the rotation of the cross section and y_c is the position of the neutral axis measured in the direction of y. The resulting strain field is represented in Figure 2. Compression strains and stresses are assumed to be positive. Finally, note that that the strain field varies linearly over the cross-section height y and depends on θ and y_c.

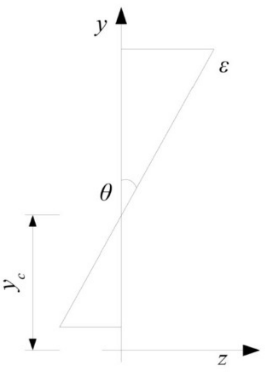

Figure 2. Strain Field.

The axial force and the bending moment resultants are given by

$$N(\theta, y_c) = \int_{\Omega} \sigma_c dxdy + \sum_{j=1}^{n_r} A_{sj}\sigma_{sj} \tag{2}$$

$$M(\theta, y_c) = \int_{\Omega} (y_c - y)\sigma_c dxdy + \sum_{j=1}^{n_r} (y_c - y_{sj})A_{sj}\sigma_{sj} \tag{3}$$

where Ω represents the cross section domain (see Figure 3), σ_c is the stress field in the concrete, A_{sj} are the cross sectional areas of the rebars (reinforcement bars), σ_{sj} are the stresses in the rebars, y_{sj} are the position of the rebars and n_r is the number of rebars. Note that both N and M depend on θ and y_c, since these two variables define the strain field and, consequently, the stress field.

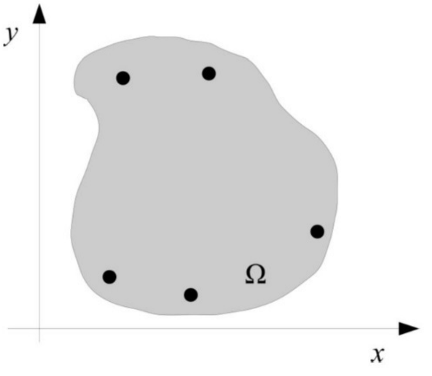

Figure 3. Cross section.

The curvature κ at any point of a beam is (Timoshenko [15]; Hibbeler [16])

$$\kappa = \frac{1}{\rho} = \frac{d^2\upsilon / dz^2}{[1 + (d\upsilon / dz)^2]^{3/2}} \tag{4}$$

where ρ is the curvature radius, υ is the transversal displacement and z is the longitudinal axis. If sections orthogonal to the neutral axis remains so after displacements take place, we can write

$$\theta = \frac{d^2\upsilon}{dz^2} \tag{5}$$

For small slopes we have $d / dz \to 0$ and, from Equation 4, $\kappa \approx \theta$. This indicates that the curvature is approximately equal to the rotation under small slopes.

3 QUADRATURE RULE: FIBERS APPROACH

For given values of θ and y_c, the contributions of the rebars for N and M (Equations 2 and 3) can be easily evaluated by summation. Evaluation of the contribution from concrete, on the other hand, requires integration of the stress field over the cross section. As discussed in the introduction, this is the main difficulty in evaluation of the moment-curvature relation for arbitrary cross sections. If the geometry of the cross section and the constitutive law are simple, the required integrals can be evaluated analytically. However, when the cross-section geometry is complex, the above integrals require numerical quadrature.

The fiber approach is employed for integration of the stress field [5]–[7]. However, we present an alternative development of the scheme that puts in evidence some interesting conceptual properties. For this purpose, we first define a rectangular integration domain

$$\bar{\Omega} = \left\{(x, y) \in \mathbb{R}^2 \mid x_l \le x \le x_u, y_l \le y \le y_u\right\} \tag{6}$$

that contains the entire cross section, i.e. that satisfy

$$\Omega \subseteq \bar{\Omega}. \tag{7}$$

The integration domain $\bar{\Omega}$ and the cross section Ω are represented in Figure 4. Note that the integration domain is a box that contains the entire cross section.

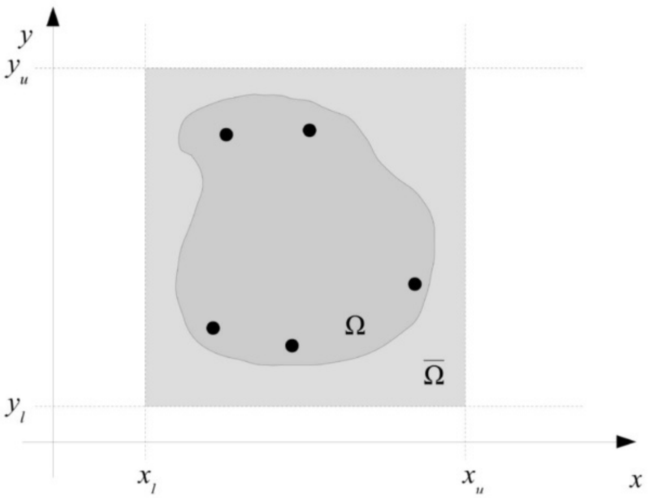

Figure 4. Cross section Ω and integration domain $\bar{\Omega}$.

The geometry of the cross section is then represented using an indicator function defined as

$$I(x, y) = \begin{cases} 1, (x, y) \in \Omega \\ 0, (x, y) \notin \Omega \end{cases} \tag{8}$$

The indicator function simply returns 1 if the point (x, y) is inside the cross-section domain Ω and 0 otherwise.

Integration of some function $f(x, y)$ over the cross section Ω can then be written as

$$\int_{\Omega} f(x, y)\,dxdy = \int_{\bar{\Omega}} I(x, y) f(x, y)\,dxdy \tag{9}$$

In this case, integration over the cross section Ω is substituted by integration over the entire integration domain $\bar{\Omega}$. Multiplication by the indicator function is employed to take into account that only points inside Ω should be considered.

We then generate a sample of points with uniform distribution on the integration domain Ω. Several schemes can be employed for this purpose, such as random sample generation [17], [18]. A uniform grid of equally spaced points in each direction is employed, as illustrated in Figure 5. This uniform grid is built as described in the computational routines in Appendix A.

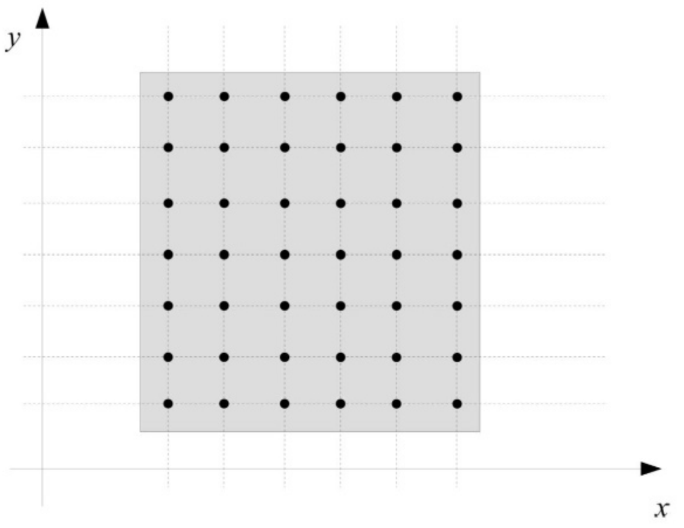

Figure 5. Uniform quadrature grid.

If n_x points are employed in each direction, then the total number of grid points is $n = n_x^2$. These grid points are collected into the sample set

$$S = \{(x_1, y_1), (x_2, y_2), \ldots, (x_n, y_n)\} \tag{10}$$

where n is the sample size. The quadrature rule for the integral from Equation 9 can then be written as

$$\int_{\Omega} f(x,y)dxdy = \int_{\bar{\Omega}} I(x,y) f(x,y)dxdy \approx \sum_{i=1}^{n} w_i I(x_i, y_i) f(x_i, y_i) \tag{11}$$

where w_i are quadrature weights and the grid points (x_i, y_i) are taken as the quadrature nodes.

To obtain the quadrature weights, note that the area of the integration domain is given by

$$\bar{A} = (x_u - x_l)(y_u - y_l) \tag{12}$$

Applying the quadrature rule from Equation 11 gives

$$\bar{A} = \int_{\bar{\Omega}} 1dxdy \approx \sum_{i=1}^{n} w_i \tag{13}$$

Since the sample points follow a uniform distribution, we can assume that all quadrature points have the same weight w_i and from Equation 13

$$w_i = \frac{\bar{A}}{n} \tag{14}$$

Substitution of the quadrature weights into Equation 11 gives the quadrature rule

$$\int_{\Omega} f(x,y)dxdy \approx \bar{A}\left[\frac{1}{n}\sum_{i=1}^{n} I(x_i,y_i)f(x_i,y_i)\right] \tag{15}$$

From Equation 15 we observe that the integral is given by multiplication of the area of the integration domain $\bar{A}$ by the sample mean of the integrand, and thus the approach is similar to Monte Carlo Simulation [17], [18] from the computational point of view. Finally, multiplication by $I(x_i, y_i)$ in Equation 15 implies that only quadrature points inside the cross section are actually considered. Consequently, the summation from Equation 15 can be evaluated by discarding quadrature points outside the cross section.

Employment of the quadrature rule from Equation 15 to Equations 2 and 3 gives

$$N(\theta,y_c) \approx \bar{A}\left[\frac{1}{n}\sum_{i=1}^{n} I(x_i,y_i)\sigma_c(x_i,y_i)\right] + \sum_{j=1}^{n_r} A_{sj}\sigma_{sj} \tag{16}$$

$$M(\theta,y_c) \approx \bar{A}\left[\frac{1}{n}\sum_{i=1}^{n} I(x_i,y_i)(y_c-y_i)\sigma_c(x_i,y_i)\right] + \sum_{j=1}^{n_r} (y_c-y_{sj})A_{sj}\sigma_{sj} \tag{17}$$

where $\sigma_c(x_i, y_i)$ is the stress on the concrete at position (x_i, y_i).

4 MOMENT-ROTATION RELATIONSHIP

To evaluate the moment-rotation diagram, the resulting moment is evaluated for a set or prescribed rotations θ_0, θ_1, θ_2, ... in a given interval $[0, \theta_f]$. Assuming m rotations increments are applied we have

$$\begin{cases} \theta_0 = 0 \\ \theta_1 = \theta_0 + \Delta\theta \\ \theta_2 = \theta_1 + \Delta\theta \\ \vdots \\ \theta_m = \theta_{m-1} + \Delta\theta \end{cases} \tag{18}$$

where

$$\Delta\theta = \frac{\theta_f}{m} \tag{19}$$

is the rotation increment.

For a given rotation θ_i, the position of the neutral axis y_c is the root of the equation

$$N(\theta_i, y_c) = 0 \tag{20}$$

where we consider, without loss of generality, that no axial forces are applied. The root of the above equation is obtained with the Bisection Method [12], [13]. The axial resultant is evaluated using Equation 16. After the position of the neutral axis y_c is found, the resulting moment can be evaluated using Equation 17.

5 CONSTITUTIVE LAWS

The proposed approach is general and can be employed together with any constitutive law for concrete and steel. In this work very simple constitutive laws are employed in order to focus on the approach rather than on the mechanical properties of the materials. More refined constitutive laws can be found in Chen [19]; CEB-FIP [20]; Bentz [14] and other more recent references on the subject.

In the case of concrete, the resistance in tension is neglected and the parabolic model is employed in compression. The resulting stress-strain relationship is

$$\sigma_c(\varepsilon_c)=\begin{cases}0 & ,\varepsilon_c<0\\ f_c\left[1-\left(1-\dfrac{\varepsilon_c}{\varepsilon_{c2}}\right)^2\right] & ,0\leq\varepsilon_c<\varepsilon_{c2}\\ f_c & ,\varepsilon_{c2}\leq\varepsilon_c<\varepsilon_{cu}\\ 0 & ,\varepsilon_c>\varepsilon_{cu}\end{cases} \tag{21}$$

where ε_c is the strain in the concrete, f_c is the resistance in compression, ε_{c2} = 2.0/1000 and ε_{cu} = 3.5/1000.

For steel, an elastic-perfectly plastic model is employed. We also assume perfect bond between steel and concrete, resulting in the stress-strain relationship

$$\sigma_s(\varepsilon_s)=\begin{cases}\varepsilon_s E_s & ,0\ \leq|\varepsilon_s|\leq\varepsilon_{sy}\\ f_y\,\varepsilon_s/|\varepsilon_s| & ,\varepsilon_{sy}\leq|\varepsilon_s|\leq\varepsilon_{su}\\ 0 & ,|\varepsilon_s|>\varepsilon_{su}\end{cases} \tag{22}$$

where ε_s is the strain in the steel, f_y is the yielding stress, ε_{su}=10/1000, ε_{sy}=f_y /E_s and E_s=210GPa. In the above equation the quantity ε_s /|ε_s| is only employed to consider the sign of the strain.

Note that positive signs are employed for compression. Besides, the resistances must be weighted by partial factors when the model is employed for design purposes. The stress-strain relation for concrete with f_c = 30MPa and for steel with f_y = 400MPa are presented in Figures 6 and 7, for illustration purposes.

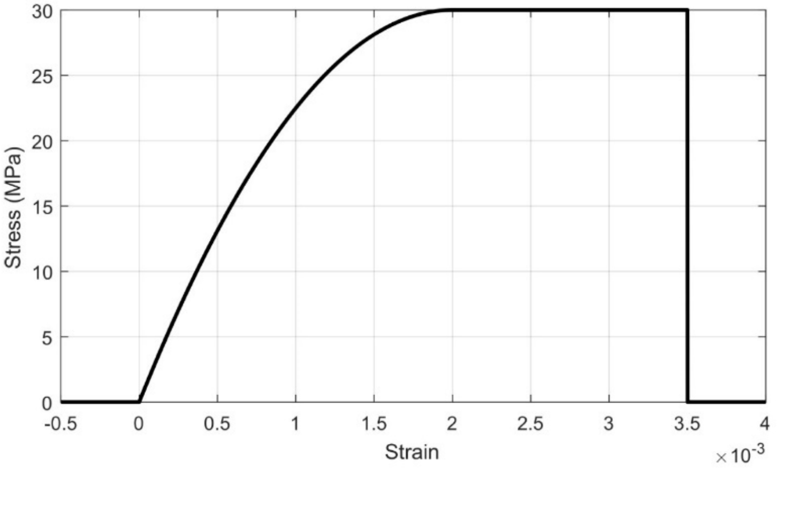

Figure 6. Stress-strain relation for concrete with f_c = 30MPa.

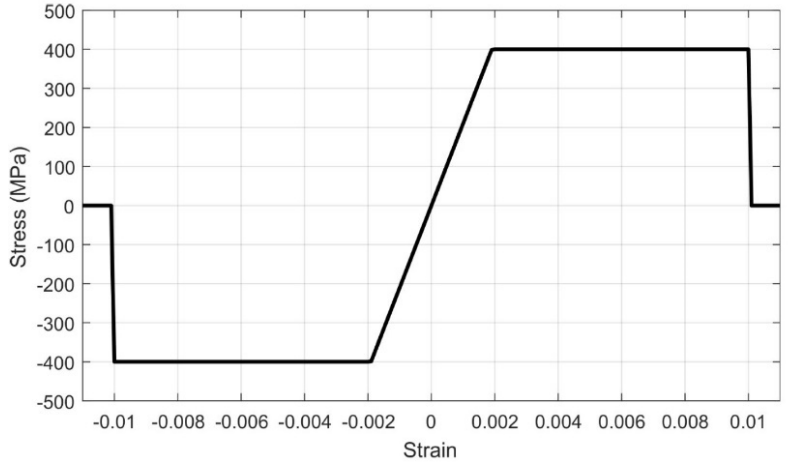

Figure 7. Stress-strain relation for steel with f_y = 400MPa.

6 EXAMPLES

6.1 Rectangular cross section

In the first example we study the cross section from Figure 8. The cross section is a rectangle with width b=200mm and height h=500mm. The material properties were taken as f_c=40MPa and f_y=500MPa. The centroids of the three bottom and two top rebars are positioned at 40mm and 460mm from the bottom of the cross section, respectively. Each rebar has a cross sectional area equal to A_{sj}=123mm^2. The limits of the integration domain were set as x_l=y_l=0mm, x_u=200mm and y_u=500mm. The sample size employed for numerical quadrature was n=10^4.

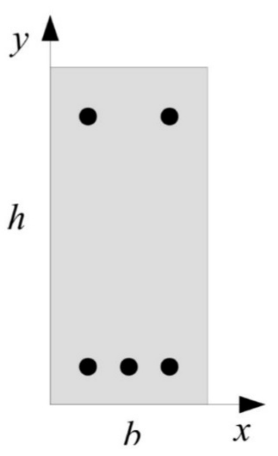

Figure 8. Rectangular cross section.

The results obtained with the approach proposed in the present work are compared to the results obtained with Response 2000 in Figure 9. As can be observed, the results obtained are very similar, which validates the proposed approach. The minor differences observed are mainly due to divergences in the constitutive laws, as there are only a few predefined constitutive laws that can be chosen in Response 2000 and some parameters cannot be modified by the user.

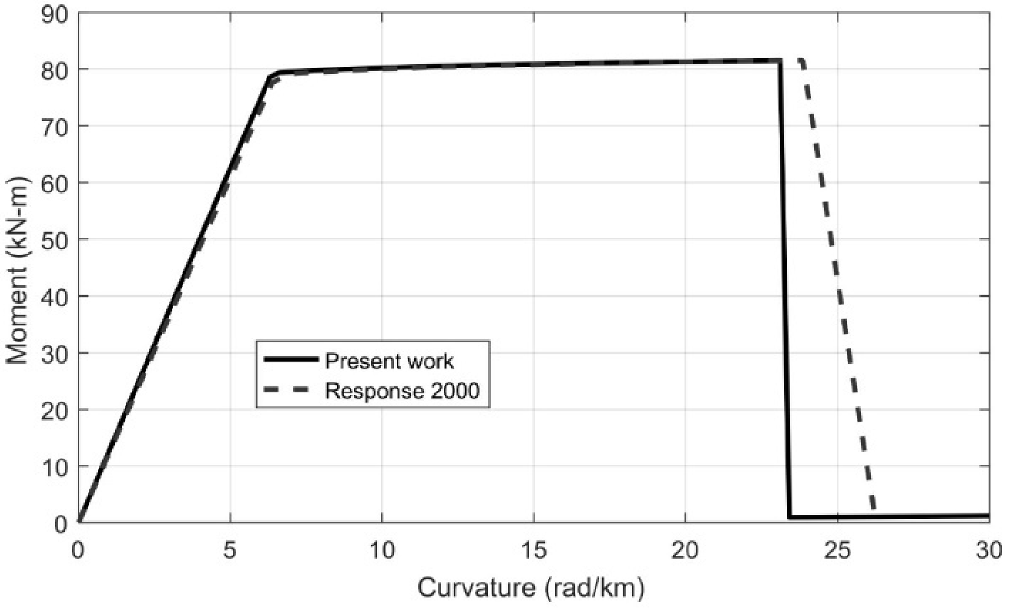

Figure 9. Moment-curvature of rectangular cross section.

6.2 Ellipsoidal cross section

In the second example we study the cross section from Figure 10. The input data of this example is detailed in the Appendix A. The cross section is an ellipse with radius a=100mm and b=200mm about axis x and y, respectively. The material properties were taken as f_c=30MPa and f_y=400MPa. The rebars have cross sectional areas A_s=123mm^2 with centroids positioned at (−30, −150) mm, (+30, −150) mm, (−70, 0) mm, (+70, 0) mm and (0, +150) mm. The limits of the integration domain were set as x_l=y_l=−200mm and x_u=y_u=+200mm. The sample size employed for numerical quadrature was n=10^4. The sample points located inside the cross section and the rebars are shown in Figure 11. We observe that the sample reproduces the geometry of the cross section, as expected.

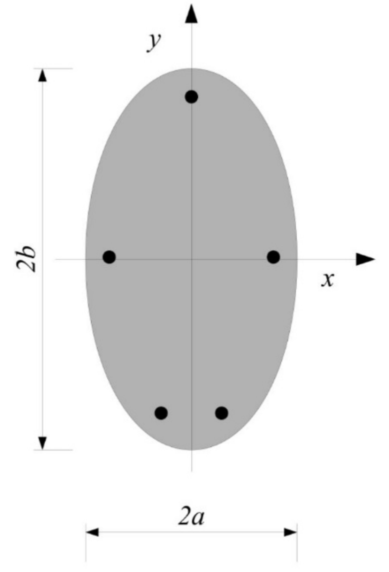

Figure 10. Ellipsoidal cross section.

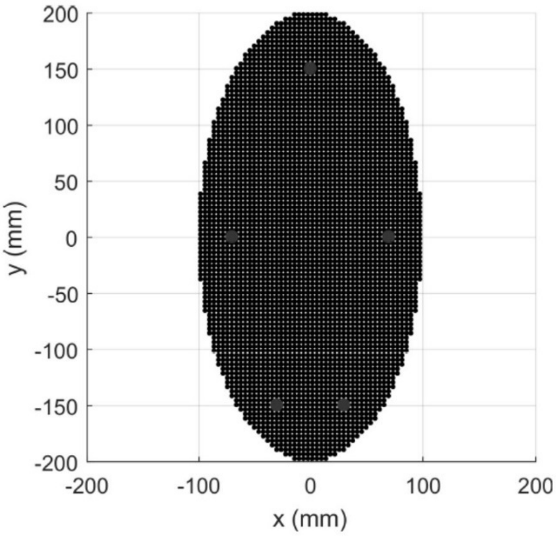

Figure 11. Ellipsoidal cross section sample points.

The moment-rotation diagram is presented in Figure 12. The results are compared to those obtained by Response 2000. Again, the results agree, indicating that the proposed approach can obtain accurate results.

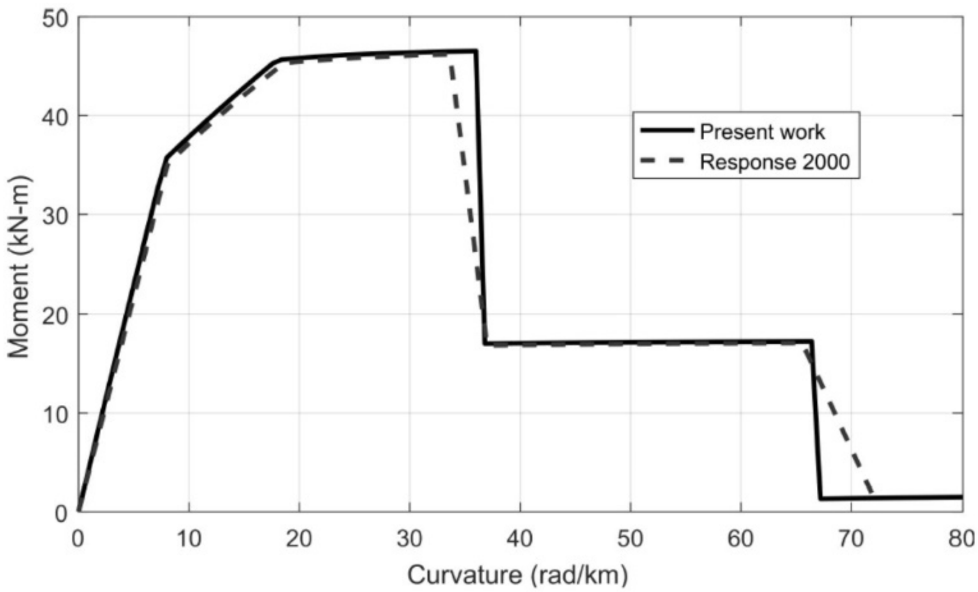

Figure 12. Moment-rotation diagram for the ellipsoidal cross section.

6.3 Bridge cross section

In the last example we study the cross section from Figure 13, where the dimensions are presented in mm. The coordinates of the vertices of the cross section are detailed in the Appendix A. The material properties were taken as f_c=50MPa and f_y=500MPa. The rebars have cross sectional areas A_s=491mm^2. The reinforcement layers are distant 50 mm, 100 mm, 400 mm, 575 mm, 750 mm, 925 mm, 1100 mm and 1450 mm from the bottom of the cross section, respectively. The limits of the integration domain were set as x_l=−1300mm, x_u=1300mm, y_l=0mm and y_u=1500mm. The sample size employed for numerical quadrature was n=10^4. The sample points located inside the cross section and the rebars are shown in Figure 14. The moment-rotation diagram is presented in Figure 15. We observe that the results are very similar to those obtained with Response 2000.

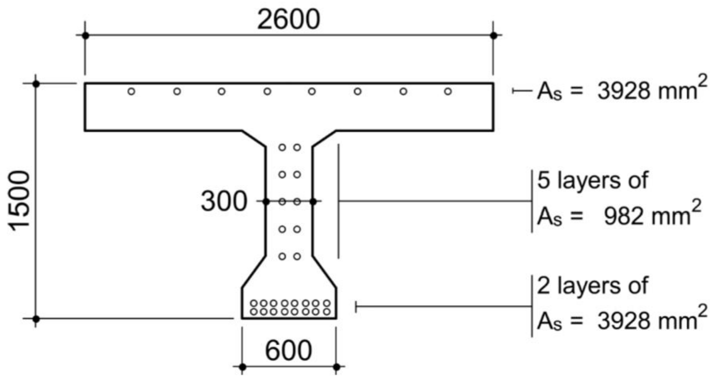

Figure 13. Bridge cross section.

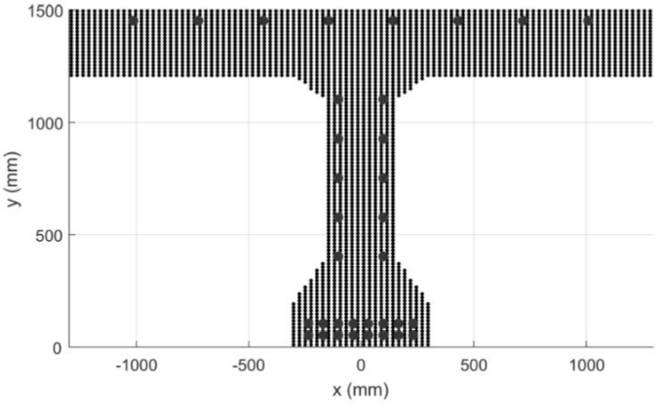

Figure 14. Bridge cross section sample points.

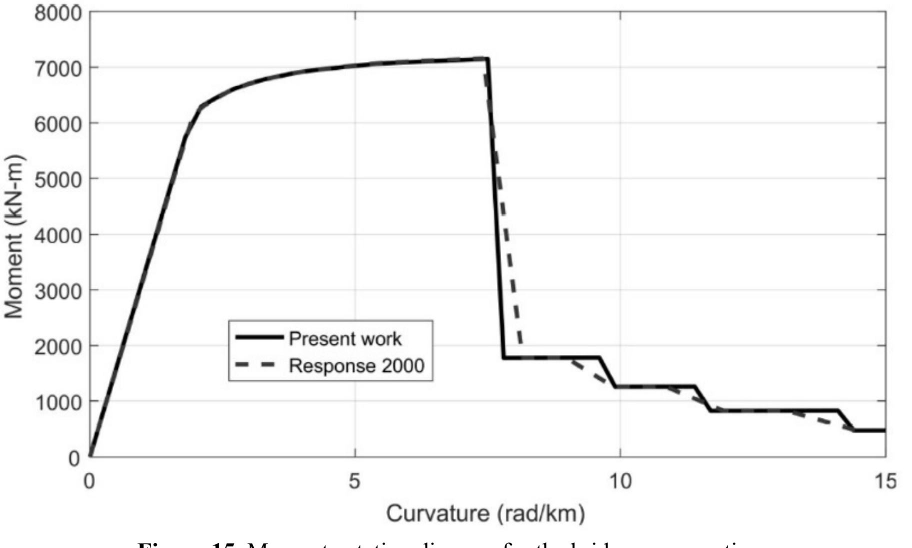

Figure 15. Moment-rotation diagram for the bridge cross section.

7 CONCLUDING REMARKS

In this work we presented a set of MATLAB computational routines for obtaining the moment-curvature relation of reinforced concrete cross sections. The routines are simple, general, and flexible, allowing wide practical application, future improvements and modifications. The routines were validated by numerical examples. An alternative development of the well-known fibers approach is also demonstrated, that is interesting from the conceptual point of view.

We emphasize that several improvements and modifications can be easily implemented in the presented routines. Axial forces can be included by modification of Equation 20 and more advanced constitutive laws can be modeled in Equations 21 and 22. It is also possible to replace Bisection Method for finding the position of the neutral axis by more advanced root finding methods. Finally, biaxial bending can be addressed by rotation of the cross-section axes.

These routines are valuable for engineering education and academic purposes. From the academic point of view, the routines are valuable since they are open source. There are many computer programs that are able to obtain the moment-curvature relation of reinforced concrete cross sections. However, no open source codes on the subject are known by the authors. Researchers wishing to test some novel constitutive law in the context of beams, for example, will likely need to implement a new computational code or employ some commercial software, what is not always desirable. The provided routines try to fill this gap on the field.

It is worth mentioning that the proposed method differs from other methods (ex: Gauss Numerical Integration) because in addition to being less computationally efficient, it adequately solves continuous functions with discontinuities. Hence, the method proposed in this work aims to solve general problems in which the constitutive law is continuous but may contain some discontinuity.

The computational routines developed in this paper can be improved for instance by adopting a different number of integration points in x and y directions, using more points on one direction than on the other. However, since our aim is to implement a didactic and elementary strategy that allows for improvements, such improvements should be carried out in future works.

From the education point of view, the routines can be employed in a wide range of situations. First, they can be used to evaluate the ultimate resistance and the moment-curvature relation in several interesting cases. The routines can also be employed to show how different constitutive laws will impact the results obtained, for example. Finally, more advanced students may modify the routines to take into improvements and modifications.

REFERENCES

[1] V. K. Papanikolaou, "Analysis of arbitrary composite sections in biaxial bending and axial load," *Comput. Struc.*, vol. 98-99, pp. 33–54, 2012, http://dx.doi.org/10.1016/j.compstruc.2012.02.004.

[2] H.-G. Kwak and S.-P. Kim, "Simplified monotonic moment-curvature relation considering fixed-end rotation and axial force effect," *Eng. Struct.*, vol. 32, no. 1, pp. 69–79, 2010, http://dx.doi.org/10.1016/j.engstruct.2009.08.017.

[3] R. Vaz Rodrigues, "A new technique for ultimate limit state design of arbitrary shape RC sections under biaxial bending," *Eng. Struct.*, vol. 104, pp. 1–17, 2015, http://dx.doi.org/10.1016/j.engstruct.2015.09.016.

[4] P. D. Simão, H. Barros, C. C. Ferreira, and T. Marques, "Closed-form moment-curvature relations for reinforced concrete cross sections under bending moment and axial force," *Eng. Struct.*, vol. 129, pp. 67–80, 2016, http://dx.doi.org/10.1016/j.engstruct.2016.09.033.

[5] W. H. Tsao and C. T. T. Hsu, "A nonlinear computer analysis of biaxially loaded L-shaped slender reinforced concrete columns," *Comput. Struc.*, vol. 49, no. 4, pp. 579–588, 1993, http://dx.doi.org/10.1016/0045-7949(93)90062-I.

[6] E. Spacone, F. C. Filippou, and F. F. Taucer, "Fibre beam-column model for non-linear analysis of R/C frames: part I. Formulation," *Earthquake Eng. Struct. Dynam.*, vol. 25, no. 7, pp. 711–725, 1996, http://dx.doi.org/10.1002/(SICI)1096-9845(199607)25:7<711:AID-EQE576>3.0.CO;2-9.

[7] M. G. Sfakianakis, "Biaxial bending with axial force of reinforced, composite and repaired concrete sections of arbitrary shape by fiber model and computer graphics," *Adv. Eng. Softw.*, vol. 33, no. 4, pp. 227–242, 2002, http://dx.doi.org/10.1016/S0965-9978(02)00002-9.

[8] A. Fafitis, "Interaction surfaces of reinforced-concrete sections in biaxial bending," *J. Struct. Eng.*, vol. 127, no. 7, pp. 840–846, 2001., http://dx.doi.org/10.1061/(ASCE)0733-9445(2001)127:7(840).

[9] H.-G. Kwak and S.-P. Kim, "Nonlinear analysis of RC beams based on moment–curvature relation," *Comput. Struc.*, vol. 80, no. 7-8, pp. 615–628, 2002, http://dx.doi.org/10.1016/S0045-7949(02)00030-5.

[10] J. L. Bonet, M. L. Romero, P. F. Miguel, and M. A. Fernandez, "A fast stress integration algorithm for reinforced concrete sections with axial loads and biaxial bending," *Comput. Struc.*, vol. 82, no. 2-3, pp. 213–225, 2004, http://dx.doi.org/10.1016/j.compstruc.2003.10.009.

[11] A. Liew, L. Gardner, and P. Block, "Moment-curvature-thrust relationships for beam-columns," *Structures*, vol. 11, pp. 146–154, 2017, http://dx.doi.org/10.1016/j.istruc.2017.05.005.

[12] K. E. Atkinson, *An Introduction to Numerical Analysis*, 2nd ed. New York, NY: Wiley, 1989.

[13] R. L. Burden and J. D. Faires, *Numerical Analysis*, 9th ed. Belmont, CA: Thomson Brooks/Cole, 2011.

[14] E. C. Bentz, “Sectional analysis of reinforced concrete members,” Ph.D. thesis, Graduate Dept. Civil Eng., Univ. Toronto, Toronto, Canada, 2000.

[15] S. Timoshenko, *Strengh of Materials*, 2nd ed. New York, NY: D. Van Nostrand Company, Inc., 1940.

[16] R. C. Hibbeler, *Mechanics of Materials*, 8th ed. Upper Saddle River, NJ: Prentice Hall, 2011.

[17] S. M. Ross, *Simulation*, 4th ed. New York, NY: Elsevier, 2006.

[18] R. Y. Rubinstein and D. P. Kroese, *Simulation and the Monte Carlo Method*, 2nd ed. Hoboken, NJ: Wiley-Interscience, 2008.

[19] W. F. Chen, *Plasticity in Reinforced Concrete.* New York, NY: McGraw-Hill, 1982.

[20] Comité Euro-International du Béton, *CEB-FIP model code 1990.* Lausanne, Switzerland: Thomas Telford, 1991.

Author contributions: Gabriel Figueiredo de Melo: development of methods, computational implementation, and manuscript writing. André Jacomel Torii: development of methods, computational implementation, and manuscript writing. Eduardo Morais de Medeiros: conceptual discussions and manuscript review. Aref Kalilo Lima Kzam: conceptual discussions and manuscript review.

Editors: Osvaldo Luís Manzoli, José Luiz Antunes de Oliveira e Sousa, Guilherme Aris Parsekian.

APPENDIX A: COMPUTATIONAL ROUTINES

In this section we present the computational routines in MATLAB programming language. Interested readers can contact the corresponding author to obtain these routines. The flowchart that explains the operation of the Moment-Curvature routine is shown in Figure 16. In addition, the authors are willing to place the computer routines on the FileExchange platform of Matlab or on another open source platform, besides keeping them in the paper.

The input data is defined in function *data*. The input data for the example of the ellipsoidal cross section is presented in Algorithm 1. In lines 2-3 the resistances of concrete and steel are defined.

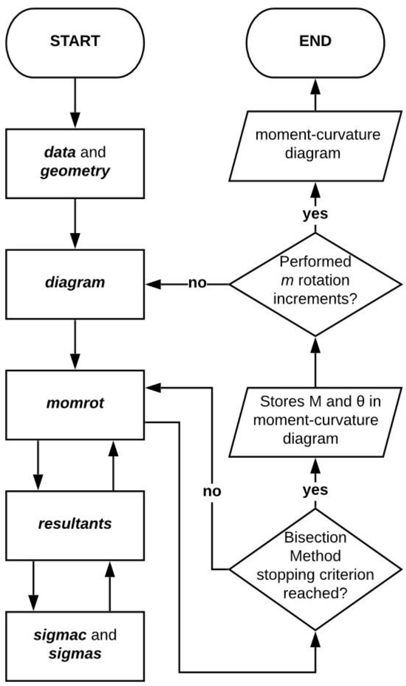

Figure 16. Moment-Curvature routines flowchart.

Algorithm 1 data.m (ellipsoidal)

```
1  function [ fc, fy, As, xl, xu, yl, yu, nx, tol, thetaf, m] = data
2  fc = 30;
3  fy = 400;
4  As = [123 -30 -150;
5  123 +30 -150;
6  123 -70 0;
7  123 +70 0;
8  123 0 +150];
9  xl = -200;
10 xu = 200;
11 yl = -200;
12 yu = 200;
13 nx = 100;
14 tol = 1e-3;
15 thetaf = 0.08 / 1000;
16 m = 100;
17 end
```

In lines 4-8 the rebars are described, using a matrix where each line represents a single rebar. The columns of matrix As contain the cross sectional areas, the *x* coordinate and the *y* coordinate of the rebars, respectively. The data at line 5 then represents a rebar with cross sectional area 123mm^2 positioned at $x = +30$mm $y = -150$mm, for example.

The limits of the rectangular integration domain are defined in lines 9-12. In line 13 we define the number of grid points in each direction. In line 14 the stopping criterion of the Bisection Method for finding the position of the neutral axis is defined. The total rotation to be applied to the section and the number of increments are defined in lines 15-16.

The indicator function of the cross section is defined in function *geometry*, that receives as input the position of some point and returns 1 if the point is inside the cross section and 0 otherwise. The function *geometry* for the examples studied is presented in Algorithms 2-4.

Algorithm 2 geometry.m (rectangular)

```
function I = geometry (x)
xv = [ 0 200 200 0 ] ;
yv = [ 0 0 600 600 ] ;
I = inpolygon (x (1), x (2), xv, yv) ;
end
```

Algorithm 3 geometry.m (ellipsoidal)

```
function I = geometry (x)
a = 100 ;
b = 200 ;
f = (x (1)/ a)^2 + (x (2)/ b)^2 - 1 ;
I = f <0;
end
```

Algorithm 4 geometry.m (bridge)

```
function I = geometry (x)
xv = [-300 -300 -150 -150 -300 -1300 -1300 1300 1300 300 150 150 300 300 ] ;
yv = [ 0 200 400 1100 1200 1200 1500 1500 1200 1200 1100 400 200 0 ] ;
I = inpolygon (x (1), x (2), xv, yv) ;
end
```

In these routines, the *x* and *y* coordinates of some point are stored in the components $x(1)$ and $x(2)$ of vector *x*, respectively. In Algorithms 2 and 4, the indicator function is evaluated using the native MATLAB function *inpolygon*. This function returns 1 when some point with coordinates $x(1)$ and $x(2)$ is inside the polygon defined by vertices xv and yv, that indicate the *x* and *y* coordinates of the vertices, respectively. In Algorithm 3, the indicator function is taken as 1 when the ellipse equation gives $f < 0$.

The moment-rotation diagram can be plotted using the commands from Algorithm 5. In line 1 the input data is read using *data*. In line 2 the function *diagram* is called with the data from the input file. The diagram is plotted in line 3. The ultimate moment M_u is the maximum bending moment resisted by the cross section and is evaluated in line 4.

Algorithm 5 Commands for plotting the moment-curvature diagram

```
1 [ fc, fy, As, xl, xu, yl, yu, nx, tol, thetaf, m ]=data ;
2 [ theta, M ] = diagram(fc, fy, As, xl, xu, yl, yu, nx, tol, thetaf, m) ;
3 plot (theta, M)
4 max(M)
```

The moment-rotation diagram is built with the function *diagram* from Algorithm 6. In lines 2-4 the quadrature weights are obtained. The number of rebars is evaluated at line 5. The uniform quadrature grid is built in lines 6-16. In lines 6-14 a uniform grid is built in the square [0, 0] × [1, 1]. Coordinate transformation to the rectangular integration domain is then made in lines 15-16. The resulting grid is stored in matrix S, where each line stores a given point and each column stores a given coordinate. The indicator function of the sample points is evaluated in lines 17-19, using the function *geometry* defined previously. Sample points outside the cross section are then deleted from the sample and the new sample size ns is evaluated in lines 20-21. In lines 22-26 the moment-rotation diagram is built, by finding the resulting bending moment for prescribed rotations with function *momrot*.

Algorithm 6 diagram.m

```
1 function [ theta, M ] = diagram (fc, fy, As, xl, xu, yl, yu, nx, tol, thetaf, m)
2 A0 = (xu - xl) * (yu - yl) ;
3 n = nx ^ 2 ;
4 w = A0 / n ;
5 nr = size (As, 1) ;
6 du = 1 / nx ;
7 u = (du / 2): du: (1-du / 2) ;
8 k = 0 ;
9 for i =1: nx
10 for j = 1: nx
11 k = k + 1 ;
12 S(k,:) = [ u(i) u(j) ] ;
13 end
14 end
15 S (:, 1) = xl + S (:, 1) * (xu - xl) ;
16 S (:, 2) = yl + S (:, 2) * (yu - yl) ;
17 for i =1:n
18 I (i) = geometry (S(i,:)) ;
19 end
20 S(I ==0,:) = [ ] ;
21 ns = size (S, 1) ;
22 dtheta = thetaf / m;
23 for i =2: m
24 theta (i) = i * dtheta ;
25 M(i) = momrot (theta(i), ns, S, w, nr, As, fc, fy, yl, yu, tol) ;
26 end
27 end
28 function M = momrot (theta, ns, S, w, nr, As, fc, fy, yl, yu, tol)
29 a = yl ;
30 b = yu ;
31 Na = resultants (theta, ns, S, w, nr, As, a, fc, fy) ;
32 h0 = b - a;
33 it = ceil (log2 (h0 / tol)) ;
34 for i = 1: it
35 c = 0.5 * (a + b) ;
36 Nc = resultants (theta, ns, S, w, nr, As, c, fc, fy) ;
37 if Na * Nc < 0
38 b = c ;
39 else
40 a = c ;
41 Na = Nc ;
42 end
43 end
44 yc = 0.5 * (a + b) ;
45 [ N, M ] = resultants (theta, ns, S, w, nr, As, yc, fc, fy) ;
46 end
47 function [ N, M ] = resultants (theta, ns, S, w, nr, As, yc, fc, fy)
48 N = 0 ;
49 M = 0 ;
50 for i =1: ns
```

```
51 y = S(i, 2) ;
52 e = tan(theta) * (y - yc) ;
53 sigma = sigmac (e, fc) ;
54 N = N + w * sigma ;
55 M = M + w * sigma * (y - yc) ;
56 end
57 for i =1: nr
58 y = As (i, 3) ;
59 e = tan(theta) * (y - yc) ;
60 sigma = sigmas (e, fy) ;
61 N = N + sigma * As (i, 1) ;
62 M = M + sigma * As (i, 1) * (y - yc) ;
63 end
64 end
65 function sigma= sigmac (e, fc)
66 ec2 = 2.0 / 1000 ;
67 ecu = 3.5 / 1000 ;
68 n = 2 ;
69 if e < 0
70 sigma = 0 ;
71 else
72 if e > ecu
73 sigma = 0 ;
74 elseif e > ec2
75 sigma = fc ;
76 else
77 sigma = fc * (1 - (1 - e / ec2)^n) ;
78 end
79 end
80 end
81 function sigma = sigmas (e, fy)
82 Es = 210000;
83 esy = fy / Es ;
84 esu = 10 / 1000 ;
85 if abs (e) > esu
86 sigma = 0 ;
87 elseif abs (e) > esy
88 sigma = fy * e / abs (e) ;
89 else
90 sigma = e * Es ;
91 end
92 end
```

Evaluation of the resulting moment for a give rotation is made using the function *momrot*, defined at line 28. In lines 29-44 the position of the neutral axis is obtained using the Bisection Method in the interval [y_l, y_u], where function *resultants* evaluate the axial force resultant. The number of iterations to be performed is evaluated in line 33, considering the size of the original interval h0 and the stopping criterion tol, since each iteration of the method halves the search interval (Atkinson [12]; Burden and Faires [13]). After the position of the neutral axis is found, the resulting moment is evaluated in line 45.

The axial and moment resultants are evaluated with the function *resultants*, defined at line 47. Lines 50-56 are related to quadrature of the stress in the concrete, while lines 57-63 are related to the contribution of the axial forces on the rebars. The concrete and steel constitutive laws are modeled in the functions *sigmac* and *sigmas*, respectively, in lines 65-92.

IBRACON Structures and Materials Journal
Revista IBRACON de Estruturas e Materiais
IBRACON
SciELO
ISSN 1983-4195 ismj.org

ORIGINAL ARTICLE

Influence of granitic rock fines addition in the alkali-aggregate reaction (AAR) in cementitious materials

Influência dos finos de rocha granítica (FRG) nas propriedades físico-mecânicas e na reação álcali-agregado (RAA) de argamassas

Bruna Silva Santos[a]
Daniel Véras Ribeiro[b]

[a]Universidade Federal da Bahia – UFBA, Programa de Pós-graduação em Engenharia Civil – PPEC, Salvador/BA, Brasil
[b]Universidade Federal da Bahia – UFBA, Departamento de Ciência e Tecnologia dos Materiais, Salvador, BA, Brasil

Received 11 March 2020
Accepted 22 June 2020

Abstract: According to previous studies, fine materials originated from reactive aggregates can act as a Alkali-Aggregate Reaction mitigator, having its effectiveness dependent on their reactivity, fineness and added content. Thus, the present work aims to study if reactive granitic rock fines can mitigate or reduce the AAR and how the fineness of the material influences its mitigation capacity. For this purpose, granitic rock fines (GRF) from 2 different deposits and Pyrex glass fines (PGF) were tested as concrete addition. Each one of these fines were used in two different finesses and added to the concrete in the contents of 20% by mass of cement. It was observed that the addition of GRF did not affect the physical-mechanical properties of concrete and allowed the reduction in the AAR, being more accentuated with the increase of its specific surface.

Keywords: alkali-aggregate reaction, granitic rock fines, durability, performance.

Resumo: Segundo estudos anteriores, materiais finos provenientes de um agregado reativo podem agir como mitigadores da reação álcali-agregado (RAA), contudo, a efetividade da ação desses finos depende do seu grau de reatividade, finura e teor adicionado. Assim, o presente trabalho visa estudar se finos de rochas graníticas reativas (FRG), passante na peneira #200, podem mitigar ou reduzir a RAA e como a finura do material influencia na sua capacidade de mitigação. Para isso, foram utilizados FRG provenientes de 2 diferentes jazidas, obtidos após moagem. Cada adição foi utilizada em três finuras diferentes e adicionadas à argamassa nos teores de 10% e 20%, em relação à massa de cimento. Observou-se que a presença dos FRG não prejudicou as propriedades físico-mecânicas da argamassa, e ainda possibilitou redução da RAA, sendo mais acentuada à medida que se aumentou a superfície específica do material.

Palavras-chave: reação álcali-agregado, fino de rocha granítica, durabilidade, desempenho.

How to cite: B. S. Santos and D. V. Ribeiro, "Influence of granitic rock fines addition in the alkali-aggregate reaction (AAR) in cementitious materials," *Rev. IBRACON Estrut. Mater.*, vol. 14, no. 2, e14203, 2021, https://doi.org/10.1590/S1983-41952021000200003

1 INTRODUCTION

According to the Brazilian Mining Institute [1], in 2017, Brazil produced about 420 million tons of aggregates for civil construction. In the crushing process of the rocks, fine particulate materials are released, with particles smaller than 75 µm. This material is often improperly discarded, generating negative environmental impacts, besides being harmful to human health.

As an alternative to add value to this material, studies about its incorporation on concrete and mortars have been made. However, such alternative should be performed with caution, because some aggregates can cause a deleterious reaction to the concrete, known as the alkali-aggregate reaction [2].

Corresponding author: Daniel Véras Ribeiro. E-mail: verasribeiro@hotmail.com
Financial support: CNPq – National Counsel of Technological and Scientific Development (Brazil).
Conflict of interest: Nothing to declare.

The alkali-silica reaction (ASR), which will be studied in this article, is defined as a deleterious reaction of the concrete and occurs when the unstable silica, contained in some aggregates, reacts with the alkaline hydroxides present in the interstitial solution of the concrete, forming an expansive gel in the presence of water [2]. Priskulnik [3] presents the chemical reaction that represents ASR from sodium hydroxide (NaOH), being analogous for KOH potassium hydroxide, according to Equations 1 and 2.

$$SiO_2 \cdot nH_2O + 2NaOH \rightarrow SiO_3Na_2 + (n+1)H_2O \tag{1}$$

$$xSiO_2 \cdot nH_2O + 2NaO \rightarrow Na_2O \cdot xSiO_2 + (n+1)H_2O \tag{2}$$

In calcium-free systems, silica is dissolved and remains in solution. However, in the presence of calcium, the silica precipitates in the solution as an alkali-silicate gel (CaO-Na_2O/K_2O-SiO_2-H_2O) [4] and causes internal pressure that, by exceeding the tensile strength of the cement matrix, causes its differential expansion, leading to mechanical failures [5].

Dunant and Scrivener [6] describe the progress of expansion in three stages. Initially, the expansion is caused by the aggregate cracking and elastic deformation of the paste. In the transition period, the cracking propagates to the paste, presenting much larger expansions. Finally, the expansion generates a matrix cracking with subsequent depletion of the reactive materials.

For AAR to occur, three factors must occur simultaneously: sufficient amount of alkali in the interstitial solution of the concrete, high humidity level and existence of potentially reactive aggregate [2]. In the absence of at least one of these factors, the reaction does not occur. However, once the reaction has started, it cannot be interrupted. Therefore, the best way to prevent its action is to prevent the AAR from occurring. For this, it is necessary to be cautious when selecting the materials used in concrete production.

Priskulnik [3] indicates several factors that can contribute to the reduction and/or mitigation of the AAR, among them: decrease of concrete permeability due to the low water/cement ratio, dosage of an adequate cement consumption and use of active mineral additions, such as silica fume and blast furnace slag, because they fix cement alkalis in the initial phase of cement hydration and decrease the pH of the interstitial concrete solution.

Some materials, such as ground glass, when incorporated into the cement matrix may be favorable to the occurrence of the AAR or act as a mitigator, depending on the particle size of the material. When the glass is used in concrete with particle sizes greater than 0.5 mm, the development of the AAR is observed. However, when ground in dimensions smaller than 100 μm, it can present a pozzolanic behavior and reduce the expansion potential of the ASR [7].

Rajabipour et al. [8] explain that larger particles (in the small aggregate particle size range) of glass have micro cracks wide enough to allow the diffusion of hydroxyles, which will result in a high concentration of dissolved silica and sodium, since these will have greater difficulty in being released to the solution outside the crack. This high concentration will result in the ASR gel.

On the other hand, at the cement-glass interface, the gel formed is not expansive, since silica and sodium are not confined. Unlike what occurs in larger particles, in smaller particles (such as powders), the intraparticle AAR is minimal, prevailing the interfacial pozzolanic reaction.

As a theoretical basis for the present research, several authors have studied the influence of rock fines in the AAR and proposed theories to explain the reduction of AAR caused by the fines generated from reactive aggregates. In a direct way, due to the reduction of cement consumption, there is the reduction of alkaline ions, making it difficult to occur the AAR [9].

The reactive silica, when finely ground, contributes to the gel forming in a distributed manner in the cement paste. However, when it is present in the aggregates, it causes the accumulation of the alkali-silica gel in specific places, making them potential expansion points [10].

Wang et al. [11] concluded that fine materials can act in two ways on cement paste. Due to their fineness, they can act as nucleation points for the paste hydration and thus accelerate the production of portlandite.

On the other hand, due to the reactivity of the fine, it can react with the portlandite, resulting in a higher content of formed C-S-H, which has the capacity to agglutinate the alkalis present, thus reducing the AAR. However, the authors warn that, although the sand fines used could contribute to a greater retention of alkalis, the binding capacity is low due to their low reactivity.

He et al. [9] argue that the substitution of cement by reactive aggregate fines causes a reduction in ASR due to several factors. The reduction of cement consumption from the substitution of cement by fine causes a reduction in the alkali content available for the reaction. In addition, the presence of amorphous silica and high specific surface causes an increase in calcium hydroxide consumption due to pozzolanic activity, contributing to the reduction of the thickness of the ASR gel around the aggregate and reducing the effects of ASR. Despite reducing the expansion caused by ASR, the substitution of 50% of cement by fine reactive reduced the compressive strength by 35%, in mortars with water/(cement + GRF) ratio equal to 0.47%.

Carles-Gibergues et al. [12] used four types of reactive aggregate powders to investigate whether these materials are efficient in compensating the expansion of ASR caused by the large aggregate. The authors replaced 10 and 20% of the aggregate mass (0.08 to 4mm) with fine (less than 0.08mm) of different finesses, with specific Blaine surfaces varying between 100 and 650 m^2/kg. As a result, it was observed that the use of the reactive fines reduced the expansion of mortars and that the efficiency of the material depended on the origin, fineness and content used.

The larger surface area of the fine contributes to the higher dissolution rate of silica, resulting in a decrease in the Ca/Si ratio in the C-S-H formed during the hydration of the cement and increasing its capacity to fix the alkalis. The depletion of free alkalis decreases the pH of the pore solution, reducing the attack on the reactive aggregates [12]. Cyr et al. [2] studied the AAR in mortars with replacement of 10 and 20% of the sand by reactive aggregate fine (<80 μm) from 11 different types of aggregates. The authors observed a reduction of the expansion that varied from 19% to 78%, depending on the type of aggregate and highlighted some parameters that affect the efficiency of the fines, namely: silica content, fineness of the fine, available alkaline content and specific surface area.

The substitution of cement for the fines causes a reduction in the mechanical resistance of concrete and mortars, therefore, in the present work we have chosen to introduce the fines as an addition to the cement mass. Thus, it was studied how this addition of rock fines influences the physical-mechanical properties of mortars and the alkali-aggregate reaction. Additionally, it was studied if this accelerated reaction harms the physical-mechanical properties of the mortars tested.

2 MATERIALS AND EXPERIMENTAL PROGRAM

2.1 Materials

For the reactivity evaluation of the aggregates and evaluation of the efficiency granitic rock fines in the mitigation of ASR (item 2.3), a special cement with high content of alkalis produced by the Brazilian Association of Portland Cement (ABCP) was used, according to NBR 15577 [13]. For the physical-mechanical tests (item 2.4), Portland Cement CPII-F 32 was used, as it does not present pozzolanic additions and is a cement that does not mitigate the alkali-aggregate reaction. Table 1 shows the chemical composition of the cements used, determined by X-ray fluorescence spectrometry (XRF), using the Bruker S2 Ranger equipment.

Table 1. Chemical composition, in oxides, of the cements used.

Materials	**Compound (wt %)**										
	SiO_2	**Al_2O_3**	**Fe_2O_3**	**CaO**	**MgO**	**SO_3**	**K_2O**	**Na_2O**	**Others**	**Na_2O_{eq}***	**LOI**
CP II-F 32	16.13	3.67	3.04	60.73	3.90	5.30	1.78	0.00	0.49	1.17	4.97
CP ABCP	16.13	4.46	2.69	56.69	3.54	5.74	1.15	1.95	0.72	2.71	6.92

*LOI = Loss on ignition at 1000°C

Distilled deionized water was used in the molding of the mortars and in the preparation of the solution. The small aggregate used came from the crushing of granitic rock and has a specific mass of 2.77 g/cm^3. It was sifted, washed and, later, each granulometric fraction was weighed in order to obtain the granulometric composition determined by NBR 15577 [13].

The fines, passing fraction in sieve #200 (75 μm), used were the granitic rock fines (GRF), from two different quarries, defined as A and B, all of them being ground in order to obtain three distinct specific surface of each material. Table 2 presents the physical characterization of GRF obtained. The specific surface area was determined by BET (Gemini VII equipment from Micromeritics) and Blaine (Acmel automatic permeability, model BSA1) methods, and the specific mass by helium pycnometry (AccuPyc II 1340 Micromeritics).

Table 2. Physical characterization of the fines used

	Blaine surface area (cm^2/g)	BET surface area (m^2/kg)	Specific gravity (g/cm^3)	Average particle diameter (μm)
FA1	2042 ± 1	11500	2.86 ± 0.01	55.13
FA2	5936 ± 37	35200		8.39
FA3	6665 ± 30	46174		4.43
FB1	3521 ± 12	25700	2.83 ± 0.01	17.61
FB2	5233 ± 4	39500		7.71
FB3	6599 ± 13	52127		3.24

2.2 Characterization of materials

After obtaining the fines, they were characterized as to their granulometric distribution. For this, the Mastersizer 3000 Hydro 3000 laser granulometer was used.

The chemical compositions of the fines were determined by X-ray fluorescence spectrometry (XRF), using the Bruker S2 Ranger equipment and the pozzolanic activity was determined by chemical titration test, according to the European standard EN 196-5 [14], replacing 25% of the cement with fine.

The mineralogical characterization of cements and fines was performed by the X-ray diffraction (XRD), using a D2 Phaser, Bruker diffractometer, with 10mA and 30Kv copper target tube, wavelength (λ) equal to 0.15406nm, without filtering system with secondary monochromator. The diffraction spectra were obtained in the range 2θ from 5° to 70°, continuous mode at 0.1/s and the phases were identified using the software DIFFRAC plus-EVA, with the Crystallography Open Database (COD) centered database.

2.3 Evaluation of the alkali-aggregate reaction

In the analysis of the evaluation of the occurrence of the alkali-aggregate reaction and assessment of the efficiency of granitic rock fines in the mitigation of ASR, the accelerated method was used in mortar bars, according to NBR 15577 [13] in parts 4 and 5.

For these tests, mortars were molded with the formulation, in mass, of 1: 2,25: 0,47x (cement: aggregate: GRF: water), being x the GRF content, equal to 0 for the reference mortar (without GRF) and 0,10 and 0,20 for mortars containing 10% and 20% of GRF, respectively.

The introduction of granitic rock fines was performed in addition to cement so that it remained constant in all specimens studied, also keeping constant the cement/aggregate ratio. Moreover, a previous study showed that the substitution of cement by GRF, despite being efficient to reduce the AAR, caused a high loss of mechanical resistance [8].

Table 3 presents the nomenclature, the formulations, the water/(cement+GRF) ratio and cement consumption of the mortars studied. It is worth mentioning that in this stage all the formulations were molded using the cement supplied by ABCP.

Table 3. Design parameters of the of the mortars mixes

Nomenclature	Mix proportion by weight	Water/ (cement + GRF) ratio	Cement consumption (kg/m^3)
REF	1: 2.25: 0.47	0.47	600.10
A10FA1/A10FA2/A10FA3	1: 0.10: 2.25: 0.47	0.43	587.77
A20FA1/A20FA2/A20FA3	1: 0.20: 2.25: 0.47	0.39	575.93
A10FB1/A10FB2/A10FB3	1: 0.10: 2.25: 0.47	0.43	587.64
A20FB1/A20FB2/A20FB3	1: 0.20: 2.25: 0.47	0.39	575.69

For each formulation, three CPs (2.5 x 2.5 x 28.5 cm^3) were molded, according to NBR 15577-4 [13]. About 24 hours after molding, the CPs were immersed for 24 hours in distilled water at 80°C and then immersed in 1N Na(OH) solution at 80°C for 28 days. The specimen expansion was measured every two days.

2.4 Evaluation of the physical-mechanical characteristics of mortars

To evaluate the physical-mechanical characteristics of the mortars, the same formulations were used in the AAR tests (item 2.3), however, in this stage CP II-F 32 cement was used. Reference mortars (without GRF) and with the addition of GRF of Blaine surface area between 5000 and 6000 cm^2/g (index 2 fines) were molded, in 20% of the cement mass. For each formulation, 22 specimens (CPs) of 4 x 4 x 16 cm^3 dimensions were molded for physical-mechanical characterization of the mortars.

For mechanical strength performance analysis, axial compression and flexural tensile strength tests were performed at 3, 7 and 28 days of cure in water at 24°C, and after 28 days immersed in Na(OH) saturated solution, following NBR 13279 [15]. Four samples were tested in flexure and five samples in axial compression, using half of the CPs ruptured in flexure. In addition, the capillary water absorption, according to NBR 9779 [16] and apparent density and porosity, following NBR 9778 [17], were determined at 28 days of cure in water saturated with lime and at 28 days in Na(OH) solution.

The data obtained were statistically analyzed using single factor variance analysis (ANOVA) and when it indicated that at least one of the GRF significantly influenced the property, Tukey's test was used to verify which fine(s) caused such change.

3 RESULTS AND DISCUSSIONS

3.1 Characterization of materials

Table 4 shows the chemical composition, in oxides, of the GRF used. It can be observed that these have higher levels of silicon (SiO_2) and aluminum (Al_2O_3) oxides than the other oxides present in the material. It is noted that the aggregate used in this research has the same origin of FA and consequently the same chemical composition.

Table 4. Chemical composition, in oxides, of the granitic rock fines studied

Materials	Constituents (%)									
	SiO_2	Al_2O_3	Fe_2O_3	CaO	MgO	SO_3	K_2O	Na_2O	Outros	LOI*
FA	54.21	15.77	9.31	5.81	4.93	0.33	2.70	3.75	1.80	1.40
FB	59.66	15.63	8.93	5.26	4.33	0.86	2.36	0.00	1.29	1.69

*LOI = Loss on ignition at 1000°C

Figure 1 shows the granulometric distribution of cements and GRF used. Fines FA1 and FB1 have D50 larger than cements, while fines FA2, FB2 have D50 smaller than cements. Fines FA3 and FB3 have D50 smaller than index 2 fines due to the longer grinding time of the fines represented by index 3.

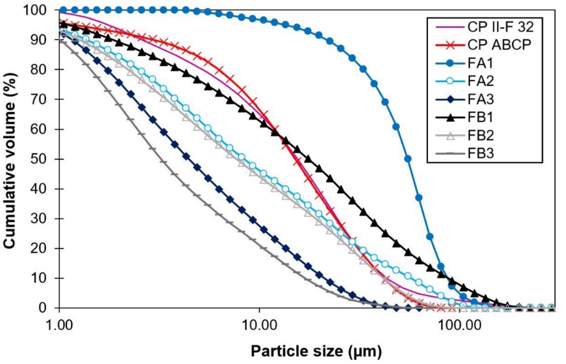

Figure 1. Particle size distribution of cements and GRF used.

Figure 2 shows the cements diffractogram (Figure 2a) and GRF (Figure 2b) used. The cements (Figure 2a) present the same crystalline phases, being identified as the phases alite (C_3S–$3CaO.SiO_2$), belite (C_2S–$2CaO.SiO_2$), C_4AF ($4CaO.Al_2O_3.Fe_2O_3$), cubic C_3A ($3CaO.Al_2O_3$), orthorebic C_3A ($3CaO.Al_2O_3$), calcite ($CaCO_3$), gypsum ($CaSO_4.1/2H_2O$), arcanite (KSO_4), and periclase (MgO).

The granitic rock fines (A and B) have very similar mineralogical compositions, with the presence of the minerals albite ($NaAlSi_3O_8$), quartz (SiO_2), annite [KFe_3^{2+} $AlSi_3O_{10}(OH)_{1,5}F_{0,5}$], microcline ($KAlSi_3O_8$), actinolite [$Ca_2(Mg,Fe^{2+})_5Si_8O_{22}(OH)_2$], magnetite ($FeO.Fe_2O_3$), dolomite [$CaMg(CO_3)_2$] and kaolinite [$Al_2Si_2O_5(OH)_4$].

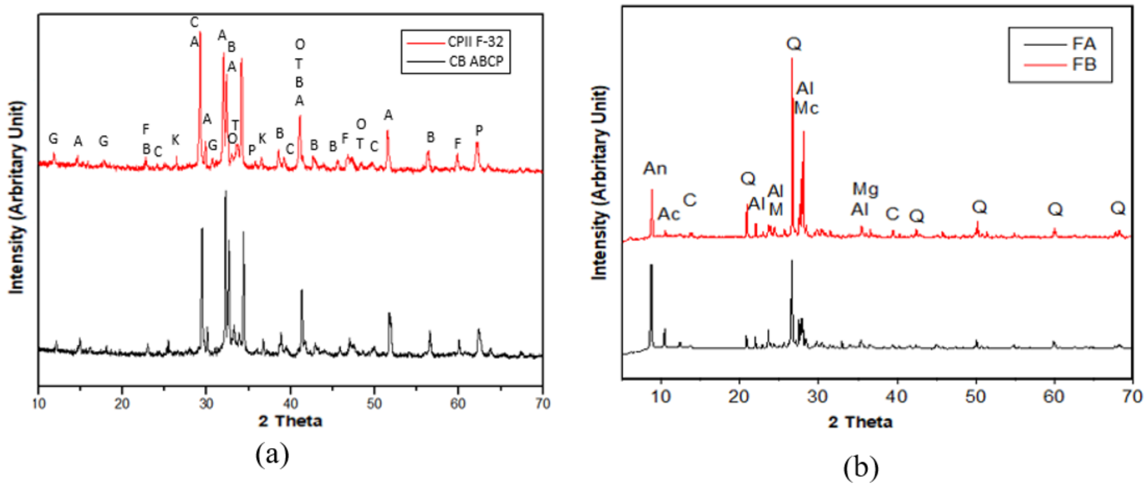

Figure 2. Identification of the crystalline phases of the (a) cements and (b) GRF studied. A-Alite; B-Belite; F-C_4AF; T-cubic C_3A, O-orthorambic C_3A, C-Calcite, G-Gypsum, K-Arcanite, P-Periclase; Al-Albite; Q-Quartz; An- Annite; M-Microcline; Ac-Actinolite; Mg-Magnetite; C-Caulinite.

As the GRF were used as mineral addition to the cement, the pozolanicity analysis was performed by the modified Fratini method, which evaluates the consumption of hydroxyl (OH^-) and calcium oxide (CaO) from pastes containing cement and the GRF. The results obtained are presented in Figure 3.

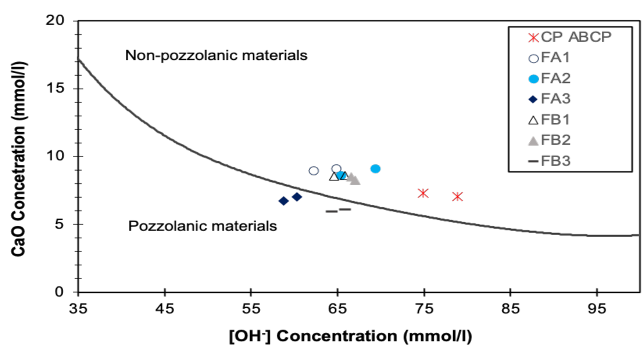

Figure 3. Result of the chemical titration test, according to standard NP EN 196-5.

The presence of alkaline ions in the solution causes the portlandite [$Ca(OH)_2$], formed during cement hydration reactions, to release hydroxyl (OH^-) in order to balance alkaline sodium (Na^+) and potassium (K^+) cations [10].

By the test performed, only FA3 and FB3 fines were characterized as pozzolanic materials. However, although FA1, FA2, FB1 and FB2 fines were characterized as non-pozzolanic materials, their presence in the mixture caused a reduction of hydroxyl ions, due to a lower amount of cement in the mixture or due to ion retention by the GRF.

The authors warn that complementary tests are necessary so that the GRF studied can be used as pozzolanic materials.

Ichikawa [18] describes that initially the aggregate is attacked by alkaline hydroxides, converting the superficial layer of the aggregate into alkaline silicate. The OH^- consumption causes the dissolution of Ca^{2+} ions of $Ca(OH)_2$, which, by reacting with the alkaline silicate layer, makes the layer more resistant, penetrates the aggregate and generates an expansive pressure.

Bektas and Wang [19] warn that the phenomena associated to AAR are complex and that, although there are no definitive conclusions about the chemistry of AAR gel, the alkali and calcium contents seem to be the key parameters for the understanding of the reaction. Ichikawa [18] complements that the high concentration of both $Ca(OH)_2$ and OH^- are necessary for the expansion due to AAR, however, their performance in the reaction is not yet fully understood.

3.2 AAR accelerated mortar bar test

For the accelerated mortar bar test, the GRF studied were added to the mixture at levels of 10% and 20% in relation to the cement mass and the results are presented in Figure 4 and Figure 5, for mortars containing FA and FB, respectively. It can be observed that, at the end of the test, only the mortars containing FA1 and FB2 fines presented expansions lower than 0.19%, being these fines characterized as reaction mitigators.

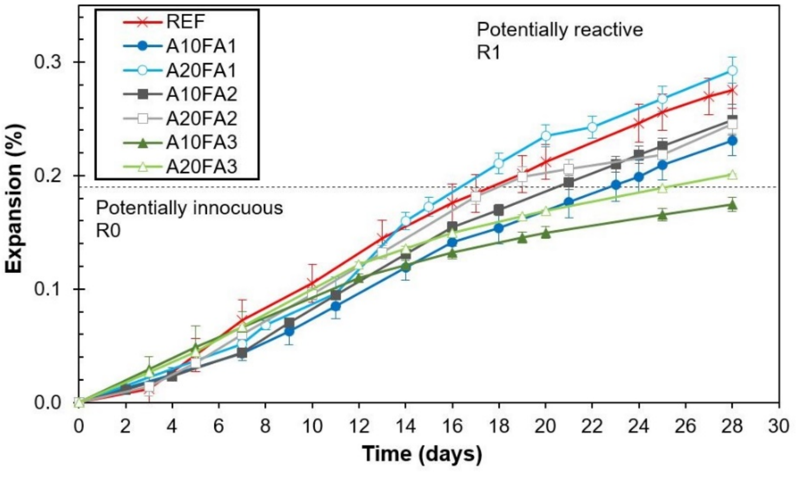

Figure 4. Expansion of the mortars, containing the fine of origin A, during the accelerated test for evaluation of the alkali-aggregate reaction (AAR) and the classification ranges.

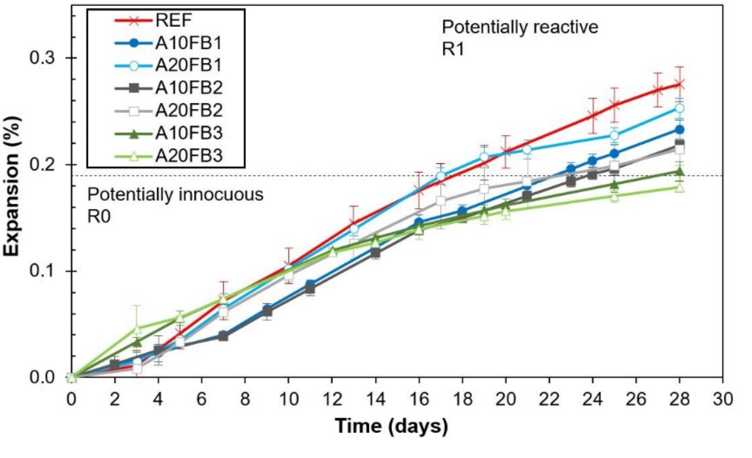

Figure 5. Expansion of the mortars, containing the fine of origin B, during the accelerated test for evaluation of the alkali-aggregate reaction (AAR) and the classification ranges

For a better view of the results, the expansions of the mortars containing the granitic rock fines A (Figure 6) and granitic rock fines B (Figure 7) at 28 days in solution of NaOH 1N at 80°C are presented.

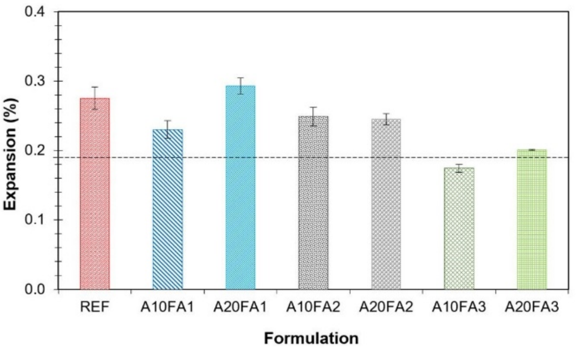

Figure 6. Expansion of mortars containing 10% and 20% of the origin A fines, after 28 days, in NaOH 1N solution

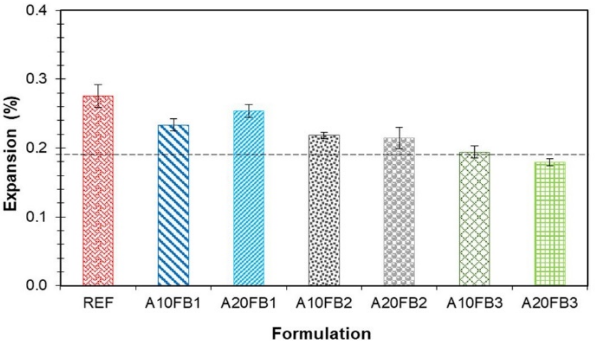

Figure 7. Expansion of mortars containing 10% and 20% of the origin B fines, after 28 days, in NaOH 1N solution.

The FA1 fine addition (Figure 6) obtained a greater expansion reduction when added at the content of 10% than for the 20% fine addition content, because the mortar A20FA1 obtained the same expansion as the reference mortar, this same effect was seen for the mortars with FB1 addition (Figure 7).

This effect suggests that the specific area of the fine is not sufficient to significantly reduce the expansion of mortars. Since, as shown in the particle size distribution, the GRF have some particles larger than 75 μm and the higher content added, the greater the amount of particles large enough to contribute to the alkali-silica reaction.

Regarding the FA2 and FB2 fines (Figure 6 and Figure 7), the addition of these materials caused a reduction in the mortar expansion. However, the addition of 10% and 20% of each fine obtained the same efficiency. These results suggest that it is necessary to add even higher amount of fines in order to mitigate the reaction in order to obtain expansions smaller than 0.19% at 28 days.

When analyzing the expansion results of mortars containing FA3 (Figure 7), it was found that 10% addition of this fine was sufficient for the expansion of the mortar to be in the expansion zone degree 0. However, by adding 20% of this same fine, there was a small increase in expansion compared to the addition of 10%. These results suggest that the optimal incorporation content for the mitigation of the expansion by FA3 fine is around 10%.

For the FB3 fine (Figure 7), the results show that 10% of addition of this fine contributed to reduce the expansion of the mortar studied, but the limit defined in standard is reached only for the 20% of fine addition. Considering the standard deviation, the expansion of mortar A10FB3 is very close to 0.19%, so it is likely that an addition around 15% of the fine FB3 is sufficient for ASR mitigation.

Such findings corroborate to the results obtained in the pozzolanic evaluation of the GRF (Figure 3), where only the fines characterized as pozzolanic (FA3 and FB3) were efficient in reducing the expansion of mortars to values below 0.19%.

A significant increase in the expansion of mortars could have occurred due to a higher content of reactive silica present (due to the sum of reactive silica contained in the aggregate and contained in the fine added). However, it is observed that the increase in the surface area of the GRF added has contributed to a significant reduction in the expansion of mortars, for all types of GRF.

The fine presence can make it difficult to expand the AAR because, due it has a higher fineness, being more reactive than the aggregate, making the hydroxyls react first with the fine and reduce the attack on the aggregate [20], this interaction of the hydroxyls with the silica present in the GRF can result in an expansive gel or the C-S-H gel, not expansive.

If the gel is expansive, the gel formed around smaller particles has a smaller thickness than the gel formed around the aggregate, causing less expansion of the mortar [9]. Therefore, the preferential attack of the hydroxyl ions to the GRF causes a smaller mortar expansion.

Due to the nature of the test, where the mortars are inserted in a solution rich in NaOH at 80ºC, it is not possible to assess whether the consumption of OH^- by the GRF causes a reduction in the AAR, since alkaline hydroxides are supplied continuously to the mortar [18].

Thus, although the accelerated test has shown that the addition of the GRF did not cause an increase in the expansion of the mortars, it is necessary that the test be performed on concrete bars or mortar bars without the insertion of the specimens in the alkaline solution. Such tests are recommended by NBR 15577 [13].

3.3 Physical-mechanical characteristics of the mortars

3.3.1 Density and apparent porosity

The apparent density and porosity values of the mortars used are shown in Figure 8a and Figure 8b, respectively.

According to ANOVA statistical analysis, the addition of the GRF did not cause a significant modification in the apparent density and porosity of the mortars studied. Likewise, the insertion of the mortars in NaOH solution did not cause a decrease in the pore structure of the mortars, when compared to the mortars submitted to the immersed cure.

The opposite behavior was observed by Ribeiro and Rey [21], who verified that thinner materials than cement fill the pores and promote a better densification of the paste and reduction of porosity.

This better packaging of the particles may not have been achieved, because the reduction in the workability of the mortars, caused by the introduction of the GRF, makes it difficult to densify them, since thinner materials require a greater amount of water to lubricate the particles and ensure workability.

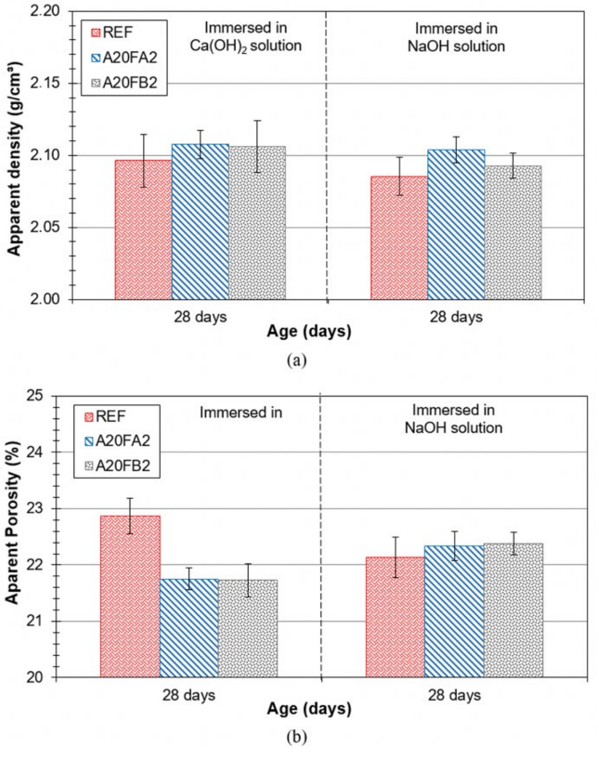

Figure 8. (a) Apparent density and (b) apparent porosity of the reference mortars and containing 20% of the GRF, at 28 days of curing and after 28 days immersed in saturated solution in lime and 28 days immersed in solution of NaOH 1N.

Regarding the type of cure, Rashidi et al. [22] identified that in reactive samples, those immersed in water have a lower total porosity than the samples immersed in NaOH solution, because they do not have enough alkali concentration for the occurrence of AAR and consequent micro cracking. However, in non-reactive samples the microstructural changes are more subtle.

3.3.2 Water capillary absorption

The capillary absorption coefficients (sortivity) of mortars are presented in Figure 9. According to statistical analysis, the addition of fine FA2 caused a significant reduction in capillary absorption. It was also observed that there were no significant changes in the results according to the curing method (wet curing saturated in lime ($Ca(OH)_2$) or in NaOH solution).

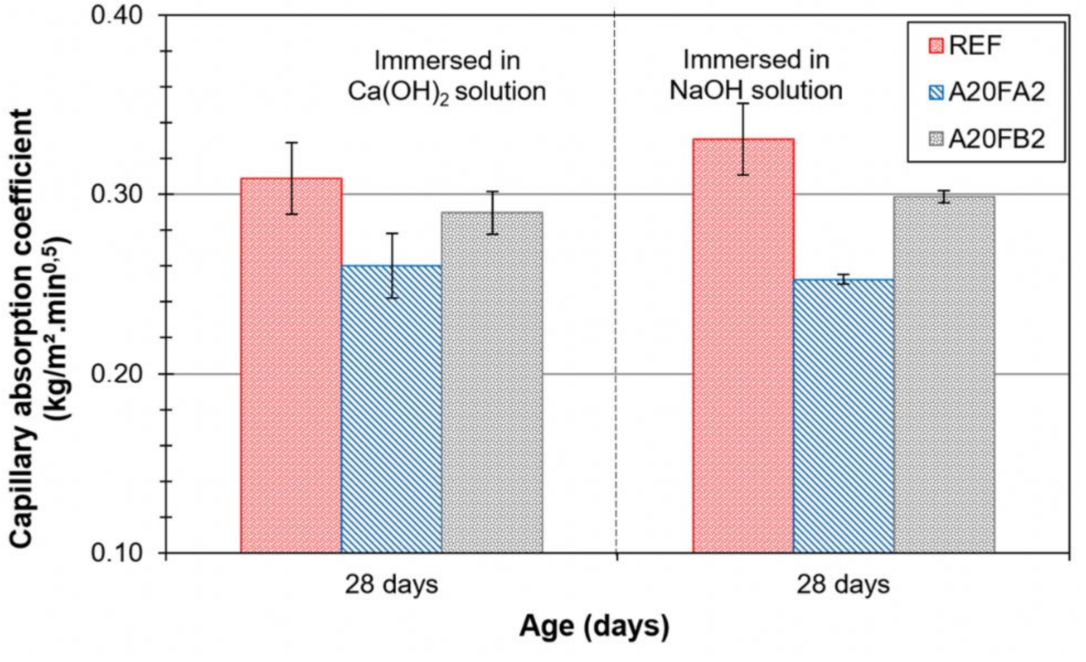

Figure 9. Capillary absorption coefficients of the reference mortars and those containing 20% of GRF at 28 days immersed in saturated solution in lime and at 28 days immersed in solution of NaOH 1N.

The presence of fine FA2 caused a decrease in capillary absorption, probably due to a reduction in the interconnectivity of the capillary pores. The mortar containing FB2 did not present any significant change in relation to the reference mortar, since these GRF and the cement present similar grain sizes.

3.3.3 Mechanical strength

Figure 10 presents the results of axial compressive strength of the mortars studied. Statistically, only the presence of the fine FB2 caused a significant increase in the resistance to axial compression, in relation to the reference mortar, at 3 days.

However, at 7 days and 28 days of curing immersed in $Ca(OH)_2$ solution at 24°C, the compressive strength of the samples was statistically the same. It is worth noting that cement consumption reduced with the increase in granitic rock fines, but the water to aggregate ratio was kept the same for all samples.

When comparing the curing methods used, it was found that the reference mortar was more significantly influenced when compared to the other formulations, having a greater reduction in compressive strength when inserted in NaOH solution at 80°C. For the mortars containing the FA2 and FB2 fines, the curing method did not significantly influence the axial compressive strength.

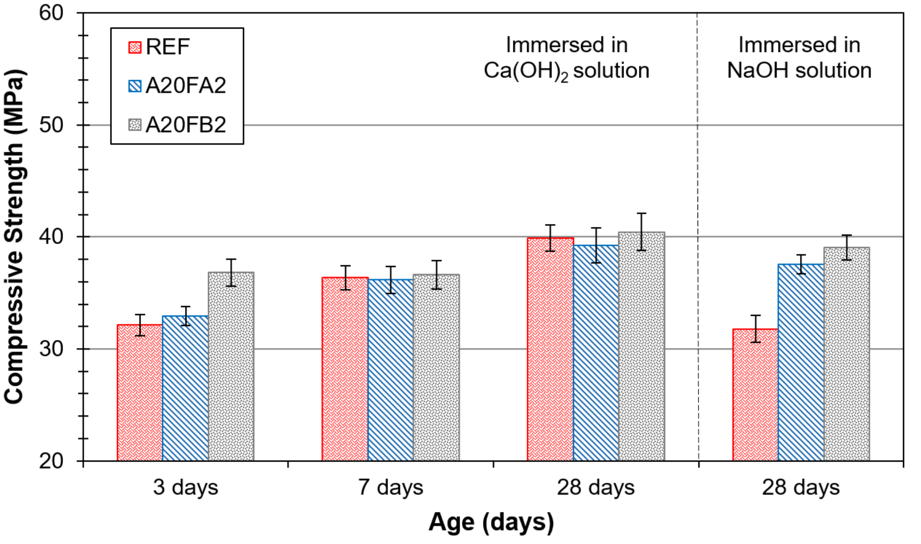

Figure 10. Compressive strength of reference mortars and containing 20% of the GRF, at 3, 7 and 28 days immersed in saturated solution in lime and at 28 days immersed in solution of NaOH 1N.

Figure 11 shows the resistance to flexural tensile strength of the mortars, which was not significantly altered due to the introduction of the GRF studied after 3 and 7 days of cure. It was also observed that the immersion of the reference mortar in NaOH solution caused a reduction in the tensile strength in bending, however the strengths of mortars containing FA2 and FB2 were not influenced by the curing method.

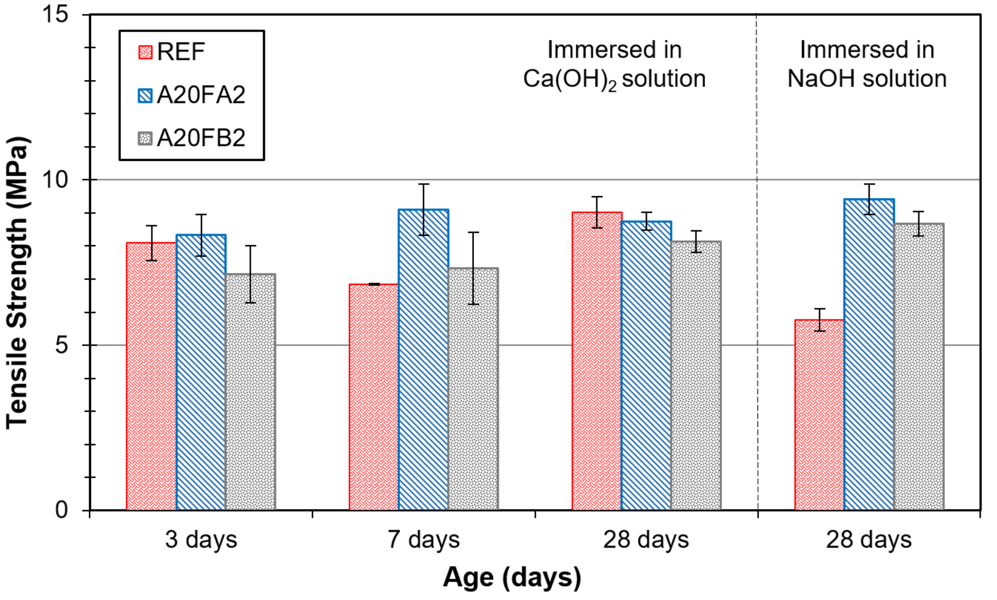

Figure 11. Tensile strength in the bending of reference mortars and containing 20% of the GRF, at 3, 7 and 28 days immersed in saturated solution of lime and at 28 days immersed in solution of NaOH 1N.

As for the curing method, it should be noted that both the curing immersed in water (saturated in $Ca(OH)_2$) and in NaOH solution at 80°C, provide an environment with basic pH, and the exchange of calcium hydroxide for sodium hydroxide favors the occurrence of the alkali aggregate reaction. Thus, the hydration reactions of the mortars are not significantly altered, which explains the maintenance of strength values to mortars containing GRF.

For the reference mortar, the expansion due to AAR may have caused a weakening in the matrix, thus reducing its mechanical resistance.

However, the tensile strength and modulus of elasticity are more sensitive to AAR cracking than to axial compression [18], [23]. This factor may be related to the microscopic damage caused by the AAR in the aggregates that impair the bond between these and the cement paste due to changes in its characteristics, such as texture, resistance, hardness, among others [24].

Souza et al. [23] describe that significant reductions in compressive strength occur when the expansion levels are high, with expansions close to 0.30%, due to the large amount of cracks in the cement paste, forming a network of cracks [25].

The small influence of the occurrence of AAR on the tensile and compression resistances of mortars in the presence of fine reactive can be explained by the reduction of the expansion pressure caused by the penetration of the expansive gel in the aggregate [18]. Thomas [10] explains that the size of amorphous silica influences the formation of the expansive gel, because finely divided materials cause the gel to form in a manner distributed throughout the cement paste, while larger particles lead to the accumulation of the alkali-silica gel in specific locations, making them points of expansion. The formation of the gel in a distributed manner causes that, if there is a breakage of the particles due to the expansion of the gel, it will interfere less in the matrix the smaller its size is.

4 CONCLUSIONS

From the results obtained, one can conclude:

- The addition of granitic rock fines reduced cement consumption without significantly altering the physical-mechanical properties of mortars;
- The addition of granitic rock fines presented a reducing effect of the ASR, which was intensified as the fineness of these fines increased, indicating that the probable increase in the amount of reactive silica dissolved in the solution did not contribute to the formation of the expansive gel, consuming the alkalis in the first ages;
- The granitic rock fines with surface area above 600 cm^2/g acted as a mitigator of the alkali-aggregate reaction, evaluated by accelerated testing on mortar bars;
- It should be noted that there is a need for complementary tests and with greater execution time, such as concrete prism tests, to prove the mitigating effect of fine;
- The immersion of mortars containing granitic rock fines in Na(OH) solution did not cause changes in their physical-mechanical properties, unlike what occurred for reference mortars.

ACKNOWLEDGEMENTS

The authors wish to thank CNPq – National Counsel of Technological and Scientific Development (Brazil), PPEC/UFBA – Postgraduate Program in Civil Engineering at the Federal University of Bahia (Brazil), CETA/UFBA - Mortar Technological Center, UEFS -Feira de Santana State University and LCM/IFBA - Materials Characterization Laboratory of Federal Institute of Bahia.

REFERENCES

[1] Instituto Brasileiro de Mineração, *Economia Mineral do Brasil*. Belo Horizonte: IBRAM, 2018, pp. 1–23.

[2] M. Cyr, P. Rivard, and F. Labrecque, "Reduction of ASR-expansion using powders ground from various sources of reactive aggregates," *Cement Concr. Compos.*, vol. 31, pp. 438–446, 2009.

[3] S. Priskulnik, “Inspeção e diagnóstico de estruturas de concreto afetadas pelas reações cimento-agregado,” in *Concreto: Ensino, Pesquisa e Realizações vol. 2*, G. Isaia, Ed., São Paulo: IBRACON, 2005, pp. 1018–1070.

[4] M. D. A. Thomas, B. Fournier, and K. J. Folliard, *Alkali-Aggregate Reactivity (AAR) Facts Book*. Washington: Federal Highway Administration, Office of Pavement Technology, 2013.

[5] I. Moundoungou, D. Bulteel, E. Garcia-Diaz, V. Thiéry, P. Dégrugilliers, and J. G. Hammerschlag, "Reduction of ASR expansion in concretes based on reactive chert aggregates: Effect of alkali neutralisation capacity," *Constr. Build. Mater.*, vol. 54, pp. 147–162, 2014.

[6] C. F. Dunant and K. L. Scrivener, "Effects of aggregate size on alkali-silica-reaction induced expansion," *Cement Concr. Res.*, vol. 42, no. 6, pp. 745–751, 2012.

[7] J. Liaudat, I. Carol, C. López, and A. Leemann, "ASR expansions at the level of a single glass-cement paste interface: experimental results and proposal of a reaction-expansion mechanism," *Constr. Build. Mater.*, vol. 218, pp. 108–118, 2019.

[8] F. Rajabipour, M. Asce, H. Maraghechi, and G. Fischer, "Investigating the Alkali-Silica Reaction of Recycled Glass Aggregates in Concrete Materials," *J. Mater. Civ. Eng.*, vol. 22, pp. 1201–1208, 2010.

[9] Z. He, L. Hu, Y. Li, J. Hu, and Y. Shao, "Use of sandstone powder as a mineral additive for concrete," *Constr. Build. Mater.*, vol. 186, pp. 276–286, 2018.

[10] M. Thomas, "The effect of supplementary cementing materials on alkali-silica reaction: A review," *Cement Concr. Res.*, vol. 41, no. 12, pp. 1224–1231, 2011.

[11] Y. Wang, J. Li, X. He, Z. Zheng, H. Zhao, and J. Yang, "Effects of wet-grinded superfine waste glass on the fresh properties and reaction characteristic of cement pastes," *Constr. Build. Mater.*, vol. 247, pp. 118593, 2020.

[12] A. Carles-Gibergues, M. Cyr, M. Moisson, and E. Ringot, "A simple way to mitigate alkali-silica reaction," *Mater. Struct.*, vol. 41, no. 1, pp. 73–83, 2008.

[13] Associação Brasileira de Normas Técnicas, *Agregados – Reatividade Álcali-Agregado*, NBR 15577, 2018.

[14] IPQ, *Métodos de Ensaio de Cimentos*, NP EN 196, 1996.

[15] Associação Brasileira de Normas Técnicas, *Argamassa para Assentamento e Revestimento de Paredes e Tetos – Determinação da Resistência à Tração na Flexão e à Compressão*, NBR 13279, 2005.

[16] Associação Brasileira de Normas Técnicas, *Argamassa e Concreto Endurecidos – Determinação da Absorção de Água por Capilaridade*, NBR 9779, 2012.

[17] Associação Brasileira de Normas Técnicas, *Argamassa e Concreto Endurecidos – Determinação da Absorção de Água, Índice de Vazios e Massa Específica*, NBR 9778, 2005.

[18] T. Ichikawa, "Alkali-silica reaction, pessimum effects and pozzolanic effect," *Cement Concr. Res.*, vol. 39, no. 8, pp. 716–726, 2009.

[19] F. Bektas and K. Wang, "Performance of ground clay brick in ASR-affected concrete: Effects on expansion, mechanical properties and ASR gel chemistry," *Cement Concr. Compos.*, vol. 34, no. 2, pp. 273–278, 2012.

[20] X. Hou, L. J. Struble, and R. J. Kirkpatrick, "Formation of ASR gel and the roles of C-S-H and portlandite," *Cement Concr. Res.*, vol. 34, no. 9, pp. 1683–1696, 2004.

[21] D. V. Ribeiro and R. O. Rey, "Avaliação dos agregados utilizados na região metropolitana de Salvador quanto à ocorrência de Reatividade Álcalis-Agregado (RAA)," *Rev. ALCONPAT*, vol. 9, no. 2, pp. 185, 2019.

[22] M. Rashidi et al., "Detecting alkali-silica reaction: A multi-physics approach," *Cement Concr. Compos.*, vol. 73, pp. 123–135, 2016.

[23] D. J. Souza, L. F. M. Sanchez, and M. T. De Grazia, "Evaluation of a direct shear test setup to quantify AAR-induced expansion and damage in concrete," *Constr. Build. Mater.*, vol. 229, pp. 116806, 2019.

[24] L. F. M. Sanchez, B. Fournier, M. Jolin, D. Mitchell, and J. Bastien, "Overall assessment of Alkali-Aggregate Reaction (AAR) in concretes presenting different strengths and incorporating a wide range of reactive aggregate types and natures," *Cement Concr. Res.*, vol. 93, pp. 17–31, 2017.

[25] L. F. M. Sanchez, T. Drimalas, B. Fournier, D. Mitchell, and J. Bastien, "Comprehensive damage assessment in concrete affected by different internal swelling reaction (ISR) mechanisms," *Cement Concr. Res.*, vol. 107, pp. 284–303, 2018.

Author contributions: BSS: conceptualization, data curation, formal analysis, methodology, writing, DVR: conceptualization, funding acquisition, supervision, writing.

Editors: Edna Possan, José Luiz Antunes de Oliveira e Sousa, Guilherme Aris Parsekian.

IBRACON Structures and Materials Journal
Revista IBRACON de Estruturas e Materiais
ISSN 1983-4195 ismj.org

ORIGINAL ARTICLE

Optimal configuration of RC frames considering ultimate and serviceability limit state constraints

Configuração ótima de pórticos de concreto armado considerando restrições de estados limites últimos e de serviço

Marcela Alejandra Juliani[a]
Wellison José de Santana Gomes[a]

[a]Universidade Federal de Santa Catarina – UFSC, Centro de Otimização e Confiabilidade em Engenharia – CORE, Departamento de Engenharia Civil, Florianópolis, SC, Brasil

Received 16 January 2020
Accepted 25 June 2020

Abstract: Most current structural design codes are based on the concept of limit states, that is, when a structure fails to meet one of its purposes, it is said that it has reached its limit state. In the design of reinforced concrete structures, the Ultimate Limit State (ULS) and the Serviceability Limit State (SLS) must be checked. Therefore, this paper presents an optimization scheme for reinforced concrete plane frames, in which the objective is to minimize the cost of structures for three cases of constraints: the first is related to ULS and SLS; the second refers only to the ULS; and the third is related only to the SLS. Computational routines for checking limit states of beams and columns are implemented in MATLAB, following the requirements of the Brazilian code. Structural analyses are performed by using the MASTAN2 software, taking into account geometric nonlinearities and a simplified physical nonlinearity method. The objective function considers the cost of concrete, reinforcement and formwork, and the optimization problems are solved by genetic algorithms. Two numerical examples of frames are presented. Regarding the optimal characteristics related to each type of limit state, it is noted that the beams and columns tend to have larger and more reinforced cross sections in the case of the ULS. Even so, optimal structures related to the ULS often do not satisfy SLS and vice versa, which indicates that the optimal characteristics related to each limit state may be different. In addition, it is observed that the SLS is less restrictive than ULS.

Keywords: optimization, reinforced concrete, limit states, genetic algorithms.

Resumo: A maioria das normas de projetos estruturais atuais se baseia no conceito de estados limites, ou seja, quando uma estrutura não atende a um de seus propósitos, diz-se que a mesma atingiu seu estado limite. No projeto de estruturas de concreto armado, deve-se verificar o Estado Limite Último (ELU) e o Estado Limite de Serviço (ELS). Portanto, este trabalho apresenta um esquema de otimização de pórticos planos de concreto armado, no qual o objetivo é minimizar o custo de estruturas para três casos de restrições: o primeiro está relacionado ao ELU e ao ELS; o segundo refere-se apenas ao ELU; e o terceiro está relacionado apenas ao ELS. São elaboradas rotinas de verificação dos estados limites de vigas e de pilares, em ambiente MATLAB, de acordo com normas brasileiras. As análises estruturais são realizadas com o uso do *software* MASTAN2, levando em consideração as não-linearidades geométricas e um método simplificado de não-linearidade física. A função objetivo considera o custo do concreto, da armadura e da forma, e são utilizados algoritmos genéticos para a otimização. São avaliados dois exemplos numéricos de pórticos. Quanto às características ótimas relacionadas a cada tipo de estado limite, nota-se que as vigas e os pilares tendem a apresentar seções transversais maiores e mais armadas no caso do ELU. Mesmo assim, muitas vezes a estrutura ótima relacionada ao ELU não satisfaz o ELS e vice-versa, o que indica que as características ótimas relacionadas a cada estado limite podem ser diferentes. Além disso, observa-se que o ELS é menos restritivo do que o ELU.

Palavras-chave: otimização, concreto armado, estados limites, algoritmos genéticos.

How to cite: M. A. Juliani and W. J. S. Gomes, "Optimal configuration of RC frames considering ultimate and serviceability limit state constraints," *Rev. IBRACON Estrut. Mater.*, vol. 14, no. 2, e14204, 2021, https://doi.org/10.1590/S1983-41952021000200004

Corresponding author: Marcela Alejandra Juliani. E-mail: marcelajulianii@gmail.com
Financial support: Scientific and Technological Research Support Foundation of Santa Catarina State (FAPESC, public notice nº 05/2015) and National Council for Scientific and Technological Development (CNPq, grant 302489/2017-7).
Conflict of interest: Nothing to declare.

1 INTRODUCTION

Due to the development of new technologies and the increase of market competitiveness, the search for more efficient and lower-cost designs has increased. At the same time, reinforced concrete has become a dominant structural material in engineering construction in many countries [1]. In this scenario, the importance of studies related to the design concept of reinforced concrete structures is valid.

To ensure the safety of a structure, the engineer must choose a design option which meets the requirements related to its purpose. However, due to the large number of variables usually involved in the design of reinforced concrete structures, there are several different configurations that can meet the required conditions, with different costs and performances. Many times, the choice of a configuration is not simple, which makes it difficult to obtain an optimal design using traditional methods. Thus, optimization techniques have been widely employed with this purpose [2]–[4].

As a result, several studies in the field of optimization of reinforced concrete structures have been developed in the last decades, with the objective of obtaining designs with optimal parameters, generally related to the minimum cost of the structures [5]–[15]. Many of these studies use genetic algorithms (GA) in the optimization [16]–[25]. In order to obtain optimal structures which can be used in practice, the requirements specified by standard designs may be applied as constraints within the optimization formulation.

The requirements presented by most current design codes, including the Brazilian code for design of concrete structures [26], are based on the concept of limit states. A limit state may be defined as the limit situation from which a structural element no longer meets one of its design goals, or in other words, when a structure fails to satisfy any of the purposes of its construction. Current Brazilian codes establish that the following limit states must be considered [26], [27]: Ultimate Limit State (ULS), related to the collapse, or to any other form of structural failure, which determines the interruption of the use of the structure; Serviceability Limit State (SLS), characterized by situations that, due to their occurrence, repetition or duration, generate structural effects that do not meet the conditions specified for the normal use of the structure, or indicate impairment of its durability.

Optimization of reinforced concrete structures considering standard design constraints have been already studied in some papers from the literature [9], [13], [15], [19], [20]. In the context of the Brazilian design standard, some studies have also been developed, for example, Bordignon and Kripka [28], Medeiros and Kripka [29], [30], Kripka et al. [31] and Correia et al. [32]. However, there is a lack in studies that discuss the characteristics of the optimal structures found and their relationships with the design constraints.

Following a research which was started by Juliani and Gomes [33], [34], the present paper proposes to analyze the optimal configuration of reinforced concrete plane frames, through the minimization of its costs, considering three cases of constraints: the first is related to ULS and SLS; the second refers only to the ULS; and the third is related only to the SLS. The design variables considered are the cross-section dimensions and the amount of longitudinal and transverse reinforcement of the structural elements. Also, for a proper representation of the real behavior of the structure, geometric nonlinearities and a simplified physical nonlinearity method are considered in the structural analysis. Although the Brazilian standard requires that designs satisfy both types of limit states simultaneously, the present paper considers them separately in some cases, in order to investigate and quantify the effects of each type on the optimal configuration. Thus, the main goal of the research is to improve the knowledge in structural design, indicating possible directions that lead to structures with minimal costs.

This paper focuses on plane frames because there are many conventional structures that can be reduced to such models, as some kinds of buildings and industrial sheds. Furthermore, the analysis of plane frames requires consideration of the global structural behavior and the interaction between the two different types of structural elements involved: beams and columns. However, this model does not take into account torsional forces, for example, restricting the analysis to axial and shear forces and bending moments, in the plane. Although limited, plane frames allow a significant reduction in the computational effort of the optimization process, when compared to spatial models. This is important because the optimization process requires many structural analysis evaluations.

The paper is organized as follows: section 2 introduces the formulation and implementation of the problem that is addressed in this paper; the optimization method used herein is described in section 3; section 4 presents two numerical examples and some conclusions drawn from the results are presented in section 5.

2 OPTIMIZATION FORMULATION AND IMPLEMENTATION

The optimization problem is usually defined by some design variables, one or more objective functions and some constraints, as described in the following.

2.1 Design variables

The cross-sections of beams and columns are assumed to be rectangular. The design variables to be determined in the optimization process are adopted as discrete and illustrated in Figure 1, where: b and h are the cross section width and height, respectively, and the height is parallel to the plane of the frame; n_s is the number of longitudinal reinforcement bars, whose diameter is represented by ϕ_s; n_{sw} is the number of transverse reinforcement bars, whose diameter is represented by ϕ_{sw}.

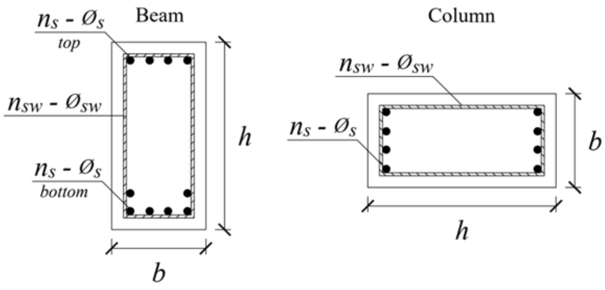

Figure 1. Typical section of a beam and a column.

In order to vary the amount of reinforcement along the beam, the structural element is discretized in a predefined number of segments. Then, for each segment, values of n_s^{top}, n_s^{bottom} and n_{sw} are determined, based on the maximum values of bending moment and shear force on the segment. The bars extend over the entire length of the segment and the anchoring of longitudinal bars is not considered. For simplification, the values of n_s^{top} and n_s^{bottom} are obtained considering the respective bars as tension reinforcement. The values of the other variables are the same over the entire length of the beam.

Since this paper deals with plane frames, the cross sections of the columns are longitudinally reinforced only on two faces, in a symmetrical way, assuming that the direction of the acting bending moment may change. Each column is discretized with one segment, so that the structural element has the same cross section throughout its length, and anchorage of the reinforcement is disregarded.

2.2 Objective function

The objective function employed corresponds to the cost of the structure, based on the cost of concrete volume, longitudinal and transverse reinforcement mass and formwork area, as described by Equation 1, where: $\mathbf{x}$ is the vector of design variables; V_c is the concrete volume; M_s and M_{sw} are the mass of the longitudinal and transverse reinforcement, respectively; A_f is the formwork area; C_c, C_s, C_{sw} and C_f represent, respectively, the unit cost of concrete, longitudinal and transverse reinforcement, and formwork; n_{el} is the number of structural elements of the frame (beams and columns). The formwork areas are given by Equation 2, where l is the length of the structural element.

$$f(\mathbf{x}) = \sum_{i=1}^{n_{el}} \left(V_{c_i} C_c + M_{s_i} C_s + M_{sw_i} C_{sw} + A_{f_i} C_f \right) \tag{1}$$

$$\begin{cases} A_f^{beam} = (2h+b)\,l \\ A_f^{column} = (h+b)\,2l \end{cases} \tag{2}$$

2.3 Constraints

The optimization constraints considered herein are based on the requirements of NBR 6118 [26], represented by the vector $\mathbf{g}$, and divided into constraints of the ultimate and serviceability limit states, as shown in Figure 2. In addition to the constraints related to the limit states, in all situations, constructive constraints are also considered; for example: maximum and minimum limits of dimensions of cross-sections, reinforcement rates and space between reinforcement bars; ductility conditions for beams; and others. All these constraints are implemented in MATLAB (MathWorks [35]), to be included in the optimization. It should be noted that constraints related to the lateral instability of the beams are not considered. The consideration of this effect can be important, especially in cases of slender beams and with insufficient lateral locking; however, this topic will not be addressed herein for simplification purposes, remaining a topic for future investigations.

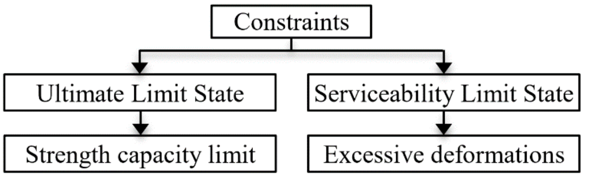

Figure 2. Constraint scheme of the problem.

Verification of the constraints requires determination of internal forces and deflections of the structure, which can be achieved by structural analysis. For this purpose, MASTAN2 software [36] is employed. In all cases, geometric nonlinearities are considered using the software formulation [37], whereas physical nonlinearities are considered in a simplified manner, based on stiffness reductions, as indicated by NBR 6118 [26]: the stiffnesses of the beams and columns are considered equal to $40\,\%$ and $80\,\%$ of the total stiffness of the concrete section, respectively. For more details about nonlinearities the readers are referred to Bathe [38] and Belytschko et al. [39]. As the present paper deals with plane frames, beams are considered subjected to the simple bending and columns to uniaxial bending.

2.3.1 Ultimate limit state constraints

Considering the behavior of the analyzed structure, the beams must withstand the design bending moment (M_{Sd}) and the design shear force (V_{Sd}).

The section of the beam is safe with respect to the bending moment if it satisfies the constraint given by Equation 3, where M_{Rd} is the design bending strength.

$$g_1(\mathbf{x}) = M_{Sd} - M_{Rd} \leq 0 \tag{3}$$

M_{Rd} is calculated from Equation 4, obtained from the equilibrium of moments in the cross section, where A_s is the cross-sectional area of longitudinal tension reinforcement, f_{yd} is the design yield strength of longitudinal steel reinforcement, d is the effective depth, λ is a parameter depending on the characteristic compressive strength of concrete (f_{ck}) and z defines the position of the neutral axis.

$$M_{Rd} = A_s f_{yd}\left(d - \frac{\lambda z}{2}\right) \tag{4}$$

The value of z is obtained from the equilibrium of forces in the cross section, according to Equation 5, where α_c is a parameter of reduction of the compressive strength of concrete and f_{cd} is the design compressive strength of concrete.

$$z = \frac{A_s f_{yd}}{\lambda \alpha_c f_{cd} b} \tag{5}$$

The strength of the section with respect to the shear force is guaranteed if the constraints given by Equations 6 and 7 are checked, where V_{Rd2} and V_{Rd3} are, respectively, the design shear strength of concrete compressive diagonals and the design shear strength of tension diagonals (supplied by concrete, $V_{\bar{c}}$, and transverse reinforcement, V_{sw}). Model II of the code (NBR 6118 [26]) is used to obtain shear strengths.

$$g_2(\mathbf{x}) = V_{Sd} - V_{Rd2} \leq 0 \tag{6}$$

$$g_3(\mathbf{x}) = V_{Sd} - V_{Rd3} \leq 0 \tag{7}$$

Equation 8 defines the value of V_{Rd2}, where α_{v2} is a parameter which depends on the f_{ck}, α is the angle of inclination of the transverse reinforcement, adopted as 90º, and θ is the angle of inclination of compressive diagonals, adopted as 30º.

$$V_{Rd2} = 0.54\alpha_{v2} f_{cd} bd\left(\cot\alpha + \cot\theta\right) sin^2\theta \tag{8}$$

V_{Rd3} is obtained from Equation 9, where A_{sw} is the cross-sectional area of transverse reinforcement bar, s is the spacing between the transverse reinforcements, f_{ywd} is the design tension in the transverse reinforcement and f_{ctd} is the design tensile strength of concrete.

$$\begin{aligned} &V_{Rd3} = V_{sw} + V_{\bar{c}} \\ &\Rightarrow V_{sw} = \frac{A_{sw}}{s} 0.9 d f_{ywd}\left(\cot\alpha + \cot\theta\right)\sin\alpha; \\ &\Rightarrow V_{\bar{c}} = \begin{cases} 0.6 f_{ctd} bd & \text{if } V_{Sd} \leq 0.6 f_{ctd} bd; \\ 0 & \text{if } V_{Sd} = V_{Rd2}\text{, interpolating linearly to intermediate values.} \end{cases} \end{aligned} \tag{9}$$

The columns must have sufficient structural capacity to withstand combined effects of axial load and bending moment, that is, M_{Rd} must be greater than M_{Sd} at the same time as N_{Rd} (design axial strength) must be greater than N_{Sd} (design axial force). To guarantee this requirement, a load-moment interaction diagram M_{Rd} x N_{Rd} is constructed for each column, which is a curve that delimits the actions that can act in the section safely. If the combination of M_{Sd} and N_{Sd} is in the safe region of the diagram, the capacity of the designed column is adequate. Figure 3 shows an example of a diagram constructed for a column.

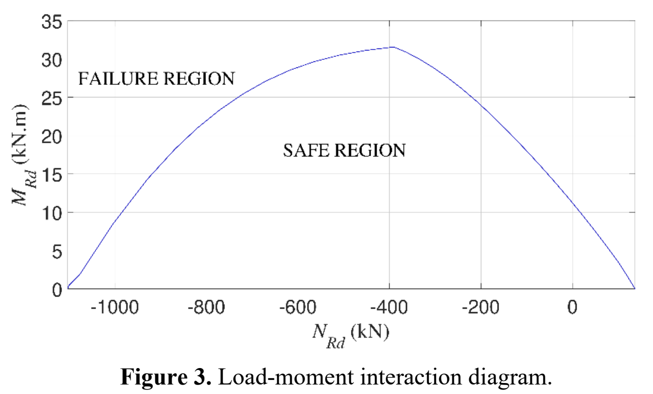

Figure 3. Load-moment interaction diagram.

During the optimization process, after the construction of the diagram, the developed algorithm searches for the M_{Rd} associated with the N_{Sd}, and if that moment value is greater than M_{Sd}, the section is considered safe (Equation 10).

$$g_4(\mathbf{x}) = M_{Sd} - M_{Rd} \leq 0 \tag{10}$$

The design solicitations (M_{Sd}, V_{Sd} and N_{Sd}) in the ULS are obtained from the normal ultimate combination of applied loads, according to NBR 6118 [26].

2.3.2 Serviceability limit state constraints

In the serviceability limit state of excessive deformations, the vertical deflection a_v of the beams are restricted by the vertical deflection limit a_v^{lim} allowed by the code, as shown in Equation 11, where the limit is given by $\frac{l}{250}$. a_v is obtained by the direct stiffness method, using the quasi-permanent load combination [26], and adding a deflection portion related to the creep of the concrete.

$$g_5(\mathbf{x}) = a_v - a_v^{lim} \leq 0 \tag{11}$$

The frame is also checked for horizontal displacements. The horizontal displacement between two consecutive story a_h must comply with the horizontal displacement limit a_h^{lim} defined by the code, where the limit is given by $\frac{l}{850}$. Equation 12 represents this constraint.

$$g_6(\mathbf{x}) = a_h - a_h^{lim} \leq 0 \tag{12}$$

The constraint given by Equation 13 determines that the horizontal displacement at the top of the frame a_h^t must meet the limit established by the code $a_h^{t_{lim}}$, adopted equal to $\frac{l_{total}}{1700}$, where l_{total} is the height of the frame.

$$g_7(\mathbf{x}) = a_h^t - a_h^{t_{lim}} \leq 0 \tag{13}$$

The horizontal displacements are obtained by the direct stiffness method, using the frequent load combination [26].

3 GENETIC ALGORITHMS

Genetic algorithms are zero-order stochastic optimization methods, developed by Holland [40] in the 1970s. They are based on the theory of evolution of species, declared by Charles Darwin in the XIX century [41]. The algorithm can be applied to solve problems that are not well suited for standard optimization algorithms, including problems in which the objective function is discontinuous, nondifferentiable or highly nonlinear. These algorithms use some terms in analogy to natural genetics: the individual is a solution, which may or may not be viable; the population is the set of solutions; the chromosome is the coding that represents the individual; the gene is the coding that represents the variable.

In general, the genetic algorithm method creates a random initial population and then performs the following steps: initially, the algorithm evaluates the fitness of each individual of the current population; then selects some of these individuals based on the value of their fitness, naming them as parents; later, children are produced from changes in the characteristics of a single parent (mutation) or by combining characteristics of a parent pair (crossover); after that, individuals with the best fitness of the current population are chosen as “elite members” (elitism); finally, the current population is replaced by the individuals generated during the mutation, the crossover and the elitism phases, forming the new generation of the population. The steps are repeated until some stop criteria are satisfied. Figure 4 presents a flowchart of the GA. For more details about optimization and genetic algorithm see Arora [3] and Sivanandam and Deepa [42].

In this paper, a genetic algorithm routine available in MATLAB, is used (MathWorks [43]). In this routine, the constraints of the optimization problem are considered by penalizing the fitness of an individual when it does not meet the constraints. The fitness of the *i*-th individual of the population can be described by Equation 14.

$$Fitness\left(\mathbf{x}^{(i)}\right)=\begin{cases} f\left(\mathbf{x}^{(i)}\right), & \text{if } \mathbf{x}^{(i)} \text{ is feasible;} \\ f_{worst}+\sum_{j=1}^{\mu}|\,\bar{g}_j\left(\mathbf{x}^{(i)}\right)|, & \text{otherwise.} \end{cases} \tag{14}$$

In this way, if the individual is feasible, the fitness function is the objective function. If the individual is infeasible, the fitness function is the value of the objective function of the worst feasible solution currently available in the population (f_{worst}), plus a sum of constraint violations, where $\bar{g}$ are the constraints violated and μ is the number of these constraints [44].

The genetic algorithm was chosen because it is an established method and widely used in similar studies. Other optimization methods could be used, which could achieve the optimal results more or less efficiently than the genetic algorithm. The focus of this work, however, was on optimization results.

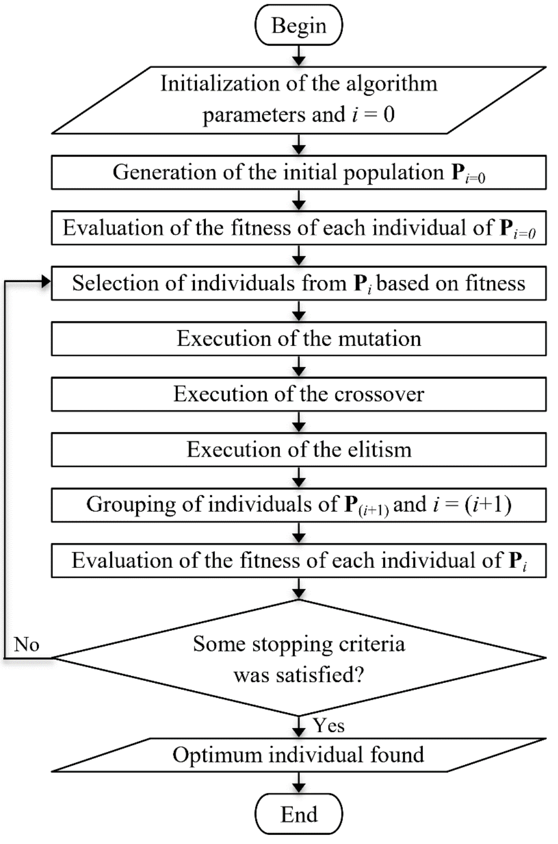

Figure 4. Basic scheme of a genetic algorithm.

4 NUMERICAL EXAMPLES

This section presents two numerical examples: a one-bay two-story frame and a two-bay six-story frame. Table 1 shows some of the input data used, common to both examples. The unit costs adopted were obtained from SINAPI [45], the Brazilian system of costs survey and indexes of construction, and include the costs of materials and labor.

Table 1. Input data of examples I and II.

	Data	Value	Unit
f_{yk}	Characteristic yield strength of longitudinal and transverse steel reinforcement	500	MPa
E_s	Modulus of elasticity of longitudinal and transverse steel reinforcement	210000	MPa
ρ_s	Unit mass of steel of the longitudinal and transverse reinforcement	7850	kg/m^3
f_{ck}	Characteristic compressive strength of concrete	25	MPa
E_{ci}	Modulus of initial elasticity of concrete	28000	MPa
ρ_c	Unit mass of reinforced concrete	2500	kg/m^3
c	Cover to reinforcement	2.5	cm
C_c	Unit cost of concrete for beams - C25	336.02	R$/m^3
	Unit cost of concrete for columns - C25	340.94	R$/m^3
C_s	Unit cost of longitudinal reinforcement - ϕ_{10}	5.84	R$/kg
	Unit cost of longitudinal reinforcement - $\phi_{12.5}$	5.21	R$/kg
C_{sw}	Unit cost of transverse reinforcement - $\phi_{6.3}$	7.44	R$/kg
C_f	Unit cost of formwork for beams	57.32	R$/m^2
	Unit cost of formwork for columns	47.06	R$/m^2

The cases of constraints applied in each example are: Case I (ULS + SLS); Case II (ULS); Case III (SLS). In relation to the optimization algorithm, the initial population of case I includes a feasible pre-defined design $\mathbf{x}^{(1)}$. Cases II and III use the optimal result of case I as the design $\mathbf{x}^{(1)}$ included in the initial population. Preliminary tests indicated a high probability of convergence to local minima. For this reason, each case is run 10 times, considering different initial populations, related to different seeds of the pseudo-random generator. The best result obtained is taken as the final of the optimization process. Based on adjustments performed in these preliminary testes, in order to achieve satisfactory results in both examples, the following parameters are adopted in the optimization algorithm: population size equal to 50 individuals; limit of generations equal to 10000; stall generation of 500 generations. The computational times presented refer to an Intel Core i7-5820K processor.

4.1 Example I: one-bay two-story frame

The example consists of a reinforced concrete plane frame, whose geometry was presented by Adamu and Karihaloo [46]. Figure 5 shows the structure and Table 2 the characteristic loads applied in addition to the weight of the structure.

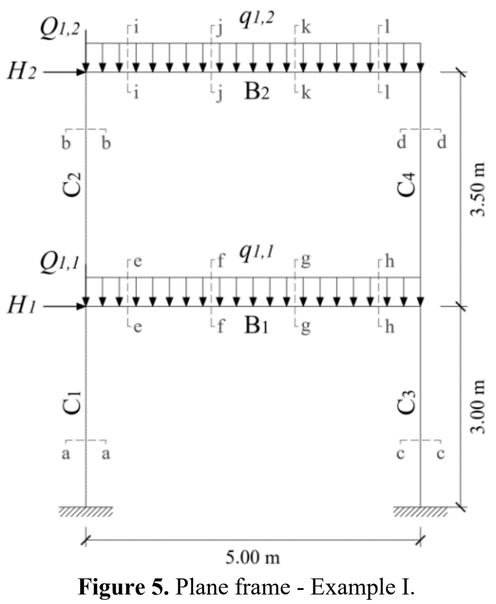

Figure 5. Plane frame - Example I.

Table 2. Characteristic loads - Example I.

Characteristic loads	Permanent loads	Variables loads
H_1	-	11.9 kN
$Q_{1,1}$	21.4 kN	14.3 kN
$q_{1,1}$	25.7 kN/m	17.1 kN/m
H_2	-	6.0 kN
$Q_{1,2}$	12.9 kN	8.6 kN
$q_{1,2}$	17.1 kN/m	11.4 kN/m

Regarding the variables, the beams B_1 and B_2 are discretized in four segments of equal length, so that each beam has 17 variables: b , h , ϕ_s^{bottom} , ϕ_s^{top} , ϕ_{sw} , $n_{s_1}^{bottom}$, $n_{s_1}^{top}$, n_{sw_1} , $n_{s_2}^{bottom}$, $n_{s_2}^{top}$, n_{sw_2} , $n_{s_3}^{bottom}$, $n_{s_3}^{top}$, n_{sw_3} , $n_{s_4}^{bottom}$, $n_{s_4}^{top}$ and n_{sw_4} , in which the numerical sub-index indicates the segment of the beam. Also, some columns are assumed to be equal, C_1=C_2 and C_3=C_4, except for the amounts of reinforcement. In this way, each pair of columns (C_1+C_2 and C_3+C_4) has 8 variables; for example, for the pair of columns C_1 and C_2 the design variables are: b , h , ϕ_s , ϕ_{sw} , $n_s^{C_1}$, $n_{sw}^{C_1}$, $n_s^{C_2}$ e $n_{sw}^{C_2}$. Thus, the problem has 50 variables in total. For the variables related to the beams, the following possible values are adopted: $b =$ [12, 26] cm and $h =$ [30, 60] cm, in increments of 2; $n_s^{bottom} =$ [2, 10], $n_s^{top} =$ [2, 10] and $n_{sw} =$ [6, 13], in increments of 1. For the variables related to the columns, the following possible values are adopted: $b =$ [19, 31] cm, $h =$ [19, 51] cm and $n_{sw} =$ [20, 36], in increments of 2; $n_s =$ [2, 8] in increments of 1. Diameter of 10 mm is adopted for the longitudinal reinforcement and 6.3 mm for the transverse reinforcement.

Figures 6 and 7 show the result obtained for case I. The total cost of the structure is R$ 2853.50, with 46.24% corresponding to the formwork, 35.88% related to the reinforcement and 17.88% related to the concrete. 1827 generations and 91400 evaluations of the objective function were required by the optimization procedure, with a computational time of 8.09 hours. For case II, the optimal sections found are the same as those obtained in case I, with a total of 501 generations and 25100 evaluations of the objective function and a computational time of 3.75 hours. Finally, the optimal sections for case III are illustrated in Figure 8. The total cost of the structure in this case is R$ 2080.21, where 53.88%, 26.62% and 19.50% correspond to the cost of formwork, reinforcement and concrete, respectively. 44800 evaluations of the objective function over 895 generations were required in this case, which corresponds to a computational time of about 4.2 hours.

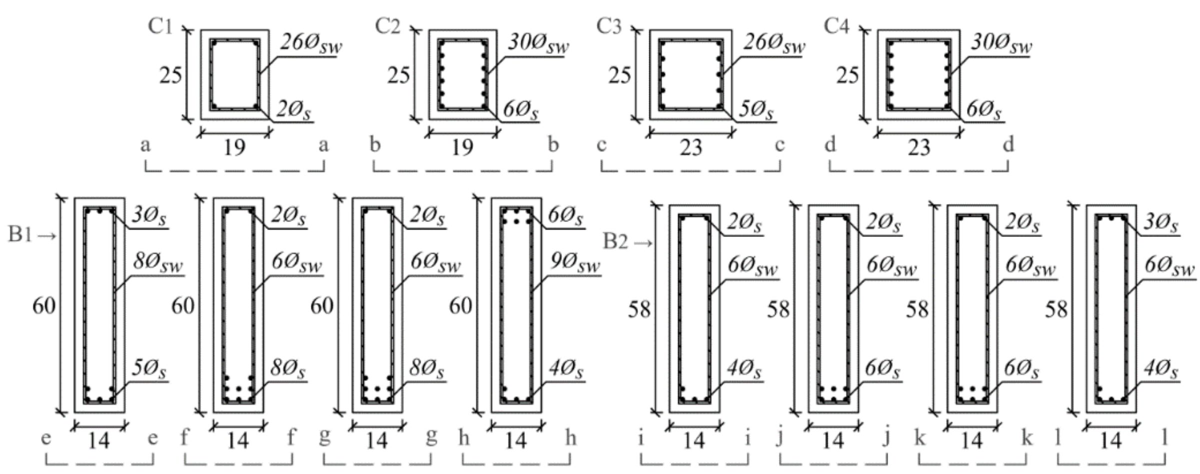

Figure 6. Detailing the optimal sections (dimensions in cm) - Example I: case I.

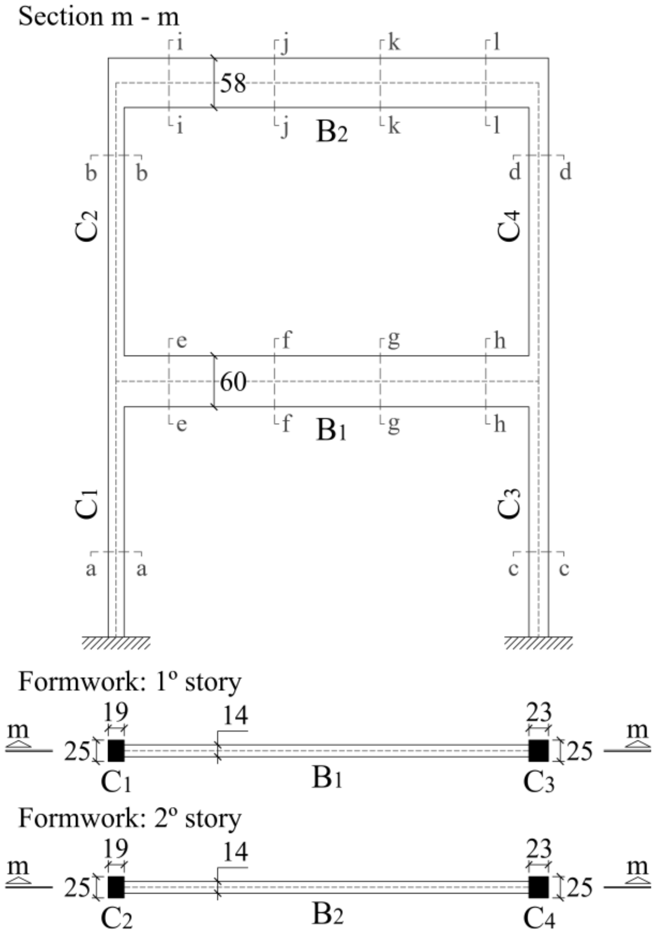

Figure 7. Optimal structure (dimensions in cm) - Example I: case I.

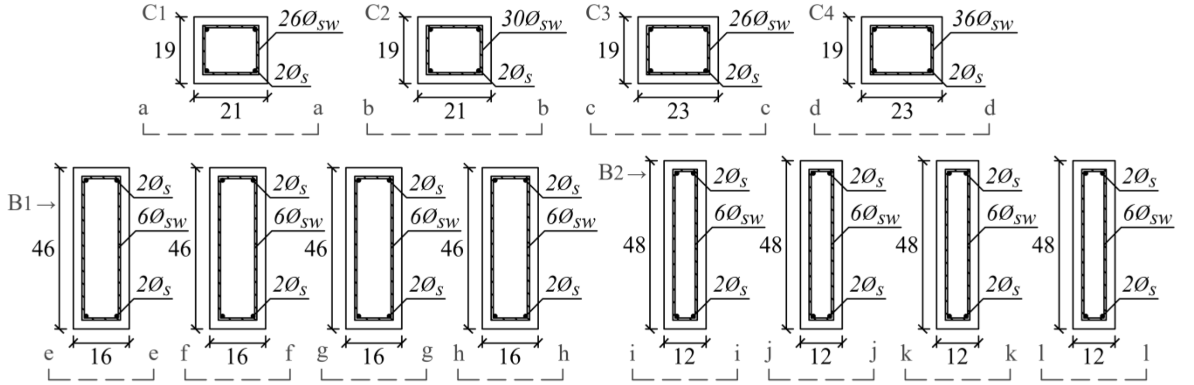

Figure 8. Detailing the optimal sections (dimensions in cm) - Example I: case III.

4.2 Example II: two-bay six-story frame

The second example consists of a structure previously studied by some authors [47], [20], [9], [12], from which the geometry was defined. The frame is illustrated in Figure 9 and the characteristic loads are described in Table 3. The weight of the structure is also considered.

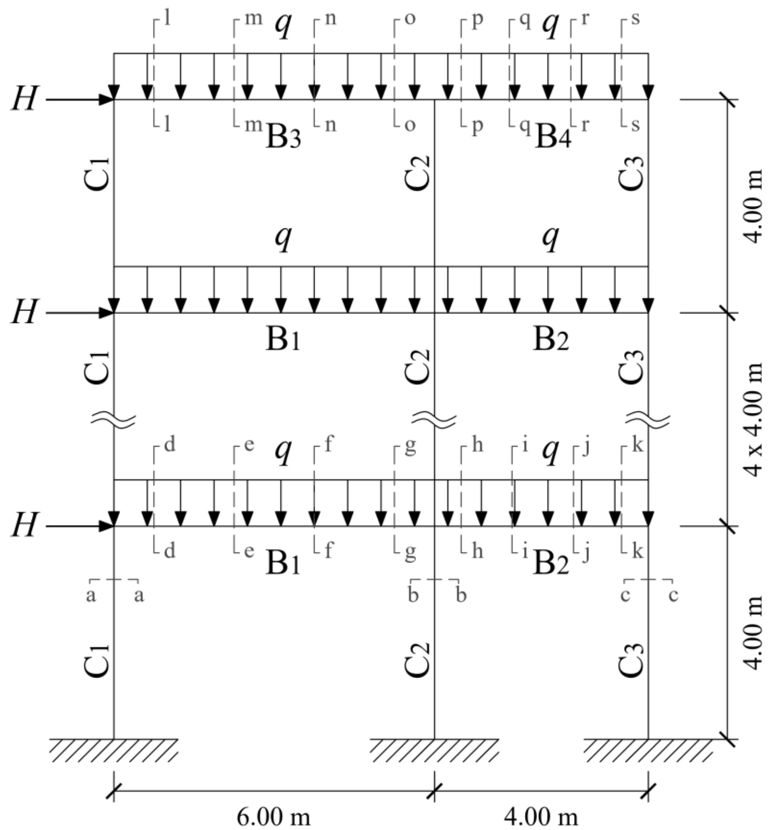

Figure 9. Plane frame - Example II.

Table 3. Characteristic loads - Example II.

Characteristic loads	Permanent loads	Variables loads
H	-	11.9 kN
q	12.9 kN/m	8.6 kN/m

Four different types of beams (B_1, B_2, B_3 and B_4) are adopted and discretized into four segments each. Therefore, each beam has 17 variables, as in Example I. Also, three different types of columns (C_1, C_2 and C_3) are adopted. Thus, each column has 6 variables: b , h , ϕ_s , ϕ_{sw} , n_s and n_{sw} . Therefore, the problem has 86 variables in total. For the variables of the beams, the following possible values are adopted: $b =$ [12, 30] cm and $h =$ [30, 60] cm, in increments of 2; $n_s^{bottom} =$ [2, 10], $n_s^{top} =$ [2, 10] and $n_{sw} =$ [5, 15], in increments of 1. While, for the columns: $b =$ [19, 39] cm, $h =$ [19, 55] cm and $n_{sw} =$ [28, 40], in increments of 2; $n_s =$ [2, 9] in increments of 1. Diameter of 12.5 mm is adopted for the longitudinal reinforcement and 6.3 mm for the transverse reinforcement.

The optimal structure for case I is presented in Figures 10 and 11. The total cost of the frame is R$ 16801.08, where 50.49%, 28.35% and 21.16% correspond to formwork, reinforcement, and concrete, respectively. Taking the cost of the design $\mathbf{x}^{(1)}$ as a reference, the convergence history of the relative cost over the generations is illustrated in Figure 12, where it is possible to observe that the optimization leads to a design configuration which is approximately 26% less expensive than the initial design. In this situation, 2646 generations and 132350 evaluations of the objective function were required, so that the computational time was about 45 hours. Figure 13 shows the result for case II, which corresponds to a total cost of R$ 16433.20, where 50.89% corresponds to the formwork, 28.70% is relative to the reinforcement and 20.41% is related to the concrete. 53900 evaluations of the objective function and 1077 generations were required, leading to a computational time of 17.85 hours. In the third case, illustrated in Figure 14, the computational time was 19.41 hours, with 1155 generations and 57800 evaluations of the objective function. The total cost of the structure is R$ 15776.73, with 52.60% corresponding to the formwork, 25.97% relative to the reinforcement and 21.44% related to the concrete.

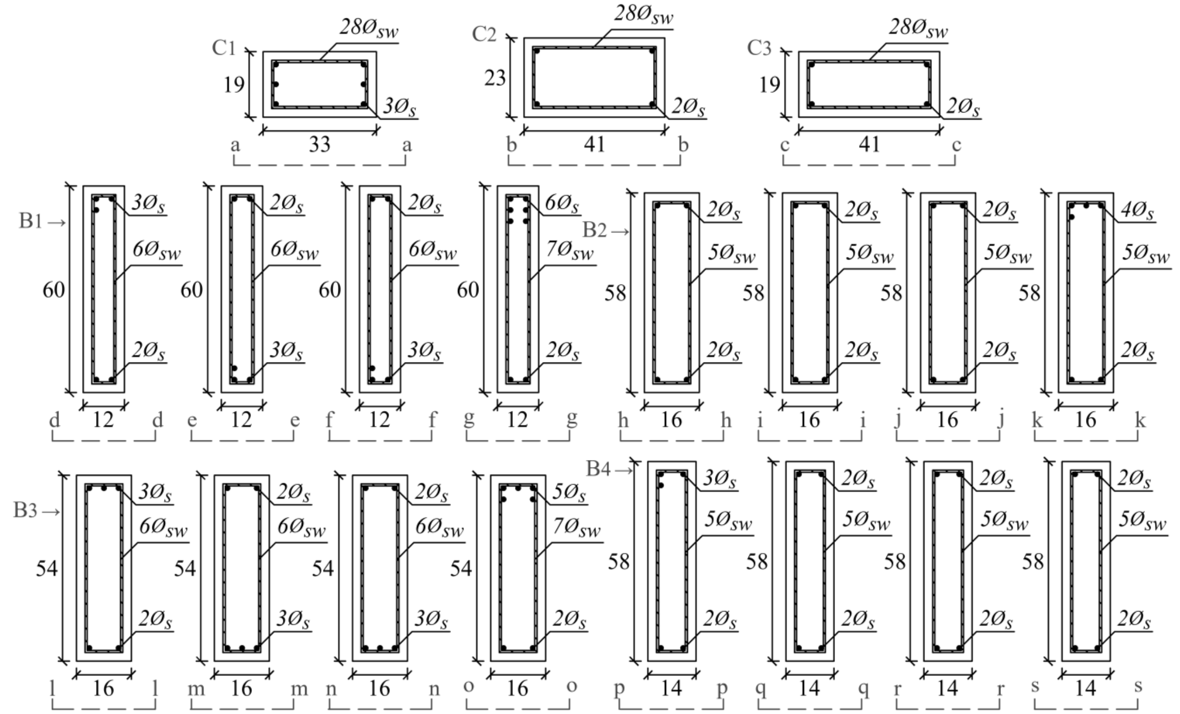

Figure 10. Detailing the optimal sections (dimensions in cm) - Example II: case I.

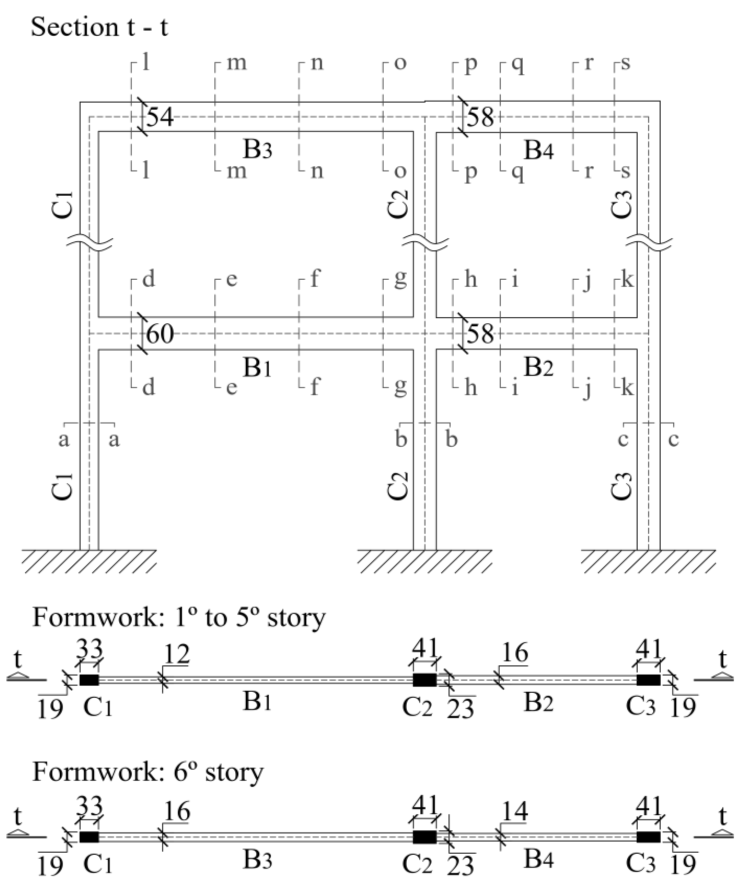

Figure 11. Optimal structure (dimensions in cm) - Example II: case I.

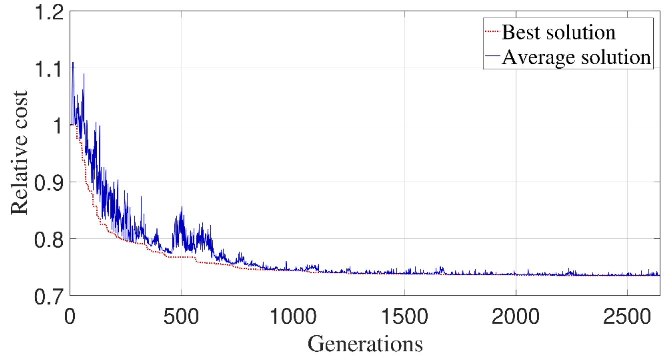

Figure 12. Convergence history - Example II: case I.

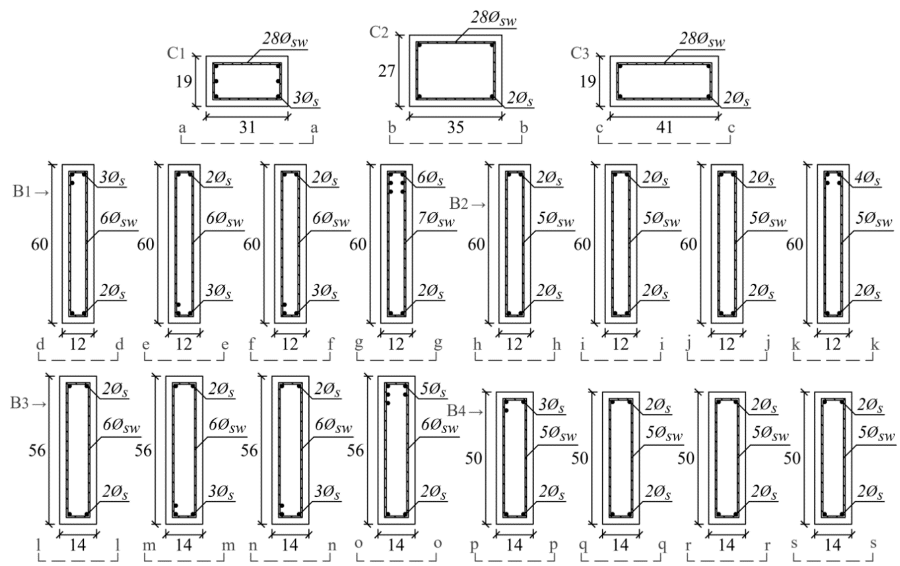

Figure 13. Detailing the optimal sections (dimensions in cm) - Example II: case II.

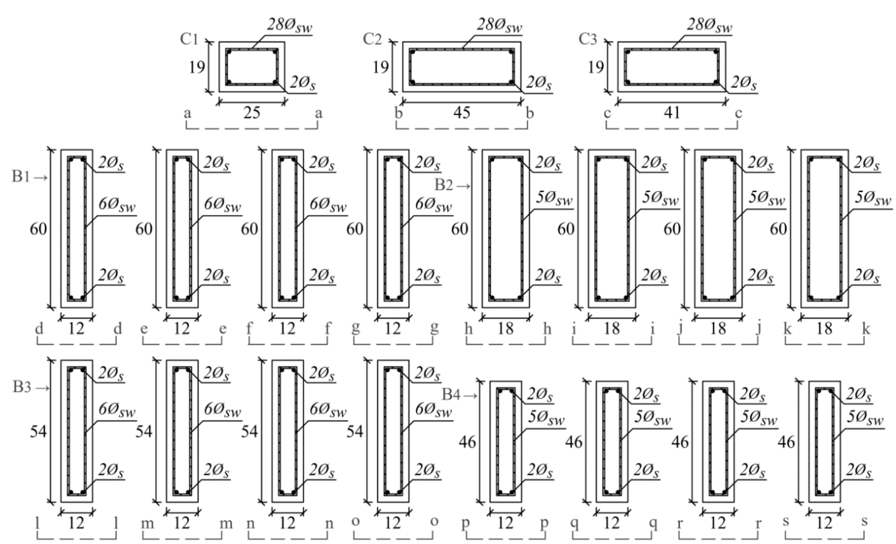

Figure 14. Detailing the optimal sections (dimensions in cm) - Example II: case III.

4.3 Discussion of results

In example I, when both limit states are considered as optimization constraints, the result is the same as when only the constraints of the ULS are taken into account; different from what occurred when considering only the SLS constraints, which leads to an optimal structure with a lower cost (27.10% less expensive). Therefore, the optimal structure for the ULS also checks the SLS constraints, but the optimal structure for the SLS does not meet all the constraints of the ULS. This situation is directly related to the design practice, in which the structure is usually designed for the ultimate conditions and then the service checks are performed. Unlike example I, cases I, II and III of example II led to different optimal sections, that is, the optimal structure for the ULS does not satisfy all the constraints of the SLS, in the same way that the optimal structure for the SLS does not satisfy all the constraints of the ULS. However, the optimal sections for case I are like the optimal sections for case II. In this example, when disregarding the SLS constraints (case II), the reduction in the total cost of the structure in relation to case I was of 2%, and when disregarding the ULS constraints (case III), this reduction was of 4%.

Among the specific constraints of both limit states, in example I, the constraint related to the design bending strength of C_2 was identified as a limiting constraint for cases I and II. For case III, the limiting constraint was related to the horizontal displacement at the top of the frame. By limiting constraint, it is understood that the constraint that was closer to being violated, since when using discrete variables in problems like the one proposed, there will be hardly any active constraints. For example II, the limiting constraint for cases I and III was the horizontal displacement at the top of the frame. For case II, the limiting constraint was related to the design bending strength of the top face of beam B_1 of the first story.

In both examples, the optimal columns related to ULS presented widths and amounts of longitudinal reinforcement equal to or greater than those related to SLS. On the other hand, the heights of the cross sections of the optimal columns according to the SLS tended to be equal to or larger than those of the ULS. It should be noted that, in case I of example I, the widths of the columns were greater than the heights due to the consideration that the columns have only one longitudinal reinforcement layer. Since the constraint of the transverse reinforcement for the columns concerns the minimum amount defined in the code, it was expected that all cases would have the same amount of such reinforcement, which happened for most situations. The optimal beams for the ULS have heights equal to or greater than the optimal beams for the SLS, just as they are equally or more reinforced in both directions. Also, there was a preponderance of minimum widths in all the elements optimum for SLS, except for one beam in each example.

In all cases of both examples, the formwork accounted for the most significant part of the optimal total cost, followed by the reinforcement.

5 CONCLUSIONS

This paper presented the optimization of reinforced concrete frames applying three different cases of constraints: related to the ULS and SLS constraints simultaneously; only those related to the ULS; and only those related to the SLS. All constraints were based on the requirements presented by the Brazilian design code, NBR 6118 [26].

The results obtained for two different examples indicated a tendency of the optimal characteristics of the structures, depending on the constraints applied. Thus, by evaluating the set of structures, it can be said that the cross sections tend to be larger and more reinforced in the case of the ULS. This is because the combinations of loads for the ULS lead to larger loads than those of the SLS.

The optimization processes of case III presented a greater reduction of cost in relation to the optimum of case I than the optimization processes of case II. It is also observed that the optimal structure considering all constraints is more like the optimal structure for the ULS than for the SLS, which indicates that SLS is generally less restrictive than ULS. Even so, optimal structure related to the ULS often does not satisfy SLS and vice versa. In addition, it is observed that, in the first example, the limiting constraint of the optimization of case I is related to section resistance (ULS). For example II, which is a higher structure, the limiting constraint in case I refers to the horizontal displacement at the top of the frame (SLS).

It is noteworthy that large differences between the costs of the optimal structures for cases I, II and III, may indicate that the structural design as a whole needs adjustments and/or modifications. Thus, making other changes to the design can be a more efficient alternative. These changes may include, for example, the adoption of different cross sections (T or hollow) and modifications in the topology (positions of the columns and different lengths of the structural elements).

Regarding to costs, there was a predominance of the formwork in the costs of the structures. It is noteworthy that the use of concrete with larger f_{ck} could result in smaller cross-sections, and consequently decrease the contribution of the formwork to the cost of the structure.

ACKNOWLEDGEMENTS

The authors gratefully acknowledge the financial support from Scientific and Technological Research Support Foundation of Santa Catarina State (FAPESC, public call nº 05/2015) and National Council for Scientific and Technological Development (CNPq, grant 302489/2017-7).

REFERENCES

[1] J. K. Wight and J. G. MacGregor, *Reinforced Concrete: Mechanics & Design*, 6th ed. Upper Saddle River, New Jersey, USA: Pearson, 2012.

[2] J. Nocedal and S. J. Wright, *Numerical Optimization.* New York, USA: Springer, 1999.

[3] J. S. Arora, *Introduction to Optimum Design*, 2nd ed. San Diego, California, USA: Elsevier Academic Press, 2004.

[4] W. R. Spillers and K. M. MacBain, *Structural Optimization.* New York, USA: Springer, 2009.

[5] S. Kanagasundaram and B. L. Karihaloo, "Minimum-cost reinforced concrete beams and columns," *Comput. Struc.*, vol. 41, no. 3, pp. 509–518, 1991, http://dx.doi.org/10.1016/0045-7949(91)90145-C.

[6] H. G. Kwak and J. Kim, "Optimum design of reinforced concrete plane frames based on predetermined section database," *Comput. Aided Des.*, vol. 40, no. 3, pp. 396–408, 2008, http://dx.doi.org/10.1016/j.cad.2007.11.009.

[7] I. Paya-Zaforteza, V. Yepes, A. Hospitaler, and F. González-Vidosa, "CO_2-optimization of reinforced concrete frames by simulated annealing," *Eng. Struct.*, vol. 31, no. 7, pp. 1501–1508, 2009, http://dx.doi.org/10.1016/j.engstruct.2009.02.034.

[8] F. Fedghouche and B. Tiliouine, "Minimum cost design of reinforced concrete T-beams at ultimate loads using Eurocode2," *Eng. Struct.*, vol. 42, pp. 43–50, 2012, http://dx.doi.org/10.1016/j.engstruct.2012.04.008.

[9] C. V. Camp and F. Huq, "CO_2 and cost optimization of reinforced concrete frames using a big bang-big crunch algorithm," *Eng. Struct.*, vol. 48, pp. 363–372, 2013, http://dx.doi.org/10.1016/j.engstruct.2012.09.004.

[10] I. Rahmanian, Y. Lucet, and S. Tesfamariam, "Optimal design of reinforced concrete beams: A review," *Comput. Concr.*, vol. 13, no. 4, pp. 457–482, 2014, http://dx.doi.org/10.12989/cac.2014.13.4.457.

[11] C. S. Kao and I. C. Yeh, "Optimal design of reinforced concrete plane frames using artificial neural networks," *Comput. Concr.*, vol. 14, no. 4, pp. 445–462, 2014, http://dx.doi.org/10.12989/cac.2014.14.4.445.

[12] A. Akin and M. P. Saka, "Harmony search algorithm based optimum detailed design of reinforced concrete plane frames subject to ACI 318-05 provisions," *Comput. Struc.*, vol. 147, pp. 79–95, 2015, http://dx.doi.org/10.1016/j.compstruc.2014.10.003.

[13] M. Aldwaik and H. Adeli, "Cost optimization of reinforced concrete flat slabs of arbitrary configuration in irregular highrise building structures," *Struct. Multidiscipl. Optim.*, vol. 54, no. 1, pp. 151–164, 2016, http://dx.doi.org/10.1007/s00158-016-1483-5.

[14] A. Habibi, F. Ghawami, and M. S. Shahidzadeh, "Development of optimum design curves for reinforced concrete beams based on the INBR9," *Comput. Concr.*, vol. 18, no. 5, pp. 983–998, 2016, http://dx.doi.org/10.12989/cac.2016.18.5.983.

[15] A. Tapao and R. Cheerarot, "Optimal parameters and performance of artificial bee colony algorithm for minimum cost design of reinforced concrete frames," *Eng. Struct.*, vol. 151, pp. 802–820, 2017, http://dx.doi.org/10.1016/j.engstruct.2017.08.059.

[16] C. A. C. Coello, A. D. Christiansen, and F. S. Hernández, "A simple genetic algorithm for the design of reinforced concrete beams," *Eng. Comput.*, vol. 13, no. 4, pp. 185–196, 1997, http://dx.doi.org/10.1007/BF01200046.

[17] V. K. Koumousis and S. J. Arsenis, "Genetic algorithms in optimal detailed design of reinforced concrete members," *Comput. Aided Civ. Infrastruct. Eng.*, vol. 13, no. 1, pp. 43–52, 1998, http://dx.doi.org/10.1111/0885-9507.00084.

[18] M. Y. Rafiq and C. Southcombe, "Genetic algorithms in optimal design and detailing of reinforced concrete biaxial columns supported by a declarative approach for capacity checking," *Comput. Struc.*, vol. 69, no. 4, pp. 443–457, 1998, http://dx.doi.org/10.1016/S0045-7949(98)00108-4.

[19] M. Leps and M. Sejnoha, "New approach to optimization of reinforced concrete beams," *Comput. Struc.*, vol. 81, no. 18-19, pp. 1957–1966, 2003, http://dx.doi.org/10.1016/S0045-7949(03)00215-3.

[20] C. V. Camp, S. Pezeshk, and H. Hansson, "Flexural design of reinforced concrete frames using a genetic algorithm," *J. Struct. Eng.*, vol. 129, no. 1, pp. 105–115, 2003, http://dx.doi.org/10.1061/(ASCE)0733-9445(2003)129:1(105).

[21] V. Govindaraj and J. V. Ramasamy, "Optimum detailed design of reinforced concrete continuous beams using genetic algorithms," *Comput. Struc.*, vol. 84, no. 1-2, pp. 34–48, 2005, http://dx.doi.org/10.1016/j.compstruc.2005.09.001.

[22] H. G. Kwak and J. Kim, "An integrated genetic algorithm complemented with direct search for optimum design of RC frames," *Comput. Aided Des.*, vol. 41, no. 7, pp. 490–500, 2009, http://dx.doi.org/10.1016/j.cad.2009.03.005.

[23] L. Mingqi and L. Xing "Genetic algorithms based methodologies for optimization designs of RC structures," in *Proc. Int. Conf. Intell. Syst. Des. Eng6 Appl.*, Changsha, 2010, pp. 787-790, http://dx.doi.org/10.1109/ISDEA.2010.32

[24] P. E. Mergos, "Optimum seismic design of reinforced concrete frames according to Eurocode 8 and *fib* Model Code 2010," *Earthquake Eng. Struct. Dynam.*, vol. 46, no. 7, pp. 1181–1201, 2017, http://dx.doi.org/10.1002/eqe.2851.

[25] M. Mangal and J. C. P. Cheng, "Automated optimization of steel reinforcement in RC building frames using building information modeling and hybrid genetic algorithm," *Autom. Construct.*, vol. 90, pp. 39–57, 2018, http://dx.doi.org/10.1016/j.autcon.2018.01.013.

[26] Associação Brasileira de Normas Técnicas, *Design of Concrete Structures – Procedure*, ABNT NBR 6118, 2014.

[27] Associação Brasileira de Normas Técnicas, *Actions and Safety of Structures – Procedure*, ABNT NBR 8681, 2003.

[28] R. Bordignon and M. Kripka, "Optimum design of reinforced concrete columns subjected to uniaxial flexural compression," *Comput. Concr.*, vol. 9, no. 5, pp. 327–340, 2012, http://dx.doi.org/10.12989/cac.2012.9.5.327.

[29] G. F. Medeiros and M. Kripka, "Structural optimization and proposition of pre-sizing parameters for beams in reinforced concrete buildings," *Comput. Concr.*, vol. 11, no. 3, pp. 253–270, 2013, http://dx.doi.org/10.12989/cac.2013.11.3.253.

[30] G. F. Medeiros and M. Kripka, "Optimization of reinforced concrete columns according to different environmental impact assessment parameters," *Eng. Struct.*, vol. 59, pp. 185–194, 2014, http://dx.doi.org/10.1016/j.engstruct.2013.10.045.

[31] M. Kripka, G. F. Medeiros, and A. C. C. Lemonge, "Use of optimization for automatic grouping of beam cross-section dimensions in reinforced concrete building structures," *Eng. Struct.*, vol. 99, pp. 311–318, 2015, http://dx.doi.org/10.1016/j.engstruct.2015.05.001.

[32] R. S. Correia, G. F. F. Bono, and G. Bono, "Optimization of reinforced concrete beams using Solver tool," *IBRACON Struct. Mater. J.*, vol. 12, no. 4, pp. 910–931, 2019, http://dx.doi.org/10.1590/s1983-41952019000400011.

[33] M. A. Juliani and W. J. S. Gomes "Influence of limit states on the optimization of reinforced concrete beams", in *Proc. 6th Int. Symp. Solid Mech.*, Joinville, 2017, pp. 943-954. http://dx.doi.org/10.26678/ABCM.MecSol2017.MSL17-0018.

[34] M. A. Juliani and W. J. S. Gomes, "Influence of limit states on the optimization of reinforced concrete plane frames," in *Proc. 38th Iberian Latin-American Congr. Comput. Methods in Eng.*, Florianópolis, 2017, http://dx.doi.org/10.20906/CPS/CILAMCE2017-0219

[35] MathWorks, *MATLAB – Primer.* Natick, Massachusetts, USA: MathWorks, 2017.

[36] R. D. Ziemian and W. McGuire, *Tutorial for MASTAN2 – Version 3.0*. New York: John Wiley & Sons, 2007.

[37] W. McGuire, R. H. Gallagher, and R. D. Ziemian, *Matrix Structural Analysis*, 2nd ed. New York: John Wiley & Sons, 2014.

[38] K. J. Bathe, *Finite Element Procedures*. Englewood Cliff, New Jersey, USA: Prentice-Hall, 1996.

[39] T. Belytschko, W. K. Liu, and B. Moran, *Nonlinear Finite Elements for Continua and Structures*. Chichester: John Wiley & Sons, 2000.

[40] J. H. Holland, *Adaptation in Natural and Artificial System*. Michigan: Univ. Michigan Press, 1975.

[41] D. E. Goldberg, *Genetic Algorithms in Search, Optimization & Machine Learning*. Boston: Addison-Wesley, 1989.

[42] S. N. Sivanandam and S. N. Deepa, *Introduction to Genetic Algorithms*. Berlin: Springer, 2008.

[43] MathWorks, *Global Optimization Toolbox – Users Guide*, Natick, Massachusetts, USA: MathWorks, 2016.

[44] K. Deep, K. P. Singh, M. L. Kansal, and C. Mohan, "A real coded genetic algorithm for solving integer and mixed integer optimization problems," *Appl. Math. Comput.*, vol. 212, no. 2, pp. 505–518, 2009, http://dx.doi.org/10.1016/j.amc.2009.02.044.

[45] Sistema Nacional de Preços e Índices para a Construção Civil, *Caixa Econômica Federal – Outubro, Florianópolis, Santa Catarina, Brazil*, 2017.

[46] A. Adamu and B. L. Karihaloo, "Minimum cost design of RC frames using the DCOC method – part I: columns under uniaxial bending actions," *Struct. Optim.*, vol. 10, no. 1, pp. 16–32, 1995, http://dx.doi.org/10.1007/BF01743691.

[47] S. Rajeev and C. S. Krishnamoorthy, "Genetic algorithm – based methodology for design optimization of reinforced concrete frames," *Comput. Aided Civ. Infrastruct. Eng.*, vol. 13, no. 1, pp. 63–74, 1998, http://dx.doi.org/10.1111/0885-9507.00086.

Author contributions: M. A. Juliani: development of codes and writing; W. J. S. Gomes: development of codes and supervision.

Editors: Maurício de Pina Ferreira, José Luiz Antunes de Oliveira e Sousa, Guilherme Aris Parsekian.

IBRACON Structures and Materials Journal
Revista IBRACON de Estruturas e Materiais
ISSN 1983-4195 ismj.org

ORIGINAL ARTICLE

Evaluation of rheological models for concrete submitted to alkali-aggregate reaction based on numerical analysis of damping - free expansion

Avaliação de modelos reológicos para concreto submetido a reação álcali-agregado baseada em análise numérica de amortecimento - expansão livre

Marlon de Barros Cavalcanti[a]
Sandro Marden Torres[b]
Marçal Rosas Florentino Lima Filho[c]
Alexsandro José Virgínio dos Santos[d]

[a]Companhia Hidro Elétrica do São Francisco – CHESF, Departamento de Engenharia de Geração Eólica, Recife, PE, Brasil
[b]Universidade Federal da Paraíba – UFPB, Departamento de Engenharia de Materiais, João Pessoa, PB, Brasil
[c]Universidade Federal da Paraíba – UFPB, Departamento de Engenharia de Energias Renováveis, João Pessoa, PB, Brasil
[d]Universidade Federal da Paraíba – UFPB, Departamento de Engenharia Elétrica, João Pessoa, PB, Brasil

Received 04 October 2019
Accepted 06 July 2020

Abstract: The Alkali-Aggregate Reaction (AAR) phenomenon in concrete structures is perceived via expansion and cracking, swelling of gel like material, causing damage and disruption in structural elements. Despite extensive standardization, AAR cases are still persistently occurring worldwide. The literature on susceptibility of concrete to AAR reported examples of false negative and positive results. Hence, long-term prediction is a problem still posing great challenge to engineers. The severity of AAR on the structural integrity can be mostly elucidated by the assessment of the historic of elastic properties. There is consensus that AAR causes decrease in the load capacity concrete, reflected by reduction of elasticity modulus due damage progresses. Non-destructive techniques are often used as first approach, as they can provide relatively fast assessment in situ as well as in large structural elements. Its data interpretation carries certain degree of complexity due intrinsic characteristic of many of these methods. This is the case of Ultrasonic Pulse Velocity (UPV), which have been considered to present several limitations for such purpose. This paper deals the potential use of the Longitudinal Resonance Frequency (LRF) method as tool to evaluate the elastic historic of AAR prone elements. The LRF possesses higher energy than UPV. Also, using modulation of frequency in input signal combined the test geometry, the LRF allow application to larger samples as well as to extract complementary information alongside the dynamic elastic modulus. This way, the LRF was applied to study concrete beams tested under controlled conditions for about 1.5 year. The independent variables to the tests are: time, frequency, aggregate type, cement content, alkali content and water to cement ratio. The dependent variables are: damping, loss factor and elasticity modulus. The analysis associate damage with vibration damping, confirming reduction of elasticity through damage with experimental validation and prediction of AAR under rheological model.

Keywords: alkali-aggregate reaction, rheological model, damping.

Resumo: O fenômeno da Reação Álcali-Agregado (RAA) em estruturas de concreto é percebido via expansão e fissuração, inchando o gel como material, causando danos e rupturas nos elementos estruturais. Apesar da extensa padronização, casos de RAA ainda ocorrem persistentemente em todo o mundo. A literatura sobre suscetibilidade de concreto a RAA relatou exemplos de resultados falso negativo e positivo. Portanto, previsão a longo prazo é um problema que ainda representa um grande desafio para os engenheiros. A severidade da RAA sobre a integridade estrutural pode ser principalmente elucidada pela avaliação do histórico das propriedades elásticas. Existe consenso de que RAA causa diminuição da capacidade de carga do concreto, refletida pela redução do módulo de elasticidade devido ao progresso dos danos. Técnicas não destrutivas são

Corresponding author: Marlon de Barros Cavalcanti. E-mail: marlonbc@chesf.gov.br, marlonbcavalcanti@gmail.com
Financial support: Companhia Hidro Elétrica do São Francisco (Chesf).
Conflict of interest: Nothing to declare.

frequentemente usadas como primeira abordagem, pois podem fornecer uma avaliação relativamente rápida in situ, bem como em grandes elementos estruturais. A interpretação dos dados carrega certo grau de complexidade devido às características intrínsecas de muitos desses métodos. Este é o caso de Velocidade de Pulso Ultrassônico (VPU), que foi considerado como apresentando várias limitações para esse propósito. Este artigo trata o potencial uso do método de Frequência de Ressonância Longitudinal (FRL) como ferramenta para avaliar o histórico elástico de elementos propensos a RAA. A FRL possui maior energia que VPU. Além disso, usando modulação de frequência no sinal de entrada combinada à geometria de teste, a FRL permite aplicação em amostras maiores, bem como extrair informações complementares ao lado do módulo elástico dinâmico. Dessa forma, a FRL foi aplicada para estudar vigas de concreto testadas sob condições controladas por cerca de 1,5 ano. As variáveis independentes para os testes são: tempo, frequência, tipo de agregado, teor de cimento, teor de álcalis e relação água/cimento. As variáveis dependentes são: amortecimento, fator de perda e módulo de elasticidade. A análise associa dano com amortecimento da vibração, confirmando a redução de elasticidade através do dano com validação experimental e predição de RAA sob modelo reológico.

Palavras-chave: reação álcali-agregado, modelo reológico, amortecimento.

How to cite: M. B. Cavalcanti, S. M. Torres, M. R. F. Lima Filho, and A. J. V. Santos, "Evaluation of rheological models for concrete submitted to alkali-aggregate reaction based on numerical analysis of damping - free expansion", *Rev. IBRACON Estrut. Mater.*, vol. 14, no. 2, e14205, 2021, https://doi.org/10.1590/S1983-41952021000200005

1 INTRODUCTION: CRITICAL LITERATURE REVIEW

Alkali-Aggregate Reaction (AAR) is an expansion deleterious phenomenon that affects concrete's long-term performance and durability. Its origin is a chemical reaction between silicon and alkaline ions present in concrete pore solution, producing highly hydrophilic gel that expands over time in presence of water, introducing stresses in the concrete structure.

The pressure induced over time by the gel produced of the AAR can cause macroscopic expansion and internal damage to the material's microstructure. The reaction does not always lead to expansion, if there is enough empty space to be filled by the gel, such as pores and cracking, the volume of the concrete remains unchanged.

The concrete affected by AAR is subject to expansion and consequently to degradation, which can affect the concrete structures operationality, not necessarily the total ruin. For example, in dams, there are records of operational problems, due to the closure of expansion joints and alteration of the original geometry of structural components.

In recent years there has been an increase in the search for reliable techniques for dynamic non-destructive testing in the detection of damage to structures and materials (Butterworth et al. [1]; Leśnicki et al. [2]; Barreto [3]; Gutenbrunner et al. [4]; among others). This is due to the fact that the damage causes changes in parameters such as damping, consequently, in stiffness, where the study of damping and its evolution over time can direct the effective methodology for detecting stiffness degradation in concretes submitted to AAR.

1.1 Damping in structural materials

Among the possible methods for determining the elasticity modulus by dynamic testing of materials can to mention: ultrasonic pulse velocity (or ultrasonic longitudinal wave vibration frequency, i.e., above 20 kHz - ABNT NBR 8802 [5]) and resonance frequency (longitudinal, transversal, flexional and torsional).

Dynamic tests by resonance frequency carry two characteristics that can have great potential in the analysis of damage to structures, which are: a) Frequency response capable of representing the state of tension; and b) Ability to measure damping, given the fact that the energy level in the method is high enough for detection and, even so, the induced stress is below which damage can be produced.

It's worth noting that, according to Butterworth et al. [1], damping is the most difficult to predict dynamic property, as it cannot be deduced of physical properties of the structure, unlike mass and rigidity, need of experimental investigation.

1.2 Damping in concrete

Work conducted by Nagy [6], for damping in concrete, consisted of equipment for sample excitation and receivers for Fast Fourier Transform (FFT) analysis, where the resonance frequency corresponds to the "peak" showed of the curve in Figure 1, which also show the calculation of the loss factor (η) by the half-power bandwidth method. Equation 1 reproduces and complements the formulation expressed in Figure 1, inserting the damping ratio parameter (ξ).

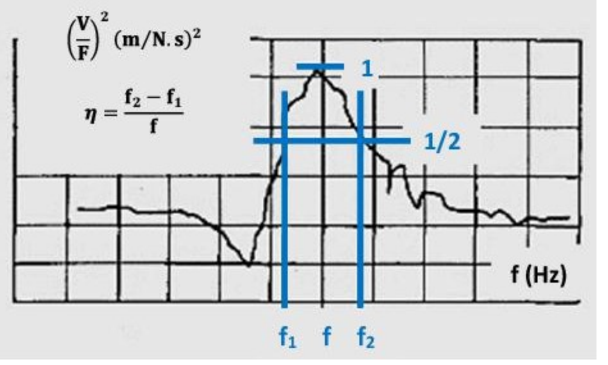

Figure 1. Schematic diagram for calculating the loss factor (adapted of Nagy [6]).

$$\frac{\Delta\omega}{\omega_{res}} = \frac{f_2 - f_1}{f} = 2\,\xi \simeq \eta \tag{1}$$

1.3 Damping and AAR

Work conducted by Leśnicki et al. [2] states that the difficulties in quantifying damage to concrete originate of its complex microstructure. Other complications arise of possible chemical reactions, such as AAR, which can considerably and continuously modify the existing microstructure.

The gel formed not only provides another phase in the already complex microstructure, but it is also hygroscopic. The swelling of the gel induces internal stress within of the concrete matrix, which, if enough, can cause interfacial detachment, cracking initiation and propagation.

The cracking resulting of the expansion imposed by the AAR, distributed in the structural member, reduce the mechanical stiffness and, consequently, the resonance frequencies of the member. These cracking can be considered part of an imperfect interconnected system, which also includes interfaces between the aggregate and the surrounding mortar or cement paste, as well as other defects.

A typical set of Frequency Response Function (FRF) graphs for undamaged concrete sample (S3) and concrete sample highly reactive to AAR (S1) are shown in Figure 2, where the differences in the resonance curves obtained are clear [2].

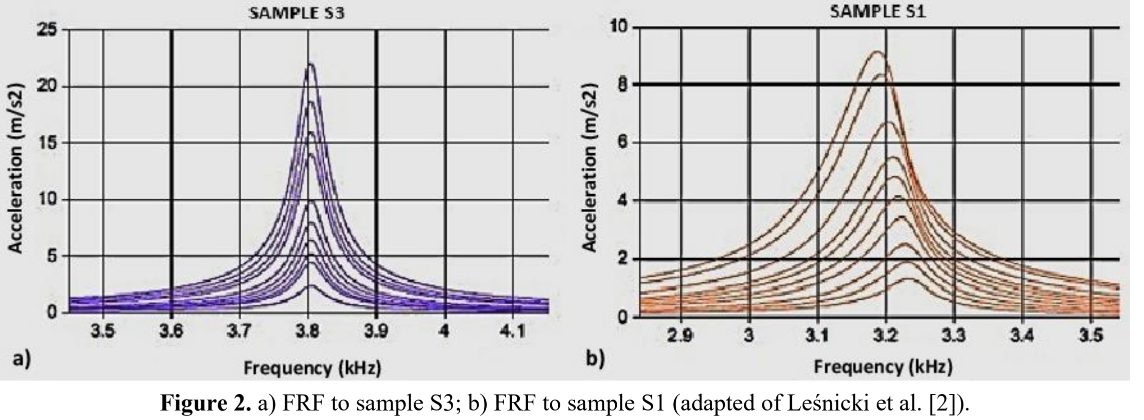

Figure 2. a) FRF to sample S3; b) FRF to sample S1 (adapted of Leśnicki et al. [2]).

The results, according Leśnicki et al. [2], show potential for the detection of AAR in concrete through resonance tests in conjunction with expansion tests, where resonance show the frequency decay in the undamaged sample (S3) of 3.8 kHz to approximately 3.2 kHz in the highly reactive sample (S1). It's also noticed a decrease in the amplitude of accelerations of one sample to the other, about 23 m/s^2 to approximately 9 m/s^2. This behavior of decreasing of the frequency and amplitude is typical of viscous damping, as showed in Figure 3, considering literature to vibration damping of classical mechanics [7].

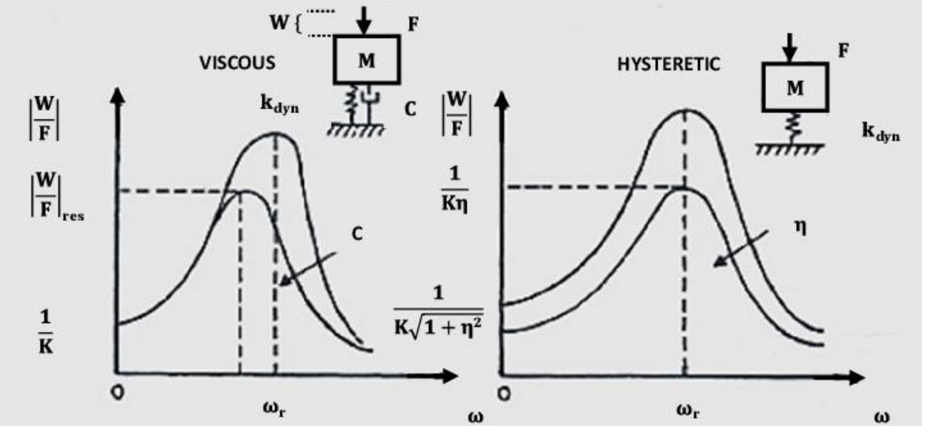

Figure 3. Dynamic response of viscous and hysteresis systems (adapted of Nashif et al. [7]).

1.4 Non-destructive testing

Within of approach proposed in the present study, based on damping, the parameters to be obtained of the resonance tests are: damping, loss factor and elasticity modulus.

1.4.1 Ultrasonic pulse velocity

Figure 4 show the results of Ultrasonic Pulse Velocity (UPV) tests carried out on the same concrete beams tested in the resonance in this study.

It's noticed an increase in UPV over the time of the tests, in which the dynamic elastic modulus is proportional the pulse propagation velocity, it can be deduced that the concrete beams, including those affected by AAR (R # - beam affected by AAR), are gaining rigidity, when in fact, the beams with reactive material are undergoing degradation, as verified in the resonance tests and where Barreto [3] confirmed that the ultrasound is not sensitive to the detection of AAR.

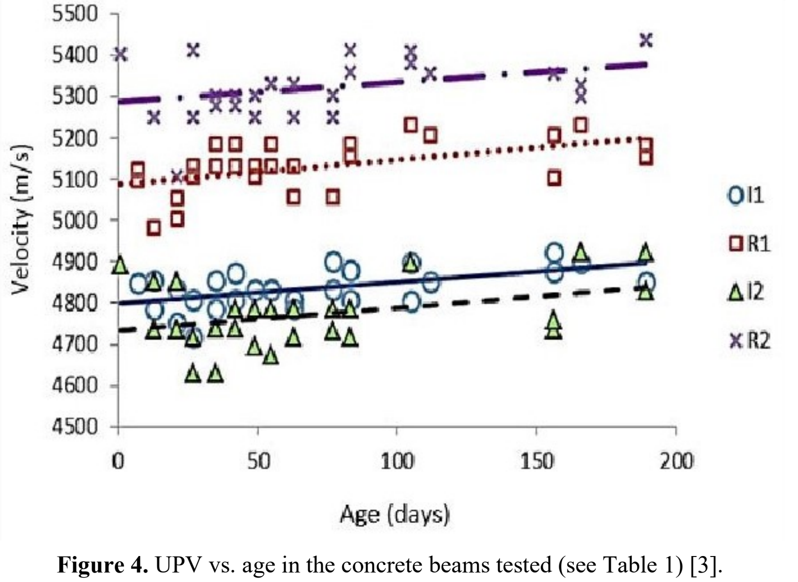

Figure 4. UPV vs. age in the concrete beams tested (see Table 1) [3].

The possible explanation for this lower sensitivity of the ultrasound, in face of the AAR phenomenon, may be correlated to the lower dissipative energy condition of the ultrasound in relation to non-Newtonian fluid, such as the

AAR gel. In addition, interference signals of the concrete microstructure and signals originating of damage coexist during the ultrasound test, as shown in Figure 5.

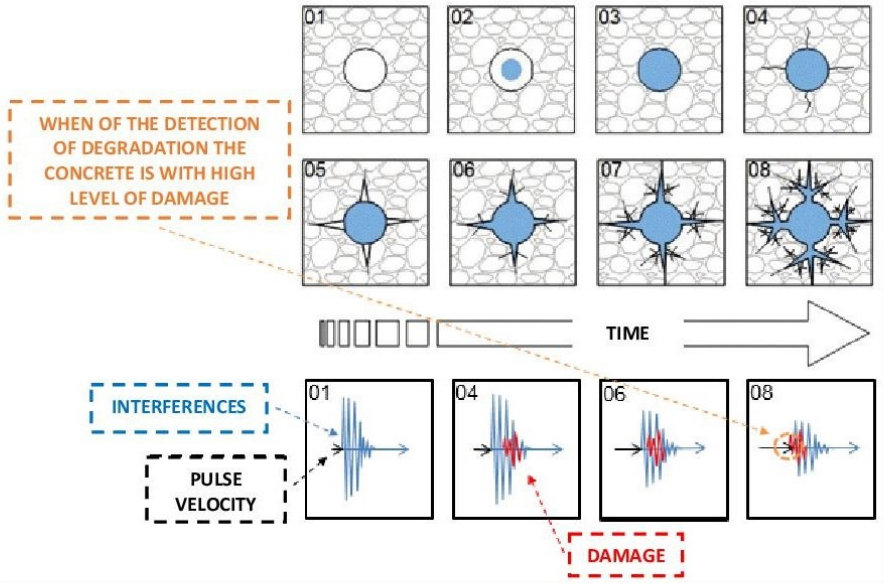

Figure 5. Illustration of UPV test vs. damage by the growth of gel of AAR (AUTHOR/UFPB).

Figure 5 sequences the growth of AAR gel in concrete void until the gel to fill the void, when the gel then starts to tension the concrete, where gel and concrete gain apparent rigidity, and cracking appear later, where the gel starts to fill the gaps, tensioning the concrete, in progressive damage cycle up to the point where the detection of degradation by ultrasound is evident.

1.4.2 Resonance frequency testing

In the case in question, for Longitudinal Resonance Frequency (LRF) tests conducted by Barreto [3], longitudinal force of sinusoidal behavior with variable frequency was applied in a time interval of 8 seconds, by the logarithmic scanning system of the equipment used (AGILENT 33220A [8]), where the manufacturer (AGILENT TECHNOLOGIES) reports that logarithmic scanning is useful to cover a wide range of frequencies, which in low resolution could be lost with the linear scanning system.

1.5 LRF in structural specimens (experimental apparatus)

1.5.1 Applied LRF to steel bar (experiment calibration)

In obtaining of the parameters of interest, considering test procedure adopted, the ASTM E 756 [9] assert that if the elasticity modulus obtained for steel (SAE 1020) is not approximately 207 GPa (data of the literature also suggest 205 to 210 GPa) and the loss factor is not approximately 0.002 to 0.001 for the 1st and 2nd modes and 0.001 or less for the higher modes, as in the numerical approach of this study, then there must be a problem with the device configuration or other in the measurement system.

In the test configuration of this study the result of the loss factor and elasticity modulus, measured dynamically, through LRF, for the steel adopted, respectively, corresponds to 0.00041 and 212.8 GPa, considering the 3rd experimental mode ("peak" at 3,948.4 Hz) (see Figure 6), being the 1st natural mode with "peak" at 3,436 Hz according to the described geometry of the steel bar (steel cylinder measuring 1.317 m in length with circular cross section of diameter 0.0508 m) and supposed 210 GPa module, where the divergence related to the 1st and 3rd experimental mode is due to the appearance of two previous "peaks" in the experimental result, arising of accessory modes and imperfections in the configuration.

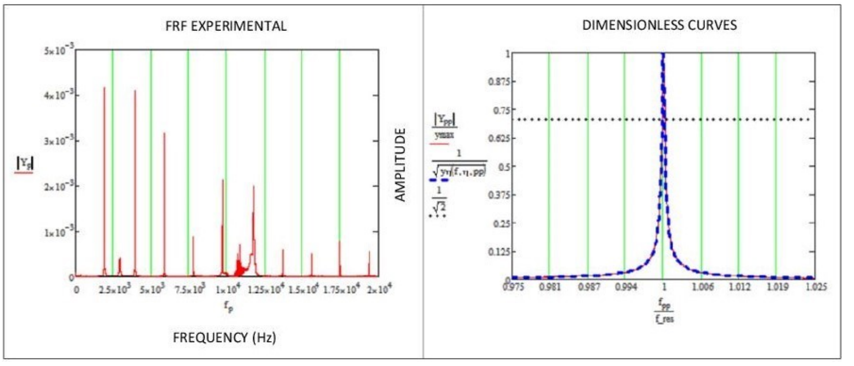

Figure 6. FRF longitudinal experimental and dimensionless resonance curve for the steel in 3rd mode; experimental - continuous line; theoretical - dashed line (AUTHOR).

However, the results of the test configuration of this study agree with the prescription of values mentioned by ASTM E 756 [9] for steel, considering the technique employed, showing the feasibility of the test procedure to be used in the analysis of concrete submitted to AAR.

1.5.2 Applied LRF to AAR concrete specimens

In concrete, inside of the test procedure applied LRF to steel bar, the longitudinal force was applied at the end of the longitudinal axis of concrete beam with approximately 28.4 kg as shown in Figure 7.

The dynamic test was performed using shaker of low intensity and accelerometer. The oscillation was performed applying a sweep of 100 Hz up to 20 kHz. The time domain data was recorded and further treated with FFT.

The signals collected to LRF test in a set of 10 measurements with a window of 10 seconds each, that corresponds one reading, had analyzed the last window with better signal stabilization.

In this case, one has sampling frequency of 1,000,000 data, which corresponds one data collected at each time interval of 10 microseconds, where results of the analysis carried out, likewise that to the steel bar, are shown to the concrete beams tested.

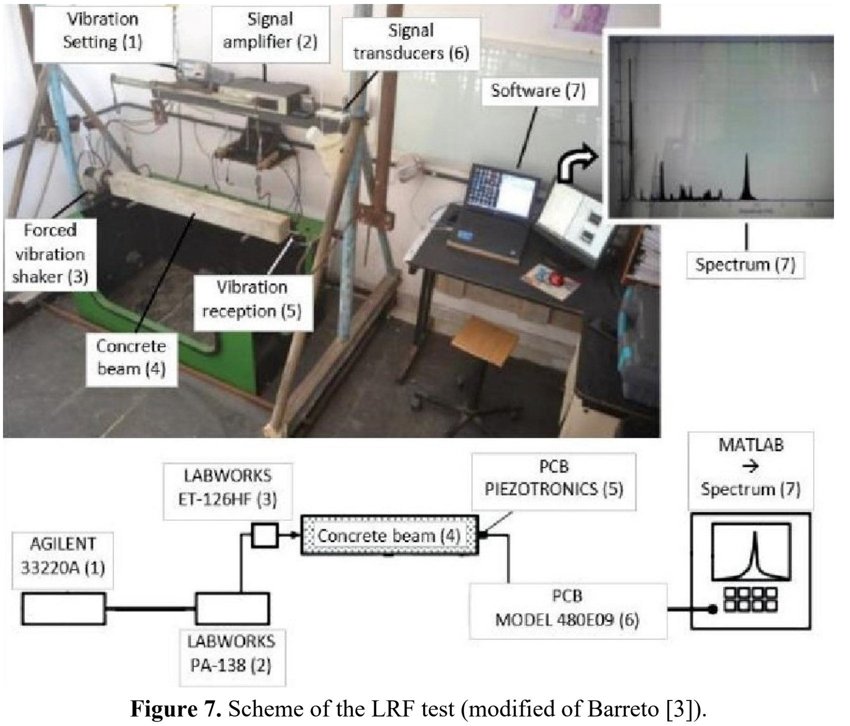

Figure 7. Scheme of the LRF test (modified of Barreto [3]).

2 METHODOLOGY

This paper is dived in two parts. The first part addresses the fundamental knowledge on main energy dissipation mechanisms. In this part, the mathematical formulations of damping in concrete structures is discussed for the most appropriate rheology and its mathematical formulation is developed with respect the finite elements method (FEM) to LRF.

In the second part, the worked approach is applied to an experimental set of data produced by Barreto [3], what consisted of acquiring data of LRF test performed to concrete beams measuring 1.14 m in length with square cross section (0.1 x 0.1 m).

The concrete beams were cast with two levels of cement content (420 and 500 kg/m^3) and two types of aggregates (reactive and innocuous) (see Table 1). Was added NaOH to the casting water (1.0 M NaOH + Deionized), which water to cement ratio (w/c) was made constant for all specimens in 0.45 (see Table 2). The samples were stored in wet room at 38 ºC for about 1.5 year.

3 RESULTS AND DISCUSSIONS

3.1 Part 1: mathematical formulations of damping in concrete

3.1.1 Damping equivalence

Considering the observations made to concrete by Leśnicki et al. [2], associating mechanics of vibration damping described by Nashif et al. [7], still having the changes in amplitude and resonance frequency, the equivalence between viscous and hysteresis damping was adopted, as can be seen by comparing the behaviors showed in Figures 2 and 3, to obtain the damping in the analysis of the resonance frequency in this study, being one of the biggest advantages in assuming hysteresis damping the possibility of using the correspondence principle in complex analysis, where complex number can be replaced by real value in damping accounting [7] (see Figure 8).

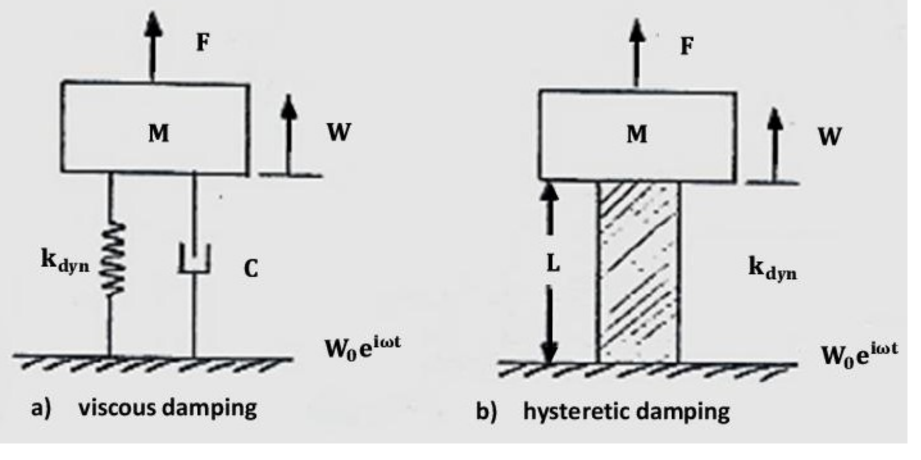

Figure 8. Damping for single degree of freedom: a) Viscous; b) Hysteresis (adapted of Nashif et al. [7]).

Another important point in the analyzes is the difference between the viscous and hysteretic damping system, where in the viscous system the energy dissipated per cycle depends linearly on the oscillation frequency, while in the hysteretic system the energy dissipated is independent of the frequency.

3.1.2 Damping calculation

In order to avoid the drawbacks of the half-power bandwidth method, can make use of least squares for curve fitting method when adjusting the theoretical curve to the experimental resonance curve.

For this, consider the parameters of the resonance test when calculating the viscous damping ratio, for single degree of freedom system, as shown in Figure 8, based on the equation of the damped motion governed by Newton's second law and equations for vibration damping by Nashif et al. [7], the equation can be expressed as:

$$w(t) = w\, e^{i\omega t} \tag{2}$$

$$K\, w(t) + C\, w'(t) + M\, w''(t) = F(t) = \overline{F} e^{i\omega t} \therefore i = \sqrt{-1} \tag{3}$$

To dimensionless excitation frequency, one has:

$$\Omega = \frac{\omega}{\omega_{res}} = \frac{\omega}{\sqrt{\frac{K}{M}}} \therefore \omega_{res} = \sqrt{\frac{K}{M}} \tag{4}$$

The damping ratio being defined as:

$$\xi = \frac{C}{2\sqrt{K\, M}} \tag{5}$$

So, the amplitude of the frequency function in the viscous system is:

$$|w| = \frac{\left|\frac{\overline{F}}{K}\right|}{\sqrt{\left(1-\Omega^2\right)^2 + 4\, \xi^2\, \Omega^2}} \tag{6}$$

For the equivalence of viscous and hysteresis responses, one has:

$$k_{dyn} = k_{sta} + C\, i\, \omega = k_{sta}\left(1 + i\, \eta\right) \tag{7}$$

$$C\, \omega = k_{sta}\, \eta \therefore k_{sta} = K = \frac{E\, A}{L} \tag{8}$$

Likewise, the amplitude in the hysteresis system is:

$$|w| = \frac{\left|\frac{\overline{F}}{K}\right|}{\sqrt{\left(1-\Omega^2\right)^2 + \eta^2}} \tag{9}$$

Where, to $\Omega \simeq 1$, one has the maximum amplitude, then:

$$|w|_{vis-max} = \left|\frac{\overline{F}}{C\, \omega}\right| = |w|_{his-max} = \left|\frac{\overline{F}}{K\, \eta}\right| \tag{10}$$

To dimensionless range, also:

$$\frac{|w|}{|w|_{max}}=|\bar{w}|=\frac{\eta}{\sqrt{\left(1-\Omega^2\right)^2+\eta^2}} \tag{11}$$

Rewriting Equation 11, one has:

$$\frac{1}{|\bar{w}|^2}=1+\frac{1}{\eta^2}\left(1-\Omega^2\right)^2 \tag{12}$$

Based on least squares for curve fitting method, according to Equation 12, obtained by algebra, as suggested by Gu and Sheng [16], at the points collected of the test close to the resonance frequency (n points), can make estimation of the loss factor (or damping ratio) by minimizing residual error.

$$\text{erro}(\eta)=\sum_{n=1}^{n}\left[y_n-f(x_n,\eta)\right]^2 \tag{13}$$

Expanding $f(x_n,\eta)$ using Taylor series around the variable $\eta=\eta_0$, where first order polynomial is enough, also:

$$f(x_n,\eta)\simeq f(x_n,\eta_0)+f'(x_n,\eta_0)(\eta-\eta_0) \tag{14}$$

$$\text{erro}(\eta)=\sum_{n=1}^{n}\left[y_n-f(x_n,\eta_0)-f'(x_n,\eta_0)(\eta-\eta_0)\right]^2 \tag{15}$$

$$y=\frac{1}{|\bar{w}|^2} \tag{16}$$

$$f(x_n,\eta)=f(\Omega_n,\eta)=1+\frac{1}{\eta^2}\left(1-\Omega_n^2\right)^2 \tag{17}$$

The estimation of the loss factor was performed using Mathcad 2000 Professional software (MathSoft [17]), where routine was developed to adjust the theoretical curve to the experimental curve on least squares, with an initial value stipulated for the loss factor (η_0).

After the first loss factor is obtained, minimizing the error, the process is repeated with this value until a second value is obtained. The iteration will be completed when the difference between the neighboring loss factors is small enough, which in this study corresponds to at least 10^{-6}. The last iteration of the loss factor corresponds to the estimated η value.

By analogy, within the procedure presented, it is possible to estimate the value of the damping (C), having then:

$$f(x_n,C)=f(\Omega_n,C)=1+\frac{M^2\,\omega_{res}^2}{C^2}\left(1-\Omega_n^2\right)^2 \tag{18}$$

Thus, in this study, preference was given on least squares for curve fitting method in obtaining the loss factor and damping, considering the data of the LRF tests performed by Barreto [3], as well as to the automation achieved with the routine developed, as for the better precision of the method adopted in relation to half-power bandwidth.

This approach made possible to calculate the elasticity modulus of the tested material by the equivalence between viscous and hysteresis damping, through of the equality in Equation 7 [7] that results in Equation 8, after adjusting the theoretical resonance curve to the experimental curve, based on the loss factor and damping, individually, resulting in the curves showed in Figure 6.

3.1.3 Damping in concrete mixes

The concrete mixes used in the beams tested by longitudinal resonance, whose data were recorded in the time domain and analyzed in this study in the frequency domain, are those of the tests carried out by Barreto [3], within of the line of research on AAR developed at the Universidade Federal da Paraíba (UFPB).

Table 1 show the nomenclature of the concrete beams built for the tests of potential for reactivity of the aggregate and tested by Barreto [3] in longitudinal resonance and ultrasound, being: C # - Cement content; I - Innocuous; R - Reactive; L - Free expansion.

Table 1. Nomenclature of concrete beams (modified of Barreto [3]).

Concrete beam	Description
I1 (C420-I-L)	Dimensions 10 x 10 x 114 cm; cement content 420 kg/m^3 of concrete; coarse aggregate innocuous; free expansion
I2 (C500-I-L)	Dimensions 10 x 10 x 114 cm; cement content 500 kg/m^3 of concrete; coarse aggregate innocuous; free expansion
R1 (C420-R-L)	Dimensions 10 x 10 x 114 cm; cement content 420 kg/m^3 of concrete; coarse aggregate reactive; free expansion
R2 (C500-R-L)	Dimensions 10 x 10 x 114 cm; cement content 500 kg/m^3 of concrete; coarse aggregate reactive; free expansion

Note: Nomenclature in parentheses "()" corresponds the adopted in this study

Table 2 show concrete mixes affected by AAR of several authors, include Paulo Afonso IV Hydroelectric Power Plant, for comparative of elasticity modulus degradation with the mixes of Barreto [3] in LRF tests.

Table 2. Concrete mixes affected by AAR of several authors for comparative of elasticity modulus degradation (AUTHOR).

Author	Mix	Reactive Aggregate	Cem. kg/m^3	w/c	E GPa	T ºC	h %	Na_2O_{eq} %
Barreto [3]	C420-R-L	Quartz, biotite, Albite and microline (coarse)	420	0.45	25.90	36 - 40	> 95	1.47
	C500-R-L		500	0.45	29.58	36 - 40	> 95	1.47
Larive [10], [11]	-	Tournaisis limestone (thin and coarse)	410	0.44	-	38	97	1.25
ISE [10]		1*						
PA-IV [10]	-	Biotite-gneiss, rosy granite and amphibolite (coarse)	357	0.53	25.00	38	100	0.92
Esposito [11]	RR1	Quartzite, quartz, limestone, volcanic rock fragments (fine and coarse)	380	0.46	42.70	38	96	1.17
	RR2	Coarse-grained quartz, quartzite, gneiss, metariolite (fine and coarse)	380	0.45	30.46	38	96	1.17
Giaccio et al. [12]	R2	Opal and chalcedony (thin)	420	0.42	32.00	38	2*	1.25
	R4	Feldspars (orthoclase and plagioclase), quartz, mica, epidote, zircon and dark minerals (coarse)	420	0.42	38.10	38		1.25
Swamy [13]	4.5% opal	Beltane Opal (thin)	520	0.44	-	20	96	1.00
Sanchez et al. [14]	Wt + HP 35	Polymeric sand, quartz and feldspar (fine)	370	0.47	-	38	100	1.25
Ahmed et al. [15]	B	Fused Silica (fine)	400	0.50	21.13	38	3*	1.75

Note: 1* - Lab and test data on cores extracted of structures; 2* - Plastic bag with 5 ml of water; 3* - In the water; E - Elasticity (28 days); T - temperature; h - humidity; Na_2O_{eq} - Alkaline Equivalent; ISE - Institution of Structural Engineers; PA-IV - Paulo Afonso IV Hydroelectric Power Plant

3.1.4 Resonance simulation in concrete specimens

Considering the LRF tests used in this study, combined with the mathematical and mechanical analysis that considered the equivalence between viscous and hysteresis damping, was used routine developed in Mathcad 2000 to obtain parameters of damping.

Longitudinal resonance simulations in finite elements of bars (1D) are also performed using Mathcad 2000, where the algorithmic damping Newmark method provided the results to be transformed of the time domain to the frequency domain, where the frequency spectra of the tests and simulations are consistent with the reality of the tested concrete, as well as in the steel used in test procedure.

Figure 9 show FRF obtained of experimental test and other possible FRFs resulting of finite elements simulation using algorithmic damping Newmark method, where displacement, velocity and acceleration are considered originated of simulated longitudinal excitation, in the same mold of the tests, for the same concrete in the same test period.

Differences exist due difficulties of approximation modeling in complex material such as concrete affected by AAR, but the results are fully compatible.

Like in Figure 6, in Figure 9 there are two "peaks" arising of other accessory modes in the test (2nd and 3rd experimental mode). In this sense, the simulation plays an important role, which corresponds previously to identify the correct "peak" of longitudinal resonance for the analysis of the viscoelastic parameters, through of adjustment of the dimensionless theoretical curve using least squares.

For the case in Figure 9, considering geometry and properties of the analyzed concrete, the longitudinal resonance in LRF test corresponded to the largest "peak" in the expected extension of the spectrum, i.e., the 1st mode.

However, it's worth noting that due to the appearance of accessory modes (transverse, flexural and torsional vibration) this situation may not always occur, emphasizing the importance of prior identification of the longitudinal resonance modes through of simulation as well as existence of behavioral adherence between experimental and theoretical resonance.

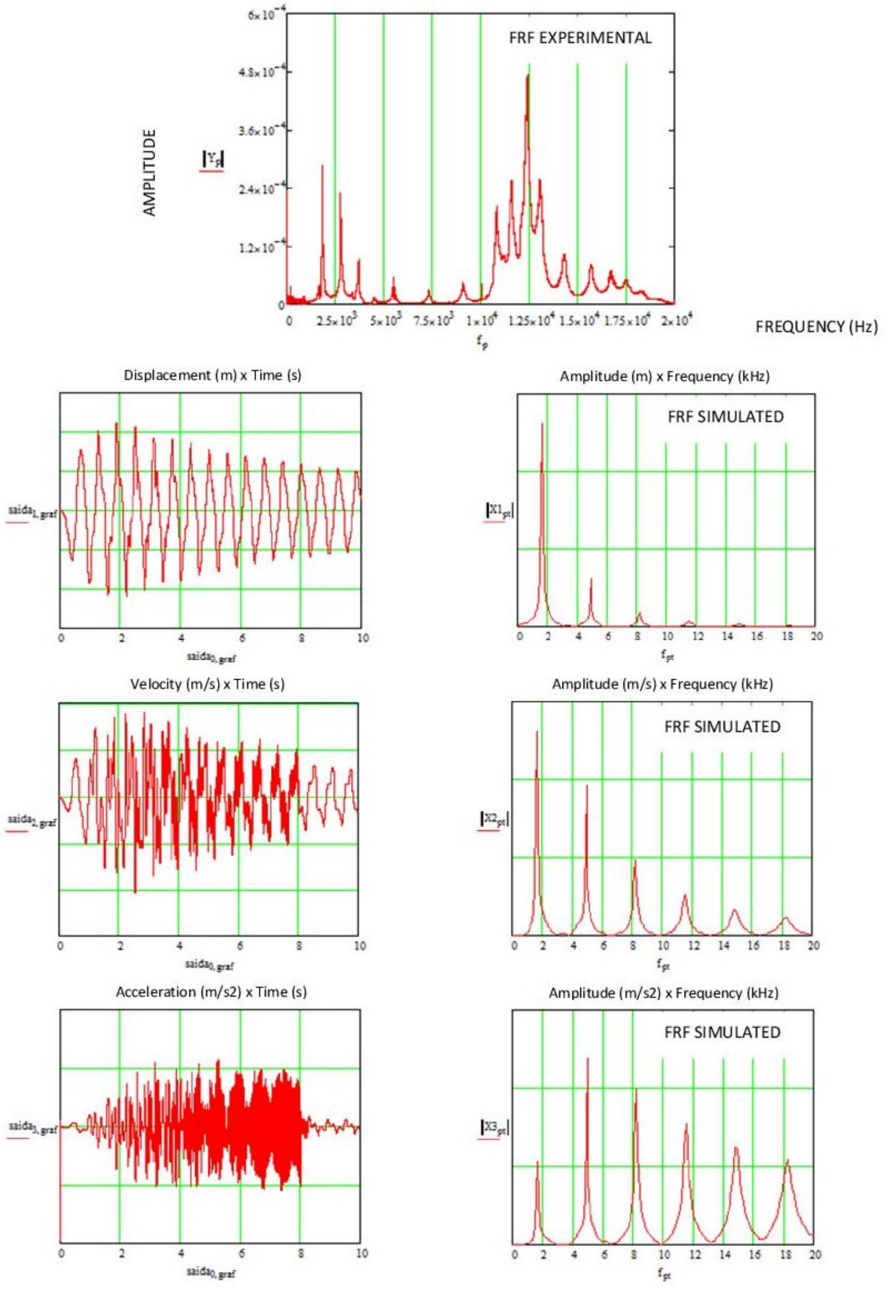

Figure 9. FRFs experimental and simulated (concrete C420-R-L for 1 day); 1st and 2nd simulated modes ≃ 1.6 and 4.9 kHz; corresponding to the simulated: 1st and 4th experimental modes ≃ 1.8 and 5.4 kHz (AUTHOR).

3.1.5 Concrete rheology

To exemplify changes in the viscoelastic behavior of the material, it's common to use rheological models (mechanical analogies), as spring to explain the instantaneous elasticity and damper to characterize the viscous behavior, that is, the late response of the material in time.

Tests and observations made as function of the time configure the material behavior in long-term and take time to complete. One possibility of reducing time is to subject the material the load in which stress or strain varies harmonically in short period of time, that is, analysis as function of the frequency. This makes it possible to identify the viscoelastic characteristics of the material more quickly.

Thus, whether in the time or frequency, the rheological behavior of materials can be represented using viscoelastic models, which combine behaviors of elastic solids and viscous fluids [18].

- Rheology in time

Figure 10 show the main families of rheological models, where their creep functions over time are described in Table 3.

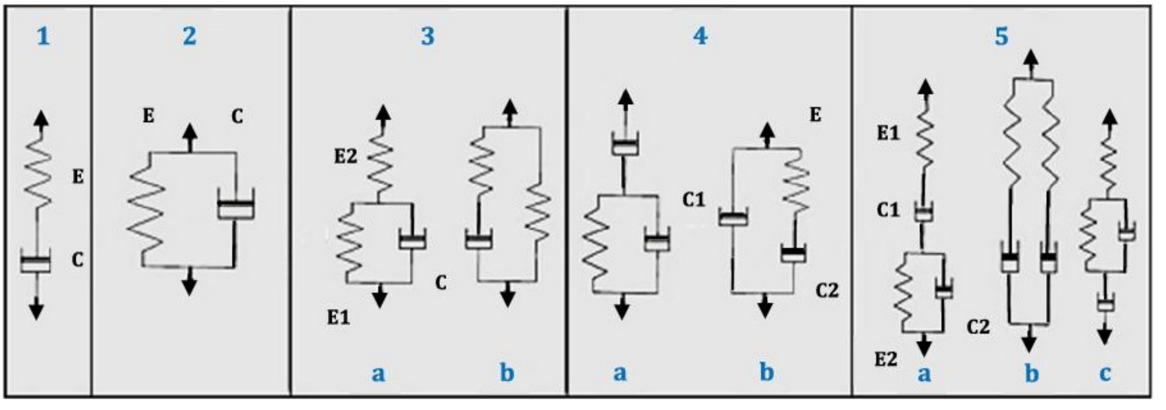

Figure 10. Rheological models: 1) Maxwell; 2) Kelvin-Voigt; 3) Zener; 4) antiZener; 5) Burgers (AUTHOR).

Table 3. Creep functions of the models (unitary) (AUTHOR).

Model	Creep Function
Maxwell	$\frac{1}{E}\left(1+\frac{E}{C}\,t\right)$
Kevin-Voigt	$\frac{1}{E}\left(1-e^{-\frac{E}{C}t}\right)$
Zener (Figure 10 - 3a)	$\frac{1}{E_1}+\frac{1}{E_2}-\frac{e^{-\frac{E_2}{C}t}}{E_2}$
antiZener (Figure 10 - 4b)	$\left(\frac{1}{C_1+C_2}\right)t+\frac{C_2}{E\left(C_1+C_2\right)}\left(1-\frac{C_1}{C_1+C_2}\right)\left(1-e^{-\frac{E(C_1+C_2)}{C_1\,C_2}t}\right)$
Burgers (Figure 10 - 5a)	$\frac{1}{E_1}+\frac{1}{E_2}-\frac{e^{-\frac{E_2}{C_2}t}}{E_2}+\frac{t}{C_1}$

- Rheology in frequency

Table 4 [19], [20] show summary of the complex modulus functions, complemented in this study by the Burgers model, as function of the frequency.

Table 4. Complex modulus of the rheology considered (Renaud et al. [19]; Semblat and Luong [20]).

Model	Complex Modulus
Histerese	$E(1+i\,\eta)$
Maxwell	$\frac{i\,\omega\,E\,C}{E+i\,\omega\,C}$
Kelvin-Voigt	$E+i\,\omega\,C$
Zener (Figure 10 - 3a)	$\frac{E_1(E_2+i\,\omega\,C)}{E_1+E_2+i\,\omega\,C}$
antiZener (Figure 10 - 4b)	$\frac{E\,i\,\omega\,C_2}{i\,\omega\,C_2+E}+i\,\omega\,C_1$
Burgers* (Figure 10 - 5a)	$\left(\frac{1}{E_1}+\frac{1}{i\,\omega\,C_1}+\frac{1}{E_2+i\,\omega\,C_2}\right)^{-1}$

* AUTHOR

Thus, the ideia in this study is to consider models for representative rheologies of viscoelastic solids, such as Zener and Burgers, that will be evaluated as to its applicability for structural engineering in damage models.

3.1.6 Quality factor

The families of rheological models considered as function of the frequency can be defined in terms of the quality factor (Q), which corresponds to one almost constant variable in the frequency range in given level of deformation introduced.

Attenuation curves are constructed taking the inverse of the quality factor (Q^{-1}), where:

$$Q(\omega)=\frac{\mathrm{Re}\left[E(\omega)\right]}{\mathrm{Im}\left[E(\omega)\right]} \tag{19}$$

Since Re[E(ω)] is the real part of the complex modulus and Im[E(ω)] is its imaginary part, to $\omega=\omega_{res}$ in the 1st and 2nd modes also:

$$Q^{-1}=\eta=2\,\xi \tag{20}$$

3.1.7 Damping and rheology

Considering numerical modeling purposes, another type of damping is often used: Rayleigh damping; which is one very convenient way to account damping in numerical models and to associate them with rheological models, as intended in this study.

Rayleigh damping is a classic method to build the global damping matrix [C] of a number system as linear combination of global matrices of mass [M] and stiffness [K], as follows:

$$[C]=\alpha[M]+\beta[K] \tag{21}$$

Equation 21 makes frequency-dependent damping, as shown in Figure 11 [21].

In the condition of resonance ($\omega=\sqrt{K/M}$) also:

$$C=\xi\,C_c=\xi 2\,M\,\omega \tag{22}$$

$$\alpha\,M+\beta\,K=\xi 2\,M\,\omega \tag{23}$$

$$\xi=\frac{1}{2}\left(\frac{\alpha}{\omega}+\beta\,\omega\right) \tag{24}$$

Thus, considering Equation 24, one has:

$$Q^{-1}(\omega) = \frac{\alpha}{\omega} + \beta\,\omega \tag{25}$$

Where α and β, considering the damping ratio ξ in the extension of the circular frequency of interest, between the 1st and 2nd vibration modes, ω_1 and ω_2, respectively, as shown in Figure 11, correspond to:

$$\alpha = \frac{2\omega_1\omega_2\left(\xi_1\omega_2 - \xi_2\omega_1\right)}{\left(\omega_2^2 - \omega_1^2\right)} \tag{26}$$

$$\beta = \frac{2\left(\xi_2\omega_2 - \xi_1\omega_1\right)}{\left(\omega_2^2 - \omega_1^2\right)} \tag{27}$$

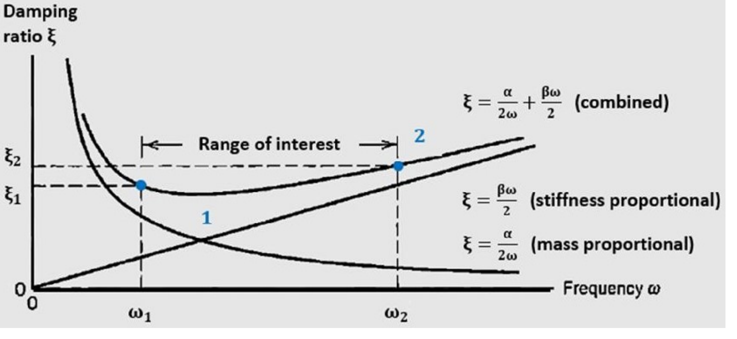

Figure 11. Proportional Damping Scheme [21].

Crucial point is to discover a rheological model that has the same attenuation dependence as those showed in Figure 11, which are based on Rayleigh damping [22].

As reference, in riveted or welded steel structures and reinforced and prestressed concrete structures the value of ξ can vary of 2-15% [23]. In particular, Gutenbrunner et al. [4] presents values of ξ for prestressed concrete bridge ranging of 1.19-1.37%.

This study, the connection of the numerical parameters of the Rayleigh damping (α and β) to the mechanical parameters described in Figure 10 are shown in Table 5.

Table 5. Relationship between numerical parameters of the Rayleigh damping and mechanical (AUTHOR).

Model	α	β
Histerese	η	
Maxwell	$\frac{E}{C}$	-
Kelvin-Voigt	-	$\frac{C}{E}$
Zener (Figure 10 - 3a)	$\frac{E_2 + \frac{E_2^2}{E_1}}{C}$	$\frac{C}{E_1}$
antiZener* (Figure 10 - 4b)	$\frac{E\left(C_1 + C_2\right)}{C_2^2}$	$\frac{C_1}{E}$
Burgers (Figure 10 - 5a)	By analogy: $E_1 = E_{maxwell}$; $E_2 = E_{2(zener)}$; $C_1 = C_{2(antizener)}$; $C_2 = C_{kelvinvoigt}$	

* Semblat [22]

3.2 Part 2: numerical validation of experimental data

Figure 12 show the evolution of FRFs and theoretical curves to loss factor (η) of the concrete C420-R-L, in five different ages, with the first three corresponding to the initial ages of the concrete (1-14-29 days), one close to half the test time (379 days) and the last in the end of the test (514 days), where it's possible to notice noise in some cases, but which did not affect the curve adjustment on least squares in the obtaining of the global viscoelastic parameters of the concrete, among them the elasticity modulus.

FRFs longitudinal experimental and theoretical dimensionless resonance curves adjusted by the loss factor (η) and damping (C), resulting of the data collected in the resonance tests and analyzed in this study, made it possible to obtain the values in Table 6.

It can be seen from Table 6 that the increase in the loss factor is accompanied through the decrease in the elasticity modulus of the concrete C420-R-L.

In sequence, Figure 13 show the elasticity modulus degradation in free expansion of the concretes C420/500-R-L, compared to several authors, likewise that Kawabata et al. [24].

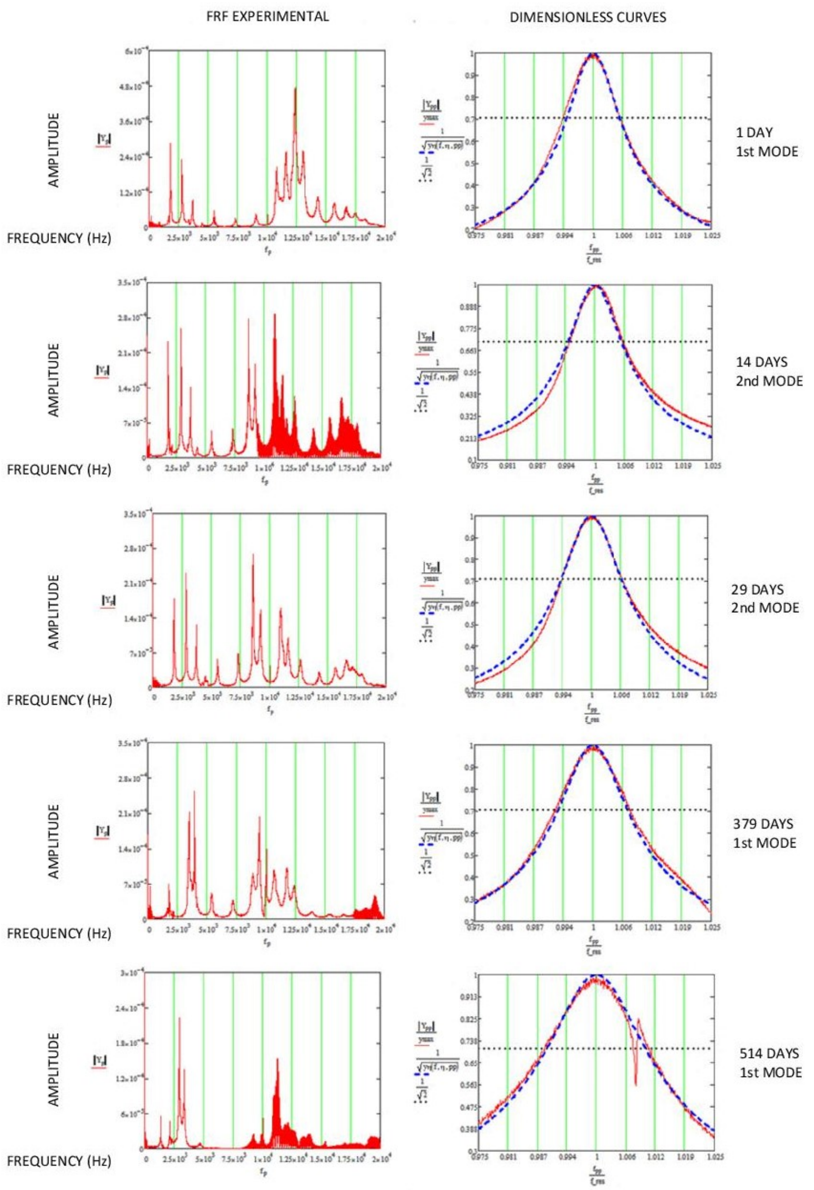

Figure 12. FRFs and curves for η (experimental - continuous line; theoretical - dashed line) (AUTHOR).

Table 6. Global parameters obtained by longitudinal resonance analysis: concrete C420-R-L (see Figure 12) (AUTHOR).

Time (days)	Expansion (%)	Amplitude	ω_{res} (Hz)	η	C (Pa . s)	E (GPa)
1	0	0.000285455	1,829.9	0.01118	580.78264	10.84121
14	0.008	0.000257711	2,871	0.01141	930.25535	26.68638
29	0.02	0.000230823	2,828.4	0.01302	1,046.09	25.90031
379	0.094	7.01E-05	1,781.7	0.01467	742.27642	10.27766
514	0.104	5.48E-05	1,350.9	0.02087	800.86654	5.90843

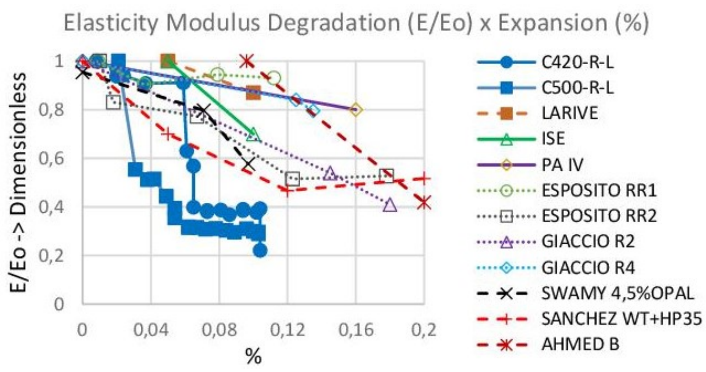

Figure 13. Elasticity modulus degradation of the concretes C420/500-R-L compared to several authors (see Table 2) (AUTHOR).

Figure 14, that considers temporal analysis of rheological models to creep and relaxation, show the prediction behavior of the Zener and Burgers models, as models capable of to predict the behavior of the concretes affected by the AAR, in creep, tested in free expansion.

Figure 15 show that the models that respond well in the frequency range applied to LRF tests, between 100 Hz and 20 kHz, are: hysteresis, Maxwell, Kelvin-Voigt and antiZener. This behavior serves to consolidate the equivalence used to the hysteresis and Kelvin-Voigt (viscous) models in the damping. Still, considering frequency analysis through of attenuation curves for loss factor have Zener, antiZener and Burgers models that take similar shape to the combined damping in Figure 11.

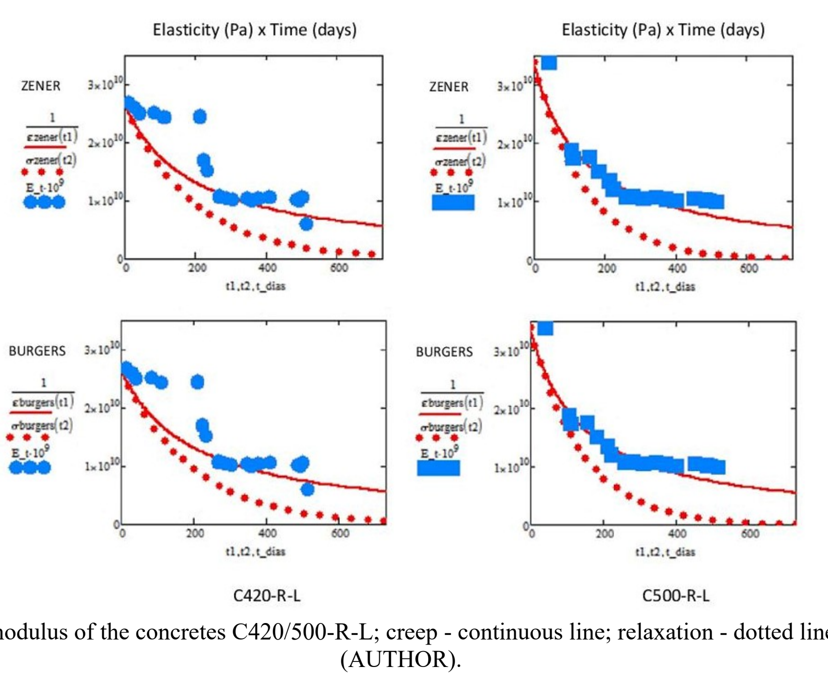

Figure 14. Elasticity modulus of the concretes C420/500-R-L; creep - continuous line; relaxation - dotted line; experimental - dot (AUTHOR).

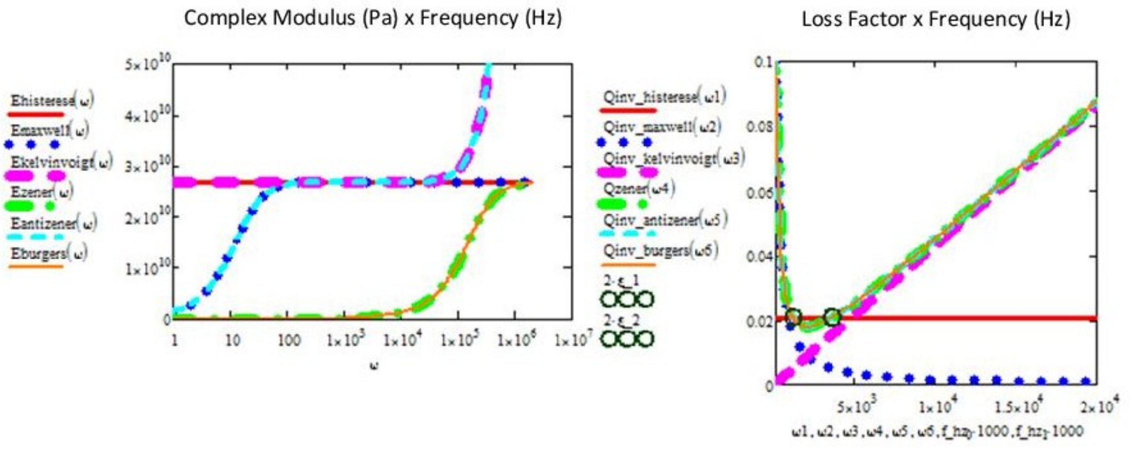

Figure 15. Complex modulus and attenuation curve (loss factor): concrete C420-R-L (AUTHOR).

4 CONCLUSIONS

- The use of modal analysis in the frequency spectrum in longitudinal resonance makes it possible to determine non-destructively the global rheological properties of concrete samples, such as: damping, loss factor and elasticity modulus;
- Using finite elements technique to simulate longitudinal resonance tests, including algorithmic damping Newmark method to obtain response patterns in the frequency, coupled with deconvolution made possible by the Rayleigh approach, mechanical parameters of the rheological models are quantified using numerical parameters of Rayleigh damping;
- Considering frequency extension, Kelvin-Voigt (viscous) and hysteresis models obtained similar response in the analyzes between approximately 100 Hz and 60 kHz, validating the equivalence adopted in this study between viscous and hysteresis damping;
- In dependence of attenuation the Zener, antiZener and Burgers models showed similar response to the combined Rayleigh damping of mass and stiffness, being antiZener (Standard Linear Liquid) modeling, for viscous fluid, atypical matter in structural engineering;
- In models whose behavior combines damping with mass and stiffness in the frequency, the validation of experimental results with behavior predicted in models representative of rheology that considers viscoelastic solids of the type Zener and Burgers complements and expands the interest of the structural engineering for those models in damage.

5 ACKNOWLEDGMENTS

This work was funded by the Companhia Hidro Elétrica do São Francisco (Chesf) as part of P&D project and had the technical support of the Universidade Federal da Paraíba (UFPB), especially of Barreto [3] for the tests performed.

6 REFERENCES

[1] J. Butterworth, J. H. Lee, and B. Davidson, "Experimental determination of modal damping from full scale testing," in *Proc. 13th World Conf. Earthq. Eng.* (310), Vancouver, Canada, Aug. 2004

[2] K. J. Leśnicki, J.-Y. Kim, K. E. Kurtis, and L. J. Jacobs, "Characterization of asr damage in concrete using nonlinear impact resonance acoustic spectroscopy technique," *NDT Int.*, vol. 44, pp. 721–727, 2011.

[3] A. M. Barreto, "Técnicas não destrutivas para detecção da reação álcali-agregado em prismas de concreto," Ph.D. dissertation, Univ. Fed. Paraíba, João Pessoa, 2019.

[4] G. Gutenbrunner, K. Savov, and H. Wenzel, "Sensitivity studies on damping estimation," in *2nd Int. Conf. Exp. Vib. Anal. Civ. Eng. Struct.*, Porto, Portugal, 2007.

[5] Associação Brasileira de Normas Técnicas, *Concreto Endurecido – Determinação da Velocidade de Propagação de Onda Ultrassônica*, ABNT NBR 8802, 2019.

[6] A. Nagy, "Cracking in reinforced concrete structures due to imposed deformations," Ph.D. dissertation, Lund Univ., Lund, Sweden, 1997.

[7] A. D. Nashif, D. I. G. Jones, and J. P. Henderson, “Modeling of structural response of damped systems,” in Braun-Brumfield Inc., Ed., *Vibration Damping*, New York, USA: Jonh Wiley & Sons Inc., 1985, Chap. 4.

[8] Agilent Technologies, *Agilent 33220A 20 MHz Waveform Generator User’s Guide*. USA: Agilent Technologies Inc., 2007.

[9] American Society for Testing and Materials, *Standard Test Method for Measuring Vibration-Damping Properties of Materials*, ASTM E 756, 1998.

[10] COPEM, “*Relatório de Modelagem e Recalibração das Estruturas da Usina de PA-IV*, CH01-C-0031-R6, 2001.

[11] R. Esposito, “The deteriorating impact of alkali-silica reaction on concrete – expansion and mechanical properties”, Ph.D. dissertation, Univ. Parma, Parma, Italy, 2016.

[12] G. Giaccio, R. Zerbino, J. M. Ponce, and O. R. Batic, "Mechanical behavior of concretes damaged by alkali-silica reaction," *Cement Concr. Res.*, vol. 38, pp. 993–1004, 2008.

[13] R. N. Swamy, "Assessment and rehabilitation of aar-affected structures," *Cement Concr. Compos.*, vol. 19, pp. 427–440, 1997.

[14] L. F. M. Sanchez, B. Fournier, M. Jolin, D. Mitchell, and J. Bastien, "Overall assessment of Alkali-Aggregate Reaction (AAR) in concretes presenting different strengths and incorporating a wide range of reactive aggregate types and natures," *Cement Concr. Res.*, vol. 93, pp. 17–31, 2017.

[15] T. Ahmed, E. Burley, S. Rigden, and A. Abu-Tair, "The effect of alkali reactivity on the mechanical properties of concrete," *Constr. Build. Mater.*, vol. 17, pp. 123–144, 2003.

[16] J. Gu and M. Sheng, "A method for damping estimation based on least square fit," *Am. J. Eng. Res.*, vol. 4, no. 7, pp. 205–209, 2015.

[17] MathSoft, *Mathcad 2000 User’s Guide*. USA: MathSoft Inc., 2000.

[18] R. F. Navarro, "Modelos viscoelásticos aplicáveis a materiais reais: uma revisão," *Rev. Eletronica Mater. Processos*, vol. 12, no. 1, pp. 1–20, 2017.

[19] F. Renaud, J.-L. Dion, G. Chevallier, I. Tawfiq, and R. Lemaire, "A new identification method of viscoelastic behavior: application to the generalized maxwell model," *Mech. Syst. Signal Process.*, vol. 25, pp. 991–1010, 2011.

[20] J. F. Semblat and M. P. Luong, "Wave propagation through soils in centrifuge testing," *J. Earthquake Eng.*, vol. 2, no. 1, pp. 147–171, 1998.

[21] R. D. Cook, D. S. Malkus, M. E. Plesha, and R. J. Witt, “Finite elements in structural dynamics and vibrations,” in *Concepts and Applications of Finite Element Analysis*, Hamilton Printing Company, Ed., 4th ed., Madison, USA: John Willey & Sons, 2002, Chap. 11.

[22] J. F. Semblat, "Rheological interpretation of rayleigh damping," *J. Sound Vibrat.*, vol. 206, no. 5, pp. 741–744, 1997.

[23] L. E. Vaz, “Análise dinâmica de estruturas,” in *Método dos Elementos Finitos em Análise de Estruturas*, Globaltec Editora Ltda., Ed., Rio de Janeiro: Elsevier Editora Ltda./Campus, 2011, Cap. 9.

[24] Y. Kawabata, J. F. Seignol, R. P. Martin, and F. Toutlemonde, “Influence of creep and stress states on alkali-silica reaction induced-expansion of concrete under restraint,” in *Proc. 15th Int. Conf. Alkali-Aggregate Reaction in Concr.* (32), São Paulo, July, 2016.

Author contributions: M. B. Cavalcanti: conceptualization, formal analysis, writing; S. M. Torres: funding acquisition, supervision, data curation; M. R. F. L. Filho: methodology; and A. J. V. Santos: methodology.

Editors: Edna Possan, José Luiz Antunes de Oliveira e Sousa, Guilherme Aris Parsekian.

IBRACON Structures and Materials Journal
Revista IBRACON de Estruturas e Materiais
ISSN 1983-4195 ismj.org

ORIGINAL ARTICLE

Application of the Analytic Hierarchy Process (AHP) to select high performance concretes

Aplicação do método da análise hierárquica para escolha de concretos de alto desempenho

Sabrina Requião Pinto[a]
Diogo Henrique de Bem[a]
Markus Samuel Rebmann[b]
Marcelo Henrique Farias de Medeiros[c]

[a]Universidade Federal do Paraná – UFPR, Departamento de Construção Civil – DCC, Programa de Pós-graduação em Engenharia Civil – PPGEC, Curitiba, PR, Brasil

[b]Universidade de São Paulo – USP, Escola Politécnica, São Paulo, SP, Brasil

[c]Universidade Federal do Paraná – UFPR, Centro de Estudos em Engenharia Civil – CESEC, Departamento de Construção Civil – DCC, Curitiba, PR, Brasil

Received 26 March 2019
Accepted 07 July 2020

Abstract: This paper describes an application of the Analytic Hierarchy Process (AHP) to choose the best cement type and mixture for the production of high performance concrete. The decision process aimed at obtaining a concrete that would best meet the requirements of three hypothetical scenarios: (a) industrial concrete floors of a chemical plant, (b) structural elements of a thirty-floor building and (c) a massive foundation block of a green building. In this regard, six different concrete mixtures were evaluated (VR4, IIIR4, V280, III280, V200 and III210) according to four criteria: mechanical properties, durability, financial cost and environmental impact. The analysis results showed that the composition with CPV-ARI cement and content of 280 kg/m^3 was the best alternative for scenario (a) and (b), while for scenario (c) the composition with cement CPIII and content of 210 kg/m^3 was the best choice.

Keywords: high performance concrete, mechanical properties, economic and environmental performance, durability, analytic hierarchy process (AHP).

Resumo: Este artigo apresenta uma aplicação do método da análise hierárquica na escolha do tipo de cimento e do traço para a produção de concretos de alto desempenho (CAD). O processo de decisão objetivou obter concretos que melhor atendessem as necessidades de três cenários: (a) piso industrial de uma fábrica de produtos químicos, (b) elementos estruturais de um edifício de 30 pavimentos e (c) um bloco de fundação de grande volume de um edifício com conceito sustentável. Para tal, a partir de seis alternativas de escolha (VR4, IIIR4, V280, III280, V200 e III210) foram avaliados 4 critérios: propriedades mecânicas, durabilidade, custo e impacto ambiental. Os resultados indicaram que a composição com cimento CPV-ARI e consumo de 280 kg/m^3 mostrou-se a melhor alternativa para os cenários (a) e (b), enquanto para o cenário (c) foi a composição com cimento CPIII e consumo de 210 kg/m^3.

Palavras-chave: concreto de alto desempenho, propriedades mecânicas, desempenho econômico e ambiental, durabilidade, processo de hierarquia analítica (AHP).

How to cite: S. R. Pinto, D. H. Bem, M. S. Rebmann, and M. H. F. Medeiros, "Application of the Analytic Hierarchy Process (AHP) to select high performance concretes," *Rev. IBRACON Estrut. Mater*., vol. 14, no. 2, e14206, 2021, https://doi.org/10.1590/S1983-41952021000200006

Corresponding author: Marcelo Henrique Farias de Medeiros. E-mail: medeiros.ufpr@gmail.com
Financial support: None.
Conflict of interest: Nothing to declare.

1 INTRODUCTION

The emergence of a worldwide tendency to privilege design aspects aimed at the durability and extension of the service life of reinforced and prestressed concrete structures was mainly stimulated by factors such as the increasing occurrence of early degradation problems in concrete structures and the increased interest for more sustainability in the Civil Construction sector [1]. This durability is basically summarized as the structure's ability to satisfactorily withstand the environmental influences previously planned and defined by the designer and the contractor [2], that is, the interaction between the concrete structure, the environment and the conditions of use, operation and maintenance [3]. In view of this scenario, there is a strong tendency to study and develop special concretes such as high performance concrete (HPC), which is not necessarily a high strength concrete, but rather a concrete that has high durability in its conditions of use. In this field, prominent works include: Aitcin [4], Sorelli et al. [5], Cordeiro et al. [6], Shi et al. [7], Zhutovsky and Kovler [8], Sirtoli et al. [9], Shen et al. [10].

In addition to the materials commonly used in the production of conventional concretes, the composition of HPC differs in that it also incorporates mineral additions, such as fly ash, silica fume or metakaolin, in addition to chemical additives, especially of the superplasticizer type. According to Jucá et al. [11], the use of these mineral additions is motivated by reasons such as improving the rheological properties of fresh concrete with finer particles, thus reducing exudation and segregation, in addition to less permeability to aggressive agents such as chlorides and carbon dioxide due to the reduction of pores in the microstructure of the cement matrix. In this sense, in order to achieve better durability properties, studies in the literature have evaluated the production of concretes with low cement content and high levels of additions, usually fly ash or blast furnace slag. However, because they are less reactive additions than metakaolin and silica fume, they tend to generate lower final resistances. Celik et al. [12] noticed that replacing up to 65% of the cement paste with a combination of volcanic ash and limestone filler reduced the coefficient of chloride permeability by 50% both at 28 and 360 days, despite obtaining lower resistances. In other studies, it was also observed that the increased substitution of cement by blast furnace slag at levels of up to 80% was able to promote a reduction in chloride permeability, creep and concrete shrinkage [13], although there is also a reduction of mechanical resistances [14].

The use of additions to concrete is also a good solution from an environmental point of view. According to Worrell et al. [15], for the production of one ton of cement, about 814 kg of carbon dioxide (CO_2) is released into the atmosphere, and this emission comes basically from the clinker production process. The substitution of clinker for additions proportionally reduces the amount of polluting emissions per ton of binder, thus ensuring a lower CO_2 rate per MPa of the concrete produced, provided that there is no drop in resistance [16]. Moreover, the content of many additions (when they are industrial waste) also makes these by-products more environmentally friendly. Additionally, the use of high performance concretes has a great advantage in terms of durability of the structures, thus ensuring a longer service life and less need for repairs and maintenance.

In this context, considering that there is a well-established association between CO_2 emissions and environmental changes, in particular global warming, there is a continuing socio-environmental need to reduce industrial CO_2 emissions, justifying strategies aimed at reducing cement content in concrete [17]. In this line of reasoning, the work of Felix and Possan [18] highlights the importance of considering the capture of carbon dioxide due to the carbonation process of concrete. This conduct of the previous work follows a line that corroborates the work of Silva et al. [19], which defends strategies for reducing the environmental impact of concrete and argues that the evaluation of concrete production chain sustainability should not be restricted to the assessment of CO_2 emissions, but it is necessary to consider a global assessment with the application of the Life Cycle Assessment (LCA). Within this line of action there are studies for the development of concretes with low cement content, generally based on the theory of optimization of particle packing, such as the works of Varhen et al. [20], Grazia et al. [21], [22], Campos et al. [17], [23].

2 CONTEXT OF THE ANALYTIC HIERARCHY PROCESS

Due to its versatility, high-performance concrete has been adopted as a solution in offshore oil drilling platforms, long span bridges, viaduct decks [24], high-resistance industrial floors, garages, chemical product warehouses, spillways and energy dissipation structures in dams [25]. Also noteworthy is the use of HPC in tall building structures due to the possibility of the reduction of structural sections and higher construction speed [26], in addition to the reduction in the overall cost of the structure [27].

In view of the large set of properties that can be influenced by the composition of high-performance concretes and the impossibility of maximizing them all at once, it is necessary to think about guided performance, that is, prioritize the most desired properties in the material for a given situation. Decision making in relation to the proportions and types of materials available can involve a series of requirements that significantly impact the overall performance of the concrete.

The Analytic Hierarchy Process (AHP) seeks the selection of alternatives in a process considering different evaluation criteria [28]. Developed by Thomas L. Saaty in the 1970s, the method helps to organize a structured and rational network for a decision problem [29]. Handfield et al. [30] highlight that the main advantage of AHP is in treating the decision as a global system, synthesizing all available information and thus making previously complex decision processes more rational. The authors add that without using a decision support methodology, the decision maker does not end up adequately considering all the factors involved, their weights and relative interactions.

In the field of Civil Engineering, the potential of hierarchical analysis has been increasingly explored, so it is possible to cite examples of studies that used it as a decision tool, such as: 1 - Pan [31], in the choice of bridge construction methods; 2 - Lai et al. [32], in the public works project; 3 - Perelles et al. [33] for the selection of structural reinforcement systems; 4 - Pretto et al. [34] for the selection of vertical barrier systems to contain groundwater contaminants; 5 – Grunberg et al. [35] for the comparison among environmentally certified sealing systems for homes; 6 - Pereira et al. [36] and Mattana et al. [37] in studies in the area of recycling construction waste for making concrete and mortar.

In view of the entire context presented, the present work aims to apply the Analytic Hierarchy Process in the choice of concretes for high-performance applications, considering 3 scenarios of practical application. The aim is to contribute to the development of a systemic selection process of concretes considering the specific conditions of each use.

3 METHOD

The methodology used in the present study consisted of applying the Analytic Hierarchy Process based on the results of an experimental study developed by Rebmann [38]. This author evaluated durability parameters and mechanical properties of concretes with high strength and low content Portland cement from mixtures composed of different cement types and contents. It is worth mentioning that despite the use of the term HSC (High-strength concrete) in the work developed by Rebmann [38], in this present study the term HPC (High-performance concrete) will be used since it is intended to encompass other properties of the concrete besides the compressive strength. In addition, to form the AHP criteria, the environmental performance represented by the CO_2 emission and the economic attractiveness (cost per m^3 of concrete) were also considered for the mixtures under study.

CP V-ARI and CP III-40-RS cements were used, as well as three different cement contents, two being of low content and one of normal content. To define these contents, the following premises were adopted:

a) For the reference mixtures (normal cement content), it was decided to follow the recommendation of maximum durability of the Brazilian standard NBR 12655 [39], that is, environmental aggressiveness class IV. For this class, the standard specifies a cement content of at least 360 kg/m^3, in addition to a water/cement ratio of not more than 0.45 and compressive strength of at least 40 MPa at 28 days.
b) For the low cement content mixtures, the following were adopted: a content of 280 kg/m^3, which is equivalent to that required for environmental aggressiveness class II; and a content of 200 kg/m^3, which is below the aforementioned normative recommendations.

In the composition of the reference mixtures, only one granulometry of each aggregate (fine and coarse) was used. On the other hand, for the low content mixtures, there was a combination of three sands and two gravels, as well as the use of mineral additions. This granulometric diversity aimed to obtain better packing both in the granular skeleton of aggregates and in the cementitious matrix.

The cone slump specified for the reference concretes was 8±2 cm. On the other hand, a superplasticizer additive was used for the other mixtures, which allowed the increase of fluidity and the obtaining of slumps greater than 17 cm.

The characteristics adopted after the dosage tests and the respective nomenclatures for each mixture are shown in Table 1.

Table 1. Characteristics and nomenclature of the mixtures evaluated. Adapted from Campos et al. [17].

Material parameter	**Mixture nomenclature**					
	VR4	**IIIR4**	**V280**	**III280**	**V200**	**III210**
Type of cement	**CP V**	**CP III**	**CP V**	**CP III**	**CP V**	**CP III**
	ARI	**40-RS**	**ARI**	**40-RS**	**ARI**	**40-RS**
Cement consumption (kg/m^3)	426.1	437.4	278.6	275.5	199.2	208

Table 1. Continued...

Material parameter	Mixture nomenclature					
	VR4	IIIR4	V280	III280	V200	III210
Active silica (kg/m^3)	-	-	16.9	17.4	12.1	13.1
Metakaolin (kg/m^3)	-	-	6.5	6.7	4.6	5.0
Filler (ground silica) (kg/m^3)	-	-	51.6	51.2	53	52.7
Sand 1 (kg/m^3)	685	676	470.8	466.9	483.4	480.6
Sand 2 (kg/m^3)	-	-	313.9	311.3	322.3	320.4
Sand 3 (kg/m^3)	-	-	196.2	194.6	201.4	200.3
Pebble (kg/m^3)	-	-	413	409.6	424.0	421.6
Gravel 1 (kg/m^3)	1.111	1.114	619.5	614.4	636.0	632.4
Mixing water (kg/m^3)	191.7	190.0	128.3	128.9	130.5	130.7
Superplasticizer (kg/m^3)	-	-	6.04	5.99	4.32	4.52
Water/binder ratio*	0.451	0.434	0.436	0.442	0.617	0.590
Mortar content (%)	50	50	56.4	56.4	54.6	54.8
Total binders (kg/m^3)	426.1	437.4	302.0	299.6	216.0	226.1

* this value refers to the ratio (mixing water + additive water)/total binders

Table 2 shows the results of mechanical properties, durability and cost of concretes obtained by Rebmann [38], as well as the CO_2 emission content calculated by the authors. The tests performed by Rebmann [38] are briefly described below.

Table 2. Database obtained from the experiments [17].

Analysis parameter	Mixture nomenclature					
	VR4	IIIR4	V280	III280	V200	III210
Compressive strength$^{(1)}$ – 28 days (MPa)	40.7	30.0	67.9	55.4	51.9	34.5
Modulus of elasticity$^{(1)}$ – 28 days (GPa)	42.1	36.1	51.4	50.8	49.0	43.5
Flexural tensile strength$^{(2)}$ (MPa)	4.5	4.7	8.3	7.2	6.2	5.1
Water absorption$^{(1)(3)}$ – 63 days (%)	5.5	5.9	3.2	2.5	3.8	3.8
Abrasion$^{(4)}$ 1000m (mm)	1.0	1.6	1.2	1.4	1.5	1.6
Permeability$^{(5)}$ (10-12m/s)	2.5	3.1	1.4	2.4	2.7	4.7
Carbonation$^{(2)}$ – 96 days (mm)	0(8)	14.6	1.7	9.8	11.1	22.3
Corrosion potential$^{(6)}$ – 17 cycles (mV)	-530	-460	-320	-440	-230	-590
Cost (R$/m^3)	249.14	253.35	330.33	328.20	277.21	283.57
CO_2 emission$^{(7)}$ (kg)	348	184	228	116	163	88

$^{(1)}$ Test on 10x20cm cylindrical specimens according to NBR 5739 [40]. $^{(2)}$ Test on 10x10x50cm prismatic specimens according to NBR 12142 [41]. $^{(3)}$ Test according to NBR 9778 [42]. $^{(4)}$ Test according to NBR 12042 [43]. $^{(5)}$ Tests based on the German Water Permeability Test (GWT). $^{(6)}$ Test according to ASTM C876 [44] with immersion and drying cycles in a solution with 3.5% NaCl $^{(7)}$ adopted emission rate of 860 kg of CO_2 per ton of clinker. $^{(8)}$ Subsequently, to allow the calculations to be carried out, this value will be admitted as 1mm, remaining as the lowest value.

3.1 Test methods

In mechanical terms, the following were evaluated: compressive strength in 10 cm × 20 cm cylindrical specimens, according to the specifications of NBR 5739:2007 [40]; static modulus of elasticity in 10 cm × 20 cm cylindrical specimens, according to the specifications of NBR 8522:2008 [45]; and flexural tensile strength at four points (Figure 1a) in 10 cm × 10 cm × 50 cm prismatic specimens, according to the specifications of NBR 12142:2010 [41]. Although other ages were assessed in the original study, in this article only the age of 28 days was considered.

In order to assess durability, different aspects of aggression to concrete were considered by which a good part of the degradation in concrete occurs, with an emphasis on porosity and permeability. Water absorption was evaluated by immersion [42] in 10 cm × 20 cm cylindrical specimens cast in PVC molds without using a release agent so as not to cause surface waterproofing. Water permeability was determined by the German Water Permeability Test (GWT) (Figure 1l and 1k). This rapid test is recommended for field evaluations in order to determine the permeability of existing structures without the need for sample extraction. In this test, the apparatus, which consists of a pressure chamber and devices to record and regulate the water pressure, is installed on the specimen. The permeability coefficient was determined, according to Darcy's law, from the water flow that permeates the specimen at a given pressure level (3 bar) after the establishment of a continuous flow.

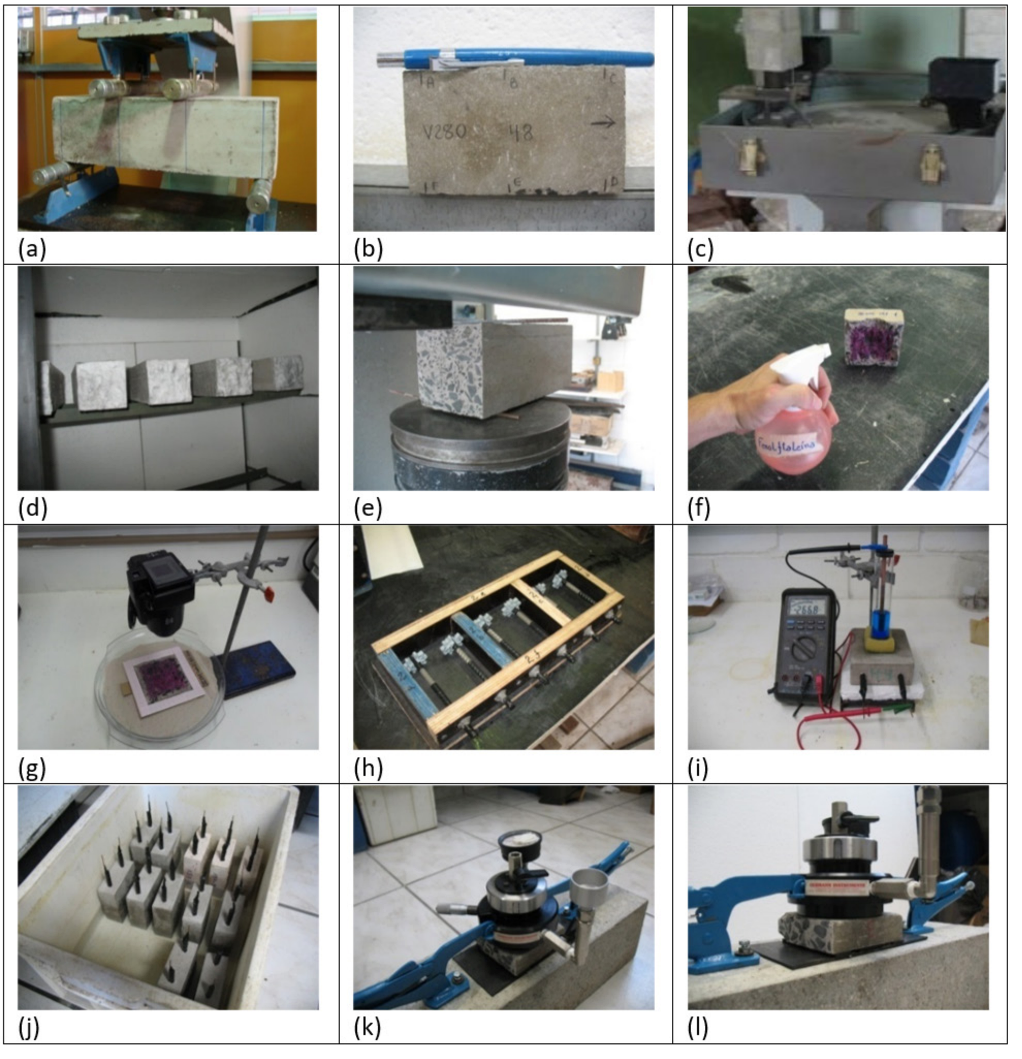

Figure 1. Illustration of details of the tests performed: (a) Four-point flexural test; (b) specimen used in the abrasion test; (c) Dorry Abrasion Machine; (d) prismatic specimens with ends sealed with wax, arranged inside the accelerated carbonation chamber; (e) slice extraction by compression (f) spraying the phenolphthalein solution on the newly fractured surface; (g) image acquisition of carbonated surface; (h) mold and reinforcement used in making specimens to test for corrosion potential; (i) assembly of the corrosion potential test, with a copper/copper sulphate electrode placed on the specimen and connected by means of a voltmeter to the working electrodes/steel bars; (j) partial immersion in sodium chloride solution to accelerate the corrosion process; (k and l) assembly of the German Water Permeability Test apparatus to assess water permeability.

Using an accelerated test, carbonation was evaluated in 10 cm × 10 cm × 50 cm prismatic specimens, molded without the use of a release agent so as not to cause waterproofing of the surface. After curing in a humidity chamber for 28 days, they were stored in the humidity of the accelerated test (65%) until mass constancy. This occurred at the age of 91 days. From this age, the specimens were kept in a carbonation chamber (Figure 1d) with a controlled temperature (25°C) and CO_2 concentration (5%). The carbonation depth was evaluated at the ages of 6, 14, 28, 56 and 96 days. At each of these ages, a slice of the specimen was extracted by transversal compression (Figure 1e) and sprinkled with phenolphthalein solution as a pH indicator (Figure 1f). The minimum, average and maximum depths were determined with the aid of image analysis (Figure 1i). In this article, the value of the average depth at 96 days was considered as an indicator.

Abrasion was evaluated on Dorry Abrasion Machine equipment (Figure 1b and 1c), and the test conditions matched the specifications of NBR 12042:1992 [43], using standard sand (IPT 50) as abrasive material. Abrasion was determined after 500 and 1,000 meters, and in this article the value for 1000 meters was analyzed.

In relation to the corrosion process, the corrosion potential was evaluated according to the procedure of ASTM C876:2009 [44]. This test measures the potential difference developed between a standard electrode (copper/copper sulfate electrode was used), positioned on the surface of the specimen, and steel bars inserted into the concrete. Concrete specimens of 5 cm × 10 cm × 10 cm were molded with 2 embedded 8 mm steel bars. These bars were previously cleaned to eliminate oxidation and then partially isolated in order to delimit a controlled area inside the specimen susceptible to the corrosion process (Figure 1h). After initial curing in a humidity chamber, the specimens were subjected to four-day cycles of drying in a heating chamber at 50°C, followed by three days of partial immersion in saline solution of 3.5% NaCl by mass (Figure 1j). Over 4 months, the difference in electrical potential between the steel bar and the standard electrode was determined at the end of the immersion steps (Figure 1i). The final value after 17 cycles was considered in this article.

3.2 Test methods Hierarchical analysis for decision making

Based on the available data, a hierarchy structure was built as shown in Figure 2.

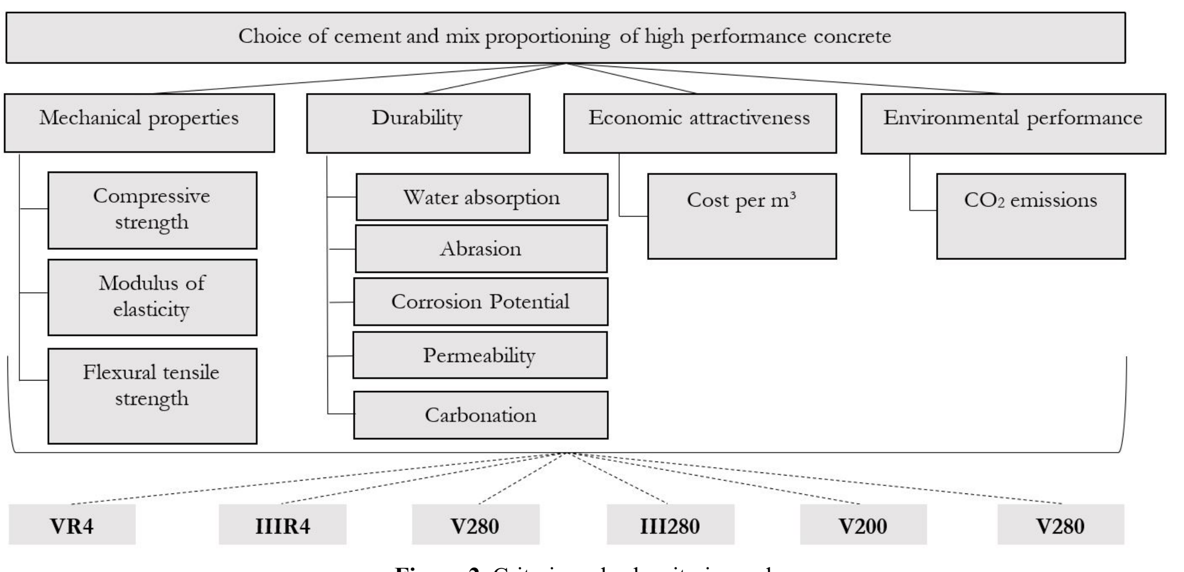

Figure 2. Criteria and sub-criteria used.

In order to allow decision making, it was also necessary to establish weights for each of the criteria and sub-criteria, thus reducing the subjectivity of the decision, as explained by Gregório [46]. However, this fact requires that the analyzers have knowledge and experience regarding the topic to be analyzed, since the main way to assign the weights is through previous knowledge or convictions.

It is a fact that the definition of a material's composition is linked to the context to which it will be applied. Therefore, in order to evaluate the application of the Analytic Hierarchy Process, hypothetical scenarios were established to guide the process of assigning weights based on their specific demands and limitations.

In this work, hierarchical analysis was applied to determine the most satisfactory material composition (mixture and type of cement) for three hypothetical applications:

a) Scenario 1: Concrete to be applied to an industrial floor of a chemical factory;
b) Scenario 2: Structural concrete to be applied to a thirty-story building in an urban, non-coastal region;
c) Scenario 3: High-volume foundation block of a green building.

The choice of these three scenarios sought to consider different performance criteria. In the first scenario, durability represents abrasion and permeability as decisive factors. In the second scenario, mechanical resistance acts with greater importance. In the third, the environmental issue is more prevalent.

Based on these three scenarios as well as the criteria and sub-criteria shown in Figure 2, their weights were determined, as shown in Tables 3 to 9. Table 3 shows the weight scale adopted and the logic of filling out the decision matrix. The decision matrices were then filled out following the logic presented in Table 4. Initially, weights were assigned between criteria A-B, B-C and C-D and from these values the other matrix weights were calculated (Table 4).

Table 3. Judgment scale and logic of filling out the decision matrix.

Judgment scale				**Weight**
A is equally as important as B				1.00
A is moderately more (less) important than B				2.00 (0.5)
A is extremely more (less) important than B				3.00 (0.33)
Analysis parameter	**A**	**B**	**C**	**D**
A	1.00	a	a × b	a × b × c
B	1/a	1.00	b	b × c
C	1/(a × b)	1/b	1.00	c
D	1/(a × b × c)	1/(b × c)	1/c	1.00

The decision of the weights for Scenario 1 (Table 4) took into account the following considerations:

a) The durability of an industrial floor is of greater relevance than factors such as cost and mechanical resistance, considering that a possible repair on this floor would cause a major disturbance to the factory's functionality.

b) Within the criterion of durability, permeability and abrasion resistance are the most important sub-criteria. The first is due to the fact that the factory works with chemical products and excessive permeability could compromise both the microstructure of the concrete itself and the quality of the soil under the floor. Abrasion resistance, on the other hand, would cause premature wear of the floor, in addition to the release of powdery material that could also compromise the factory operability.

c) Within the criterion of mechanical properties, the flexural tensile strength was considered the most important sub-criterion due to the forces that occur on these slabs.

Table 4. Decision matrix of criteria, mechanical properties sub-criteria and durability sub-criteria (Scenario 1 - Industrial floor).

Analysis parameter (Main criteria)	**Mechanical properties**	**Durability**	**Economic attractiveness**	**Environmental performance**
Mechanical properties	1.0	0.33	1.0	2.0
Durability	3.0	1.0	3.0	6.0
Economic attractiveness	1.0	0.33	1.0	2.0
Environmental performance	0.5	0.17	0.50	1.0

Analysis parameter (Mechanical properties sub-criteria)	**Compressive strength**	**Modulus of elasticity**	**Tensile strength**
Compressive strength	1.0	2.0	0.67
Modulus of elasticity	0.5	1.0	0.33
Tensile strength	1.5	3.0	1.0

Table 4. Continued...

Analysis parameter (Durability sub-criteria)	Absorption	Abrasion	Corrosion potential	Permeability	Carbonation
Absorption	1.0	0.33	1.0	0.33	1.0
Abrasion	3.0	1.0	3.0	1.0	3.0
Corrosion potential	1.0	0.33	1.0	0.33	1.0
Permeability	3.0	1.0	3.0	1.0	3.0
Carbonation	1.0	0.33	1.0	0.33	1.0

For scenario 2, there was a significant change in the weights (Table 5) due to the following arguments:

a) Mechanical performance has priority over durability because it is a structural element that is related to the short-term safety of the people who use this building. Durability, on the other hand, ensures that this use is possible for a maximum period of time. However, without adequate mechanical resistance, durability is also compromised.

b) Within the durability criteria, the sub-criteria related to corrosion potential and carbonation are more relevant in this scenario, since corrosion of reinforcement by carbonation is one of the most critical problems with regard to the durability of a building located in an urban and non-coastal region.

Table 5. Decision matrix of criteria, mechanical properties sub-criteria and durability sub-criteria (Scenario 2 - building structure).

Analysis parameter (Main criteria)	Mechanical properties	Durability	Economic attractiveness	Environmental performance
Mechanical properties	1.0	2.0	4.0	8.0
Durability	0.5	1.0	2.0	4.0
Economic attractiveness	0.25	0.5	1.0	2.0
Environmental performance	0.13	0.25	0.5	1.0

Analysis parameter (Mechanical properties sub-criteria)	Compressive strength	Modulus of elasticity	Tensile strength
Compressive strength	1.0	2.0	4.0
Modulus of elasticity	0.5	1.0	2.0
Tensile strength	0.25	0.5	1.0

Analysis parameter (Durability sub-criteria)	Absorption	Abrasion	Corrosion potential	Permeability	Carbonation
Absorption	1.0	1.0	0.33	1.0	0.33
Abrasion	1.0	1.0	0.33	1.0	0.33
Corrosion Potential	3.0	3.0	1.0	3.0	1.0
Permeability	1.0	1.0	0.33	1.0	0.33
Carbonation	3.0	3.0	1.0	3.0	1.0

For scenario 3 (Table 6), the following questions were taken into account:

a) Environmental performance has priority over other criteria, followed by durability, mechanical properties and lastly, economic attractiveness.
b) Within the durability sub-criteria, corrosion potential and permeability are more relevant in this scenario, since these are the main ones that could affect the service life of a foundation block.
c) In the sub-criterion of mechanical properties, compressive strength is the most relevant given the mechanical functioning of a foundation block (compression rods).

Table 6. Decision matrix of criteria, mechanical properties sub-criteria and durability sub-criteria (Scenario 3 - foundation block).

Analysis parameter (Main criteria)	**Mechanical properties**	**Durability**	**Economic attractiveness**	**Environmental performance**
Mechanical properties	1.00	0.50	1.00	0.33
Durability	2.00	1.00	2.00	0.66
Economic attractiveness	1.00	0.50	1.00	0.33
Environmental performance	3.03	1.50	3.00	1.00

Analysis parameter (Mechanical properties sub-criteria)	**Compressive strength**	**Modulus of elasticity**	**Tensile strength**
Compressive strength	1.0	2.0	2.0
Modulus of elasticity	0.5	1.0	1.0
Tensile strength	0.5	1.0	1.0

Analysis parameter (Durability sub-criteria)	**Absorption**	**Abrasion**	**Pot. Corrosion**	**Permeability**	**Carbonation**
Absorption	1.00	2.00	0.66	1.32	2.64
Abrasion	0.50	1.00	0.33	0.66	1.32
Corrosion Potential	1.52	3.03	1.00	2.00	4.00
Permeability	0.76	1.52	0.50	1.00	2.00
Carbonation	0.38	0.76	0.25	0.50	1.00

4 RESULTS AND DISCUSSION

Subsequent to the assignment of weights, the results must be normalized in order to be able to apply the Analytic Hierarchy Process, seeking to place them in the same order of magnitude as well as following the same analysis logic. In other words, the greater the value assigned to the parameter, the more satisfactory the evaluated item is. For this, working with the data in Table 2, an inversion was made of the results whose analysis parameters indicate that lower values would mean better performance, such as abrasion. Finally, the normalized data set was obtained from the process of dividing each result by the highest value obtained from the row, as shown in Table 7.

Table 7. Standardized Data.

	VR4	IIIR4	V280	III280	V200	III210
Compressive strength - 28 days	0.58	0.43	1.00	0.80	0.77	0.51
Modulus of elasticity - 28 days	0.82	0.70	1.00	0.99	0.95	0.85
Flexural tensile strength	0.54	0.57	1.00	0.87	0.75	0.61
Water absorption - 63 days	0.45	0.42	0.78	1.00	0.66	0.66
Abrasion 1000 m	1.00	0.63	0.83	0.71	0.67	0.63
Permeability	0.56	0.45	1.00	0.58	0.52	0.30
Carbonation	1.00	0.07	0.59	0.10	0.09	0.04
Corrosion potential – 17 cycles	0.43	0.50	0.72	0.52	1.00	0.39
Cost	1.00	0.98	0.75	0.76	0.90	0.88
CO_2 Emission	0.25	0.48	0.39	0.76	0.54	1.00

Multiplying the normalized results presented in Table 7 by 100 and also by the relative importance presented in Table 4 (Scenario 1), Table 5 (Scenario 2) or Table 6 (Scenario 3), the performance index of each mixture was obtained for each sub-criterion of the 2nd level analysis. Table 8 shows the performance indices for Scenario 1.

Table 8. Performance index of mechanical properties and durability (Scenario 1 - Industrial floor).

Mechanical properties	**VR4**	**IIIR4**	**V280**	**III280**	**V200**	**III210**
Compressive strength	19.23	14.42	33.17	26.44	25.48	16.82
Modulus of elasticity	13.58	11.65	16.58	16.39	15.81	14.03
Tensile strength	27.24	28.46	50.25	43.59	37.54	30.88
Performance index	60.05	54.52	100.00	86.42	78.82	61.73
Durability	VR4	IIIR4	V280	III280	V200	III210
Water absorption	4.98	4.65	8.56	10.96	7.21	7.21
Abrasion	33.22	20.76	27.68	23.73	22.15	20.76
Corrosion potential	4.81	5.54	7.96	5.79	11.07	4.32
Permeability	18.79	15.15	33.56	19.57	17.40	10.00
Carbonation	11.19	0.77	6.58	1.14	1.01	0.50
Performance index	72.99	46.18	78.42	60.17	57.93	42.34

With the performance indices of the second level calculated, the analysis of the first level is completed. For this, it is first necessary to again normalize the performance indices of the mechanical properties and durability criteria together with the results of cost and CO_2 release (Table 9).

Table 9. Standardized data for 1st level analysis (Scenario 1 - Industrial floor).

	VR4	IIIR4	V280	III280	V200	III210
Mechanical properties	0.60	0.55	1.00	0.86	0.79	0.62
Durability	0.87	0.56	1.00	0.73	0.70	0.51
Economic attractiveness	1.00	0.98	0.75	0.76	0.90	0.88
Environmental performance	0.25	0.48	0.39	0.76	0.54	1.00

Then, the values in Table 9 were multiplied by 100 and by the relative importance shown in Table 4 (Scenario 1). Finally, the results of each column were added to obtain the performance index for each mixture for this particular application (Table 10).

In the same way, it is also possible to find the performance indices for Scenario 2 (Table 11) and Scenario 3 (Table 12).

Table 10. Final Performance Index (Scenario 1 - Industrial floor).

	VR4	IIIR4	V280	III280	V200	III210
Mechanical properties	10.82	9.83	18.03	15.58	14.21	11.13
Durability	47.28	30.36	54.64	39.65	38.12	27.72
Economic attractiveness	18.21	17.91	13.74	13.83	16.37	16.00
Environmental performance	2.30	4.36	3.52	6.91	4.92	9.11
Performance index	78.63	62.46	89.93	75.97	73.62	63.97

Table 11. Final Performance Index (Scenario 2 - Building structure).

	VR4	IIIR4	V280	III280	V200	III210
Mechanical properties	34.28	28.27	53.33	45.96	43.63	33.04
Durability	26.67	12.68	20.77	16.34	20.45	11.59
Economic attractiveness	13.33	13.11	10.06	10.12	11.98	11.71
Environmental performance	1.69	3.19	2.57	5.06	3.60	6.67
Performance index	75.13	57.61	92.63	78.10	80.03	63.14

Table 12. Final Performance Index (Scenario 3 - Foundation block).

	VR4	IIIR4	V280	III280	V200	III210
Mechanical properties	8.96	7.60	14.22	12.26	11.50	8.80
Durability	21.02	16.21	28.44	22.89	25.54	15.70
Economic attractiveness	14.22	13.99	10.73	10.80	12.78	12.50
Environmental performance	10.90	20.61	16.64	32.70	23.27	43.10
Performance index	55.12	58.42	70.04	78.66	73.10	80.11

From the results obtained, it was found that the V280 mixture presented the highest final performance index for both hypothetical scenarios 1 and 2, therefore being the best choice for these situations. This may be mainly related to the fact that the V280 mixture performed better in most of the criteria considered, except for the parameters of abrasion, absorption, corrosion potential and CO_2 emission, as shown in Table 12. Therefore, this mixture was not the best in Scenario 3, but rather was the mixture III210.

It can also be noted that, despite not being the mixture with the best abrasion performance, which is one of the main requirements for floors, V280 was still the mixture with the best indication for scenario 1 (industrial floor) due to its better performance in the other criteria.

The mixture that presented the worst performance in scenarios 1 and 2 was also the same, IIIR4. This mixture, unlike the V280, presented the most unsatisfactory performance in practically all the analyzed criteria. Thus, it is observed that just meeting regulatory requirements (such as NBR 6118 [2] and NBR 12655 [39]) is not enough to choose the best solution.

The mixtures with CPV-ARI cement presented advantages in scenarios 1 and 2 compared to the mixtures with CPIII cement. The opposite occurred in Scenario 3, in which there was an advantage for the mixtures with CPIII cement. In addition, the mixtures with low cement content were also shown to be superior to the reference mixtures in all analyzed scenarios. Such considerations confirm the conclusions obtained by Rebmann [38] that it is possible to produce adequate concretes that meet design, cost and sustainability requirements, even though they use a cement content lower than that specified in NBR 6118 [2] and NBR 12655 [39].

As can be seen in Figures 3 to 5, the V280 mixture presented a better performance regarding mechanical property and durability criteria. Only in one scenario, in which environmental or economic performance was the most relevant variable (Scenario 3), was this mixture not the best choice.

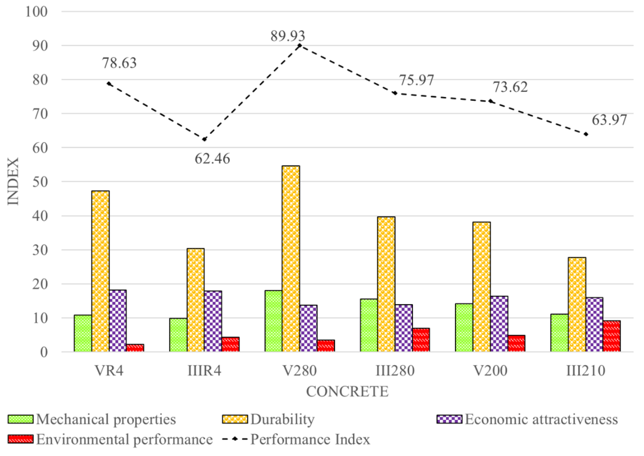

Figure 3. Partial indices of criteria and final performance index - Scenario 1 (industrial floor).

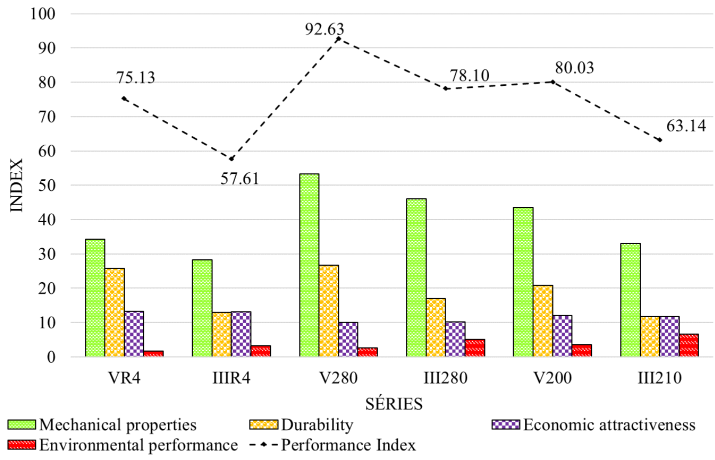

Figure 4. Partial indices of criteria and final performance index - Scenario 2 (building structure).

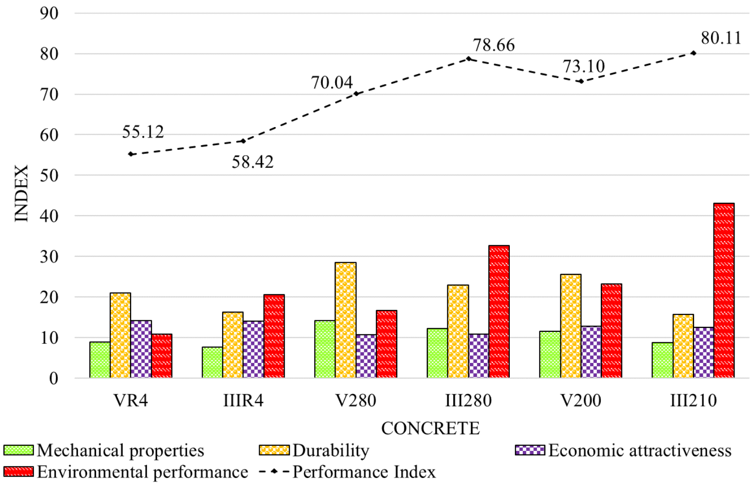

Figure 5. Partial indices of criteria and final performance index - Scenario 3 (foundation block).

5 CONCLUSIONS

The basic premise of this work was the application of the Analytic Hierarchy Process (AHP) as a tool for choosing the composition of high-performance concretes for three practical application scenarios: (scenario 1) industrial floor of a chemical factory; (scenario 2) reinforced concrete structure of a thirty-story building in an urban, non-coastal region and (scenario 3) high-volume foundation block for a green building.

The following conclusions were drawn from this work:

- The results showed that, in scenarios 1 and 2, the concrete composed of CPV-ARI cement with a content of about 280 kg/m^3 (V280) was considered the alternative that best met the choice criteria. The use of CPV-ARI cement in general proved to be superior to CPIII cement for these first two scenarios analyzed.
- The differences between the requirements of the studied scenarios 1 and 2 resulted in only one change in the choice order of the mixtures. In scenario 1 (the industrial floor), the second choice option would be the concrete with a content of 426.1 kg/m^3 of CPV-ARI cement and the fourth option would be the concrete with a content of 200 kg/m^3 of CPV-ARI cement. In scenario 2 (the building structure), this order is reversed.
- Analyzing scenario 3, the mix with 210 kg/m^3 of CPIII cement was the best option.
- Although AHP has proven to be an accessible and easy to apply tool, it became evident that its effectiveness depends on a good structuring of the problem and weight system. In this way, AHP can be considered an instrument that can assist with problems systemically and thus contribute with information that feeds the decision-making process.
- This type of research can serve as support for the future development of artificial intelligence systems in order to systematize and implement means of rational decision making that can be conducted by computers. In this way, the main focus of this work should be given to the process that is being proposed and exemplified in order to glimpse its potential for use in the systemic choice of concretes more suitable for different applications.

ACKNOWLEDGEMENTS

The authors would like to thank the support of the Graduate Program in Civil Construction Engineering (PPGECC) and the Civil Engineering Studies Center (CESEC) of the Federal University of Paraná (UFPR), in addition to the São Carlos School of Engineering (EESC) and the Polytechnic School (POLI), both from the University of São Paulo (USP).

REFERENCES

[1] J. R. Clifton, "Predicting the service life of concrete," *ACI Mater. J.*, vol. 90, no. 6, pp. 611–617, 1993.

[2] Associação Brasileira de Normas Técnicas, *Projeto de Estruturas de Concreto*, NBR 6118, 2014.

[3] M. H. F. Medeiros, J. J. D. O. Andrade, and P. Helene, “Durabilidade e vida útil das estruturas de concreto,” in *Concreto: Ciência e Tecnologia*, G. C. Isaia, Ed., São Paulo: IBRACON, 2011, pp. 887–902.

[4] P. C. Aitcin, "The durability characteristics of high performance concrete: a review," *Cement Concr. Compos.*, vol. 25, no. 4-5, pp. 409–420, 2003.

[5] L. Sorelli, G. Constantinides, F. J. Ulm, and F. Toutlemonde, "The nano-mechanical signature of ultra high performance concrete by statistical nanoindentation techniques," *Cement Concr. Res.*, vol. 38, no. 12, pp. 1447–1456, 2008.

[6] G. C. Cordeiro, R. D. Toledo Fo., and E. M. R. Fairbairn, "Use of ultrafine rice husk ash with high-carbon content as pozzolan in high performance concrete," *Mater. Struct.*, vol. 42, no. 7, pp. 983–992, 2009.

[7] H. Shi, B. Xu, and X. Zhou, "Influence of mineral admixtures on compressive strength, gas permeability and carbonation of high performance concrete," *Constr. Build. Mater.*, vol. 23, no. 5, pp. 1980–1985, 2009.

[8] S. Zhutovsky and K. Kovler, "Effect of internal curing on durability-related properties of high performance concrete," *Cement Concr. Res.*, vol. 42, no. 1, pp. 20–26, 2012.

[9] D. Sirtoli, M. Wyrzykowski, P. Riva, S. Tortelli, M. Marchi, and P. Lura, "Shrinkage and creep of high-performance concrete based on calcium sulfoaluminate cement," *Cement Concr. Compos.*, vol. 98, pp. 61–73, 2019.

[10] D. Shen, X. Liu, X. Zeng, X. Zhao, and G. Jiang, "Effect of polypropylene plastic fibers length on cracking resistance of high performance concrete at early age," *Constr. Build. Mater.*, vol. 244, pp. 117874, 2020.

[11] T. R. P. Jucá, F. A. Teixeira, C. H. A. F. Pereira, L. E. Guimarães, and E. J. P. Figueiredo, “Influência das adições minerais na corrosão de armaduras induzidas por cloretos,” in *An. 43° Congr. Bras. Concr.*, Foz do Iguaçu, 2001, pp. 1-15.

[12] K. Celik et al., "High-volume natural volcanic pozzolan and limestone powder as partial replacements for Portland cement in self-compacting and sustainable concrete," *Cement Concr. Compos.*, vol. 45, pp. 136–147, 2014.

[13] H. El-Chabib and A. Syed, "Properties of self-consolidating concrete made with high volumes of supplementary cementitious materials," *J. Mater. Civ. Eng.*, vol. 25, no. 11, pp. 1579–1586, 2013.

[14] H. Zhao, W. Sun, X. Wu, and B. Gao, "The properties of the self-compacting concrete with fly ash and granulated blast furnace slag mineral admixtures," *J. Clean. Prod.*, vol. 95, pp. 66–74, 2015.

[15] E. Worrell, J. A. Laitner, M. Ruth, and H. Finman, "Productivity benefits of industrial energy efficiency measures," *J. Energy*, vol. 28, no. 11, pp. 1081–1098, 2001.

[16] R. Yu, P. H. J. H. Spiesz, and H. J. H. Brouwers, "Development of an eco-friendly Ultra-High Performance Concrete (UHPC) with efficient cement and mineral admixtures uses," *Cement Concr. Compos.*, vol. 55, pp. 383–394, 2015.

[17] H. F. Campos, T. M. S. Rocha, G. C. Réus, N. S. Klein, and J. Marques Fo., "Determinação do teor ótimo de substituição do cimento Portland por pó de pedra por métodos de empacotamento de partículas e análise do excesso de água na consistência de pastas," *RIEM-IBRACON Struct. Mater. J.*, vol. 12, no. 2, pp. 221–239, 2019. http://dx.doi.org/10.1590/s1983-41952019000200002.

[18] E. F. Felix and E. Possan, "Balance emissions and CO2 uptake in concrete structures: simulation based on the cement content and type," *RIEM-IBRACON Struct. Mater. J.*, vol. 11, no. 1, pp. 135–162, 2018.

[19] M. G. Silva, V. Gomes, and M. R. M. Saade, "Contribuição da avaliação de ciclo de vida na seleção de misturas de concreto de menor impacto ambiental," *RIEM-IBRACON Struct. Mater. J.*, vol. 11, no. 6, pp. 1354–1380, 2018. http://dx.doi.org/10.1590/s1983-41952018000600010.

[20] C. Varhen, I. Dilonardo, A. D. Figueredo, R. C. O. Romano, and R. G. Pileggi, "Effect of the substitution of cement by limestone filler on the rheological behaviour and shrinkage of microconcretes," *Constr. Build. Mater.*, vol. 125, pp. 375–386, 2016.

[21] M. Grazia, L. Sanchez, R. Romano, and R. Pileggi, "Evaluation of the fresh and hardened state properties of Low-Cement Content (LCC) systems," *Mag. Concr. Res.*, vol. 1, pp. 1–46, 2018. http://dx.doi.org/10.1680/jmacr.18.00271.

[22] M. T. Grazia, L. Sanchez, J. A. F. S. Mesquita, R. C. O. Romano, and R. G. Pilerggi, "Investigation of the use of continuous particle packing models (PPMs) on the fresh and hardened properties of low-cement concrete (LCC) systems," *Constr. Build. Mater.*, vol. 195, pp. 524–536, 2019.

[23] H. F. Campos, N. S. Klein, J. Marques Fo., and M. Bianchini, "Low-cement high-strength concrete with partial replacement of Portland cement with stone powder and silica fume designed by particle packing optimization," *J. Clean. Prod.*, vol. 261, 121228, 2020.

[24] P. K. Mehta and P. J. M. Monteiro, *Concreto: Microestrutura, Propriedades e Materiais*, 4. ed. São Paulo: IBRACON, 2014.

[25] S. E. S. Mendes, "Estudo experimental de concreto de alto desempenho utilizando agregados graúdos disponíveis na região metropolitana de Curitiba," M.S. thesis, Univ. Fed. Paraná, Curitiba, 2002.

[26] G. C. Isaia, "O concreto: da era clássica à contemporânea," in *Concreto: Ensino, Pesquisa e Realizações*, G. C. Isaia, Ed., São Paulo: IBRACON, 2005, vol. 1, pp. 1–44.

[27] F. G. V. Campos, "CAD: mais que durável, um grande negócio," *Rev. IBRACON*, vol. 24, pp. 27–34, 2000.

[28] H. G. Costa, *Introdução ao Método de Análise Hierárquica: Análise Multicritério no Auxílio à Decisão*. Niterói, 2002.

[29] A. Ameri, "Application of the Analytic Hierarchy Process (AHP) for Prioritize of Concrete Pavement," *Glob. J. Hum. Soc. Sci. Interdiscip.*, vol. 13, no. 3, pp. 19–28, 2013.

[30] R. Handfield, S. V. Walton, R. Sroufe, and S. A. Melnyk, "Applying environmental criteria to supplier assessment: a study in the application of the Analytical Hierarchy Process," *Eur. J. Oper. Res.*, vol. 141, no. 1, pp. 70–87, 2002.

[31] N. Pan, "Fuzzy AHP approach for selecting the suitable bridge construction method," *Autom. Constr. J.*, vol. 17, no. 8, pp. 958–965, 2008.

[32] Y. Lai, W. Wang, and H. Wang, "AHP and simulation-based budget determination procedure for public building construction projects," *Autom. Constr. J.*, vol. 17, no. 5, pp. 623–632, 2008.

[33] D. H. Perelles, M. H. F. Medeiros, and M. R. Garcez, "Aplicação da análise hierárquica como ferramenta de tomada de decisão para escolha do compósito de reforço com polímeros reforçados com fibras," *Rev. ALCONPAT*, vol. 3, no. 4, pp. 165–180, 2013.

[34] J. H. F. Pretto, P. Batista, A. L. Leite, A. C. M. Kormann, M. H. F. Medeiros, and R. B. Boszczowski, "Barreiras verticais de contenção de contaminantes em águas subterrâneas: análise hierárquica," *Rev. Geotecnia Lisb.*, vol. 1, pp. 21–42, 2015.

[35] P. R. M. Grunberg, M. H. F. Medeiros, and S. F. Tavares, "Certificação ambiental de habitações: comparação entre LEED for Homes, Processo Aqua e Selo Casa Azul," *Rev. Ambiente Soc.*, vol. 17, no. 2, pp. 195–214, 2014.

[36] E. Pereira, M. H. F. Medeiros, and S. M. Levy, "Durabilidade de concretos com agregados reciclados: uma aplicação de análise hierárquica," *Rev. Ambiente Constr.*, vol. 12, no. 3, pp. 125–134, 2012.

[37] A. J. Mattana, M. H. F. Medeiros, N. G. Silva, and M. R. M. M. Costa, "Análise hierárquica para escolha entre agregado natural ou areia de britagem de rocha para confecção de argamassas de revestimento," *Rev. Ambiente Constr.*, vol. 12, no. 4, pp. 63–79, 2012.

[38] M. S. Rebmann, "Durabilidade de concretos estruturais com baixo consumo de cimento portland e alta resistência," M.S. thesis, Esc. Eng. São Carlos, Univ. São Paulo, São Paulo, 2011.

[39] Associação Brasileira de Normas Técnicas, *Concreto de Cimento Portland – Preparo, Controle, Recebimento e Aceitação – Procedimento*, NBR 12655, 2006.

[40] Associação Brasileira de Normas Técnicas, *Concreto – Ensaio de Compressão de Corpos de Prova Cilíndricos*, NBR 5739, 2007.

[41] Associação Brasileira de Normas Técnicas, *Concreto – Determinação da Resistência à Tração na Flexão em Corpos-de-Prova Prismáticos*, NBR 12142, 2010.

[42] Associação Brasileira de Normas Técnicas, *Argamassa e Concreto Endurecidos: Determinação da Absorção de Água, Índice de Vazios e Massa Específica*, NBR 9778, 2005.

[43] Associação Brasileira de Normas Técnicas, *Materiais Inorgânicos – Determinação do Desgaste por Abrasão*, NBR 12042, 1992.

[44] American Society for Testing and Materials, *Standard Test Method for Half-Cell Potentials of Uncoated Reinforcing Steel in Concrete*, ASTM C-876, 1991.

[45] Associação Brasileira de Normas Técnicas, *Concreto – Determinação do Módulo Estático de Elasticidade à Compressão*, NBR 8522, 2008.

[46] C. A. G. Gregório, "Método para análise de oportunidades de imobilização em imóveis corporativos," M.S. thesis, Esc. Politéc., Univ. São Paulo, São Paulo, 2010.

Author contributions: S. R Pinto: conceptualization, methodology, analysis, writing. D. H. de Bem: conceptualization, methodology, analysis, writing. M. S. Rebmann: conceptualization, methodology, data acquisition, experimental procedures, analysis, writing. M. H. F. de Medeiros: conceptualization, methodology, supervision, writing.

Editors: Edna Possan, José Luiz Antunes de Oliveira e Sousa, Guilherme Aris Parsekian.

Rev. IBRACON Estrut. Mater., vol. 14, no. 2, e14207, 2021

IBRACON Structures and Materials Journal
Revista IBRACON de Estruturas e Materiais
ISSN 1983-4195 ismj.org

ORIGINAL ARTICLE

Analysis of the effect of the secondary moment on curved beams of full cross section

Análise do efeito do hiperestático de protensão em vigas curvas de seções transversais maciças

Thiago Cunha da Silva[a]
Emil de Souza Sánchez Filho[a]

[a]Universidade Federal Fluminense – UFF, Programa de Pós-graduação em Engenharia Civil, Niterói, RJ, Brasil

Received 10 July 2018
Accepted 01 July 2020

Abstract: This paper analysis the effect of the secondary moment on curved beams using the equivalent nodal loads method. A case study was carried out applying the equivalent nodal loads method to a two-span prestressed curved beam, using a curved finite element as the structural model, analyzing the effect of the secondary moment for each case and comparing it with its equivalent in straight beam. It was found that the stiffness parameters EI and GJ influence the secondary moment. The results demonstrates that the beam opening angle reduces the effect of secondary moment, and that the greater the angle, the greater is the reduction that occurs in its secondary moment compared to its equivalent straight beam.

Keywords: prestressed concrete, secondary moment, continuous beam, curved beam, curved finite element.

Resumo: Neste artigo estuda-se o efeito do hiperestático de protensão em vigas curvas, por meio do método das cargas nodais equivalentes. É realizado um estudo de caso, aplicando-se o método das cargas nodais equivalentes em uma viga curva protendida de dois vãos, utilizando-se como modelo estrutural um elemento finito curvo, analisando-se o efeito do hiperestático de protensão para cada caso e comparando-o com o seu equivalente em viga reta. Constatou-se analiticamente que os parâmetros de rigidez EI e GJ influenciam na obtenção do hiperestático de protensão. Os resultados demonstram que o ângulo de abertura da viga reduz o efeito do hiperestático de protensão e que, quanto maior esse ângulo, maior é a redução que ocorre em seu hiperestático de protensão em comparação ao seu equivalente em viga reta.

Palavras-chave: concreto protendido, hiperestático de protensão, viga contínua, viga curva, elemento finito curvo.

How to cite: T. C. Silva and E. S. Sánchez Filho, "Analysis of the effect of the secondary moment on curved beams of full cross section," *Rev. IBRACON Estrut.* Mater., vol. 14, no. 2, e14207, 2021, https://doi.org/10.1590/S1983-41952021000200007

1 INTRODUCTION

Prestressed concrete has increasingly become the solution for the design of certain structures. Its use is due to the great structural advantages obtained, managing to overcome large spans, reduce the dead weight of the structures, and lower the cost of foundations.

One of the most frequent uses in prestressed concrete is in slabs and bridge beams, as the geometry of bridges often requires curved sections that make it difficult to design, considering that curved elements have peculiar characteristics that complicate structural analysis. However, the study of prestressed concrete in curved beams is still little known in scientific and academic environment, especially in the case of statically indeterminate structures. Among the tests performed on curved prestressed elements, those of Zhang et al. [1], Amorn et al. [2] and Choi et al. [3] stand out.

Corresponding author: Thiago Cunha da Silva. E-mail: thiagocunha0307@gmail.com
Financial support: This study was financed partially by Coordenação de Aperfeiçoamento de Pessoal de Nível Superior - Brasil (CAPES) Finance Code 001.
Conflict of interest: Nothing to declare.

The calculation of prestressing in statically indeterminate structures must take into account the effect of secondary moments. Cohn and Frostig [4] found that the secondary moments is of relevant importance in the ultimate limit state, which makes it necessary to obtain its magnitude more accurately.

Some methods proposed for the determination of the secondary moment are mentioned: Kong [5] developed a method for calculating the secondary moments based on the influence line; Raju [6] presents the usual way of calculating the secondary moment, using the equivalent distributed load method and the flexibility method; Cunha [7] presented a method that is based on the concept of equivalent nodal loads.

In this article, the effect of the secondary moment on statically indeterminate curved beams is studied, comparing the result with its straight beam equivalent, in addition to demonstrating the influence that the curvature of the structure has in determining the equivalent nodal loads.

2 EQUIVALENT NODAL LOADS

For the calculation of the secondary moment in curved beams, the concept of equivalent nodal load developed by Cunha [7] is used. The determination of equivalent nodal loads in prestressed structures is carried out similarly on to obtaining values of equivalent nodal load in the matrix analysis of structures. Soriano [8], Martha [9] and Przemieniecki [10] demonstrate how load values are obtained for external loads and charts with their respective values.

A curved prestressed element with fixed ends is considered and analyzed as a beam element, thus the flexibility method is applied to obtain the load values. Figure 1 illustrates the prestressed bar element whose layout has a generic configuration, in order to make the method applicable to any situation. The load value to be obtained is the equivalent bending moment, as torsion due to prestressing loading is disregarded.

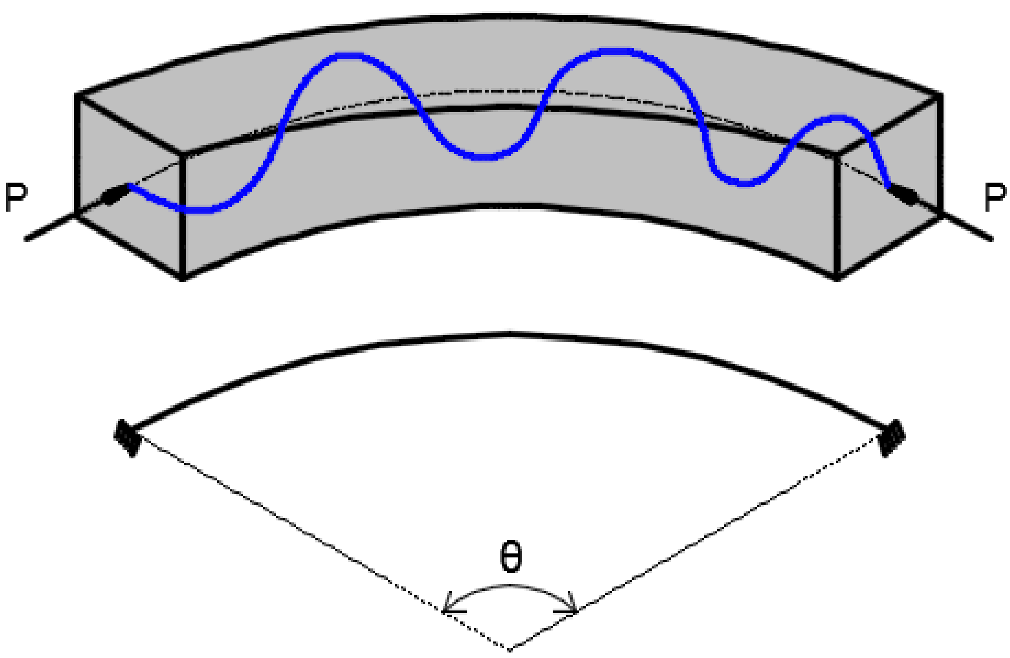

Figure 1. Curved fixed ends bar subjected to prestressing.

According to Cunha [7], the vertical reaction that appears in the fixed support should be disregarded from the calculations, because only the effect of the bending moment due to prestressing generates the secondary moment.

The deduction of equivalent nodal loads is obtained through the flexibility method (Figure 2). Considering that it is a curved element, when applying the unitary bending moment, the torsion moment occurs. The diagram of primary bending moment due to prestressed is given in a generic configuration, with the goal of making the method usable for any problem. In this study the warping of the section is disregarded.

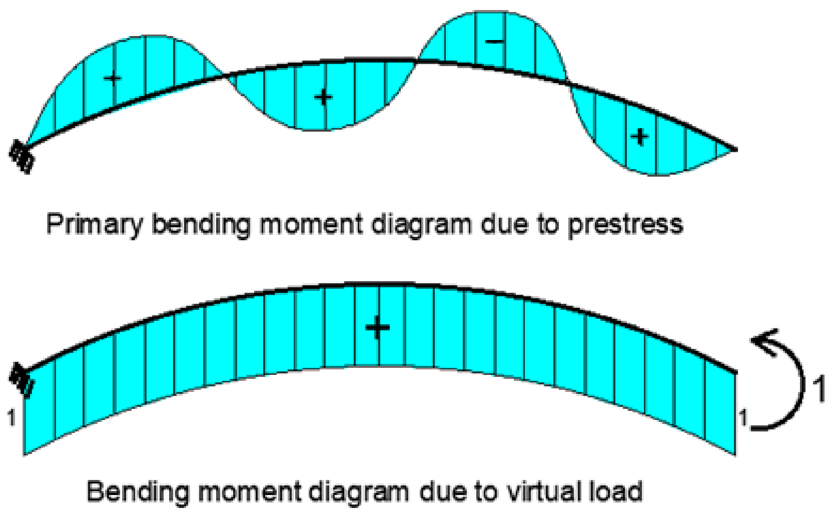

Figure 2. Application of the flexibility method for obtaining equivalent nodal loads.

Figure 3 shows a differential curved bar element used as a reference for deducting the differential equations of equilibrium, where the elements of higher order are neglected. The deduction of all differential equations of equilibrium for curved beam is presented in detail in Cunha [7] and Montánari [11].

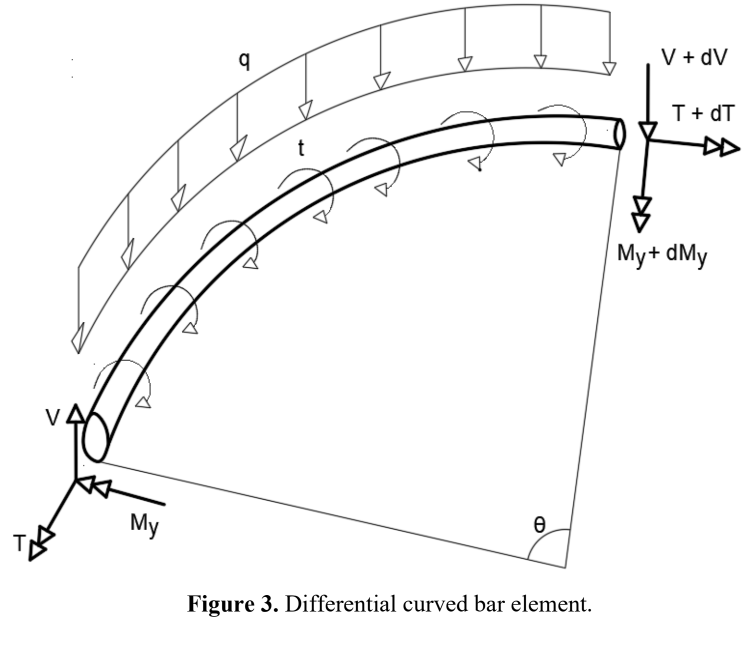

Figure 3. Differential curved bar element.

The curved beam equilibrium equation that relates the bending moment with the torsion moment can be obtained from the sum of the moments in x direction (normal axis to the section of the element) and from geometric relationship $ds = rd\theta$, obtaining:

$$\frac{dT}{ds} + \frac{M_y}{r} = -t \tag{1}$$

Considering that only the effect of prestressing on the structure is studied, the external torsion loading is null, so $t = 0$, thus:

$$\frac{dT}{ds} + \frac{M_y}{r} = 0 \tag{2}$$

The bending moment is unitary and constant along the structure (Figure 2). Replacing its value and integrating it into Equation 2, the torsion moment acting on the structure is obtained due to virtual unitary load.

$$T_1 = -\frac{L}{r} \tag{3}$$

Equations 5 and 6 depict the flexibility coefficients of the flexibility method

$$\Delta_{11} = \int_0^1 \frac{T_1^{\,2}}{GJ} ds + \int_0^1 \frac{M_1^{\,2}}{EI} ds \tag{4}$$

$$\Delta_{11} = \frac{L^3}{r^2 GJ} + \frac{L}{EI} \tag{5}$$

$$\Delta_{10} = \int_0^L \frac{m\bar{m}}{EI} = \frac{\int_0^L Pz(s)\,ds}{EI} \tag{6}$$

that gathered in the compatibility equation

$$\Delta_{10} + x_1 \Delta_{11} = 0 \tag{7}$$

$$\left(\frac{L^3}{r^2 GJ} + \frac{L}{EI}\right) x_1 + \int_0^1 Pz(s) 1 \frac{ds}{EI} = 0 \tag{8}$$

Results in

$$x_1 = -\frac{r^2 GJ}{L\left(L^2 EI + r^2 GJ\right)} \int_0^L Pz(s)\,ds \tag{9}$$

In equation 9 using the following notation we have

$$\mu = \frac{r^2 GJ}{\left(L^2 EI + r^2 GJ\right)} \tag{10}$$

where m = bending moment due to prestressing; $\bar{m}$ = bending moment due to unit load; P = prestressing force applied; L = span length; r = beam radius of curvature; EI = span flexural stiffness; GJ = span torsional rigidity; Δ_{10} = displacement at point 1 due to the load applied at point 0; Δ_{11} = displacement at point 1 due to unit load at point 1; $z(s)$ = height of the prestressing cable.

The value μ shown in Equation 10 is called by Cunha [7] as a reduction factor due to curvature. Thus, the equivalent nodal load is given by

$$M_1 = -\mu \frac{\int_0^L Pz(s)\,ds}{L} \tag{11}$$

Equation 11 is valid only when the prestressing force is centered, that is, when there is no resulting eccentricity in the section that generates torsion. If there is an eccentricity, the effect of torsion due to prestressing should be considered in determining the load values.

Figure 4 shows the equivalent nodal loads due to prestressing for fixed ends situation.

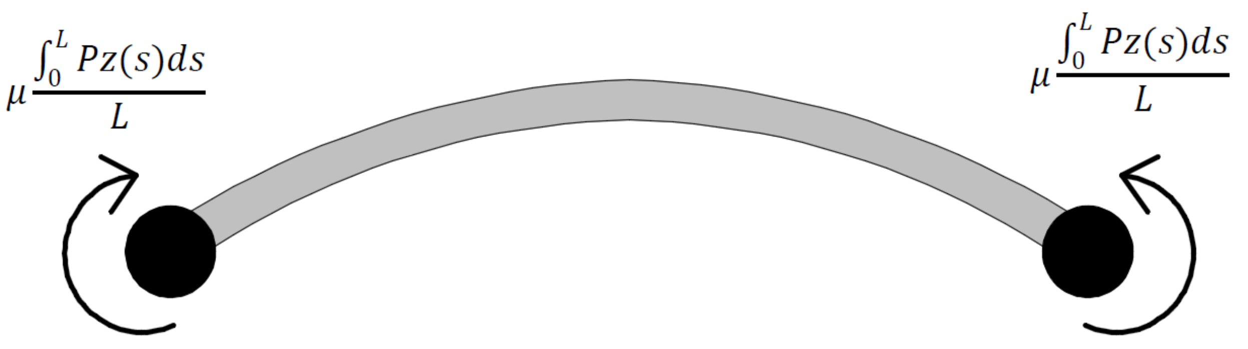

Figure 4. Prestressing equivalent nodal load.

The orientation of the nodal load is a function of the $\int_0^L Pz(s)\,ds$ portion, which, if positive, the orientation is the same as shown in Figure 4. If on the contrary, the orientation goes in the opposite direction.

The $\int_0^L z(s)\,ds$ portion is the area between the centroid of the section and the prestressing profile along its entire length. The strategy for using this method consists of dividing the beam into sections, calculating the area between the prestressing profile and the centroid in each section and multiplying it by the average prestressing force of the section, considering prestressing losses.

It is observed that the equivalent nodal load is presented as a parameter to assess the influence that the secondary moment has on the structure. As this is the calculation of the area between the centroid of the section and the profile, if the sum of the areas is null, the secondary moment does not occur, Raju [6] defines this characteristic as a concordant prestressing path.

3 STIFFNESS MATRIX OF CURVED FINITE ELEMENT

The stiffness matrix of a curved element of constant section and curvature to be used was deduced by Palaninathan and Chandrasekharan [12], based on Lee's studies [13]. The original element has six degrees of freedom per node (Figure 5).

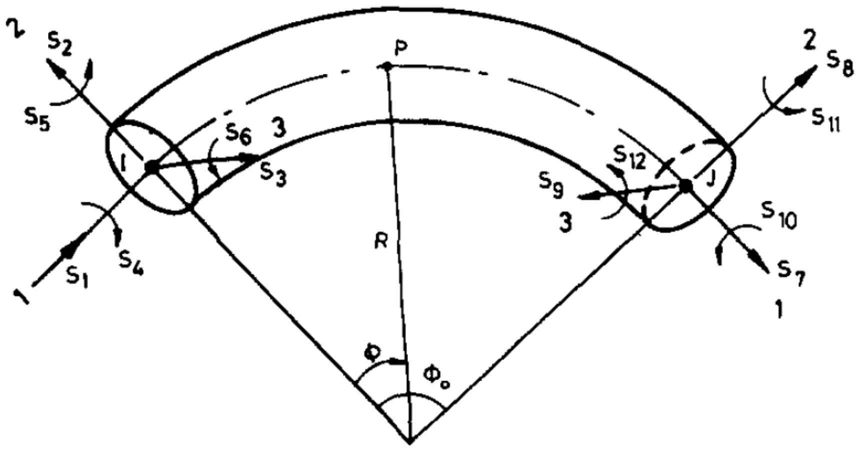

Figure 5. Curved beam element, Palaninathan and Chandrasekharan [12].

However, the number of degrees of freedom was reduced to three, being the vertical force, the bending moment and the torsion moment, transforming it into a curved grid finite element (Figure 6).

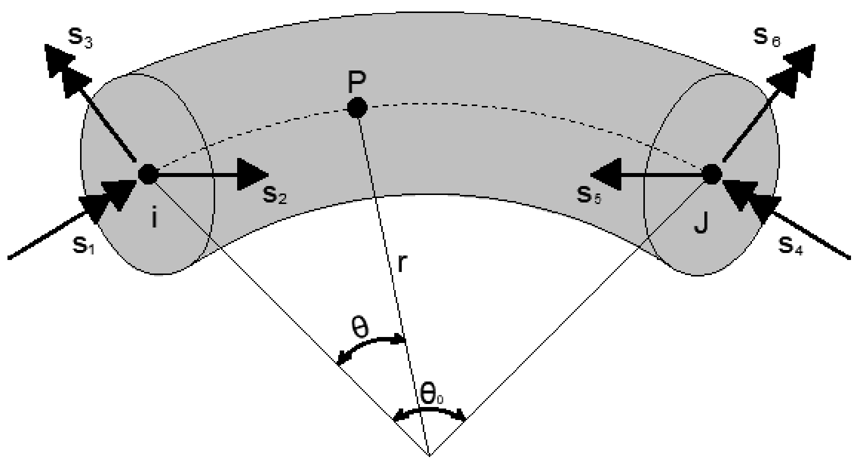

Figure 6. Curved grid finite element.

The reduction in the number of degrees of freedom aims at simplifying the structural calculation, since the inversion of the 12 × 12 stiffness matrix would result in a large computational work, in addition to the other variables involved.

The internal forces and the moments acting at point P are expressed in values of the forces from node i as follows

$$V' = V_2 \tag{12}$$

$$T' = T_1 \cos(\varnothing) - M_3 \mathrm{sen}(\varnothing) - V_2 r\left(1 - \cos(\varnothing)\right) \tag{13}$$

$$M' = T_1 \mathrm{sen}(\varnothing) + M_3 \cos(\varnothing) + V_2 r \,\mathrm{sen}(\varnothing) \tag{14}$$

The strain energy in the element, disregarding the section warping effect, is given by

$$U = \frac{r}{2}\int_0^{\varnothing}\left(\frac{T'^2}{GJ}+\frac{M'^2}{EI}\right)d\varnothing \tag{15}$$

Using Castigliano's theorem we obtain

$$U_1 = \frac{\partial U}{\partial T'} = \frac{r}{GJ}\int_0^{\varnothing} T'\frac{\partial T'}{\partial T'}d\varnothing + \frac{r}{EI}\int_0^{\varnothing} M'\frac{\partial M'}{\partial T'}d\varnothing \tag{16}$$

$$U_2 = \frac{\partial U}{\partial V'} = \frac{r}{GJ}\int_0^{\varnothing} T'\frac{\partial T'}{\partial V'}d\varnothing + \frac{r}{EI}\int_0^{\varnothing} M'\frac{\partial M'}{\partial V'}d\varnothing \tag{17}$$

$$U_3 = \frac{\partial U}{\partial M'} = \frac{r}{GJ}\int_0^{\varnothing} T'\frac{\partial T'}{\partial M'}d\varnothing + \frac{r}{EI}\int_0^{\varnothing} M'\frac{\partial M'}{\partial M'}d\varnothing \tag{18}$$

Developing the integrals and applying Castigliano’s theorem we have the following system of equations

$$\begin{pmatrix} u_1 \\ u_2 \\ u_3 \end{pmatrix} = \begin{pmatrix} a_{11} & a_{12} & a_{13} \\ a_{12} & a_{22} & a_{23} \\ a_{13} & a_{23} & a_{33} \end{pmatrix}\begin{pmatrix} V' \\ T' \\ M' \end{pmatrix} \tag{19}$$

By developing the integral of the strain energy and using the following equation to simplify the values obtained, results

$$\lambda = \frac{EI}{GJ} \tag{20}$$

$$\Delta_{AA} = \frac{1}{EI}\begin{pmatrix} \frac{r^2}{2}(\lambda Cr + Br) & \frac{r^2}{2}(B-\lambda V) & \frac{r^2}{2}(\lambda S - D) \\ \frac{r^2}{2}(B-\lambda V) & \frac{r}{2}(\lambda N + B) & \frac{r}{2}(\lambda D - D) \\ \frac{r^2}{2}(\lambda S - D) & \frac{r}{2}(\lambda D - D) & \frac{r}{2}(\lambda B + N) \end{pmatrix} \tag{21}$$

Where

$$N = \theta + \frac{\operatorname{sen}(2\theta)}{2} \tag{22}$$

$$B = \theta - \frac{\operatorname{sen}(2\theta)}{\theta} \tag{23}$$

$$C = 3\theta + \frac{\operatorname{sen}(2\theta)}{\theta} - 4\operatorname{sen}(\theta) \tag{24}$$

$$S = \frac{3}{4} - \cos(\theta) + \frac{\cos(2\theta)}{4} \tag{25}$$

$$V = 2\text{sen}(\theta) - \theta - \frac{\text{sen}(2\theta)}{2} \tag{26}$$

$$D = \frac{\cos(2\theta)}{2} - \frac{1}{2} \tag{27}$$

The stiffness matrix of the element is given by the joining of matrices K_{AA}, K_{AB}, K_{BA} e K_{BB}, thus

$$k = \begin{bmatrix} K_{AA} & K_{AB} \\ K_{BA} & K_{BB} \end{bmatrix} \tag{28}$$

The K_{AA} matrix is obtained by inverting the flexibility matrix Δ_{AA}

$$K_{AA} = \Delta_{AA}^{-1} \tag{29}$$

The matrix T relates the forces of the final node j to the forces of the initial node i

$$T = \begin{bmatrix} -1 & 0 & 0 \\ r(1-\cos(\theta)) & -\cos(\theta) & \text{sen}(\theta) \\ r\text{sen}(\theta) & -\text{sen}(\theta) & -\cos(\theta) \end{bmatrix} \tag{30}$$

The K_{BA} matrix is obtained by

$$K_{BA} = TK_{AA} \tag{31}$$

In a similar way, the flexibility matrix is obtained

$$\Delta_{BB} = \frac{1}{EI}\begin{pmatrix} \frac{r^2}{2}(\lambda Cr + Br) & \frac{r^2}{2}(B - \lambda V) & -\frac{r^2}{2}(\lambda S - D) \\ \frac{r^2}{2}(B - \lambda V) & \frac{r}{2}(\lambda N + B) & -\frac{r}{2}(\lambda D - D) \\ -\frac{r^2}{2}(\lambda S - D) & -\frac{r}{2}(\lambda D - D) & \frac{r}{2}(\lambda B + N) \end{pmatrix} \tag{32}$$

The K_{BB} matrix is obtained by inverting the flexibility matrix

$$K_{BB} = \Delta_{BB}^{-1} \tag{33}$$

being that

$$K_{AB} = TK_{BB} \tag{34}$$

With this data, the stiffness matrix of the element can be assembled.

4 NUMERICAL EXAMPLE

The effect of the secondary moment on a continuous beam with two spans of constant curvature is studied and the results are compared with straight continuous beam of length equivalent to the radius and angle adopted in each case. The support conditions for both beams are of restriction to vertical and horizontal reaction. The study is carried out on a beam with a radius of 40 m, varying its angle from 10 ° to 10 ° increments, up to 90 °.

Mathcad software was used to calculate the example, basing its implementation routine on studies carried out by Vaz [14] and Soriano [8], using as a basis the matrix analysis of structures and the finite element method.

In order to simplify the study of the effect of the secondary moment on curved beams, it is settled that, in all cases, the lengths of the spans are equal, thus, $L_1 = L_2$.

The prestressing path is straight with an applied load of 1000 kN. In order to facilitate the study, a constant prestressing loss of 20% was also admitted along its entire path and its eccentricity e = 40 cm. The portion corresponding to the prestressing of the equivalent nodal load (Equation 11) is the following value.

$$\frac{\int_0^{L_1} Pz(s)\,ds}{L_1} = \frac{\int_0^{L_2} Pz(s)\,ds}{L_2} = 800\text{x}0.4 = 320 \text{ kN} \cdot \text{m} \tag{35}$$

Equation 35 is constant in all cases, since there is no change in the eccentricity or in load path profile. However, the equivalent nodal load (Equation 11) changes in all cases as a function of the reduction factor due to the curvature μ.

The modified curved finite element of Palaninathan and Chandrasekharan [10] was used for the calculation of the curved beam and for the straight beam the bar element.

Two span continuous curved beam

Figure 7 shows the section data.

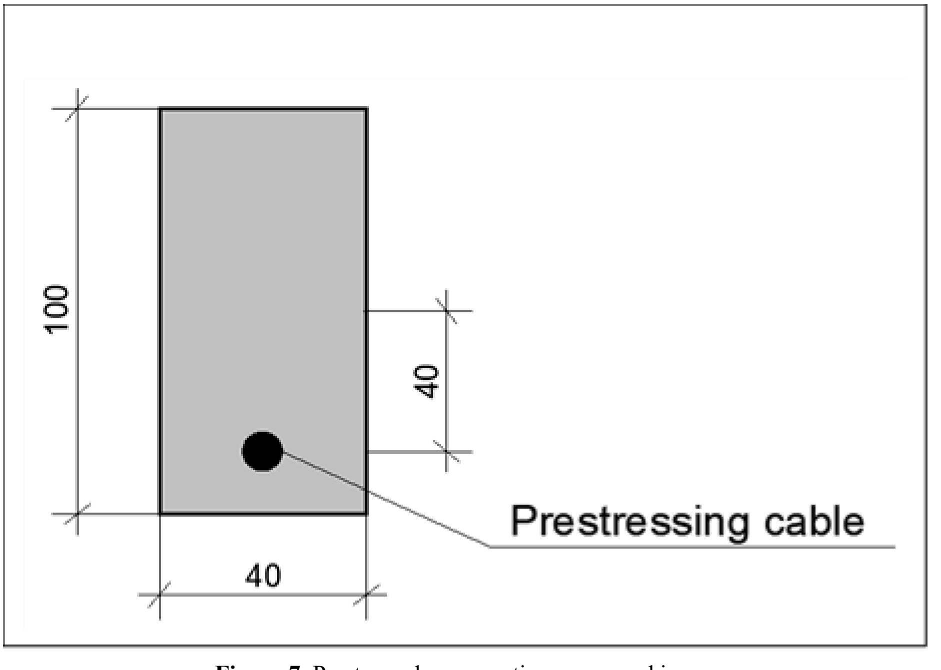

Figure 7. Prestressed cross section, measured in cm.

The ratio between flexural stiffness and torsional stiffness is equal to 1 for all cases presented.

The boundary conditions adopted in the structure are shown in Figure 8, which are the restriction to vertical displacement in all nodes of the structure.

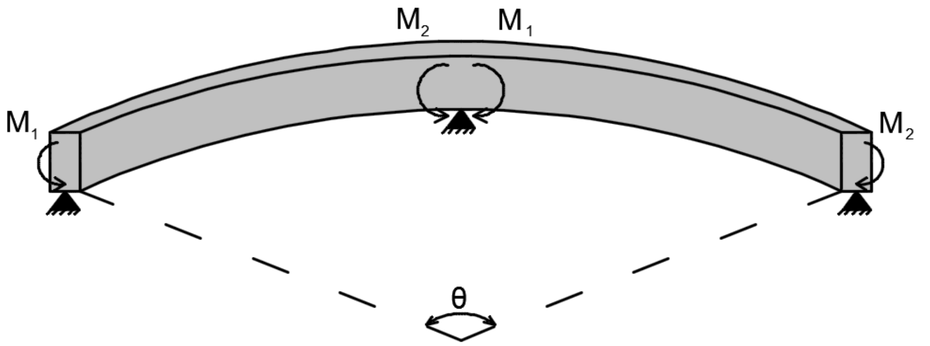

Figure 8. Two-span curved continuous beam.

Table 1 presents the results obtained in each case and Figure 9 shows, in a generic way, the effect of the secondary moment in the curved beam.

Table 1. Two-span curved continuous beam subjected to centered prestressing $(r = 40\,m)$.

Radius (m)	**40**	**λ = 1**			
Angle (Degrees)	**μ**	**Redundant Reaction (kN) (Curved Beam)**	**Equivalent Span Length (m)**	**Redundant Reaction (kN) (Straight Beam)**	**Ratio (Curved / Straight)**
10	0.99	272.70	3.49	275.02	99.2%
20	0.97	132.97	6.98	137.51	96.7%
30	0.94	85.12	10.47	91.67	92.8%
40	0.89	60.44	13.96	68.75	87.9%
50	0.84	45.22	17.45	55.00	82.2%
60	0.78	34.89	20.94	45.84	76.1%
70	0.73	27.49	24.43	39.29	70.0%
80	0.67	21.95	27.93	34.38	63.8%
90	0.62	17.75	31.42	30.56	58.1%

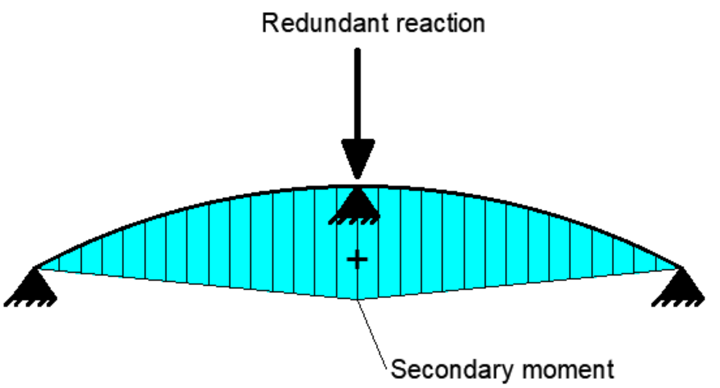

Figure 9. Effect of the secondary moment in curved beam.

5 ANALYSIS OF RESULTS

It is assessed that the secondary moment in a curved structure has its value reduced as function of the beam opening angle. For small opening angles, between 10 ° and 30 °, the reduction that occurs in its secondary moment is insignificant, reaching a maximum of 7.2% when compared to its straight equivalent beam. Garrett and Cochrane [15] arrived at similar analytical results, concluding that a curved beam with an opening angle of less than 30° can be calculated as a straight beam with good precision of the results. Tests carried out by Amorn et al. [2] and compared by a straight beam model in Cunha [7] prove that curved beams with a small opening angle, including prestressed ones, can be approximated by a straight beam with a negligible difference in result, which corroborates the results obtained.

The radius of the structure does not influence the obtaining of factor μ, as this depends directly on the opening angle of the structure and the stiffness parameters EI and GJ. The reduction factor μ has a greater influence on the structure when its opening angle increases, because the larger its opening, the greater the interaction between the bending moment and the torsion moment, as can be seen in Equation 14.

The secondary moment has its value reduced by down to approximately 42% (90° angle), showing that in curved structures, with a high opening angle, the secondary moment has significantly less influence than in rectilinear structures.

It should be noted that the results obtained took into account that the flexural stiffness has a numerical value equal to the torsional stiffness, it can be deduced that if $\lambda > 1$, that is, the flexural stiffness is superior to the torsional stiffness, a reduction of the factor μ occurs and if $\lambda < 1$ result in its increase. It should be highlighted that the stiffness parameters, in addition to being important in determining the μ factor, are also relevant in determining the coefficients of the curved finite element stiffness matrix.

It is noteworthy that this study did not take into account the distortion due to shear, as well as the effect of prestressing in thin-walled sections, whether open or closed. The results obtained are valid only for full sections, where shear has little influence on the distortion of the section.

6 CONCLUSIONS

In curved beams, the reduction factor due to curvature μ is the main cause of the decrease in secondary moment. It has been proven that beams with a high opening angle have a greater reduction in their secondary moment. It is worth noting that the relationship between flexural stiffness and torsional stiffness also contribute to the variation of the μ factor intensity, it was found that if the flexural stiffness is greater than the torsional stiffness it results in a reduction of the μ factor and if otherwise, it increases. Therefore, it is inferred that the main variables for the calculation of the secondary moment, in a curved beam, are the opening angle of the structure and its stiffness parameters EI and GJ.

By the method of equivalent nodal load it is verified that, in prestressed beams whose tracing is straight, the secondary moment occurs accentuated, since the area between the centroid and the prestressing cable is larger than in beams whose tracing is variable.

The results conveyed that in curved beams with a small opening angle (between 10 ° and 30 °) the difference that occurs between the secondary moment of the curved beam and its equivalent of straight beam is negligible in the centered prestressing, reaching less than 7.2%, even with reduction factor applied. There is a significant decrease in secondary moment, mainly in beams whose opening angle is high.

The curved element used for the beam calculation is more complicated to be computationally implemented. While the stiffness matrix of the structure stays smaller than if discretization was used in bar elements, the number of variables involved ends up significantly impairing its computational performance.

The proximity of the results obtained, when comparing the result of straight beam with that of curved beam, allows us to consider it reasonable to discretize the structure instead of using curved elements for small opening angles, being recommended to use curved element for higher opening angles.

Ultimately, it is worth mentioning that the reduction factor must be used in curved beams whose approach has been modeled from straight bar elements. The fact that the modeling occurs with bar elements does not exempt the application of the reducing factor, which is a factor that seeks to consider the interaction between the torsion moment and the bending moment.

CITATIONS

[1] N. Zhang, C. C. Fu, and H. Che, "Experiment and numerical modeling of prestressed concrete curved slab with spatial unbonded tendons," *Eng. Struct.*, vol. 33, no. 3, pp. 747–756, Mar 2011.

[2] W. Amorn, C. Y. Tuan, and M. K. Trados, "Curved, precast, pretensioned concrete I-girders bridges," *Civ. Eng. Fac. Publ.*, vol. 11, no. 11, pp. 48–66, Dec 2008.

[3] J. Choi, C. R. Woods, T. D. Hrynyk, and O. Bayrak, "Behavior of curved post-tensioned concrete structures without through-thickness reinforcement," *ACI Struct. J.*, vol. 114, no. 114, pp. 983–994, Aug 2017.

[4] M. Z. Cohn and Y. Frostig, "Inelastic behavior of continuous prestressed concrete beams," *J. Struct. Eng.*, vol. 109, no. 10, pp. 2292–2309, Oct 1983.

[5] J. Kong, "A practical method for the calculation of secondary prestress moments," *Hong Kong Inst. Eng.*, vol. 11, no. 4, pp. 49–52, Dec 2004.

[6] K. Raju, *Prestressed Concrete*, 4th ed. India: McGraw-Hill, 2013.

[7] T. Cunha, "Torsional moment analysis in prestressed curved beam," M.S. thesis, Civ. Eng. Postgrad. Program, Fluminense Fed. Univ., Rio de Janeiro, RJ, Brazil, 2018.

[8] H. L. Soriano, *Análise de Estruturas – Formulação Matricial e Implementação Computacional.* Rio de Janeiro: Ciência Moderna Ltda, 2005.

[9] L. F. Martha, *Análise de Estruturas: Conceitos e Métodos Básicos*, 1a ed. Rio de Janeiro: Elsevier, 2010.

[10] J. S. Przemieniecki, *Theory of Matrix Structural Analysis.* New York: McGraw-Hill, 2012.

[11] I. Montánari, "Protensão em vigas curvas," Ph.D. dissertation, Fed. Univ. São Carlos, São Carlos, SP, Brazil, 1980.

[12] R. Palaninathan and P. S. Chandrasekharan, "Curved beam element stiffness matrix formulation," *Comput. Struc.*, vol. 21, no. 4, pp. 663–669, 1985.

[13] H.-P. Lee, "Generalized stiffness matrix of a curved-beam element," *AIAA J.*, vol. 7, no. 10, pp. 2043–2045, Oct 1969.

[14] L. E. Vaz, *Método dos Elementos Finitos em Análise de Estruturas.* Rio de Janeiro: Elsevier, 2011.

[15] R. J. Garrett and R. A. Cochrane, "The analysis of prestressed beams curved in plan with torsional restraint at the supports," *Struct. Eng.*, vol. 48, no. 3, pp. 128–132, Mar 1970.

Author contributions: TC: writing, formal analysis, methodology; ES: writing, formal analysis, methodology.

Editors: Leandro Mouta Trautwein, José Luiz Antunes de Oliveira e Sousa, Guilherme Aris Parsekian.

IBRACON Structures and Materials Journal
Revista IBRACON de Estruturas e Materiais
ISSN 1983-4195 ismj.org

ORIGINAL ARTICLE

Degradation of the EBR-CFRP strengthening system applied to reinforced concrete beams exposed to weathering

Degradação do sistema de reforço EBR-CFRP em vigas de concreto armado expostas ao intemperismo

Gláucia Maria Dalfré[a]
Guilherme Aris Parsekian[a]
Douglas da Costa Ferreira[a]

[a]Universidade Federal de São Carlos – UFSCar, Programa de Pós-graduação em Engenharia Civil, São Carlos, SP, Brasil

Received 16 January 2020
Accepted 08 July 2020

Abstract: Little is known about the behavior and durability of strengthening systems applied on concrete substrata and the possible loss of performance due to the degradation of the intervening materials by the structure's natural aging process and exposure of the externally strengthened elements to aggressive environments. In this context, the present work presents an experimental analysis of the behavior of reinforced concrete beams strengthened with Carbon Fiber Reinforced Polymer (CFRP), applied according to the Externally Bonded Reinforcement (EBR) technique, maintained in a laboratory environment (indoor and protected) or exposed to weathering (outdoor exposure). In addition, specimens of the intervenient materials were also molded and exposed to the same environmental conditions as the beams. The results indicate that weather-exposed epoxy adhesives present reductions up to 70% in their mechanical properties after exposure, while the CFRP composite properties remain similar. It was also found that the strengthening system provided 50% and 28% increments in the load-carrying capacity and stiffness of the elements, respectively. However, the tests conducted after 6 months of weathering exposure showed a 10% reduction in the load-carrying capacity of the strengthened elements.

Keywords: reinforced concrete beams, strengthening, CFRP, degradation, EBR technique.

Resumo: Pouco se sabe a respeito do comportamento e da durabilidade do sistema de reforço aderido ao substrato de concreto e a possível perda de desempenho frente à degradação dos materiais intervenientes face ao processo natural de envelhecimento das estruturas e, também, devido à exposição dos elementos reforçados externamente a ambientes agressivos. Neste âmbito, o presente trabalho baseia-se na análise experimental do comportamento de vigas de concreto armado reforçadas a flexão com mantas de fibra de carbono (CFRP, *Carbon Fiber Reinforced Polymer*) aplicadas segundo a técnica EBR (*Externally Bonded Reinforcement*) mantidas em ambiente laboratorial (interno e protegido) e expostas a intempéries (exposição exterior). Para além disso, corpos de provas dos materiais constituintes do sistema de reforço também foram confeccionados e expostos nas mesmas condições ambientais das vigas. Os resultados demonstraram que os adesivos epoxídicos apresentam reduções de até 70% em suas propriedades mecânicas quando expostos às intempéries enquanto o compósito de CFRP permanece com suas propriedades inalteradas após mesma exposição. Para as vigas de concreto armado reforçadas, foi verificado que o sistema de reforço proporciona incrementos de 50 e 28% na capacidade de carga e rigidez dos elementos reforçados, respectivamente. No entanto, os ensaios realizados após 6 meses de exposição às intempéries demonstraram uma redução de 10% no incremento da capacidade de carga dos elementos reforçados.

Palavras-chave: vigas de concreto armado, reforço, CFRP, degradação, técnica EBR.

How to cite: G. M. Dalfré, G. A. Parsekian, and D. C. Ferreira, "Degradation of the EBR-CFRP strengthening system applied to reinforced concrete beams exposed to weathering", *Rev. IBRACON Estrut. Mater.*, vol. 14, no. 2, e14208, 2021, https://doi.org/10.1590/S1983-41952021000200008

Corresponding author: Gláucia Maria Dalfré. E-mail: glaucia.dalfre@ufscar.br
Financial support: Coordination for the Improvement of Higher Education Personnel (CAPES).
Conflict of interest: Nothing to declare.

1 INTRODUCTION

Strengthening a structural element means restoring or increasing its supporting conditions in relation to those for which it was initially designed. Carbon Fiber Reinforced Polymer (CFRP) strengthening systems can be applied to various reinforced concrete elements such as beams, columns, slabs. Design errors, project reading misinterpretation, changes in the structure use, or the natural weathering of buildings are some of the main reasons for strengthening a structure [1].

Among the main materials used for this purpose, Fiber Reinforced Polymers (FRPs) are of high prominence because their mechanical properties are superior to the conventional materials used in strengthening techniques. Of the main characteristics of FRPs, high strength and stiffness, and low weight are the main properties that favor their use in strengthening works [2].

CFRPs are the most widely used materials for structural strengthening [3]. One main advantage of CFRPs is the resistance to chemical agents and corrosion [4]. According to Barros [5], prefabricated and in-situ cured systems are the most used in strengthening techniques. Prefabricated systems are supplied in the form of laminates or circular section bars, with their fibers oriented in the longitudinal direction of the element. In-situ cured matrix and fiber are supplied separately, and CFRP composite manufacturing is carried out at the strengthening application site. In this case, the fibers may be either unidirectional or bidirectional in orientation and supplied in the form of sheets or fabrics.

Of the various ways of applying strengthening systems, the Externally Bonded Reinforcement (EBR) technique is widely used. It originated in Europe, proposed and developed in Switzerland, and it was first used to strengthen a bridge using CFRP sheets in the city of Lucerne in 1991. Since then, the EBR technique has continued to be used in strengthening interventions [6], [7] due to its advantages, such as the ease of application and good mechanical performance [8].

Further, the EBR technique allows for increments in bending with the bonding of the strengthening system on the tensile face of the beams, or even by shear, by strengthening the lateral faces of the beams, or with the strengthening systems working simultaneously.

According to Karbhari [9] and Gangarao et al. [10], composite materials used in civil construction can be exposed to various aggressive agents. Determining the effects of environmental aggressiveness on the adhesion of the concrete-adhesive FRP, especially over prolonged periods, is of extreme importance [11]. There is a need for further knowledge of their long-term performance, durability, and design life in the face of conditions such as moisture, seawater salinity, and thermal cycles, among others.

The present work aimed to evaluate the long-term durability and mechanical behavior of the flexural strengthening system's constituent materials, as well as reinforced concrete beams strengthened with CFRP, applied according to the EBR technique, maintained in a laboratory environment (internal and protected) or exposed to weathering (outdoor exposure).

2 STATE OF THE ART

2.1 Degradation of FRPs when exposed to weathering

All materials used in the construction industry are subject to degradation, originated by chemical, physical, or mechanical sources. Applying an FRP strengthening system to a determined concrete element, these degradation mechanisms should be considered to achieve better long-term behavior and durability [12]. Degradation mechanisms can occur either individually or together in the degradation of the composite FRP material (Figure 1).

It is generally known that degradation mechanisms directly affect the most sensitive part of the strengthened structure, i.e., the bond between the concrete substrate and the FRP composite. Bonding usually relies on epoxy-based resins, which are susceptible to degradation in harsh environments. These resins are susceptible to ultraviolet (UV) radiation, temperature, humidity, and acid rain [13]. Unless a protective layer is used, the FRP gets directly exposed to the external environment and, consequently, to the possible aggressive agents or eventualities, as shown in Figure 2.

Direct exposure to UV radiation from polymers can result in photodegradation, a mechanism that causes the decomposition or dissociation of chemical bonds between polymer chains, driven by the UV radiation present in solar waves. This radiation causes the degradation of polymers, leading to discolouration, surface oxidation, embrittlement, and polymer matrix microfissuration [12].

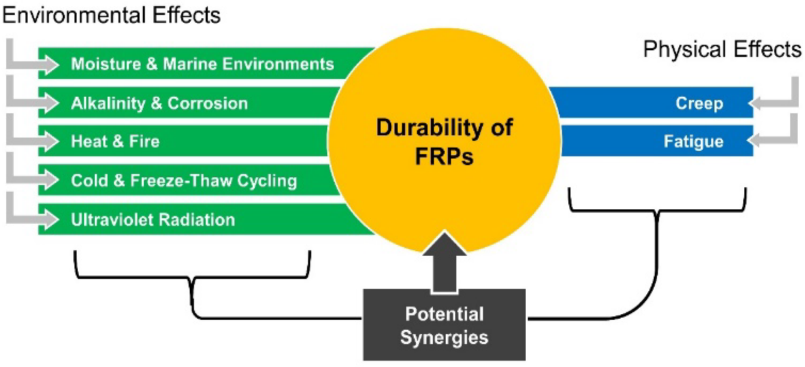

Figure 1. Degradation mechanisms of FRP systems [12]

Figure 2. Sewage station with CFRP sheets externally applied according to the EBR technique [14]

Zhao et al. [15] evaluated three types of degradation in polymeric resins (ester-vinyl, epoxy, and epoxy ester) when exposed to UV radiation. In the study, specimens with 200 mm, 20 mm, and 4 mm in length, width, and thickness, respectively, were prepared and cured for seven days at room temperature. Subsequently, they were exposed to UV radiation (280–315 nm) at a temperature of 57–63ºC and humidity of 90–95%. The radiation cycles lasted 12 hours (8 hours of UV radiation and 4 hours of condensation) for a total period of 90 days (Table 1). The ester-vinyl resin presented higher degradation, with a reduction of 65% and 69% in tensile strength and modulus of elasticity, respectively. After exposure, the resin specimens presented significant changes in their colouration.

Table 1 Mechanical properties of resins after exposure to UV radiation [15]

Exposure period	Maximum tensile stress (MPa)			Modulus of elasticity (MPa)		
	Vinyl ester	Epoxy	Ester epoxy	Vinyl ester	Epoxy	Ester epoxy
Reference	39,7	41,0	34,5	2544,7	1944,0	2024,7
30 days	17,1	39,8	30,7	1223,0	2438,9	2385,3
90 days	13,8	42,0	31,4	777,6	1547,9	1740,1

Some fiber types also suffer from degradation caused by UV radiation. According to ISIS [12], carbon and glass fibers are generally not affected by UV radiation, while aramid fibers undergo slight degradation in the face of UV exposure. Homam and Sheikh [16] studied the isolated effect of exposure to UV rays on FRP composites with epoxy resin. In a controlled environment, CFRP and GFRP specimens were exposed to 22°C to 38°C temperature of, 40% relative humidity of radiation from UV-A lamps at 156 W/m^2. The specimens were tested for uniaxial tensile and shear using the single-lap bond test. Slight increases in tensile strength and stiffness were observed in the specimens of both composites exposed to UV radiation as compared to those maintained in the laboratory environment for exposure periods of 1200 and 4800 hours. Notably, exposure to UV rays did not significantly affect the shear strength of the composites. The bond between the FRP composite and the concrete substrate was susceptible to degradation due to UV radiation. Kabir et al. [17] studied the concrete/adhesive/FRP bonding in external environments. The authors report the exposure to external environments as the most harmful situation for concrete bond-adhesive-FRP.

2.2 Climate regions: Köpper–Geiger classification system

The intensity of weathering effects depends on the climate and microclimate of the place where the structure is allocated. One way to categorize the climate is through the Köppen–Geiger climate classification system, which is used worldwide in different areas (such as climatology, meteorology, geography, bioclimatology, and ecology) and takes into account the average annual and monthly values of temperature and precipitation in addition to climate seasonality. Climatic types are separated by large groups, types, and subtypes. Table 2 presents the nomenclatures and climatic types, while Figure 3 shows the climate classification of Brazil [18].

Figure 3 indicates that tropical climate (Zone A – an average temperature equal to or higher than 18°C every month and significant precipitation) is predominant in Brazil, covering 81.4% of the country's total area. Dry climate (Zone B – low precipitation throughout the year) is present in some parts of the northeastern states of Brazil, while subtropical climates are dominant in the South and Southeast [18].

According to the Brazilian Agricultural Research Company (EMBRAPA) [19], the city of São Carlos in the state of São Paulo (latitude 21°57'42" (S), longitude 47°50'28" (W), and altitude 860 meters above sea level), which is where this research was developed, has a local climate defined as humid subtropical with dry winter and hot summer (known as Cwa). Figure 4 shows other regions of the world that have similar Cfa and Cwa climate types, as per the Köpper–Geiger climate classification system, for which the results obtained in this research can also be expanded.

Table 2 Köpper–Geiger classification system [18]

Group	Type	Subtype (where applicable)
A - Tropical		**f** - Equatorial (no dry season, with precipitation ≥ 60 mm each month)
		m - Monsonic (with a drier month)
		w - Savanna with drier season in winter
		s - Savanna with drier season in summer
B - Dry	**w** - Arid	**h** -Low latitude and longitude; average annual temperature ≥18°C
		k - medium latitude and high altitude; average annual temp. <18°C
	s - Semiarid	**h** -Low latitude and longitude; average annual temperature ≥18°C
		k - medium latitude and high altitude; average annual temp. <18°C
C - Moist Subtropical	**f** - Oceanic climate, no dry season	**a** - Hot summer
		b - Cool summer
		c - Short and cold summer
	w - With dry winter	**a** - Hot summer
		b - Cool summer
		c - Short and cold summer
	s - With dry summer	**a** - Hot summer
		b - Cool summer
		c - Short and cold summer
D - Temperate Continental	**f** - No dry season	**a** - Hot summer
		b - Cool summer
		c - Short and cold summer
		d - Very cold winter
	w - With dry winter	**a** - Hot summer
		b - Cool summer
		c - Short and cold summer
		d - Very cold winter
	s - With dry summer	**a** - Hot summer
		b - Cool summer
		c - Short and cold summer
		d - Very cold winter
E - Polar		**T** - Tundra (temperature in the hottest month between 10 and 0°C)
		F - Glacial (temperature in the hottest month <0°C)

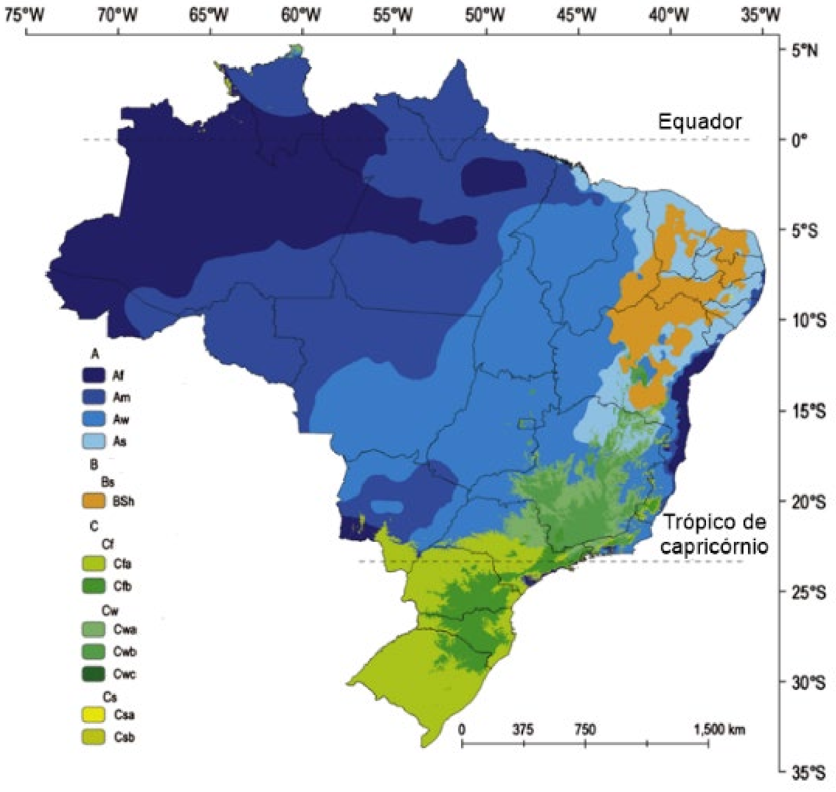

Figure 3. Brazil climate classification in the Köpper-Geiger system [18]

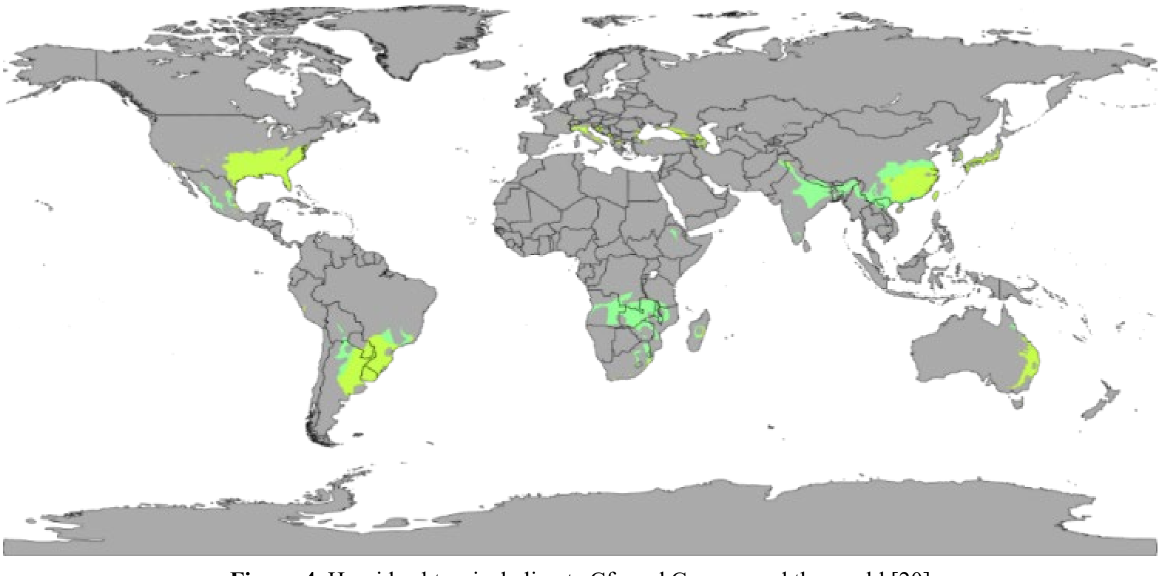

Figure 4. Humid subtropical climate Cfa and Cwa around the world [20]

3 EXPERIMENTAL PROGRAM

The research aimed to evaluate the degradation of reinforced concrete beams strengthened with CFRP sheets and exposed to weathering in a humid subtropical climate with dry winter and hot summer (Cwa) in non-accelerated tests. The beams and intervening materials (epoxy resins and CFRP composites) were exposed to two distinct environments: (a) laboratory environment (internal, protected), inside a controlled temperature and humidity chamber for a period of

6 months (reference), and (b) external environment, wherein the materials were exposed to weathering for the same period of time.

3.1 Beam geometry, degradation environments, strengthening system, and bending test configuration

3.1.1 Beams

The experimental program consisted on twelve simply supported beams of 120 x 200 x 2500 mm^3, 20-MPa, and positive longitudinal reinforcement composed by two CA-50 steel bars (10-mm diameter; reinforcement ratio of 0.75%). To avoid shear rupture, CA-60 steel stirrups (5-mm diameter and 10-cm spacing) with two top longitudinal reinforcement bars of CA-50 and 6.3 mm diameter (Figure 5). The beams were designed in the deformation domain 2, based on NBR 6118 [21].

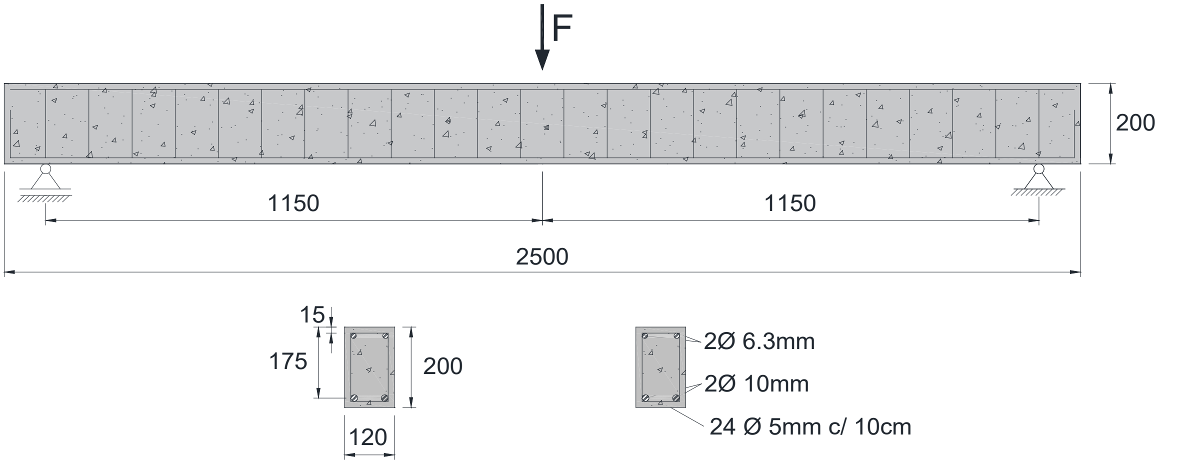

Figure 5. Characteristic of reinforced concrete beams (units in mm).

3.1.2 Strengthening system

Eight beams were reinforced with unidirectional 300-g/m^2 weight carbon fiber sheets of 0.13 mm thickness. The sheet was cut into 110 x 2200 mm strips to fit the tension surface of the reinforced concrete beam (Figure 6).

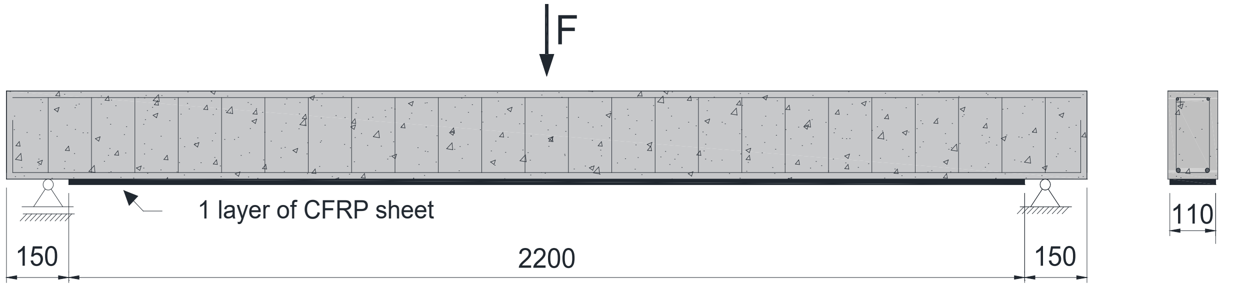

Figure 6. Details of the strengthening system (units in mm)

The CFRP sheets were applied externally to the beams when they were 186 days old. The substrate was cut with a diamond thinning disc grinder until the entire layer of cement paste was removed and the aggregates were exposed. After, compressed air was applied to the surface for disposing of any solid particles. A layer of the primer resin (Resin A) was applied to improve the adhesion conditions between the CFRP and concrete substrate. The CFRP was bonded using the epoxy lamination resin (Resin B), which was applied 45 minutes after the primer. The primer and saturation resins were prepared into three steps: agitation of each component, mixture of component A to B in the proportion indicated by the manufacturer, and mechanical mixture until a uniform color was obtained. The primer resin was spread on the concrete surface using a brush. The CFRP sheet was covered with lamination resin and applied to the concrete substrate before the application of the strengthening system. While strengthening, we tried to ensure the alignment of the fibers in the longitudinal direction of the beam, to check the non-formation of air bubbles in the back of the CFRP composite, and to avoid the accumulation of excess resin. The steps and procedures used to strengthen the reinforced concrete beams are depicted in Figure 7.

3.1.3 Degradation environments

Of the twelve beams made, four had no strengthening, and the others were strengthened in flexure with one layer of CFRP sheet applied according to the EBR technique. Two exposure environments were adopted in this research (Figure 8), as given below.

- Laboratory environment (LAB): internal to a chamber, protected, and with monitoring of ambient temperature and humidity, which served as a reference for the other tests (Figure 8a)
- Exposure to weathering (WEA): external environment, free of obstacles that promoted shading in beams and specimens, and with monitoring of humidity, temperature, and radiation (Figure 8b).

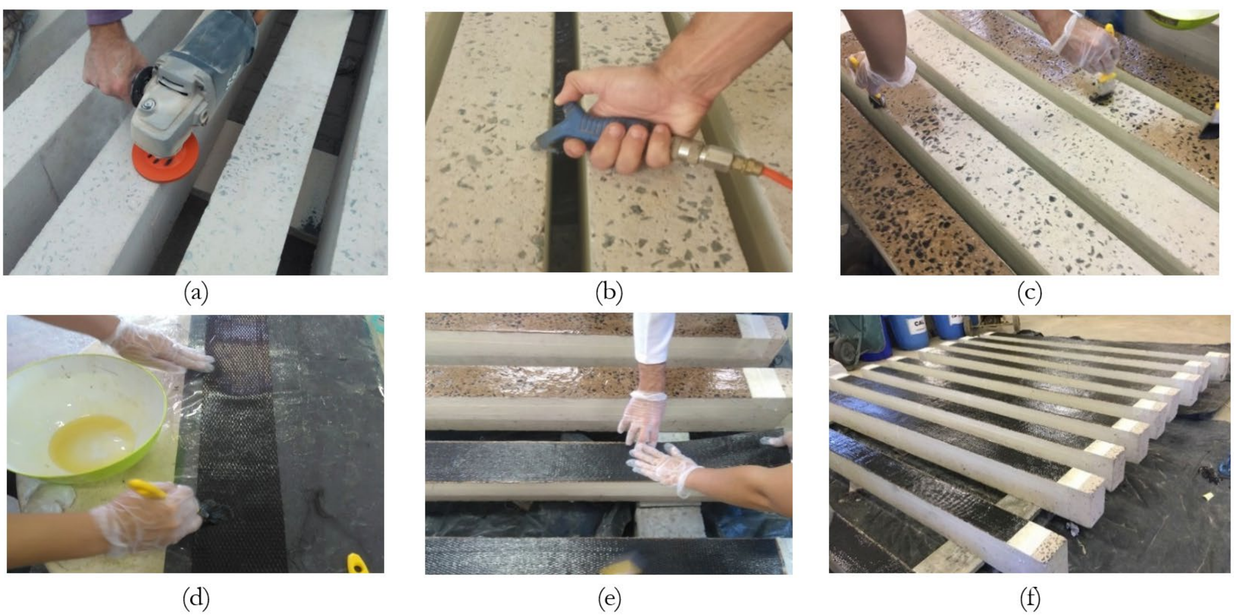

Figure 7. (a) Preparation of the concrete surface, (b) surface cleaning with compressed air, (c) application of the primer, (d) impregnation of the CFRP composites, (e) application of CFRP to the concrete substrate and (f) final aspect of the strengthened members

Each beam was identified as Vx_y_z, where "x" is the number of tested elements, "y" corresponds to the elements used as reference (REF, of *Reference),* maintained in a laboratory environment (LAB, of *laboratory*), or exposed to weathering (WEA, of *Weathering*), and "z" due to the use or not of strengthening material (0 or 1 layer of CFRP sheet). The strengthening system was also analyzed, specifically the epoxy resins and the CFRP composites. Table 3 presents a summary of the experimental program wherein Vx_REF_0 and Vx_REF_CFRP refer to the beams without and with strengthening, respectively, maintained in the same environment and tested on the same date – 200 days after concreting – which were considered as references for the other analyses. The Vx_LAB_CFRP and Vx_WEA_CFRP refer to the beams strengthened with CFRP and maintained in laboratory chamber environment or exposed to weathering, tested 6 months after the application of the strengthening. The other beams will be tested 2 years after strengthening and exposure to the environments previously mentioned.

(a) (b)

Figure 8. Exposure environments: (a) isolated and protected chamber and (b) exposure to weather (outdoor environment)

Table 3 Test program for reinforced concrete beams

Group identification	Strengthening	Environment	Identification of beams	Condition for performing the test	Number of beams
V_REF_0	No strengthening	LAB	V1_REF_0 V2_REF_0	Test conducted at the age of 200 days	2
V_REF_CFRP	CFRP	LAB	V1_REF_CFRP	Strengthening performed at the age of 186 days	2
			V2_REF_CFRP	Test performed at the age of 200 days (14 days after application of the strengthening system, time considered to be the complete cure of epoxy resin)	
V_LAB_CFRP	CFRP	LAB	V1_LAB_CFRP V2_LAB_CFRP	Strengthening carried out at the age of 200 days	2
V_WEA_CFRP	CFRP	WEA	V1_WEA_CFRP V2_WEA_CFRP	Test performed 380 days after concreting (6 months after the application of the strengthening system)	2

3.1.4 Test configuration

The three points bending tests were performed with midspan point load, using a universal EMIC testing machine (model DL 60000 available at the Structural Systems Laboratory [LSE] of the Federal University of São Carlos [UFSCar]).

A self-reaction system was designed to allow testing the beam inside the universal testing machine. A double corbel element (Figure 9a) was designed using 31.75-mm and 25.40-mm thick. The corbel was fixed to the testing machine base and supported a 250-cm long steel section (W200 x 26.6). The corbel was screwed to the base of the test machine using six steel hexagon screws type M12, and the metal profile was mounted on it with eight steel hexagon screws type M10. The concrete beams were supported on the metal profile at a roller and at a fixed support, as shown in Figure 9b.

To measure the rotation of the supports and displacement of the steel beam ends, two Linear Variable Differential Transformers (LVDTs) with 25-mm stroke and two potentiometers with 20-mm stroke were used, positioned as shown in Figure 9b, 9c.

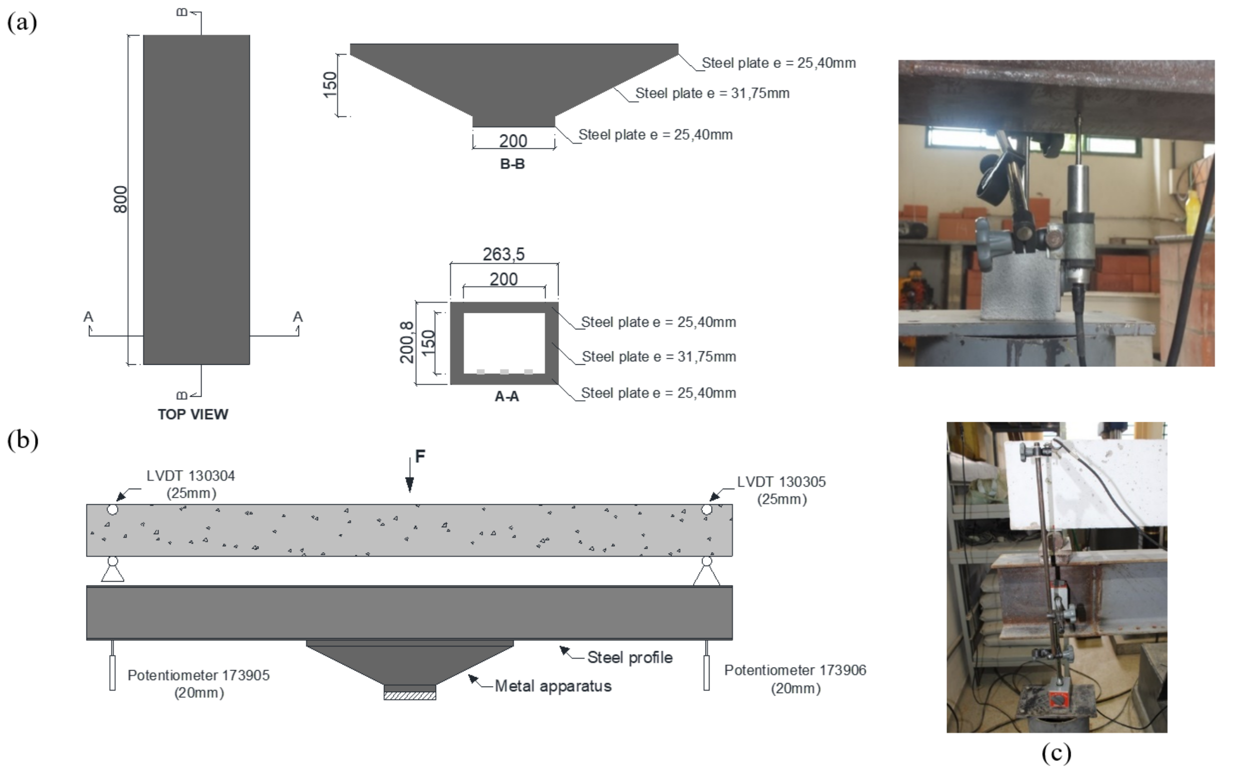

Figure 9. (a-b) Steel apparatus and (c) details of the positioning of the LVDTs and potentiometers used to measure the displacement of the metal beam and rotation of the supports (units in **Figure 9a:** mm)

The loading was applied at 0.50mm/min displacement. The load application was double recorded using an external 200-kN load cell (with reading resolution of 0.01 kN), in addition to the test machine load cell, which had a load cell with a maximum capacity of 600 kN and reading resolution of 0.1 kN. The displacements and deformations in concrete, longitudinal reinforcement and CFRP composite were recorded using an ADS-2000 model data acquisition system (manufactured by LYNX). Beam instrumentation included a displacement transducer and six electrical strain gauges. A *Vishay* displacement transducer, with a linear range of 50mm, was used to measure the vertical displacement of the beams. This was fixed to an external support and positioned at the midspan at the beams.

The deformations in the concrete were measured on an electric strain gauge of type PA-06-1500BA-120 (resistance of 120 Ω and length of the reading grid of 40 mm; produced by Excel Sensors), which was positioned in the middle of the beams (SG1). The deformations in the longitudinal strengthening were measured on electrical strainers of type KFG-20-120-C1-11 (resistance of 120 Ω and length of the reading grid of 20 mm; produced by KYOWA), which was positioned in the section of the central section of one of the longitudinal strengthening (SG2). In relation to CFRP composite deformations, electrical strain gages of type KFG-20-120-C1-11 (the same used in longitudinal strengthening) and type PA-06-250BA-120 (resistance of 120 Ω and reading grid length of 6 mm; produced by Excel Sensors), positioned along the strengthening material (SG3 to SG5). Figure 10 shows the instrumentation used.

3.1.5 Characterization of materials

Characterizing the concrete included an analysis of the axial compressive strength and modulus of elasticity. Molding and curing procedures were performed, as prescribed by NBR 5738 [22], and cylindrical specimens 200 mm in height and 100 mm in diameter were molded. 24 hours after the casting, the specimens were demolded and positioned in the same environment as the beams.

The CFRP composite manufacturing system, which supplies the fiber and matrix separately, is known as the "*in situ*" cured system. In this experiment, an *in situ* cured system was used.

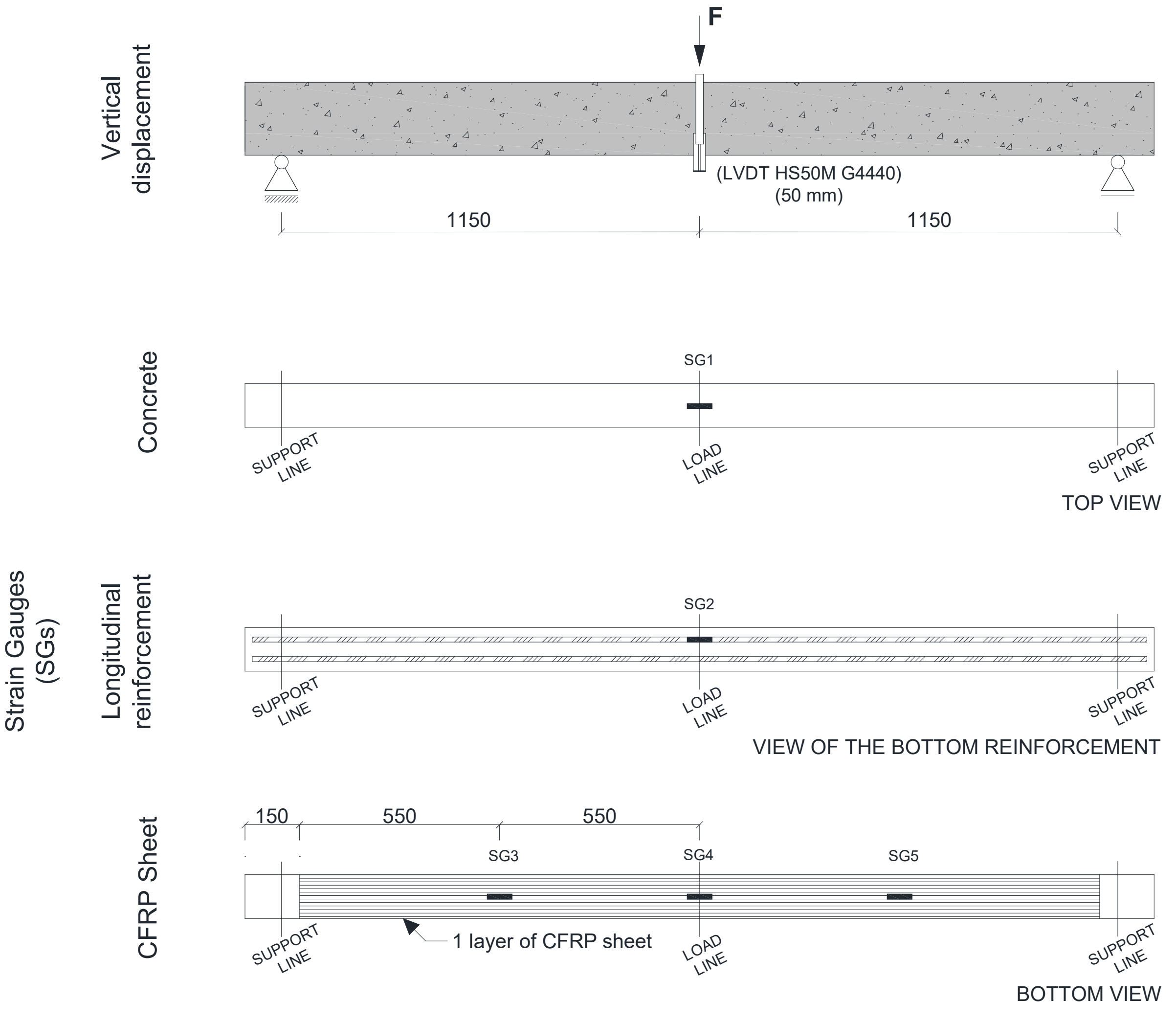

Figure 10. Instrumentation used in beam testing (units in mm)

A layer of unidirectional carbon fiber mat weighing 300 g/m^2 was impregnated with epoxy resin. The carbon fiber sheet had to have at least tensile strength of 3800 MPa, modulus of elasticity of 240 GPa, and deformation at rupture of 15.5‰. More information on the characterization of the CFRP composites and experimental results can be found in Ferreira [23].

The adhesives used to fix the composite strengthening system to the concrete substrate were supplied by the same manufacturer of the carbon fiber sheet used in this work. In the experiment, bi-component epoxy primer and lamination resins were used. The characterization tests of epoxy resins and CFRP composites were carried out at the Polymer Laboratory of the Materials Engineering Department (DEMa) of UFSCar. More information on the characterization of adhesives and the experiment results can also be found in Ferreira [23].

The mechanical properties of the steel were evaluated by axial tensile tests, according to the recommendations of NBR 6892-1 [24]. A minimum of three specimens, 50 cm in length and randomly chosen, were tested for each bar diameter used. Both steel and concrete characterization tests were performed at LSE.

4 RESULTS AND DISCUSSION

This section presents the results of the tests of characterization of the materials and the behavior of concrete beams without strengthening and reinforced with a layer of CFRP sheet.

4.1 Environmental data

The temperature and average humidity readings in the laboratory environment were 23.3ºC (± 0.03%) and 36.5% (± 0.24%), respectively. The values in parentheses represent the Coefficient of Variation (COV). For exposure to weathering (external environment), Figure 11 presents the data of temperature, humidity, and UV radiation throughout the exposure period of the beams and concrete specimens, i.e., from May to November 2018. During this period the maximum and minimum temperatures were 34.2ºC and 4.7ºC, and the maximum and minimum humidity were 95% and 16%, respectively. Regarding UV radiation, the surface weather station recorded a peak of 4112 kJ/m^2 and an average of 788 kJ/m^2 over the exposure period.

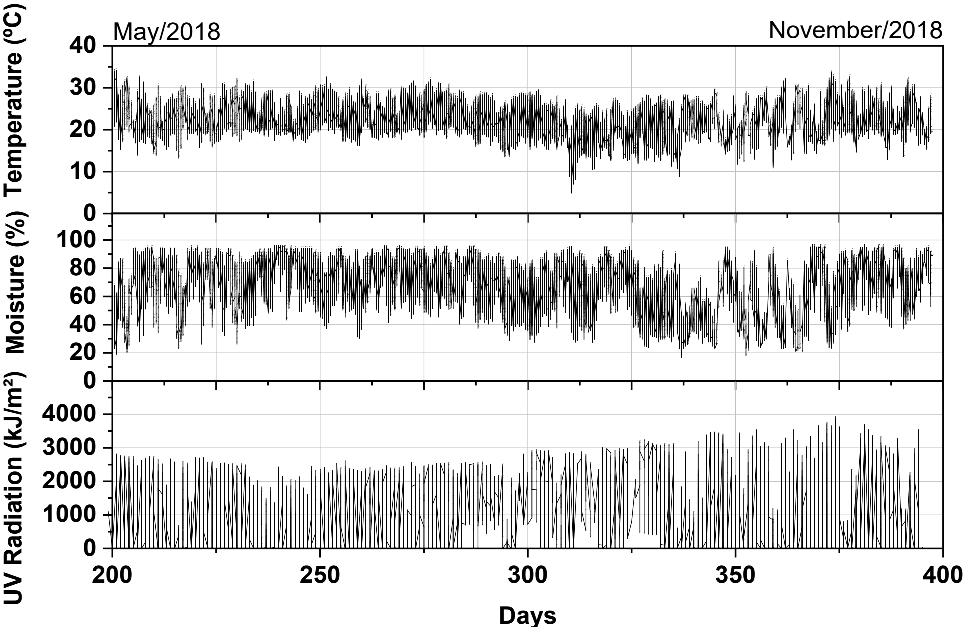

Figure 11. Weather data for the weather exposure. Source: INMET

4.2 Mechanical properties

4.2.1 Concrete

Concrete properties were tested 28 days after concreting and also on the day of the beam tests, which were performed at the age of 200 days (REF) and 380 days (LAB and WEA). The results showed the mean values of compressive strength of 22.0 MPa (± 3.50%) and 28.5 MPa (± 0.54%) and modulus of elasticity of 29.3 GPa (± 7.03%) and 31.6 GPa (± 5.32%) obtained at 28 and 200 days, respectively. For the specimens that were kept in the laboratory environment (LAB) or exposed to weathering (WEA), mean values of 27.4 MPa (± 0.50%) and 25,2 MPa (± 6.94%) for compressive strength and 31.2 GPa (± 2.87%) and 28.5 GPa (± 3.06%) for modulus of elasticity, respectively, were obtained in the test performed at the age of 380 days.

4.2.2 Steel

Regarding the characterization of steel, for bars with a diameter of 5 mm, type CA-60, an average yielding stress was observed at 2.0‰ of 646.9 (± 4.04%) MPa and a maximum tensile stress of 670.6 (± 3.62%) MPa (Figure 12a). For steel with a diameter of 10 mm, a typical behavior of CA-50 steel was verified with a plastic plateau (Figure 12b), with an average yielding stress of 547.4 MPa (± 2.13%), mean yielding strain of 2.8‰ (± 1.59%), and a maximum tensile stress of 591.5 MPa (± 6.25). The elasticity modules verified for the 10 mm and 5 mm bars were 196.9 GPa (± 1.58%) and 191.3 GPa (± 7.19%), respectively.

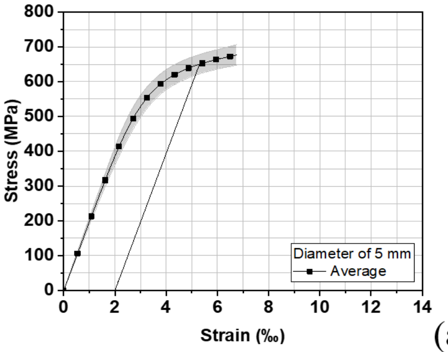

(a)

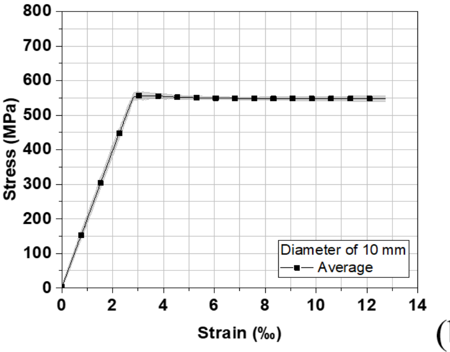

(b)

Figure 12. Stress versus deformation of materials: (a) stirrups and (b) steel of longitudinal reinforcement

4.2.3 Epoxy resins

The characterization tests for the resins were experimentally performed at the ages of 7 and 14 days and 4 and 8 months after the application of the strengthening system, as presented in Figure 13. Considering 14 days of cure for Resin A (Figure 13a), which was maintained in a laboratory environment, the material presented a small increase in maximum tension and modulus of elasticity (5.7% and 4.5%, respectively) at 4 months. After 8 months of exposure and with the results of the tests performed at 14 days as a reference, there was no major change in the maximum tensile stress of the primer, which presented a small reduction of 2.9%. However, a 9.1% reduction in the modulus of elasticity was verified in the assays. There was also a small reduction in the ductility of the specimens after 8 months of exposure in a laboratory setting. Therefore, there were no significant changes in the mode of rupture and stress-strain behavior throughout the exposure period in the laboratory environment.

Considering the exposure to weather of Resin A (Figure 13b) and with the tests performed at 14 days as a reference, a reduction of 39.1% in tensile strength and 4.5% in the modulus of elasticity was noted at 4 months. At 8 months of exposure, a sharper reduction in tensile strength (about 51.0%), while the modulus of elasticity showed a reduction of 9.1%. It was also verified, for both ages, that the reduction of ductility of the specimens with alteration in the mode of rupture from ductile to fragile without a defined plasticization interval. Further, Resin B, which was maintained in a laboratory environment (Figure 13c) did not present major changes in its mechanical properties (reduction of only about 3.1% of tensile strength) up to 4 months of exposure. However, after 8 months, there was a considerable reduction of 23.8% and 19.2% in tensile strength and modulus of elasticity, respectively. This reduction in tensile strength and modulus of elasticity did not alter the behavior of the stress-strain diagram, and the maximum stress level continued to be reached with close deformations. At 7 days of cure, the tensile strength was already close to that obtained in the complete cure indicated by the manufacturer (14 days). For Resin B's exposure to weather (Figure 13d), the stress-strain diagrams did not present major changes at 7 and 14 days, only a small increase in the maximum tension. After 4 months, there were remarkable losses in its mechanical properties, with a reduction in its tensile strength and modulus of elasticity of 63.3% and 9.1%, respectively. At 8 months, the maximum tensile strength decreased sharply (about 69.2%), while the modulus of elasticity showed a reduction of 18.2%. Observed, also, the reduction of ductility for both ages of exposure with alteration in the mode of rupture, which occurs abruptly and without any stretch of plasticization. Unlike Resin A, Resin B yielded a considerable loss in its mechanical properties after 8 months of exposure to the laboratory environment. Another divergence found in the epoxy resins is related to their mechanical properties at 14 days of curing. It was noted that both the tensile strength and modulus of elasticity of Resin B were higher (about 16%) than those of Resin A despite the equivalent curing time.

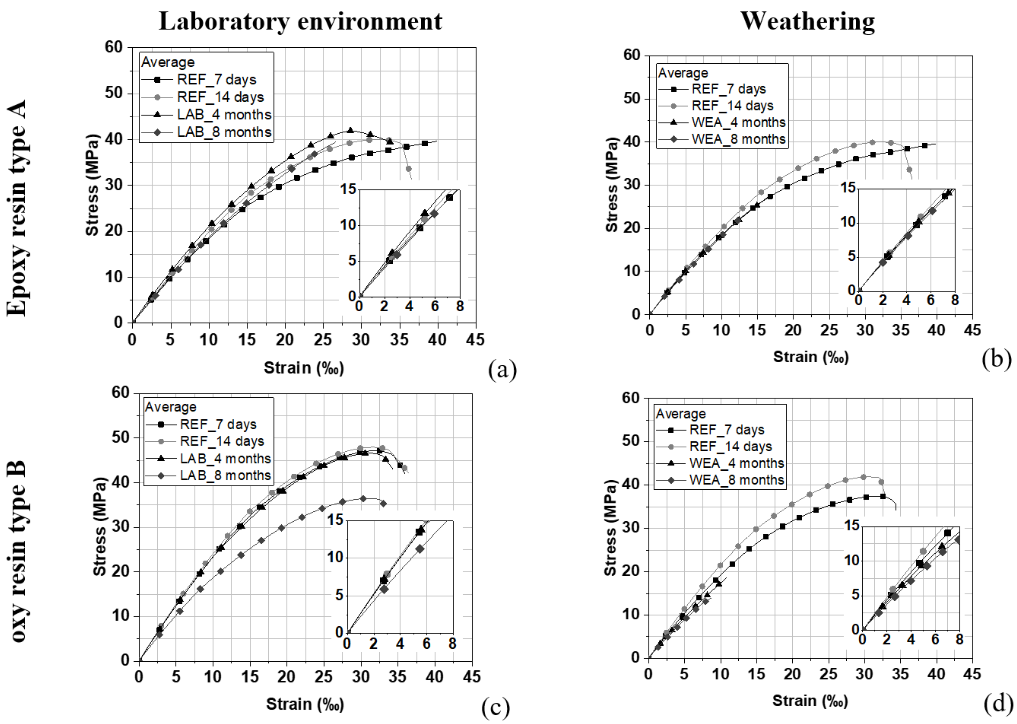

Figure 13. Stress versus strain relationship of primer (a-b) and saturation (c-d) resins maintained in a laboratory environment or exposed to weathering

In a study carried out by Fernandes et al. [25], epoxy resins were also kept in a laboratory environment for a period of 2 years. The results, as in the present study, also showed small reductions in their mechanical properties, specifically 5.5% and 6.9% in tensile strength and modulus of elasticity, respectively. The findings for the epoxy saturation resins (Resin B) exposed to weather were also verified in a research conducted by Escobal [26]. The author evaluated the degradation of epoxy saturation resins exposed to weather (external environment with monitored temperature and humidity) for a total period of 4 months. The results showed losses of 44% in tensile strength after 4 months of exposure. Escobal [26] also evaluated the same epoxy resins exposed to accelerated aging cycles, contained by UV radiation, temperature of 60ºC, and water vapor at 50ºC. The results showed a considerable reduction in the tensile strength of the resins (about 60%), as verified in the present work for resins A and B exposed to the weather. The results found by Zhao et al. [15] were also similar to those in this study. The authors evaluated epoxy resin specimens exposed to UV radiation cycles (simulating exposure in an external environment) for a period of 90 days. At the end of the trials, the authors verified a maximum reduction of 20.4% in the modulus of elasticity of the specimens.

4.2.4 CFRP composites

For CFRP composites (Figures 14a, 14b), the specimens presented a linear elastic behavior until their rupture, typical of fragile materials. Regarding their exposure to the laboratory environment (Figure 14a), a more significant variation was seen in the behavior of the specimens after the ages of 4 and 8 months. Further, a greater reduction in the tensile strength of the specimens occurred after 4 months of exposure (reduction of about 15% of tensile strength). During this same period, there was a small reduction of 1.73% in the modulus of elasticity. After 8 months of exposure, the CFRP composite specimens gained resistance and showed a lower loss in tensile strength, at about 11%, while the modulus of elasticity reduced by only 3.3%. The last deformation also showed reductions of 14% and 7% over 4 and 8 months' exposure to the laboratory environment, respectively. It was verified that a greater loss occurred in the test performed at 4 months.

For weather exposure (Figure 14b), and taking as reference the tests performed at 14 days, a reduction in tensile strength, modulus of elasticity, and last deformation of 18%, 4.9%, and 13.3%, respectively, after 4 months of exposure was verified. At the age of 8 months, the specimens of the CFRP composite presented reductions of 1.4%, 1.3%, and 0.7% in tensile strength, modulus of elasticity, and last deformation, respectively. Once again, there was a significant variation in the behavior of the samples for the analyzed ages. Although the properties of CFRP composites present reductions over exposure time, these oscillations do not mean that the material has degraded. Therefore, it is important to verify the coefficient of variation in the properties of the samples, which, as mentioned before, present considerable variation.

Cromwell et al. [27] also found that the exposure of CFRP laminates to aggressive environments, such as constant humidity and saline solution, does not cause major changes in their tensile strength and modulus of elasticity or ultimate deformation.

In another research by Dalfré [28], there was no significant change in tensile strength and modulus of elasticity of CFRP composite specimens exposed to cycles of constant humidity and humidity for a total period of 2 years.

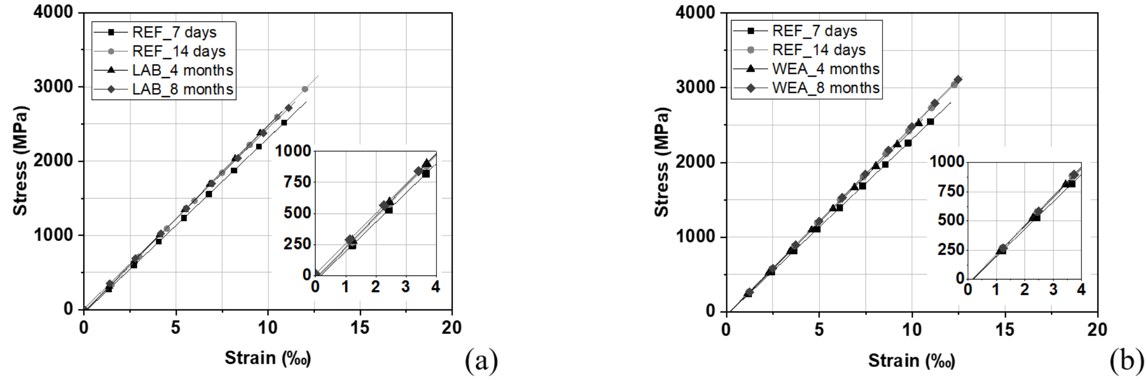

Figure 14. Stress versus strain relationship of CFRP composites maintained in laboratory environment (a) or exposed to weathering (b)

4.2 Concrete beams behavior

The behavior of the reinforced concrete beams (with and without strengthening) exposed to the laboratory environment and weathering was analyzed based on ductility, increased load capacity, deformation of materials (concrete, steel, and CFRP), and rupture mode of the strengthening system.

The stop criterion adopted for the reference beams tests without strengthening was established in terms of the deformation of the bending strengthening (at the time the deformation in the steel reached the average value of 11‰), while that adopted in the reinforced beams of reference and exposed in laboratory environment and weather was established in terms of the failure of the strengthening system, followed by a sudden loss of load and detachment of the material.

Table 4 presents a summary of the average results obtained in the tests of the beam sets for the yielding of the steel reinforcement (ε_{sy}), for the concrete crushing ($\varepsilon_{c,esm}$), and the instant that the beams reach maximum loading ($F_{\max}$). The indicator of effectiveness of the bending strengthening system in terms of increased load capacity (IR) is also presented, which was obtained by analyzing the average load ($F = (F_{V1} + F_{V2})/2$) recorded for the beams without strengthening and strengthened (reference and exposed to the environments), respectively.

Table 4 Resume of the average experimental results

Group of beams	Yielding of the steel reinforcement (ε_{sy})					Concrete crushing ($\varepsilon_{c,esm}$)					Maximum force recorded					
	F_{sy} kN	u_{sy} mm	ε_c ‰	$\varepsilon_{f,\max}$ ‰	IR %	$F_{c,esm}$ kN	u_{esm} mm	ε_{sy} ‰	$\varepsilon_{f,\max}$ ‰	IR %	$F_{\max}$ kN	$u_{F\max}$ mm	ε_c ‰	ε_s ‰	$\varepsilon_{f,\max}$ ‰	IR %
REF_0	21.8	10.3	1.8	----	----	25.4	15.6	5.2	----	----	27.0	25.2	6.1	11.4	----	---
REF_CFRP	26.1	9.3	1.8	2.9	19.7	31.5	13.3	5.5	----	24.0	40.6	32.7	9.8	13.5	9.9	50.0
LAB_CFRP	22.8	8.6	1.2	3.1	4.6	25.4	16.0	8.3	----	0.0	38.0	39.9	3.2	17.4	----	40.7
WEA_CFRP	23.9	9.0	*	2.9	9.6	----	----	----	----	----	36.5	32.5	----	11.6	----	35.1

*Mechanically damaged strain gauge

In order to evaluate the effectiveness of the strengthening system with CFRP sheets applied according to the EBR technique, Figure 15 presents a comparison between the Load and vertical displacement of the reference beams without strengthening (V1_REF_0 and V2_REF_0) and strengthened (V1_REF_CFRP and V2_REF_CFRP). Upon analysis of Table 4 and Figure 15, it is possible to verify the effectiveness of the CFRP EBR strengthening system for the reinforced beams without strengthening and the increase in the load capacity of the strengthened beams.

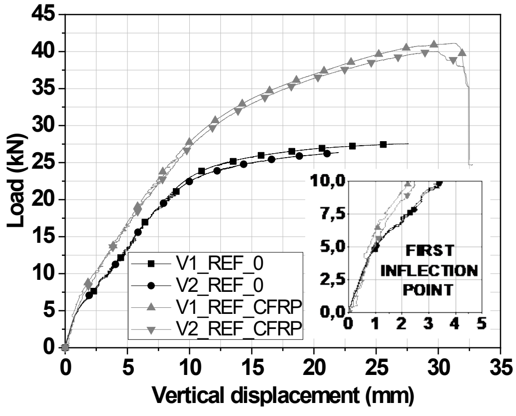

Figure 15. Load versus displacement of reference beams without strengthening and strengthened

In relation to the beginning of the steel yield, it was verified that the strengthening provided an increase in the load capacity corresponding to the beginning of the longitudinal steel yielding and the maximum force of 19.7% and 50%, respectively. In addition, a reduction in the average vertical displacement of 9.7% for the strengthened reference beams, compared to the reference beams without strengthening due to the reduction of cracking that the strengthening system promotes, restricting the reduction of element inertia was observed.

As failure modes, the reference beams without strengthening, V1_REF_0 and V2_REF_0, designed in Domain 2, presented a ductile rupture characterized by the yielding of the longitudinal tensile reinforcement and later crushing of the compressed concrete. All the strengthened beams (V1_y_CFRP and V2_y_CFRP), after great deformation and high curvature of the elements, showed appearances of cracks parallel to the strengthening material in the moments before the failure of the element. Therefore, it appears that the use of the CFRP EBR strengthening system alters the failure mode of the strengthened elements. The failure, which was previously ductile and ruled by the deformation of the longitudinal strengthening, became almost fragile with the detachment of the CFRP sheet adhered to the concrete substrate. Figure 16 presents a comparison between Load and vertical displacement relationship of the reference beams without strengthening (V1_REF_0 and V2_REF_0) and strengthened (V1_REF_CFRP and V2_REF_CFRP), with those exposed in laboratory environment (V1_LAB_CFRP and V2_LAB_CFRP) and to weathering (V1_WEA_CFRP and V2_WEA_CFRP), respectively.

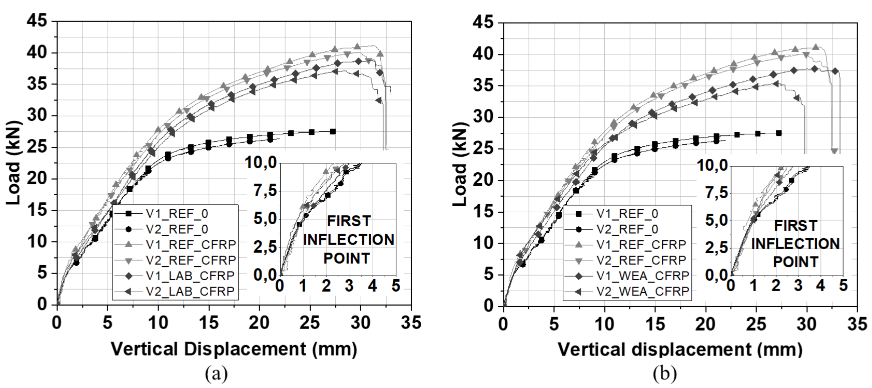

(a) (b)

Figure 16. Relationship between Load versus vertical displacement of reference beams exposed to the environments: (a) laboratory and (b) weathering

For the yielding of the steel reinforcement of the strengthened beams maintained in laboratory environment or exposed to weathering, an average increase in load capacity of 4.6 and 9.6%, respectively, was observed in relation to the yielding of the steel in the beams without strengthening. For the maximum strength, an average increase in load capacity of 40.7 and 35.1% in the reference beams without strengthening (REF_0), respectively, was observed. Analyzing the yielding of the steel reinforcement of the exposed beams and considering the results obtained in the tests of the strengthened reference beams (REF_CFRP), it was noted that the elements maintained in laboratory environment and exposed to weathering presented a reduction of the average load of 12.6 and 8.4%, respectively. It was also observed that the maximum force recorded in the strengthened beams exposed to weathering suffered a reduction of 6.4 and 10.0%, respectively, when exposed to the environments previously presented. Finally, taking into account the maximum force recorded in the tests with the strengthened beams (Table 4), exposure to weather was more aggressive for the strengthening system, since its ultimate load was lower than that of the elements maintained in laboratory environment.

Concerning the failure load of the strengthened elements exposed to the environments, it was verified that there were no changes comparing it to the strengthened reference beams, presenting an almost fragile failure, preceded by pops and a lower load than verified for the strengthened reference beams, with the detachment of the CFRP sheet adhering to the concrete substrate (Figure 17).

Figure 17. Verified failure mode on the strengthened beams

5 CONCLUSIONS

This work reports findings from an experimental program conducted to evaluate the efficiency of the EBR technique in increasing the load capacity of reinforced concrete beams strengthened in flexure with CFRP composites and also to evaluate the behavior of EBR-CFRP strengthening systems when exposed to weathering. Two exposure environments were adopted in this study (laboratory and weathering). Beams maintained in laboratory condition for 200 days, with and without strengthening, were considered as reference (REF), while the remaining beams were exposed to degradation environments and tested at the age of 380 days. The results obtained allowed for the following conclusions to be obtained:

- The efficiency of the EBR technique in increasing the load capacity of bending reinforced concrete beams with CFRP sheets was verified by means of significant increases in the load capacity of the strengthened elements. In relation to the steel reinforcement yielding, it was verified that the strengthening provided an increase in the load capacity corresponding to the beginning of the longitudinal strengthening yield and the maximum force of 19.7% and 50%, respectively. In addition, there was a reduction in the average vertical displacement of 9.7% for strengthened reference beams, compared to those without strengthening, respectively, due to the reduction of cracking that the strengthening system promotes, restricting the reduction of the element's inertia;
- Analyzing the beginning of the steel yielding of the exposed beams and taking into account the results obtained in the tests of the strengthened reference beams (REF_CFRP) showed that the elements exposed to the laboratory environment and those exposed to weathering presented a reduction in the average load at steel yielding of 12.6 and 8.4%, respectively. It is also possible to observe that the maximum force recorded in the strengthened beams exposed to these environments suffered a reduction of 6.4 and 10.0%, respectively.
- Moreover, it was noted that the evolution of the curing time from 7 to 14 days of the primer and saturation epoxy resins maintained in laboratory environment resulted in statistically equivalent values, i.e., the curing time affected neither the mechanical properties of the specimens nor the behavior of the stress-deformation diagram.

- Also, in relation to the epoxy resins maintained in laboratory environment, it was observed that the saturation resin presented losses of 23.8% and 19.2%, respectively, in tensile strength and modulus of elasticity after 8 months of exposure in addition to an alteration in the failure mode, while the primer resin's properties remained statistically unchanged.
- The analysis of primer epoxy resin exposed to weathering was observed for the tests performed after 4 and 8 months of exposure reductions of 39 and 50% of tensile strength, respectively, in addition to the change in the failure mode of the specimens, while the modulus of elasticity resulted in statistically equivalent values.
- From the analysis of the saturation epoxy resin exposed for 4 and 8 months to the weathering, it was found that the tensile strength reduced by about 64 and 70%, respectively, from the reference condition with 14 days of cure, and the failure mode changed from ductile to fragile without a plasticization interval. Regarding the modulus of elasticity, it was observed that the values were statistically similar up to 4 months of exposure, but after 8 months, a reduction of 18.2% in the modulus of elasticity was verified, as compared to the reference condition.
- The CFRP composites exposed to the laboratory environment and weathering showed no increase in their mechanical properties over the temporal evolution of the curing time from 7 to 14 days, and the results of the tests were statistically equivalent.

ACKNOWLEDGEMENTS

The authors wish to thank Polymer Laboratory of the Department of Materials Engineering (DEMa) and Structural Systems Laboratory (LSE) of the Federal University of São Carlos (UFSCar) for allowing us to conduct the tests for this research. We are also grateful to Coordination for the Improvement of Higher Education Personnel (CAPES) for their support in carrying out this study.

REFERENCES

[1] V. J. Ferrari, I. J. Padaratz, and D. D. Loriggio, "Reforço à flexão em vigas de concreto armado com manta de fibra de carbono: mecanismos de incremento de ancoragem," *Acta Scientiarum*, vol. 24, no. 6, pp. 1783–1791, 2002.

[2] Y. T. Obaidat, S. Heyden, O. Dahlblom, G. Abu-Farsakh, and Y. Abdel-Jawad, "Retrofitting of reinforced concrete beams using composite laminates," *Constr. Build. Mater.*, vol. 25, pp. 591–597, 2010.

[3] A. P. Machado and B. A. Machado, *Reforço de Estruturas de Concreto Armado com Sistemas Compostos FRP*. São Paulo: Pini, 2015.

[4] M. Long, C. Djelal, S. Kesteloot, B. Bigourdan, P. Y. Le Gac, and J. Szulc, "Durability of CFRP concrete bonding in a marine environment," in *Proc. Eur. Conf. Compos. Mater.*, Venice, Italy, 2012.

[5] J. A. Barros, "Materiais compósitos no reforço de estruturas de betão – parte I: propriedades e técnicas," *Constr. Mag.*, vol. 22, pp. 26–35, 2007.

[6] J. R. Silva, "Reforço híbrido à flexão de vigas "T" de concreto armado com compósitos de fibras de carbono e fibras de vidro," Ph.D. dissertation, Dept. Struct. Civ. Constr., Univ. Brasilia, Brasília, 2014.

[7] C. Czaderski and U. Meier, "EBR strengthening technique for concrete long-term behaviour and historical survey," *Polymers*, vol. 10, no. 1, pp. 77–94, 2018.

[8] L. F. P. Juvandes, "Aplicações de compósitos FRP no reforço de estruturas," in *Proc. 1st Construct.Mater. Days*, 2011, pp. 239–270. https://goo.gl/AGJQ42 (accessed Sep. 19, 2018).

[9] V. M. Karbhari, *Durability of Composites for Civil Structural Applications*. Cambridge: Woodhead, 2007.

[10] H. V. S. Gangarao, N. Taly, and P. V. Vijay, *Reinforced Concrete Design with FRP Composites*. Boca Raton: Taylor & Francis, 2007.

[11] American Concrete Institute, *Guide to Accelerated Conditioning Protocols for Durability Assessment of Internal and External Fiber-Reinforced Polymer (FRP) Strengthening*, ACI Committee 440.9R, 2015.

[12] ISIS, *Durability of FRP Composites for Construction – The Canadian Network of Centers of Excellence on Intelligent Sensing for Innovative Structures* (Educational Module 8). Manitoba, Canada: ISIS Canada Corp., 2006.

[13] M. M. Shokrieh and A. Bayat, "Effects of ultraviolet radiation on mechanical properties of glass/polyester composites," *J. Compos. Mater.*, vol. 41, no. 20, pp. 2443–2455, 2007.

[14] M. C. Oliveira, "Análise do comportamento estrutural e durabilidade de pilares de concreto armado reforçados com mantas de GFRP," M.S. thesis, Dept. Civ. Eng., Fed. Univ. São Carlos, São Carlos, 2019.

[15] J. Zhao, G. Cai, L. Cui, A. Si Larbi, and K. D. Tsavdaridis, "Deterioration of basic properties of the materials in FRP-strengthening RC structures under ultraviolet exposure," *Polymers*, vol. 9, no. 12, pp. 402, 2017.

[16] S. M. Homam and S. A. Sheikh, "Durability of fiber reinforced polymers used in concrete structures," in *Proc. 3rd Int. Conf. Adv. Mater. Bridges Struct.*, Ottawa, Ontario, Canada, 2000, pp. 751–758.

[17] M. I. Kabir, R. Shrestha, and B. Samali, "Experimental study on durability of CFRP-concrete bond subjected to temperature, humidity and outdoor environment," in *Proc. 4th Asia-Pacific Conf. FRP in Struct.*, Melbourne, Australia, Dec. 2013, pp. 11–13.

[18] C. A. Alvares, J. L. Stape, P. C. Senthelas, J. L. M. Goncalves, and G. Sparovek, "Köppen's climate classification map for Brazil," *Meteorol. Z.*, vol. 22, no. 6, pp. 711–728, 2013.

[19] Empresa Brasileira de Pesquisa Agropecuária. "Meteorologia." Embrapa. http://www.cppse.embrapa.br/meteorologia/index.php?pg=caracterizacao (accessed Nov. 15, 2019).

[20] Wikipedia. https://pt.wikipedia.org/wiki/Clima_subtropical_%C3%BAmido#/media/File:K%C3%B6ppen_World_Map_Cfa_and_Cwa_(Humid_subtropical).svg (accessed July 16, 2019).

[21] Associação Brasileira de Normas Técnicas, *Projeto de Estruturas de Concreto – Procedimento*, NBR 6118, 2014.

[22] Associação Brasileira de Normas Técnicas, *Concreto – Procedimento para Moldagem e Cura de Corpos de Prova*, NBR 5738, 2015.

[23] D. C. Ferreira, "Avaliação da degradação de vigas reforçadas com FRP quando expostas ao intemperismo," M.S. thesis, Dept. Civil Engineering, Fed. Univ. São Carlos, São Carlos, 2019.

[24] Associação Brasileira de Normas Técnicas, *Materiais Metálicos – Ensaio de Tração*, NBR 6892-1, 2018.

[25] P. Fernandes, P. Silva, L. Correia, and J. Sena-Cruz, "Durabilidade de um adesivo epóxi e um laminado de CFRP expostos a distintas condições ambientais," in *Proc. 3rd Semin. Proj. Reinforce Concr. Struct. FRPs*, 2015, pp. 8–14.

[26] A. D. Escobal, *Caracterização da Degradação de Adesivos Estruturais Utilizados em Sistemas de Reforço de Estruturas de Concreto Armado*. São Carlos: Sci. Initiation Res. Project, 2016.

[27] J. R. Cromwell, K. A. Harries, and B. M. Shahrooz, "Environmental durability of externally bonded FRP materials intended for repair of concrete structures," *Constr. Build. Mater.*, vol. 25, no. 5, pp. 2528–2539, 2010.

[28] G. M. Dalfré, *Estudo da Degradação da Aderência de Compósitos Colados a Superfícies de Concreto Armado Quando Submetidos a Ciclos de Umidade e Carbonatação*, Universal Project, CNPq 483720/2013-5, 2016.

Author contributions: GMD, GAP: conceptualization, supervision, writing; DCF: experimental program, data analysis.

Editors: Maurício de Pina Ferreira, José Luiz Antunes de Oliveira e Sousa.

Rev. IBRACON Estrut. Mater., vol. 14, no. 2, e14209, 2021

IBRACON Structures and Materials Journal
Revista IBRACON de Estruturas e Materiais
ISSN 1983-4195 ismj.org

ORIGINAL ARTICLE

Corrosion evaluation of CA-50 steel in pore waters extracted from cement pastes with steel slags using electrochemical techniques

Avaliação da corrosão do aço CA-50 em meios de águas de poro extraídas de pastas de cimento com escórias de aciaria usando técnicas eletroquímicas

Renan Esposito Vieira[a]
Marina Martins Mennucci[b]
Valdecir Angelo Quarcioni[c]
Hercílio Gomes de Melo[b]

[a]Universidade de São Paulo (USP), Escola Politécnica, Departamento de Engenharia Química, São Paulo, SP, Brasil
[b]Universidade de São Paulo (USP), Escola Politécnica, Departamento de Engenharia Metalúrgica e de Materiais, São Paulo, SP, Brasil
[c]Instituto de Pesquisas Tecnológicas do Estado de São Paulo (IPT), Laboratório de Materiais de Construção Civil, São Paulo, SP, Brasil

Received 14 January 2020
Accepted 08 July 2020

Abstract: There is an interest in the cement industry in the use of steel slags in cement, but chemical and/or pyrometallurgical modifications are necessary to reduce the free CaO, MgO, and iron contents. However, the potential effects of its application in the reinforcement corrosion, whether in solid (concrete) or liquid medium (pore water), have not yet been addressed. In this context, the present study shows a corrosion analysis of the CA-50 steel in pore water medium extracted from cement pastes with 25% by weight of steel slag, in natural state or pyrometallurgical modified, by means of polarization curves, electrochemical impedance spectroscopy (EIS), and microstructural analysis. For comparison, tests were performed in pore waters presented in literature and representative from Ordinary Portland Cement (OPC) or activated Blast Furnace Slag (BFS) and, to simulate aggressive conditions, 1.0% NaCl was also added to the solutions. The steel remained passive in all media without 1.0% NaCl, but the EIS results indicated more protective characteristics in the medium simulating the modified steel slag. The main corrosion product identified by SEM images after the tests on aggressive media was lepidocrocite (γ-FeOOH), and the steel did not corrode in media with steel slags and 1.0% NaCl. This was attributed mainly to the higher alkalinity of these media in comparison to other usual pore waters, promoting longer protection of the steel.

Keywords: pore water, corrosion, steel slag, electrochemical impedance spectroscopy.

Resumo: Existe interesse na indústria cimenteira no uso de escórias de aciaria em cimento, porém são necessárias modificações químicas e/ou pirometalúrgicas para redução dos seus teores de CaO e MgO livre e de ferro. Entretanto, ainda não se abordaram os potenciais efeitos de sua aplicação na corrosão de armaduras, seja em meios sólidos (concreto endurecido) ou líquidos (águas de poro). Nesse contexto, o presente estudo apresenta a análise da corrosão do aço CA-50 em meios de águas de poro extraídas de pastas de cimento com 25% em massa de escória de aciaria (in natura ou modificada pirometalurgicamente) através de curvas de polarização, espectroscopia de impedância eletroquímica (EIE) e análises microestruturais. Para comparação, foram realizados ensaios em águas de poro de composições especificadas na literatura para cimento Portland comum e de escória de alto forno ativada com cimento, e posteriormente adicionou-se 1,0% de NaCl às soluções para simular agressividade. O aço se manteve passivo em todos os meios sem 1,0% de NaCl, porém os resultados de EIE indicaram características mais protetoras no meio representativo de escória de aciaria modificada. O principal produto de corrosão identificado pelas micrografias do aço após os ensaios nos meios agressivos foi a lepidocrocita (γ-FeOOH), e não houve corrosão do aço nos meios com escórias de aciaria e 1,0% de NaCl. Isso foi atribuído principalmente à maior alcalinidade destes meios em comparação com outras águas de poro convencionais, o que promoveu proteção mais prolongada do aço.

Palavras-chave: água de poro, corrosão, escória de aciaria, espectroscopia de impedância eletroquímica.

Corresponding author: Renan Esposito Vieira. E-mail: revieira92@gmail.com.
Financial support: None.
Conflict of interest: Nothing to declare.

How to cite: R. E. Vieira, M. M. Mennucci, V. A. Quarcioni, and H. G. Melo, "Corrosion evaluation of CA-50 steel in pore waters extracted from cement pastes with steel slags using electrochemical techniques," *Rev. IBRACON Estrut. Mater.*, vol. 14, no. 2, e14209, 2021, https://doi.org/10.1590/S1983-41952021000200009

1 INTRODUCTION

The use of additions in Portland cement brings benefits to the cement industry, as it allows a great reduction of CO_2 emissions from the process and resources used in manufacturing. Among the most common addition is blast furnace slag, which is a byproduct of the manufacture of pig iron in the steel process and whose chemical composition of oxides is very similar to that of Portland cement (rich in CaO, SiO_2, and Al_2O_3), attributing good hydrological characteristics to the material [1]. As blast furnace slag, steel slag is a byproduct of the refining and steelmaking stage, and also has reactive oxides of Portland cement in its composition. However, the high contents of CaO and free MgO, as well as the presence of inert phases (such as the "RO phase", which is a solid solution of CaO, MgO, FeO, and MnO that promotes expansion in hardened cement) and considerable amounts of iron oxides, lead to the need for modifications by chemical or pyrometallurgical processes, as employed by authors in the literature [2]–[6], to allow the addition of higher contents in cement maintaining stability. The authors who used modified steel slag in their tests registered benefits, especially in mechanical terms, for the cement composite, which increases the interest in its application [2]–[6].

Generally, the literature focuses on studies of chemical, physical, and mechanical properties of cement composites with steel slag, not addressing the interactions and potential effects of this addition on the performance of concrete reinforcement. This analysis can be performed in solid media (involving tests with embedded reinforcement in mortar or concrete) or liquid media (tests on metals immersed in pore water). In the case of pore water media, Hooton et al. [7] pointed out that the extraction and analysis of this fluid from hardened cementitious materials has become, in recent times, a tool of great relevance and application in durability studies, once the correlation between the chemical composition of pore water and the solid phases of hardened material allows the prediction of phenomena that directly influence their behavior. For the specific case of reinforcement corrosion studies, pore water is easier to perform since it does not require the molding of specimens, and has, therefore, been used by several authors [8]–[15]. These tests are able to present coherent results in relatively short periods due to the good simulation of the alkalinity of the concrete interior.

Pore water is present in pores larger than 50 Å in diameter of the hardened composite and is free from physical influences of the solid, not yet reacted and in direct contact with the reinforcement [16]. This fluid provides a great deal of information about the hydration of the material, the influence of the presence of additions and additives in the cement, aspects of alkali-aggregate reactions, alkali-silica, among many others [17]. Its extraction does not present any standardized procedure, and the best known and applied method in the literature is that of extraction by "application of triaxial pressure induced by force on the top of cylindrical specimens" [17]–[20]. The apparatus for this procedure is designed with defined parameters and materials, so that it supports several loads on the specimen. Such apparatus was initially presented by Barneyback and Diamond [18], and, in this study, the extractor used is similar to that of Oliveira [17], presented in Figure 1.

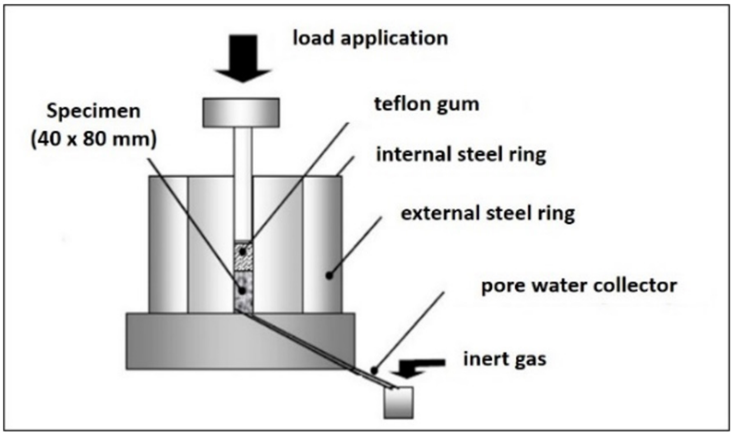

Figure 1. General scheme of the pressure pore water extractor used in this study. **Source:** Oliveira [17].

The pore water used in reinforcement corrosion studies is generally a mix of calcium, sodium, and potassium hydroxides in specific relations that result in high pH solutions. Authors such as Chen et al. [12], Koleva et al. [13], and Liu et al. [15] defended the feasibility of carrying out the studies in these liquid media, but indicating that their results are approximate for cement systems. In these studies, it is also common the use of electrochemical techniques such as the determination of Open Circuit Potential (OCP), polarization (linear or potentiodynamic), and electrochemical impedance spectroscopy (EIS). In the case of EIS, studies published by Sánchez et al. [10], Zhang et al. [11], and Liu et al. [15] presented relevant results and proved their efficacy for the analysis of passivation and corrosion of reinforcement immersed in pore waters. Sánchez et al. [10] studied the passivation mechanism for low carbon steel in pore water mainly through the results of EIS fitted by equivalent electrical circuits (EEC) and found important differences in the mechanisms related to different ages and spontaneous or potential induced growth of the passive layer. It was verified that there is a predominant diffusion control in the passivation for some ages and conditions, besides the surface charge transfer inherent to the system, which was evidenced by the obtained Nyquist diagrams from these tests. Zhang et al. [11] were able to discuss the differences between the influence of pH and chloride content variations in the medium for the passivation and corrosion of low carbon steel. The significant influence of the chloride content on the behavior of these steels was also confirmed by Liu et al. [15] in their study through EIS.

Considering the context, the present study investigated the passivation and corrosion of CA-50 steel in pore water media extracted by pressure from cement pastes with steel slag, in a natural state or modified by a pyrometallurgical process (for cement application), by means of electrochemical techniques (polarization curves and EIS) and microstructural analysis. In addition, tests were also performed in two pore waters extracted by Oliveira [17] from common Portland cement and activated blast furnace slag with cement pastes. The effect of chloride on the corrosion resistance of the material was evaluated by adding 1.0% NaCl to pore waters with different compositions, and this percentage was selected considering that the Atlantic Ocean has a salinity of approximately 3.5% [21]–[23] and the accelerated test literature varies the aggressiveness from 0.4% to 10% [8]–[13], [24].

2 MATERIALS AND EXPERIMENTAL PROGRAM

For the tests, specimens with 8 mm diameter and 10 mm long were cut from a CA-50 steel bar, and embedded in bakelite. The chemical composition of CA-50 steel determined by induction coupled plasma optical emission spectroscopy (ICP-OES) is shown in Table 1.

Table 1. Approximate composition of CA-50 steel.

Iron (Fe)	Carbon (C)	Manganese (Mn)	Phosphorus (P)	Silicon (Si)	Sulfur (S)
99.0%	0.18%	0.59%	0.02%	0.20%	0.02%

Source: Results obtained by the Laboratório de Processos Metalúrgicos / IPT.

Initially, two synthetic pore waters were prepared according to the compositions determined by Oliveira [17] and which are representative of common Portland cement paste (“AP1”, “Pore Water 1”) and cement activated blast furnace slag paste (“AP2”, “Pore Water 2”). For reference, consider Table 2 with the chemical compositions of these materials used by Oliveira [17].

Table 2. Chemical characterization of Portland Cement V - High Initial Resistance (CPV-ARI) and blast furnace slag used by Oliveira [17] (% by mass).

						CPV-ARI cement (classic way)						
CaO	**SiO_2**	**Al_2O_3**	**MgO**	**Fe_2O_3**	**LI**	**IR**	**CO_2**	**SO_3**	**S^{2-}**	**Na_2O**	**K_2O**	**CaO_f**
65.6	19.2	4.98	0.36	3.17	n.d.	n.d.	1.76	2.96	n.d.	0.02	0.57	n.d.
						CPV-ARI cement (flame photometry)						
					Na^+	K^+						
					0.006	0.303						
						Blast furnace slag (classic way)						
CaO	SiO_2	Al_2O_3	MgO	Fe_2O_3	LI	IR	CO_2	SO_3	S^{2-}	Na_2O	K_2O	CaO_f
42.47	33.78	13.11	7.46	0.51	1.67	0.53	1.18	0.15	1.14	0.16	0.32	0.1
						Blast furnace slag (flame photometry)						
					Na^+	K^+						
					0.004	0.001						

n.d. – not determined. Source: Oliveira [17].

1.0% NaCl was added to the prepared pore water, resulting in "AP1 + 1.0% NaCl" and "AP2 + 1.0% NaCl" solutions, and, for reference, a 1.0% NaCl solution was also used. After this step, pore water was obtained by pressure extraction of cement pastes with 25% by mass of steel slag, either in natura (EA) or modified by pyrometallurgical process (EAm). The characterizations of CP V-ARI cement and steel slag obtained by X-ray Fluorescence (XRF) and other wet method are presented in Table 3.

Once the mixtures (named "75CPV25EA" for the mix of CP V-ARI with 25% EA and "75CPV25EAm" for the mix of CP V-ARI with 25% EAm) were prepared, cylindrical specimens with 40 mm diameter and 80 mm height were molded, according to geometric requirements of the extractor used in the study (Figure 1), with a water/cement ratio of 0.5, which were cured for three days at a temperature of (23 ± 2) °C and relative humidity of 95%. After this period, the specimens were demolded and taken for pore water extraction, which was performed by applying a load of 450 MPa at a rate of 2.5 MPa s^{-1}.

Table 3. Chemical characterization of Portland cement and steel slag (%).

High Initial Resistance Portland Cement (CP V-ARI)													
CaO	**SiO_2**	**Al_2O_3**	**MgO**	**Fe_2O_3**	**Others** (1)	**LI** (2)	**IR** (2)	**CO_2** (2)	**SO_3** (2)	**S^{2-}** (2)	**Na_2O** (2)	**K_2O** (2)	**CaO_f** (2)
63.3	19.3	4.81	1.18	2.60	0.55	2.67	0.28	1.45	4.26	nd	0.49	0.95	1.85
In natura (EA) and pyrometallurgical modified (EAm) steel slag													
%	CaO	S	SiO_2	Al_2O_3	MgO	MnO	P_2O_5	Fe_2O_3	K_2O	Others (3)	FeO (4)	Fe^0 (4)	CaO_f (2)
EA	37.7	0.03	10.3	2.58	9.44	4.12	1.15	11.3	0.95	0.58	19.4	0.40	5.71
EAm	34.3	0.05	30.7	11.7	9.10	3.70	0.95	1.22	0.38	0.46	7.50	0.40	0.21

nd – not detected. (1) Others: TiO_2, Cr_2O_3, Mn_2O_3, SrO, ZnO, P_2O_5. (2) Parameters are determined according to current technical standards of the classic Portland cement way. LI - Loss to Ignition; IR - Insoluble Residue; CaO_f - Free CaO. (3) Others: TiO_2, Cr_2O_3, SrO, ZnO. (4) Parameters are determined according to wet method procedures. Fe_0 - metallic iron. Source: Results obtained by the Laboratório de Materiais de Construção Civil / IPT.

After extraction, the fluids were stored in hermetically sealed plastic flasks and taken immediately for determination of pH and volume extracted. Then, a volume (0.5 mL or 1.0 mL) was diluted to 10 mL and acidified with HNO_3 for further determination of Ca^{2+}, Na^+, and K^+ ions (by atomic absorption spectroscopy, AAS), OH^- (by direct calculation from pH) and Cl^- (by ion chromatography). The pore water was characterized and extracted in duplicates and, with the results, synthetic compositions were prepared with $Ca(OH)_2$, NaOH, and KOH. As for AP1 and AP2 solutions, 1.0% of NaCl was also added to the pore water to simulate aggressiveness.

Considering the procedure presented and the results obtained for the extracted pore water compositions, which will not be discussed in the present work, Table 4 summarizes the composition and pH of the pore water used for the electrochemical tests.

Table 4. Compositions and pH of the pore water of the study.

Solutions / Reagents	**$Ca(OH)_2$**	**NaOH**	**KOH**	**NaCl**	**pH**
Pore Water 1 (AP1) (1)	Sat.(2)	0.004%	0.10%	-	12.6
Pore Water 1 + 1.0% NaCl (AP1 + NaCl)				1.0%	12.5
Pore Water 2 (AP2) (1)	Sat.(2)	0.20%	0.20%	-	12.9
Pore Water 2 + 1.0% NaCl (AP2 + NaCl)				1.0%	12.8
Pore Water "75CPV25EA"	0.02%	0.53%	1.27%	0.01%	14.0
Pore Water "75CPV25EA + 1.0% NaCl"				1.0%	13.9
Pore Water "75CPV25EAm"	0.01%	0.62%	1.45%	0.01%	14.0
Pore Water "75CPV25EAm + 1.0% NaCl"				1.0%	14.0
1.0% NaCl Solution	-	-	-	1.0%	7.20

(1) Compositions obtained by Oliveira [17] and adopted for subsequent trials as references. (2) $Ca(OH)_2$ solubility at 25° C is 1.1 g L^{-1} [20].

The electrochemical tests were performed in a three-electrode cell with a platinum counter electrode, Ag/AgCl reference electrode saturated with KCl, and CA-50 steel embedded as a working electrode (0.50 cm^2). For all tests, the working electrodes were sanded with #320, #400, #600 and #1200 grain silicon carbide sandpaper.

- Potentiodynamic polarization: performed after one hour of OCP (Open Circuit Potential) stabilization. The cathodic and anodic curves were obtained with different electrodes, being the cathodic in the range of +0.01 V to -1.0 V and the anodic in the range of -0.01 V to +1.0 V, both ranges relative to OCP, or until the current density reaches $|10^{-3}|$ A cm^{-2}. The scan rate was 1.0 mV s^{-1}.
- Electrochemical Impedance Spectroscopy (EIS): the evolution of the impedance behavior was followed with the immersion time of CA-50 steel in 1 h, 3 h, 6 h, 9 h, 12 h, 24 h, 48 h, 72 h, and 120 h in the different pore waters without and with 1.0% chloride. The frequency range was 10^4 Hz to 10^{-2} Hz, at OCP, with a perturbation amplitude of 10 mV(rms) and eight measurements per decade of frequency. The pH of the solutions was also monitored over time.
- Scanning Electron Microscopy (SEM) and Energy Dispersion X-ray Spectroscopy (EDS): SEM micrographs were obtained from the specimens after anodic polarization tests on media containing 1.0% NaCl in a FEI Quanta 450 FEG equipment.

3 RESULTS AND DISCUSSIONS

Figure 2 shows the polarization curves obtained for CA-50 steel in pore water without (a) and with the addition of 1.0% NaCl (b). For these media, the cathodic curves were very similar, presenting the control regions by oxygen diffusion (from -0.7 V/Ag-AgCl and with |i| between 10^{-4} - 10^{-5} A cm^{-2}) and by hydrogen reduction (below -1.0 V/Ag-AgCl). According to Feng et al. [25] and Vago and Calvo [26], in alkaline media, the composition of the oxides formed on the surface of ferrous materials directly influences the evolution of the cathodic process, and it is suggested that such compositions, resulting from the reactions of oxygen, start to occur with greater intensity from -0.7 V/Ag-AgCl, which explains the behaviors verified in Figures 2a and 2b, in which the curves are dependent on the potential up to this value.

Unlike the cathodic branch, the anodic behaviors presented particular points. To assess the discussion, consider Table 5, which presents the electrochemical parameters obtained from the polarization curves of Figure 2. For the chloride-free media, Figure 2a, there is a little difference between the behaviors in the different solutions of pore water, and the curves for the media “AP1” and “AP2” showed slightly more polarized near the corrosion potential. However, the passive current densities for CA-50 steel were similar in all media, being slightly higher for “75CPV25EAm” pore water. Around +0.6 V/Ag-AgCl (Table 5), the sudden increase in current density observed for the experiments presented in Figure 2a is attributed to the evolution of oxygen [8], [12], [13], confirmed by the formation of bubbles on the surface of the working electrodes. Finally, it is highlighted that the integrity of the specimens was maintained, showing passive behavior in the pore water in the absence of chlorides.

In the case of Figure 2b, the addition of 1.0% NaCl had a significant influence on anodic behaviors, allowing to differentiate the corrosion resistance of CA-50 steel in the studied pore water solutions. In the “AP1” and “AP2” media (compositions in Table 4) [17], the anodic curves are characterized by a small passive region that extends up to approximately 0 V (Ag/AgCl), followed by a sudden increase in the current, characterizing the oxide layer breakdown and the beginning of localized corrosion.

The pitting and corrosion potentials and the corrosion current densities of these media are close and in the same order of magnitude (Table 5), indicating the proximity of steel performance, although the anodic curve in medium “AP1 + 1.0% NaCl” has shown to be more depolarized than in medium “AP2 + 1.0% NaCl”, indicating greater susceptibility to corrosion.

Still referring to the results presented in Figure 2b, when it comes to the steel slag with 1.0% NaCl media, a different anodic evolution between the two solutions can be observed. For the medium involving in natural slag, the anodic curve is more depolarized than in the modified slag medium, not allowing the precise definition of a passive current density, which indicates greater instability of the passive oxide layer in this medium. However, even considering this response, the steel remained passive until the evolution of oxygen in approximately +0.6 V/Ag-AgCl (Table 5). On the other hand, in the 75CPV25EAm + 1.0% NaCl pore water, the anodic polarization curve was quite similar to that obtained in the medium without chloride, indicating greater stability of the passive layer in this medium. Note that for the 75CPV25EAm + 1.0% NaCl anodic curve the increasing current density is also attributed to oxygen evolution.

Comparing the results of the anodic curves obtained in the pore water of common cement pastes (AP1 + 1.0% NaCl and AP2 + 1.0% NaCl) with those obtained in the pore water of slag cement pastes (“75CPV25EA + 1.0% NaCl” and “75CPV25EAm + 1.0% NaCl”), relevant differences are verified. As explained in the previous paragraph, the addition of 1.0% NaCl was not sufficient to promote localized corrosion of the steel in these two latter media, indicating that this content is still below the limit chloride concentration [12], [15]. This behavior may be directly related to the higher alkalinity of these pore water solutions (Table 4), helping to maintain the integrity of the passive film.

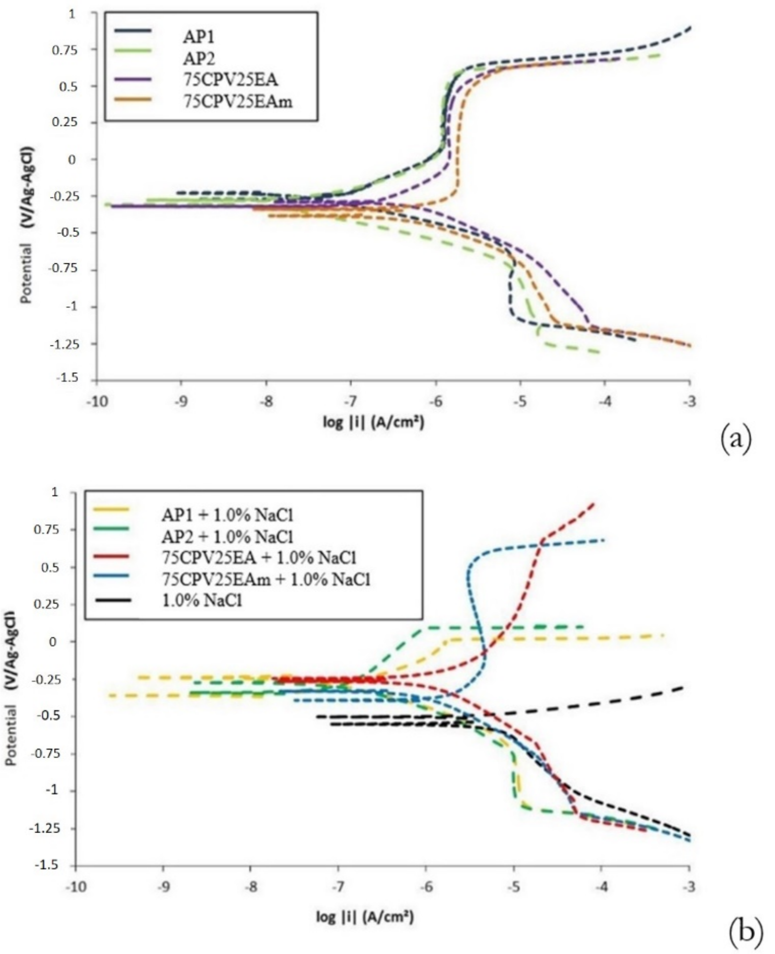

Figure 2. Polarization curves for CA-50 steel in pore water without (a) and with the addition of 1.0% NaCl (b). Each branch of the curves was obtained with a different electrode.

Table 5. Electrochemical parameters determined from the triplicate of the CA-50 steel polarization curves in the different pore water simulant solutions.

Solutions	$i_{passive}$ (μA cm^{-2})	$i_{corr}^{(1)}$ (μA cm^{-2})	E_{corr} (V/Ag-AgCl)	E_{O_2/OH^-} (V/Ag-AgCl)	$E_{pitting}$ (V/Ag-AgCl)
Pore Water 1 (AP1)	1.32 ± 0.25	0.79	(-0.27 ± 0.04)	(+0.67 ± 0.01)	-
Pore Water 1 + 1,0% NaCl (AP1 + NaCl)	-	0.65	(-0.36 ± 0.01)	-	(-0.008 ± 0.02)
Pore Water 2 (AP2)	1.38 ± 0.17	0.71	(-0.27 ± 0.01)	(+0.59 ± 0.02)	-
Pore Water 2 + 1,0% NaCl (AP2 + NaCl)	-	0.71	(-0.33 ± 0.04)	-	(+0.05 ± 0.04)
Pore Water “75CPV25EA”	1.38 ± 0.13	0.38	(-0.31 ± 0.04)	(+0.57 ± 0.05)	-
Pore Water “75CPV25EA + 1,0% NaCl”	-	2.69	(-0.34 ± 0.06)	(+0.53 ± 0.01)	-
Pore Water “75CPV25EAm”	1.70 ± 0.13	0.38	(-0.31 ± 0.05)	(+0.62 ± 0.04)	-
Pore Water “75CPV25EAm + 1,0% NaCl”	3.07 ± 0.91	4.68	(-0.40 ± 0.02)	(+0.64 ± 0.03)	-
1,0% NaCl Solution	-	10.0	(-0.51 ± 0.01)	-	-

(1) i_{corr} was determined from the analysis of the curves in Figures 2a and 2b

Figures 3 and 4 show the evolution of EIS test results with time for pore waters without (Figure 3) and with 1.0% NaCl (Figure 4).

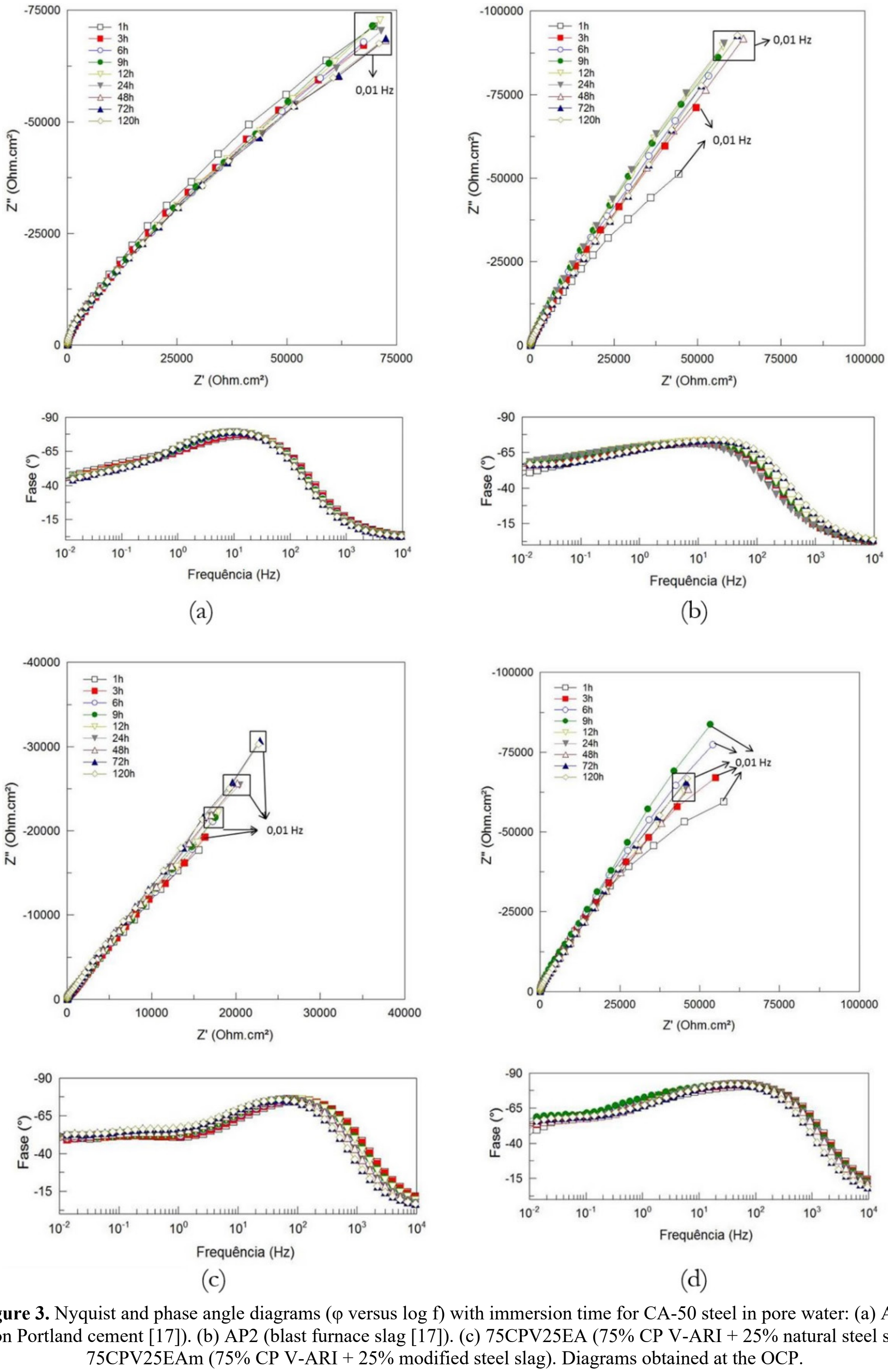

Figure 3. Nyquist and phase angle diagrams (φ versus log f) with immersion time for CA-50 steel in pore water: (a) AP1 (common Portland cement [17]). (b) AP2 (blast furnace slag [17]). (c) 75CPV25EA (75% CP V-ARI + 25% natural steel slag). (d) 75CPV25EAm (75% CP V-ARI + 25% modified steel slag). Diagrams obtained at the OCP.

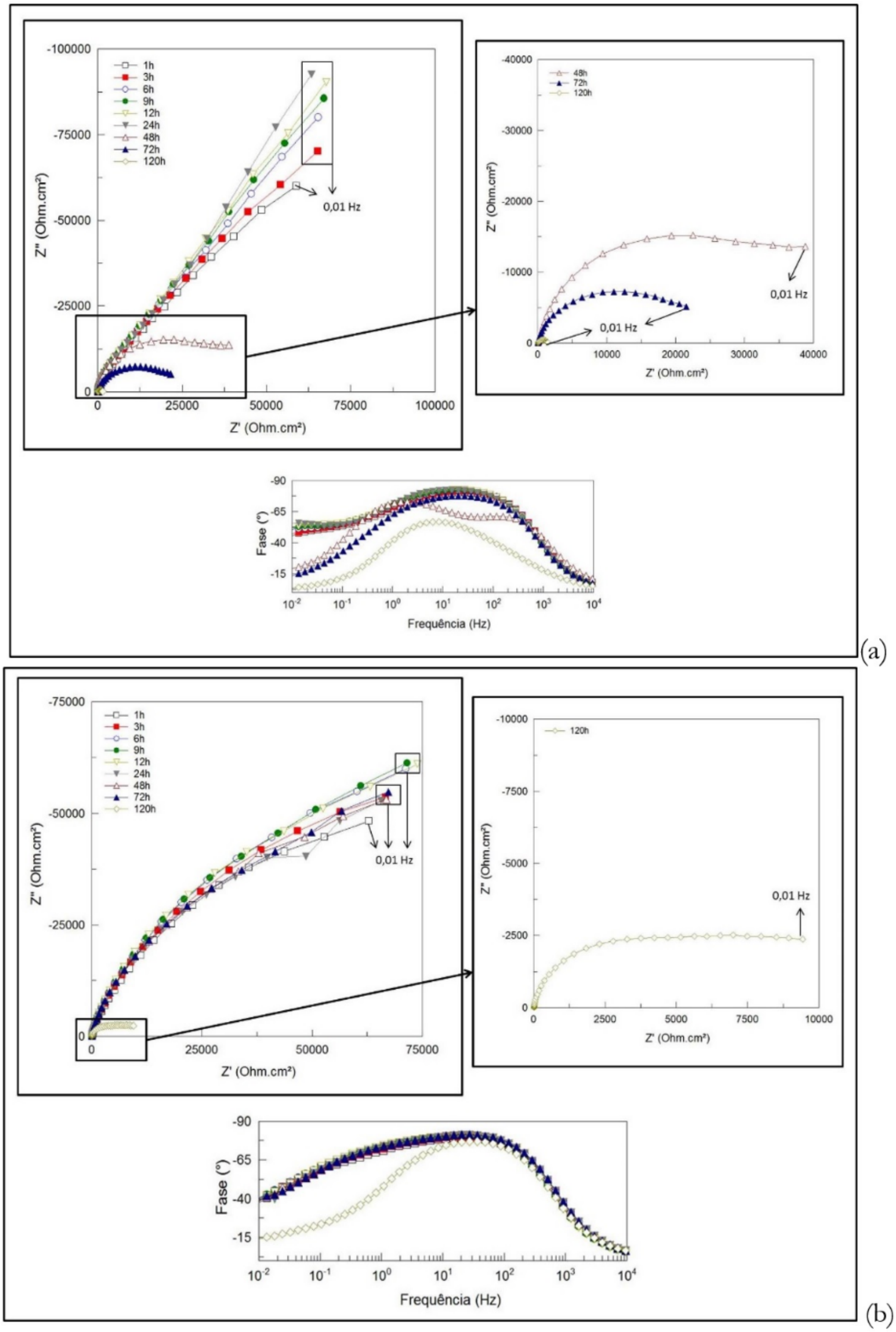

Figure 4. Nyquist and phase angle diagrams (φ versus log f) with immersion time for CA-50 steel in pore water: (a) AP1 + 1.0% NaCl (common Portland cement [17]). (b) AP2 + 1.0% NaCl (blast furnace slag [17]). (c) 75CPV25EA + 1.0% NaCl (steel slag in natura). (d) 75CPV25EAm + 1.0% NaCl (modified steel slag). Diagrams obtained at the OCP.

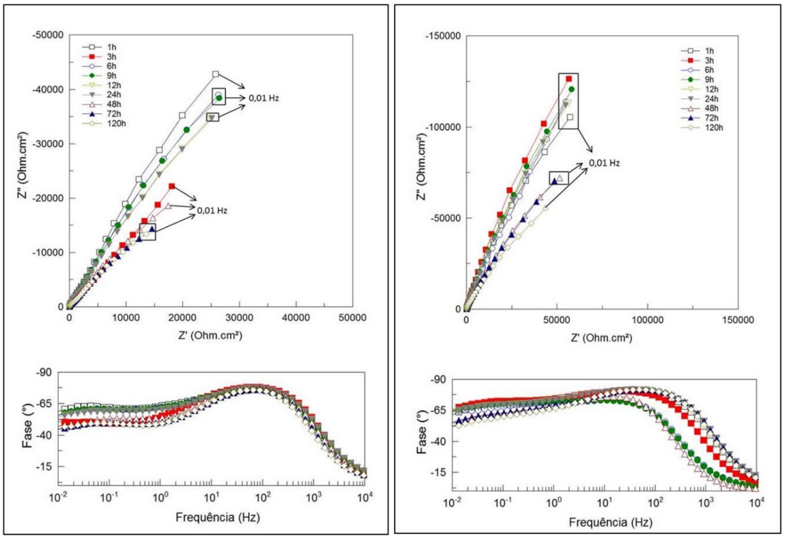

(c) (d)

(Continuation) **Figure 4.** Nyquist and phase angle diagrams (φ versus log f) with immersion time for CA-50 steel in pore water: (a) AP1 + 1.0% NaCl (common Portland cement [17]). (b) AP2 + 1.0% NaCl (blast furnace slag [17]). (c) 75CPV25EA + 1.0% NaCl (steel slag in natura). (d) 75CPV25EAm + 1.0% NaCl (modified steel slag). Diagrams obtained at the OCP.

In the absence of chlorides (Figure 3), the phase angle diagrams showed the presence of two-time constants in all media, being one strongly capacitive at high frequencies (HF), with phase angles above 70°. In the region of low frequencies (BF), there was a decrease in the phase angle, and its variation with frequency presents a linear trend, which indicates the existence of diffusion-controlled processes, a fact confirmed by the Nyquist diagrams. For all media, the evolution of the Nyquist diagrams indicated the stability of the impedance module with the immersion time and, in the first hours, the most intense variations are related to the evolution of the passive film and the stabilization of the potential of steel in the media. The pH monitoring for these media, as well as for those containing 1.0% NaCl, is presented in Table 6. For pore waters AP1 and AP2 (Table 4) [17], there was a small drop in pH in 72 h, while for pore waters representative of steel slag the pH remained very alkaline up to 120 h.

Table 6. pH monitoring of pore water during impedance tests.

Solutions	Initial	24 h	48 h	72 h	120 h
Pore water 1 (AP1)	13.3	13.2	13.1	11.1	11.0
Pore water 1 + 1.0% NaCl (AP1 + NaCl)	13.2	13.1	12.9	11.5	11.1
Pore water 2 (AP2)	13.2	13.1	12.5	11.0	10.9
Pore water 2 + 1.0% NaCl (AP2 + NaCl)	13.1	13.1	12.4	11.5	10.8
Pore water "75CPV25EA"	14.0	14.0	13.9	13.8	13.7
Pore water "75CPV25EA + 1.0% NaCl"	14.0	14.0	13.8	13.9	13.8
Pore water "75CPV25EAm"	14.0	13.9	13.9	13.9	13.7
Pore water "75CPV25EAm + 1.0% NaCl"	14.0	14.0	13.9	13.9	13.9

For pore water containing 1.0% NaCl, diagrams presented in Figure 4, there was a difference in the impedance behavior of CA-50 steel between the solutions of Portland cement (AP) and slag cement. For the tests in "AP1 + 1.0% NaCl" and "AP2 + 1.0% NaCl", the Nyquist diagrams showed a capacitive and stable behavior during the first hours of testing, but since 48 h for the first solution and 72 h for the second, there was a strong drop in the impedance of the steel and changes in the shapes of the Bode diagrams, indicating the beginning of localized attack, which was confirmed by visual analysis of the specimens after the tests. On the other hand, in the pore waters of steel slag, the specimens maintained relatively stable behavior up to 120 h, which is evident through the high values of the impedance module. However, during the test, the impedance modules showed variations over time, which alternated between increases and decreases and may be associated with the action of chloride ions, promoting instability in the passive film.

The information displayed in Table 6 is very relevant to explain the observed behaviors. In the case of the media used by Oliveira [17], which are AP1 and AP2 (compositions in Table 4), with and without 1.0% of NaCl, there was a drop in pH throughout the test, and the process was intensified in 72 hours. At the end of the test (120 h), the pH of the pore water was around 11 for all solutions. This pH value is not sufficient to promote carbonation, which tends to occur at pHs below 10 [27], [28]. Thus, the destabilization of the passive layer is due to the presence of chloride ions, causing localized corrosion. On the other hand, the pore water related to the steel slag kept the steel passive up to 120 h even in aggressive media (with the addition of 1.0% NaCl). The high pH, which was kept practically unchanged throughout the test, promoted more intense protection of the steel, and the addition of 1.0% NaCl did not allow reaching the limit chloride concentration for the occurrence of localized attack of the passive layer at this pH value.

Figure 5 presents selected micrographs of the SEM analysis of the corroded regions of CA-50 steel in the media "AP1 + 1.0% NaCl" and "AP2 + 1.0% NaCl" after the anodic polarization tests. It is verified, in both media, the formation of a corrosion product with morphology denominated in the literature as "birds nest " (Figures 5a, 5b and 5c), which is associated with lepidocrocite (γ-FeOOH), and which is common for steel in the related media [28]. This observation is confirmed by the EDS spectrum obtained for a region with this product (Figure 5d), showing high levels of Fe and O. Also, it was related, for the two media, the formation of corrosion products with a dry mud aspect and presenting cracks (Figure 5f) which, according to Raman et al. [29], are constituted of mixtures of amorphous phases. The enlargement of a region of Figure 5e, presented in Figure 5g, indicates the presence of goethite (α-FeOOH) in the "AP1 + 1.0% NaCl" medium, which emerged from amorphous precipitates.

For the sample tested in the solution "AP2 + 1.0% NaCl", it was also verified the formation of deformed circular structures that are associated in the literature with magnetite and are called donuts [29], according to Figures 5h and 5i. Figure 5i shows the formation of lepidocrocite inside a donut, and the results of EDS for the donut in Figure 5h indicated high levels of Mn and S, which suggests that the process started in a region with inclusions of MnS, present in the microstructure of CA-50 steel in this study.

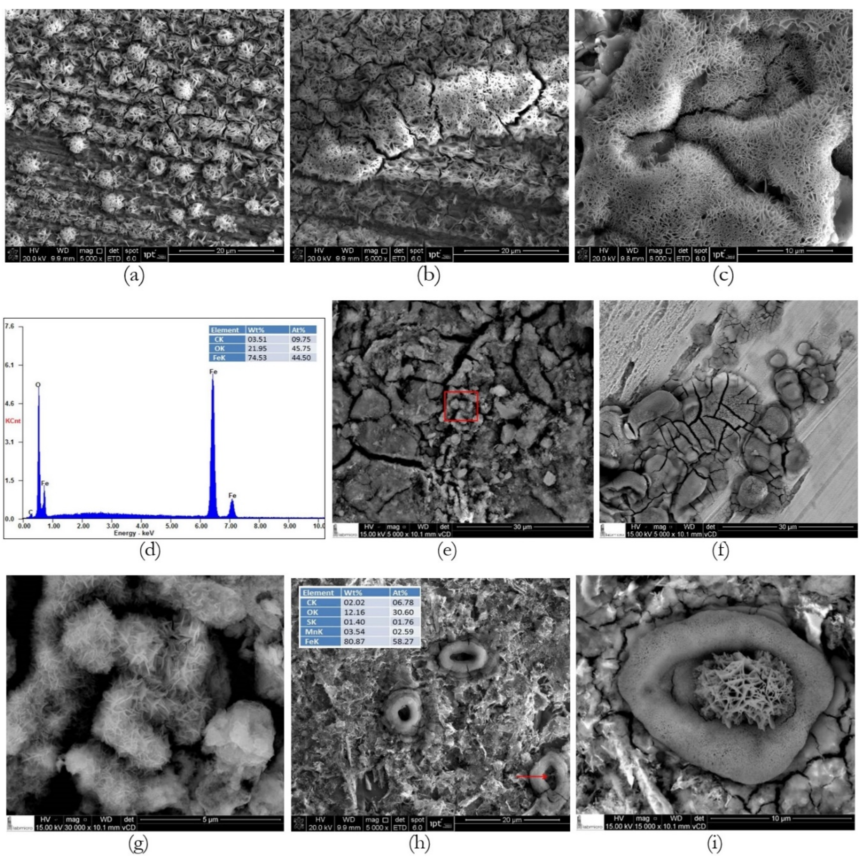

Figure 5. SEM images from the surface of CA-50 steel after anodic polarization. (a) and (b) "AP1 + 1.0% NaCl", lepidocrocrite (γ-FeOOH) with "birds nest" morphology. Increase of 5000 X. (c) "AP2 + 1.0% NaCl", lepidocrocyte formation (γ-FeOOH). Increase of 8000 X. (d) EDS spectrum of the region showed in **figure (a)**. Formation of amorphous structures with dry mud morphology (cracks) in (e) "AP1 + 1.0% NaCl" and (f) "AP2 + 1.0% NaCl". (g) Enlargement of the region showed in (e), with goethite formation (α-FeOOH). (h) Donut-shaped structures (Fe_3O_4) present on the surface, with EDS result for a specific donut (indicated in the figure). (i) Donut-shaped structure with lepidocrite (γ-FeOOH). **Source:** Results obtained by Laboratório de Corrosão e Proteção / IPT and Laboratório de Microscopia Eletrônica de Varredura / PMT / USP.

4 CONCLUSIONS

- CA-50 steel showed a passive behavior in all pore waters without the addition of 1.0% NaCl in both the polarization and impedance tests during the time, which proves the efficiency of the protection given to the material by alkaline environments.
- The pore water extracted from cement pastes with steel slag (studied pore water) was more alkaline than that proposed by Oliveira [17] for cement and blast furnace slag (pore water AP1 and AP2 with compositions in Table 4) and adopted as reference. Until the end of the impedance tests (5 days), the pH practically did not change for the former, while for the reference media, it showed a slight drop with time.
- Tests on media with 1.0% NaCl indicated advantages conferred by the studied pore waters (75CPV25EA and 75CPV25EAm) to CA-50 steel. In the polarization and EIS tests during the time, the higher alkalinity conferred greater protection to the steel, preventing its corrosion even in the presence of high chloride concentration, while in the reference media [17] the steel corroded. There was evidence of pitting potential in the anodic curves and a strong drop in impedance for longer immersion times, indicating an attack of the passive layer in the reference media. On the other hand, the EIS results for the studied pore waters (cement pastes with steel slag) indicated a downward trend in the impedance modulus with time, which can be attributed to the aggressiveness of the chloride. However, this did not promote the corrosion of the steel.
- The SEM images of the corroded region after anodic polarization in the reference pore water [17] indicated that the predominant corrosion product is lepidocrocite (γ-FeOOH), characteristic of chloride attack on steel in alkaline media. Also occurred goethite (α-FeOOH, in AP1 + 1.0% NaCl) and magnetite (Fe3O4) formations in the form of donuts (AP2 + 1.0% NaCl). The electrodes tested in pore water of cement pastes with steel slag remained intact.

ACKNOWLEDGEMENTS

The authors thank InterCement Brazil and the Empresa Brasileira de Pesquisa e Inovação Industrial (EMBRAPII) for allowing the realization of this study in the scope of the larger project. Also, thanks to the labs of Materiais de Construção Civil (LMCC), Processos Metalúrgicos (LPM), Corrosão e Proteção (LCP) and Análises Químicas (LAQ) of IPT for the results of characterization and microstructure of materials, as well as the Laboratório de Microscopia Eletrônica de Varredura/PMT/USP for results of microstructure of steel.

REFERENCES

[1] A. Nonat, “A hidratação dos cimentos,” in *Durabilidade do Concreto: Bases Científicas para a Formulação de Concretos Duráveis de Acordo com o Ambiente*, J. Ollivier and A. Vichot, Ed., São Paulo: IBRACON, 2014.

[2] H. Alanyali, M. Çöl, M. Yilmaz, and S. Karagöz, "Concrete produced by steelmaking slag (basic oxygen furnace) addition in Portland cement," *Int. J. Appl. Ceram. Technol.*, vol. 6, no. 6, pp. 736–748, 2009, http://dx.doi.org/10.1111/j.1744-7402.2008.02317.x.

[3] M. Gautier, J. Poirier, F. Bodénan, G. Franceschini, and E. Véron, "Basic oxygen furnace (BOF) slag cooling: laboratory characteristics and prediction calculations," *Int. J. Miner. Process.*, vol. 123, pp. 94–101, 2013, http://dx.doi.org/10.1016/j.minpro.2013.05.002.

[4] F. F. Chotoli, V. A. Quarcioni, C. Fredericci, R. E. Vieira, and J. B. Ferreira No., “Modified oxygen steelmaking slag to produce cements – Part 1: chemical and mineralogical characterization,” in *Proc. 14th Int. Cong. Chem. Cem.*, 2015.

[5] F. F. Chotoli, V. A. Quarcioni, J. B. Ferreira No., and R. F. C. Santos, “Modified oxygen steelmaking slag to produce cements – Part 2: hydration and physical-mechanical characterization,” in *Proc. 14th Int. Cong. Chem. Cem.*, 2015.

[6] A. B. Masuero, “Estabilização das escórias de aciaria elétrica com vistas a sua utilização como substituição ao cimento,” Ph.D. dissertation, Esc. Eng., Univ. Fed. Rio Grande do Sul, Porto Alegre, 2001.

[7] R. D. Hooton, M. D. A. Thomas, and T. Ramlochan, "Use of pore solution analysis in design for concrete durability," *Adv. Cement Res.*, vol. 22, no. 4, pp. 203–210, 2010., http://dx.doi.org/10.1680/adcr.2010.22.4.203.

[8] M. Moreno, W. Morris, M. G. Alvarez, and G. S. Duffó, "Corrosion of reinforcing steel in simulated concrete pore solutions – effect of carbonation and chloride content," *Corros. Sci.*, vol. 46, no. 11, pp. 2681–2699, 2004, http://dx.doi.org/10.1016/j.corsci.2004.03.013.

[9] M. S. Moreno, “Películas passivas modificadas por el empleo de inhibidores de corrosión para la protección de armaduras. Sistemas de prevención de la corrosión,” Ph.D. dissertation, Fac. Cien, Univ. Autonoma de Madrid, Madri, 2007. Accessed: Feb. 1, 2020. [Online]. Available: https://repositorio.uam.es/handle/10486/670581

[10] M. Sánchez, J. Gregori, C. Alonso, J. J. García-Jareño, H. Takenouti, and F. Vicente, "Electrochemical impedance spectroscopy for studying passive layers on steel rebars immersed in alkaline solutions simulating concrete pores," *Electrochim. Acta*, vol. 52, no. 27, pp. 7634–7641, 2007, http://dx.doi.org/10.1016/j.electacta.2007.02.012.

[11] F. Zhang, J. Pan, and C. Lin, "Localized corrosion behavior of reinforcement steel in simulated concrete pore solution," *Corros. Sci.*, vol. 51, no. 9, pp. 2130–2138, 2009, http://dx.doi.org/10.1016/j.corsci.2009.05.044.

[12] W. Chen, R. G. Du, C. Q. Ye, Y. F. Zhu, and C. J. Lin, "Study on the corrosion behavior of reinforcing steel in simulated concrete pore solutions using in situ Raman spectroscopy assisted by electrochemical techniques," *Electrochim. Acta*, vol. 55, no. 20, pp. 5677–5682, 2010, http://dx.doi.org/10.1016/j.electacta.2010.05.003.

[13] D. A. Koleva, N. Boshkov, K. Van Breugel, and J. H. W. Wit, "Steel corrosion resistance in model solutions containing waste materials," *Electrochim. Acta*, vol. 58, pp. 628–646, 2011, http://dx.doi.org/10.1016/j.electacta.2011.10.010.

[14] A. Cesen, T. Kosec, A. Legat, and V. B. Bosiljkov, "Corrosion properties of different forms of carbon steel in simulated concrete pore water," *Mater. Technol.*, vol. 48, no. 1, pp. 51–57, 2014.

[15] R. Liu, L. Jiang, J. Xu, C. Xiong, and Z. Song, "Influence of carbonation on chloride-induced reinforcement corrosion in simulated concrete pore solutions," *Constr. Build. Mater.*, vol. 56, pp. 16–20, 2014, http://dx.doi.org/10.1016/j.conbuildmat.2014.01.030.

[16] P. K. Mehta and P. J. M. Monteiro, *Concreto: Estrutura, Propriedades e Materiais*. São Paulo: PINI, 1994.

[17] C. T. A. Oliveira, "Água de poro de pastas de cimento de escória," Ph.D. dissertation, Esc. Politéc., Univ. São Paulo, São Paulo, 2000. Accessed: Feb. 1, 2020. [Online]. Available: https://repositorio.usp.br/item/001076162

[18] R. S. Barneyback Jr. and S. Diamond, "Expression and analysis of pore fluids from hardened cement pastes and mortars," *Cement Concr. Res.*, vol. 11, no. 2, pp. 279–285, 1981, http://dx.doi.org/10.1016/0008-8846(81)90069-7.

[19] M. P. Kulakowski, "Contribuição ao estudo da carbonatação em concretos e argamassas compostos com adição de sílica ativa," Ph.D. dissertation, Esc. Eng., Univ. Fed. Rio Grande do Sul, Porto Alegre, 2002. Accessed: Feb. 1, 2020. [Online]. Available: https://lume.ufrgs.br/handle/10183/3594

[20] K. A. Anders, B. P. Bergsma, and C. M. Hansson, "Chloride concentration in the pore solution of Portland cement paste and Portland cement concrete," *Cement Concr. Res.*, vol. 63, pp. 35–37, 2014, http://dx.doi.org/10.1016/j.cemconres.2014.04.008.

[21] Universidade Federal do Rio Grande do Sul. "Salinidade do ambiente marinho." UFRGS. http://mdmat.mat.ufrgs.br/acqua/Textos/concentracao.htm (accessed Feb. 1, 2020).

[22] M. Carvalho-Borges, I. B. M. Orselli, M. L. C. Ferreira, and R. Kerr, "Seawater acidification and anthropogenic carbon distribution on the continental shelf and slope of the western South Atlantic Ocean," *J. Mar. Syst.*, vol. 187, pp. 62–81, 2018, http://dx.doi.org/10.1016/j.jmarsys.2018.06.008.

[23] R. R. Oliveira, L. P. Pezzi, R. B. Souza, M. F. Santini, L. C. Cunha, and F. S. Pacheco, "First measurements of the ocean-atmosphere CO_2 fluxes at the Cabo Frio upwelling system region, Southwestern Atlantic Ocean," *Cont. Shelf Res.*, vol. 181, pp. 135–142, 2019, http://dx.doi.org/10.1016/j.csr.2019.05.008.

[24] G. R. Meira and P. R. R. Ferreira, "Revisão sobre ensaios acelerados para indução da corrosão desencadeada por cloretos em concreto armado," *Ambiente Constr.*, vol. 19, no. 4, pp. 223–248, 2019, http://dx.doi.org/10.1590/s1678-86212019000400353.

[25] L. Feng, H. Yang, and F. Wang, "Experimental and theoretical studies for corrosion inhibition of carbon steel by imidazoline derivative in 5% NaCl saturated $Ca(OH)_2$ solution," *Electrochim. Acta*, vol. 58, pp. 427–436, 2011, http://dx.doi.org/10.1016/j.electacta.2011.09.063.

[26] E. R. Vago and E. J. Calvo, "Electrocatalysis of oxygen reduction at Fe_3O_4 oxide electrodes in alkaline solutions," *J. Electroanal. Chem.*, vol. 339, no. 1-2, pp. 41–67, 1992, http://dx.doi.org/10.1016/0022-0728(92)80444-9.

[27] J. J. O. Andrade, "Contribuição à previsão da vida útil das estruturas de concreto armado atacadas pela corrosão de armaduras: iniciação por cloretos," Ph.D. dissertation, Esc. Eng., Univ. Fed. Rio Grande do Sul, Porto Alegre, 2001. Accessed: Feb. 1, 2020. [Online]. Available: https://www.lume.ufrgs.br/handle/10183/2613

[28] P. Campestrini, E. P. M. Van Westing, and J. H. W. De Wit, "Influence of surface preparation on performance of chromate conversion coatings on Alclad 2024 aluminium alloy. Part II: EIS investigation," *Electrochim. Acta*, vol. 46, no. 17, pp. 2631–2647, 2001, http://dx.doi.org/10.1016/S0013-4686(01)00476-5.

[29] A. Raman, S. Nasrazadani, and L. Sharma, "Morphology of rust phases formed on weathering steels in various laboratory corrosion tests," *Metallography*, vol. 22, no. 1, pp. 79–96, 1989, http://dx.doi.org/10.1016/0026-0800(89)90024-4.

Author contributions: R. E. Vieira: conceptualization, writing (methodology, results, review); M. M. Mennucci: conceptualization, formal analysis, review, writing; H. G. de Melo, V. A. Quarcioni: data curation, formal analysis.

Editors: Mauricio de Pina Ferreira, José Luiz Antunes de Oliveira e Sousa, Guilherme Aris Parsekian.

IBRACON Structures and Materials Journal
Revista IBRACON de Estruturas e Materiais
ISSN 1983-4195 ismj.org

ORIGINAL ARTICLE

Humidity and specimen preparation procedure: influence on compressive strength of concrete blocks

Umidade e modo de preparação do corpo de prova: influência na resistência a compressão de blocos de concreto

Guilherme Aris Parsekian[a]
André Luis Christoforo[a]
Amanda Duarte Escobal Mazzú[a]
Gláucia Maria Dalfré[a]

[a]Universidade Federal de São Carlos – UFSCar, Programa de Pós-graduação em Engenharia Civil, São Carlos, SP, Brasil

Received 01 April 2020
Accepted 10 July 2020

Abstract: It is extremely important that the quality control of the concrete block used in structural masonry is conducted based on standard procedures that allow reliable estimation of the properties of these components. This work aims to analyze and evaluate the influence of the concrete block moisture on the result of the compression test. Hollow concrete blocks were prepared and subsequently maintained in different environments for various periods of time and under different conditions of temperature and humidity to determine the influence of the type of drying on the relative humidity of the block at the time of testing and consequently on its compressive strength. As a conclusion, it can be stated that, because it is necessary to use water in the process, the grinding rectification of the faces of the blocks led them to have high humidity, above 70%. If tested in this condition, the results of the compressive strength tests will be lower than that of blocks under usual environmental conditions. No differences were found in the average block strength when they were kept dry in the controlled environment of the laboratory during periods of 24 or 48 h. After grinding, it is not necessary to dry the blocks inside an oven at 40ºC before the tests; simply leaving them at a usual room temperature of 23ºC and humidity of 40 ± 5% for 24h is sufficient. The attempt to accelerate drying in an oven at 100ºC is not adequate because this leads to an increase in the compressive strength. From the results, it was possible to determine expressions to correlate the compressive strength as a function of the moisture of the block at the time of the test. The best-fit expressions are distinct for each block type, but the formulations are consistent in indicating a considerable difference in resistance as a function of moisture.

Keywords: moisture, concrete hollow block, compressive strength, statistical analysis, experimental analysis.

Resumo: É de extrema importância que o controle de qualidade de blocos de concreto aplicados na alvenaria estrutural seja realizado com base em procedimentos normalizados que permitam a estimativa das propriedades desses componentes de forma confiável. Este trabalho objetiva analisar e avaliar a influência da umidade do bloco de concreto no resultado do ensaio de compressão. Blocos vazados de concreto simples foram submetidos à processo de retificação e foram posteriormente mantidos em diferentes ambientes, por variados períodos de tempo e sob diferentes condições de temperatura e umidade, de modo a se observar a influência do tipo de secagem sobre a umidade relativa do bloco no momento do ensaio e, consequentemente, sob seu comportamento à compressão. Como conclusão pode-se afirmar que logo após a retificação das face dos blocos, esses apresentam umidade elevada, acima de 70% e, se ensaiados nessa condição, os resultados de resistência a compressão serão menores que os de blocos em condições ambientais usuais. Não foram verificadas diferenças de resistência para as secagens realizadas nos períodos de 24 ou 48 h em ambiente laboratorial. Após a retificação não é necessário colocar os blocos em estufa a 40 °C antes dos ensaios, bastando deixá-los em temperatura e umidade ambiente usuais de 23 °C e 40 ± 5%, respectivamente, durante 24 h. A tentativa de acelerar a secagem em estufa a 100 °C não é adequada pois leva a um aumento da resistência a compressão. A partir dos resultados foi possível determinar expressões para corrigir a resistência

Corresponding author: Guilherme Aris Parsekian. E-mail: parsekian@ufscar.br
Financial support: The São Paulo Research Foundation, FAPESP.
Conflict of interest: Nothing to declare.

a compressão em função da umidade do bloco no momento do ensaio. As expressões de melhor ajuste são distintas para cada tipo de bloco, porém as formulações são consistentes em indicar considerável diferença na resistência em função da umidade.

Palavras-chave: umidade, blocos vazados de concreto, resistência a compressão, análise estatística, análise experimental.

How to cite: G. A. Parsekian, A. L. Christoforo, A. D. E. Mazzú, and G. M. Dalfré, "Humidity and specimen preparation procedure: influence on compressive strength of concrete blocks," *Rev. IBRACON Estrut. Mater.*, vol. 14, no. 2, e14210, 2021, https://doi.org/10.1590/S1983-41952021000200010

1 INTRODUCTION

In Brazil, concrete hollow blocks are one of the most used components in the construction industry due to the simplicity of their production process, which is associated with the ease in obtaining raw materials in Brazil, and the low cost of production, in addition to other advantages provided by the physical characteristics of the blocks.

The great demand for concrete blocks encourages an increase in production and consequently the development of technologies aimed at ensuring the quality of the material. Thus, the regulation and standardization of the quality tests and the specified properties of concrete blocks are important and guarantee the use of specific standards such as the ABNT NBR (Brazilian standard). ABNT specifies various tests to determine the characteristics and properties of concrete blocks, such as water absorption, dimensional tolerance, surface texture, and compressive strength.

The most common control test for hardened concrete is compressive strength testing since it is simple to perform and several of the desirable characteristics of concrete and blocks are qualitatively related to this property, in addition to the importance of knowledge of the concrete compressive strength for structural design [1]. According to Silva [2], the compressive strength test receives greater attention because it is a key factor of masonry resistance in general.

Masonry concrete blocks to be used in structural applications must have a specified compressive strength. Studies have shown that the moisture of blocks at the time of the test directly influences the results of the compressive strength test. Busnello [3] conducted a study to analyze the influence of drying methods and moisture conditions on the results of the compressive strength test of concrete blocks. According to the author, by varying the humidity of the block at the time of the test is it possible to observe differences in its compressive strength of up to 85%. The highest compressive strengths were obtained for blocks with lower humidity.

The NCMA TEK 18-7 [4] indicates that the moisture of the concrete block at the time of the compressive strength test is one of the main variables that needs to be considered, and lower or higher humidity at the time of the test results in increases or decreases of 20% in the results, respectively.

A study by Butcher [5] indicated increases of up to 10% in the compressive strength due to the total drying of concrete of 34 MPa and increases of less than 5% when the drying period is less than 6 h. Shiina [6] identified reductions between 9 and 21% in the compressive strength of concrete submitted to 48 h of wetting. According to the concrete inspection manual of the American Concrete Institute [7], differences in compressive strength of up to 25% can be observed by comparing dry and wet samples of cylindrical concrete specimens.

Permeability is a relevant characteristic that has been mentioned as a source of the variation of compressive strength since it allows a greater amount of water to be in the pores of more permeable concretes [8]. Although there is no universally accepted interpretation of the influence of water on concrete, Galloway et al. [9] stated that the presence of water in concrete pores leads to the dilation of the cement gel, reducing the cohesion of solid particles and consequently its compressive strength. Guo and Waldron [10] presented a mathematical approach to explain the influence of moisture on various physical parameters of concrete, including compressive strength. The model developed by the authors, which was mainly based on the theory of elasticity, demonstrated that compressive strength is the physical factor that is most influenced by moisture, indicating an increase of about 67% in the tangential tension to the circumference of a cylindrical concrete specimen when its cavities are filled with water.

Busnello's study [3] was mainly responsible for a series of changes in the Brazilian standard NBR 12118 [11] for the execution of compressive strength tests in concrete hollow blocks. One of the main points indicated in this version of the standard is the need to wait for 24 h for the ground blocks to dry. The justification is that there is a need to use water to perform the grinding rectification of the faces, which increases the humidity of the block and consequently decreases the result of compression resistance. However, some of the changes introduced difficulties in the execution of the tests, such as the increase in the waiting time for drying the block, resulting in a more laborious test procedure in general. The text of this standard specifies moisture ranges to be observed at the time of the test for acceptance of the results, and these ranges vary depending on the resistance of the block.

For the execution of the compressive strength test of concrete blocks, the block must have its top and bottom faces regularized to ensure the perpendicularity between the faces and the applied load, which allows the uniform transfer of load to the block, and consequently, greater reliability of the results. NBR 12118 [11] recommends that this regularization be performed by either applying pastes or mortars capable of resisting the expected stresses or through grinding, which consists of the wear of a thin layer of the face of the block. According to Bezerra [12], rectification must be performed in such a way so as to preserve the structural integrity of the layers below the removed thin layer, resulting in a surface without ripples, bulging, and without breakings at the edges of the concrete block.

The grinding process has the advantage of reduced execution time compared to the time associated with the preparation of pastes and mortars and of a less laborious execution process. However, as mentioned earlier, during the grinding process, the blocks are inevitably moistened by the water, a fact that should be considered at the time of the compressive strength test.

The fact that moisture helps in the process of curing and development of concrete compressive strength is already widely known. According to Popovics [13], the moisture condition to which concrete specimens are submitted in the days prior to the compressive strength test affects the results obtained. However, with different compositions, concrete specimens submitted to air drying in the days prior to the compressive strength test showed higher resistance. According to the author, in a concrete specimen that is externally subjected to wetting (happens during the grinding process in which the wetting is superficial, generating a moisture gradient), the surface tries to expand creating biaxial tensile stresses in the core of the specimen, which opposes this expansion. Thus, stresses are generated in the third direction of the specimen, thus leading to the reduction of its compressive strength. In the case of concrete blocks, elements that have relatively thin walls, with internal and external surfaces, there is the possibility that the stresses generated by external wetting are even higher.

The American standard ASTM C140/C140M [14] recommends that concrete blocks be subjected to air drying at a temperature of 24 ± 8°C and not dried in an oven since drying in an oven can lead to a state of stresses that can alter the test result, causing increased resistance to apparent compression. This standard, similar to the Australian/New Zealand standard AS/NZS 4456 [15], further recommends that the humidity condition of the block at the time of the test should be close to the condition observed when the block was received, thus ensuring that the actual capacity of the block is determined. The British standard BS EM 772-1 [16] presents a detailed method for determining the allowed block moisture condition before the compressive strength test, considering the type of material that composes the block and the type of capping (regularization of the work faces of the block) that is used.

The most current version of the ABNT NBR 12118 [11] describes, separately, the treatments to which blocks capped with pastes and mortars and rectified blocks should be submitted. In the case of rectified blocks, periods and temperature ranges are included for drying in an oven and air drying. In the case of air drying, the standard recommends that the blocks be placed in a laboratory environment for 72 h. On the other hand, for drying in an oven, these should be kept in an oven for 24h ± 30 min, with a temperature of 40 ± 2 °C.

In contrast to the Brazilian standard, the British and American standards establish that concrete blocks must be tested in the wet condition, a condition that, according to Neville [1], is more easily reproduced since dry conditions include several degrees of drying.

Thus, it is necessary to standardize the treatment of masonry concrete blocks for the humidity condition to reduce the influence of this factor on the test.

The existence of only a few studies for the specific case of concrete hollow blocks justifies the need to seek more information regarding the influence of moisture of these blocks on their compressive strength, considering that this can be directly related to the safety assurance and quality control of the material.

Thus, this work aims to determine the influence of the moisture of masonry concrete blocks on their compressive strength, submitting rectified concrete blocks to drying in different environments, for various periods of time and under different conditions of temperature and humidity, besides analyzing whether the wetting caused by the grinding process is relevant.

2 MATERIALS AND METHODS

To evaluate the influence of moisture of masonry concrete blocks on their compressive strength, rectified concrete blocks with different moisture levels were submitted to tests to determine their compressive strength. The drying methods used to obtain the different moisture levels for the rectified blocks are presented in Table 1.

Table 1. Drying method and moisture condition of the blocks.

Condition	Drying/saturation method	Temperature/Humidity	Duration (hours)
1	Air-conditioned room	23ºC / 40 ± 5%	24
2	Air-conditioned room	23ºC / 40 ± 5%	48
3	Oven	100 ± 5 ºC	24
4	Oven	40 ± 5 ºC	24
5	Saturated in water	Environment	24
6	No*	Environment	-

* concrete blocks tested right after rectification. Source: Tchalekian [17]

Three different types of concrete blocks with dimensions of 14 × 19 × 29 cm (group A), 19 × 19 × 39 cm (group B), and 14 × 19 × 39 cm (group C) with specified compressive strengths of 12, 8, and 22 MPa, respectively, were analyzed. Each group was composed of six concrete blocks for each moisture condition, totaling 36 blocks for each group, totaling 108 blocks analyzed. Three blocks, for each moisture condition, from each group, were used to determine the relative humidity of the blocks by measuring their dry and saturated masses. The blocks used for the determination of the relative humidity were not submitted to the compressive strength test. The blocks used in the relative humidity test were submitted to the same processes and environmental conditions as those used for compressive strength tests until the moment of the test. At that moment, the humidity control blocks were taken to the oven. Thus, their conditions mirrored the moisture of the blocks tested in compression.

2.1 Preparation of concrete blocks

Prior to exposure to the environments presented in Table 1, the dimensions of the blocks were measured with the aid of a caliper, thus allowing the calculation of the gross area, with the resistance calculated in relation to this area.

All blocks were submitted to wet rectification, which was performed on the top and bottom faces of the blocks. Before the fixation of the blocks in the grinding support, all particles that could interfere in the leveling of the samples were removed with the help of a brush. The process of rectification and the measurement of the dimensions of the blocks are exemplified in Figure 1.

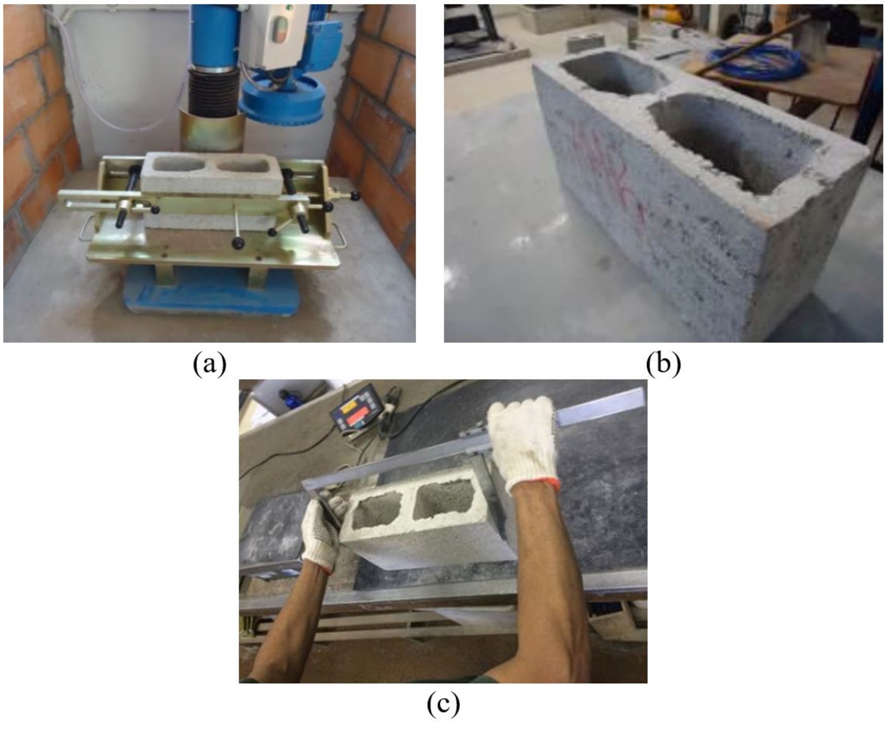

Figure 1. (a) grinding process, (b) rectified block and (c) dimension measurement. Source: Tchalekian [17]

After rectification, the blocks were placed in the environments detailed in Table 1, and in the case of drying in an oven (shown in Figure 2a), the blocks were positioned in such a way so as to facilitate the circulation of air between the samples. The blocks to be saturated were placed into a water tank and fully submerged, as shown in Figure 2b.

The method described in NBR 12118 [11] was used to determine the relative humidity of the blocks. For this, the dry mass, wet mass, and mass at the time of the test were determined, and the relative humidity was calculated using Equation 1.

Figure 2. Exhibition environments - Oven (a) and Water tank (b). Source: Tchalekian [17]

$$U=\left(\frac{m-m_1}{m_2-m_1}\right)\cdot 100 \tag{1}$$

where U is the relative moisture content of the block in percentage, m is the mass of the block at the time of the test in grams, m_1 is the mass of the dry block in grams in an oven at (110 ± 5)°C, and m_2 is the mass of the saturated block in grams.

The compressive strength tests were performed at the Structural Systems Laboratory (LSE) of the Federal University of São Carlos (UFSCar) using an EMIC universal testing machine, model PC200-ESP, which was configured to applied the load at the speed required in the standard. A data acquisition system, LYNX model ADS-2000, was used to record the load. During the tests, the specimens were positioned with their center of gravity aligned with the load axis of the test machine platens and with the thicker side of the webs at the top, which is the position that blocks are employed.

By applying the method recommended by NBR 6136 [18], it was possible to estimate the value of compressive strength ($f_{bk,est}$) for each group using Equation 2.

$$f_{bk,est}=2\cdot\left(\frac{f_{b(1)}+f_{b(2)}+\ldots f_{b(i-1)}}{i-1}\right)-f_{b(i)} \tag{2}$$

where $f_{bk,est}$ is the estimated characteristic resistance of the sample (MPa); $f_{b(1)}$, $f_{b(2)}$, ..., are the individual compressive strength values of the specimens, ordered increasingly, n is the number of blocks; and $i=n/2$ if n is even or $i=(n-1)/2$ if n is odd. $f_{bk,est}$ should not be taken as less than $\psi\cdot f_{b(1)}$, where ψ accounts for the number of blocks and is given in Table 1 of ABNT NBR 6136 [18].

2.2 Statistical treatment

For each type of concrete hollow block (A, B and C) and moisture condition presented in Table 1, one experimental treatment (Tr) was designed, totaling six different experimental treatments (Tr), and, for each treatment, six blocks were tested.

The Tukey multiple comparison test, at the 5% level of significance, was used to identify possible significant differences between the values of compressive strength (f_b) for the six treatments (per block type). In the Tukey test, "A" denotes the treatment of higher mean value, "B" the second highest mean value, and so on, and equal letters imply treatments with statistically equivalent means.

Significant differences reported by the Tukey test between treatments Tr 1 and Tr 2 show that the drying period (24 or 48 h) of the samples evaluated in an air-conditioned room were considered significant for the compressive strength values. If a significant difference between treatments 3 and 4 is assumed, it implies that the temperature of the oven (40 or 100ºC) affects the values of f_b. If there is a significant difference between treatments 1, 2, 3, 4 and treatment 5, it implies that there is no difference in the resistance values between the dry blocks in the air-conditioned room or that of blocks saturated in water at room temperature and kept in an oven; the same for treatment 6 (unsaturated and dry at room temperature).

In order to establish a unique relationship between compressive strength (f_b) and relative moisture content (U) for the three types of blocks (A, B, and C), the mean values of f_b for the respective moisture content ($f_{b,U(\%)}$) for each block type were normalized by the mean values of f_b for the condition of 0% humidity ($f_{b,0\%}$). The consideration of block B along with blocks A and C impaired the accuracy of the regression models. Due to this, different best-fit models are generated (Equations 3 and 4), the first one for the set involving blocks A and C and a second model exclusively for block B. The regression models presented in Equations 3 and 4, based on ANOVA (at the level of 95% reliability) at two parameters (αo and α_1) were created. Considered significant by ANOVA, the best fit by block type was defined based on the coefficient of determination value (R^2).

$$f_{b,U(\%)} / f_{b,0\%} = \alpha_0 + \alpha_1 \cdot U + \varepsilon \text{ [linear]} \tag{3}$$

$$f_{b,U(\%)} / f_{b,0\%} = \alpha_0 \cdot U^{\alpha_1} + \varepsilon \text{ [geometric]} \tag{4}$$

Based on the formulation of the ANOVA of the regression models of Equations 3 and 4, a p-value lower than the significance level implies that the models are significant, and not significant otherwise (i.e., for p-value ≥ 0.05). The Anderson-Darling test (5% significance) was used to verify normality (p-value ≥ 0.05) in the distribution of the residues, to validate the ANOVA model.

3 RESULTS AND DISCUSSION

3.1 Compressive strength and relative humidity tests

The average results obtained for the blocks of group A are presented in Table 2 while the average results obtained for the blocks of groups B and C are presented in Tables 3 and 4, respectively.

Table 2. Results obtained for group A blocks.

Condition	Number of blocks	Relative Humidity of the Block (%)	f_{bm} (MPa)	f_{bk} (MPa)	Coefficient of Variation (%)
1	6	31%	14.08	12.60	8.03
2	6	31%	15.61	13.84	6.90
3	6	0%	19.83	19.02	2.36
4	6	32%	16.25	14.44	8.31
5	6	100%	12.94	10.61	6.35
6	6	80%	14.73	12.37	7.27

Source: Tchalekian [17]

Table 3. Results obtained for group B blocks.

Condition	Number of blocks	Relative Humidity of the Block (%)	f_{bm} (MPa)	f_{bk} (MPa)	Coefficient of Variation (%)
1	6	30%	9.87	9.30	2.13
2	6	27%	10.47	9.47	5.02
3	6	0%	12.70	12.13	2.24
4	6	32%	14.38	12.92	4.86
5	6	100%	12.13	9.66	6.86
6	6	72%	12.35	8.02	15.57

Source: Tchalekian [17]

Table 4. Results obtained for group C blocks.

Condition	Number of blocks	Relative Humidity of the Block (%)	f_{bm} (MPa)	f_{bk} (MPa)	Coefficient of Variation (%)
1	6	50%	12.57	10.51	11.23
2	6	49%	12.39	10.95	7.18
3	6	0%	14.91	12.27	10.33
4	6	38%	12.44	9.50	14.59
5	6	100%	11.74	7.89	15.00
6	6	86%	10.28	7.97	14.17

Source: Tchalekian [17]

3.2 Statistical treatment

The mean values, the mean confidence intervals (at the 95% reliability level), and the Tukey test results of the compressive strength values as a function of the experimental mental treatments for each block type are summarized in Figure 3.

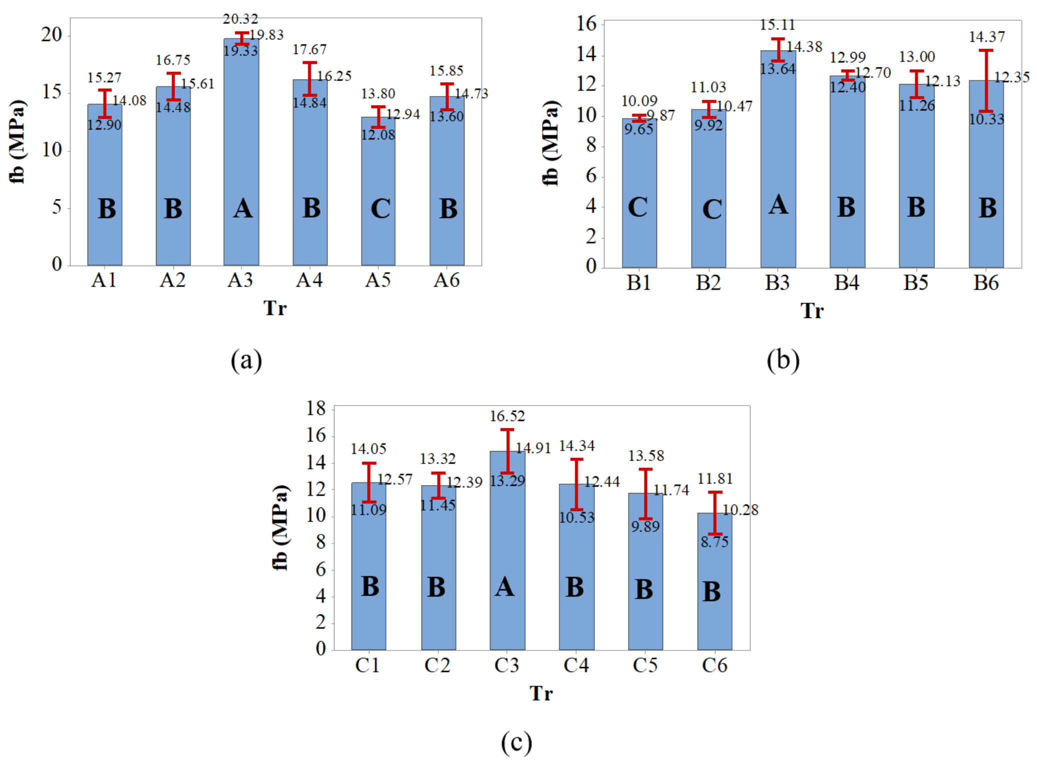

Figure 3. Results of compressive strength (f_b - MPa) for the six experimental treatments.

As shown in Figure 3a, the highest value f_b was for treatment A3, which consisted of the use of the oven at 100ºC for 24 h. The second highest mean value f_b was observed for treatments A1, A2, A4, and A6. This implies that the exposure time of 24 or 48 h of samples in an air-conditioned room did not significantly affect the compressive strength values. An increase of approximately 22% in f_b was observed when the temperature of the oven increases from 40ºC to 100ºC, and it should be noted that treatments A1, A2, and A4 were equivalent to treatments A6, which consisted of drying the block in the environment. Thus, for blocks with dimensions of 14 × 19 × 29 cm, the air-drying period of 72 h recommended by ABNT NBR 12118 [11] for blocks kept in a laboratory environment (air-conditioned room) or dried in an oven with a temperature of 40°C for 24 h, the results obtained were statistically equivalent to the results obtained without the samples undergoing any type of drying. As mentioned in the American standard, drying in an oven at 100°C for 24 h increased the compressive strength values, probably due to the presence of a previous state of tensions.

For blocks of dimensions 19 × 19 × 39 cm, as shown in Figure 3b, the highest value f_b was obtained for treatment B3, which consisted of the use of an oven at 100ºC for 24 h. The second highest mean value is to treatments B4, B5, and B6, which were considered statistically equivalent; treatments B1 and B2 resulted in the lowest mean values of compressive strength. Furthermore, as it occurred with blocks of dimensions 14 × 19 × 29 cm, the drying time of 24 or 48 h in an air-conditioned room neither significantly affect the values of compressive strength. The temperature of 100ºC increased approximately) the compressive strength between treatments B5 and B6.

As shown in Figure 3c, and as observed for the two other types of block, treatment C3 resulted in the highest mean value of f_b, the other treatments are equivalent to each other and significantly lower than treatment C3. This implies that the drying time of 24 or 48 h in an air-conditioned room did not significantly affect the values of the compressive strength nor did the temperature of 40°C or 100°C in the oven significantly affect the values of compressive strength. These results are equivalent to the conditions of saturating in water for 24 h or drying in the environment.

The mean values and confidence intervals of the mean (at the 95% reliability level) relative humidity (U_r) for the six experimental treatments per block type are presented in Figure 4.

For all types of block, the relative humidity obtained by air drying in a laboratory environment (air-conditioned room) for 24 h or 48 h and the relative humidity obtained by drying in an oven at 40°C for 24 h were similar. The drying condition in an oven at 100ºC for 24 h led to the total drying of all types of block used, implying much higher results in f_b in all cases.

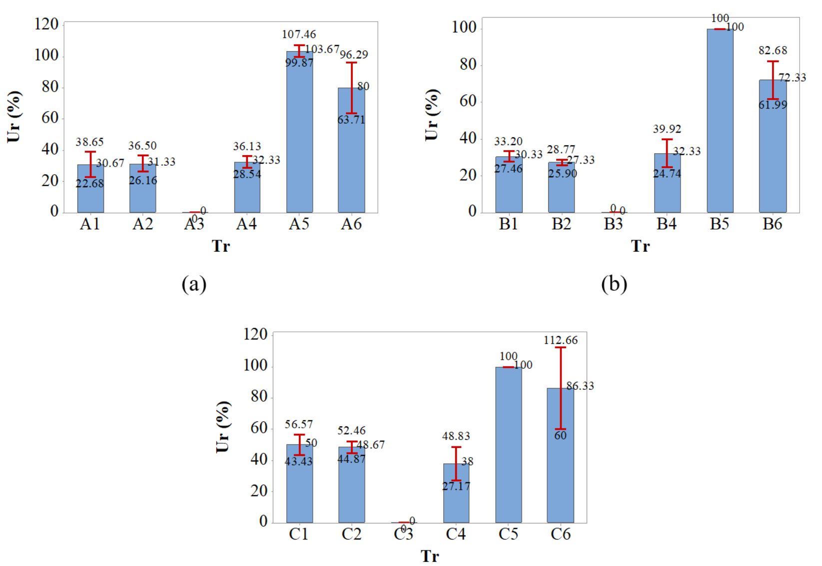

(a) (b) (c)

Figure 4. Relative humidity results (U_r - %) referring to the six experimental treatments per block type - 14×19×29cm (a), 19×19×39cm (b) and 14×19×39cm (c).

The results obtained with the use of the regression models (best adjustments based on equations 3 and 4) for the set of blocks of 14 cm (blocks A and C) and 19 cm (block B) are presented in Figure 5.

For blocks A (14 × 19 × 29 cm; f_{bk} = 12 MPa) and C (14 × 19 × 39 cm; f_{bk} = 22 MPa), as shown in Tables 2 and 4, the highest values of the mean resistance f_b are associated with the lowest relative humidity content (0%), and as the relative humidity progressively increases, the compressive strength experiences successive reductions as expected; however, for block B (19 × 19 × 39 cm; f_{bk} = 8 MPa), the resistances f_b at 0% and 100% relative humidity were practically equivalent.

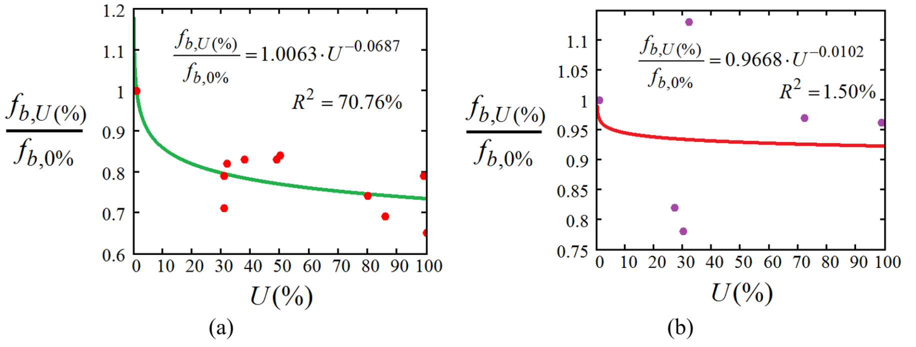

Figure 5. Ratio values between wet and dry compressive strength as a function of relative moisture content considering the grouping of the results of blocks A and C (a) and blocks B (b) alone.

As shown in Figure 5a, the model considering the set of results between $f_{b,U(\%)}/f_{b.0\%}$ and the relative humidity (U) of blocks A and C provided a coefficient of determination (R^2) approximately equal to 71%, which is considered significant by ANOVA (5% significance). In contrast, the model for block B is non-significant by the analysis of variance and small precision; R^2 value of less than 2% as shown in Figure 5b. For both the models the p-values of the normality test were higher than 0.05, which verified the validity of these models. However, the geometric (Equation 4) was observed to best adhere to the results. Only as a reference, for blocks A or C, the increase in humidity from 30% to 100% promotes a reduction of 6.41% for $f_{b,U(\%)}/f_{b.0\%}$.

4 CONCLUSIONS

This work aimed to analyze the influence of the relative humidity of masonry concrete blocks on their compressive strength. For this, sets of blocks with dimensions of 14 × 19 × 29 cm, 19 × 19 × 39 cm, and 14 × 19 × 39 cm were rectified, submitted to different humidity conditions for different periods of time and under different temperature conditions, and subsequently submitted to compressive strength test.

The conclusions of this research are the following:

- The relative humidity condition of the block influences the compressive strength of masonry concrete blocks;
- Drying concrete blocks in the oven for 24 h at a temperature of 100ºC considerably increases their compressive strength;
- Drying blocks in an oven for 24 h at 40ºC results in compressive strengths similar to those of drying the blocks at a temperature of 23ºC;
- When blocks are dried at a temperature of 23ºC, drying times of 24 h and 48 h results in similar compressive strengths;
- Blocks tested immediately after the grinding procedure have relative humidity in the range of 72–86% and compressive strengths similar to those of blocks that are saturated to 100% humidity before the test, with both cases resulting in lower resistance values than that from other humidity situations. Therefore, testing saturated or ground blocks soon after the grinding procedure will lead to lower compressive strengths.

There is no difference between waiting 24 or 48 h for the blocks to dry; it is not necessary to put them in an oven at 40ºC; just leave them in the ambient temperature and humidity of 23ºC and 40 ± 5%, respectively. Trying to accelerate the drying at 100ºC is not suitable, as it leads to increased compressive strength.

Expressions to correct the compressive strength as a function of the moisture for 14 cm and 19 cm blocks at the time of test were developed. For 14 cm blocks, the increase of humidity from 30% to 100% promotes a reduction of 6.41% for $f_{b,U(\%)}/f_{b.0\%}$...

For the 19 cm blocks, the moisture has a smaller influence on the compressive strength of the block. The reason for this behavior needs to be further studied.

ACKNOWLEDGEMENTS

The authors would like to thank the Laboratory of Structural Systems of UFSCar for their support in conducting the tests, the Foundation for Research Support of the State of São Paulo (FAPESP), process no. 2016/10460-7, and the undergraduate student Daniel Borsero Tchakelian for conducting the tests. This work was carried out with the support of the Coordination for the Improvement of Higher Education Personnel—Brazil (CAPES)—Financing Code 001. The authors would also like to thank Glasser Pisos e Pré-Moldados for donating the blocks.

REFERENCES

[1] A. M. Neville, *Propriedades do Concreto*, 5th ed. Porto Alegre: Bookman, 2016, pp. 626–627.

[2] A. F. Silva, "Avaliação da resistência à compressão da alvenaria estrutural," M.S. thesis, Fac. Eng. Ilha Solteira, Univ. Est. Paul., 2007. [Online]. Available: http://hdl.handle.net/11449/91473

[3] E. C. Busnello, "Aprimoramento tecnológico e contribuições na execução de ensaios de bloco de concreto para redução da dispersão de resultados," in *Sem. Alv. Estrut. Blocos de Concr. Concrete Show*, São Paulo, 2011. [Online]. Available: http://www.blocobrasil.com.br/downloads/file/25-nbr-12-118-2011-aprimoramento-tecnologico-e-contribuicoes-na-execucao-de-ensaios-de-bloco-de-concreto-para-reducao-da-dispersao-de-resultados-emerson-cremm-busnello

[4] National Concrete Masonry Association, *Compressive Strength Testing Variables for Concrete Masonry Units*, NCMA TEK 18-7. Herndon: NCMA, 2004.

[5] W. S. Butcher, "The effect of air drying before test: 28-day strength of concrete," *Constructional Rev.*, pp. 31–32, 1958.

[6] K. Shiina, Influence of temporary wetting at the time of test on compressive strength and Young's modulus of air-dry concrete," in *Proc. 36th Gen. Meet.*, 1982, pp. 113-115.

[7] American Concrete Institute, *ACI Manual of Concrete Inspection*, 4th ed. Detroit: ACI, 1957.

[8] American Concrete Institute, *Guide for Obtaining Cores and Interpreting Compressive Strength Results*, ACI Committee 214.4R, 2003.

[9] J. W. Galloway, H. M. Harding, and K. D. Raithby, "Effect of moisture changes of flexural and fatigue strength of concrete," *Transp. Road Res. Lab.*, no. 864, 1979.

[10] J. S. Guo and P. Waldron, "An elastic model to quantify the effect of moisture on the mechanical properties of concrete at the time of test," *Mag. Concr. Res.*, vol. 53, no. 3, pp. 151–162, 2001.

[11] Associação Brasileira de Normas Técnicas, *Blocos Vazados de Concreto Simples para Alvenaria – Métodos de Ensaio – Versão Corrigida*, NBR 12118:2013, 2014.

[12] A. C. S. Bezerra, "Influência das variáveis de ensaio nos resultados de resistência à compressão de concretos: Uma análise experimental e computacional," M.S. thesis, Univ. Fed. Minas Gerais, 2007. [Online]. Available: http://hdl.handle.net/1843/ISMS-74UPHH

[13] S. Popovics, "Effect of curing method and final moisture condition on compressive strength of concrete," *ACI J.*, vol. 83, no. 4, pp. 650–657, 1986.

[14] American Society for Testing and Materials, *Standard Test Methods for Sampling and Testing Concrete Masonry Units and Related Units – Designation*, C140/C140M-16, 2016.

[15] Australian/New Zealand Standard, *Masonry Units, Segmental Pavers and Flags – Methods of Test*, AS/NZS 4456.4:2003, 2003.

[16] BSI Standards, *Methods of Test for Masonry Units*, BS EN 772-1:2011+A1:2015, 2015.

[17] D. B. Tchalekian, *Avaliação da Influência da Umidade na Resistência à Compressão de Blocos Vazados de Concreto – Relatório Final de Iniciação Científica*. São Carlos: Universidade Federal de São Carlos, 2016.

[18] Associação Brasileira de Normas Técnicas, *Blocos Vazados de Concreto Simples para Alvenaria – Requisitos – Versão Corrigida*, NBR 6136:2016, 2016.

Author contributions: G. A. Parsekian: supervision, experimental methodology, experimental analysis, writing; A. L. Christoforo: statistical methodology, statistical analysis, writing; A. D. E. Mazzú: conceptualization, writing, formatting; G. M. Dalfré: writing.

Editors: Fernando S. Fonseca, José Luiz Antunes de Oliveira e Sousa.

IBRACON Structures and Materials Journal
Revista IBRACON de Estruturas e Materiais
ISSN 1983-4195 ismj.org

ORIGINAL ARTICLE

Combined evaluation of oscillatory rheometry and isothermal calorimetry for the monitoring of hardening stage of Portland cement compositions blended with bauxite residue from Bayer process generated in different sites in Brazil

Avaliação combinada de reometria oscilatória e calorimetria isotérmica para o monitoramento do estágio de endurecimento de composições de cimento Portland misturadas com resíduos de bauxita do processo Bayer coletados em diferentes locais no Brasil

Roberto Cesar de Oliveira Romano[a]
José Augusto Ferreira Sales de Mesquita[a]
Heitor Montefusco Bernardo[a]
Danilo Aguiar Niza[a]
Marcel Hark Maciel[a]
Maria Alba Cincotto[a]
Rafael Guiliano Pileggi[a]

[a]Universidade de São Paulo – USP, Escola Politécnica, Departamento de Engenharia de Construção Civil, Laboratório de Microestrutura e Ecoeficiência de Materiais, São Paulo, SP, Brasil

Received 08 April 2020
Accepted 10 July 2020

Abstract: Bauxite residue (BR), a by-product of alumina and aluminum production, consists of high aluminum, silica, and iron content, and sodium from the bauxite ore digestion during the Bayer process. This waste is still being disposal into the lakes of mud, causing some environmental problems. So, the search for its application has gained interest. Studies reported in literature point out that one of the most promising applications is in association with Portland cement, which can also help to reduce the environmental impact caused by the CO2-emissions in its production. In this work, a combined evaluation of oscillatory rheometry and isothermal calorimetry was performed for the monitoring of the hardening stage of Portland cement (PC) compositions blended with BR generated in different sites in Brazil. The time-sweep test was applied to obtain the consistency gain of suspensions over-time, allowing us to understand the physical parameters of consolidation, while the changes in the hydration reaction showed considerable differences in the chemical contribution. As a conclusion, it was clear the impact of each BR, mainly due to the aspects related to soluble aluminates, silicates, and sodium, which in association with the soluble ions from PC, affected the chemical reaction and agglomeration/flocculation forces of particles.

Keywords: rheological properties, reuse of bauxite residue, Portland cement, chemical reactions.

Resumo: O resíduo de bauxita (BR), um subproduto da produção de alumina e alumínio, apresenta alto teor de alumínio, silício e ferro proveniente da bauxita, e sódio da digestão do minério durante o processo Bayer. Esse resíduo ainda está sendo descartado nos lagos de lama, causando alguns problemas ambientais. Assim, a busca por uma aplicação em larga escala tem ganhado cada vez mais atenção. Estudos relatados na literatura apontam que uma das aplicações mais promissoras está associada ao cimento Portland, o que também pode ajudar a reduzir o impacto ambiental causado pelas emissões de CO_2 durante a produção do ligante hidráulico. Neste trabalho, uma avaliação combinada de reometria oscilatória e calorimetria isotérmica foi realizada para o monitoramento do estágio de endurecimento de composições de cimento Portland (PC) misturadas com BR

Corresponding author: Roberto Cesar de Oliveira Romano. E-mail: rcorjau@gmail.com
Financial support: Alcoa Foundation, Companhia Brasileira do Alumínio – CBA, FAPESP, CNPq.
Conflict of interest: Nothing to declare.

geradas em diferentes locais no Brasil. O ensaio de varredura no tempo foi aplicado para monitorar o ganho de consistência das suspensões ao longo do tempo, permitindo avaliar os parâmetros físicos da consolidação, enquanto as mudanças na reação de hidratação mostraram as diferenças consideráveis realacionadas com a contribuição química. Como conclusão, ficou claro o impacto de cada BR, principalmente devido aos aspectos relacionados aos aluminatos, silicatos e sódio solúveis, que em associação com os íons solúveis do PC, afetaram a reação química e as forças de aglomeração/floculação das partículas.

Palavras-chave: propridades reológicas, resuso de resíduo de bauxita, cimento Portland, reação química.

How to cite: R. C. O. Romano et al., "Combined evaluation of oscillatory rheometry and isothermal calorimetry for the monitoring of hardening stage of Portland cement compositions blended with bauxite residue from Bayer process generated in different sites in Brazil" *Rev. IBRACON Estrut. Mater.*, vol. 14, no. 2, e14211, 2021, https://doi.org/10.1590/S1983-41952021000200011

INTRODUCTION

Bauxite residue (BR), commonly known worldwide as red mud, is a highly alkaline material generated from the production of alumina in the Bayer process, in which bauxite is dissolved in caustic soda. A common estimative is that 1 ton of BR is generated for each 1 ton of alumina produced (i.e. the amount of aluminum oxide trihydrate produced and expressed as 100%, nominal aluminum oxide (Al_2O_3) equivalent, independently of further processing), but some statistics illustrate that this proportion can variate depended on the ore richness, being between 0.8 and 1.3 [1].

Independently of that, the global BR inventory reached around 4.6 billion tons in 2018, with a worldwide production rate of almost 200 million tons per year. Brazil has the third-largest bauxite deposit on the planet, being the fourth-largest producer of alumina and is the fifth country in the exportation of aluminum or alloys. Accompanying the advancement of this industry, the generation of waste has grown more and more, and the search for applications for BR is an alternative that has gained strength year-on-year [2]–[8].

So, there has been an important amount of work done in recycling and reusing this kind of material, but despite the development of some minor applications, and the fact that no large-scale application has yet been achieved the residue still has to be discarded in lakes of mud [5], [9], [10].

Romano et al. [11], [12] applied different methods for monitoring the chemical reaction of Portland cement in association with using bauxite residue, detecting, beyond the ordinary hydrated products of pure Portland cement, the formation of sodium silicoaluminate hydrate (NASH), and calcium aluminate. Fujii et al. [13] evaluated the impact of using superplasticizers in the consolidation of Portland cement suspensions blended with bauxite residue, concluding that the stage of hardening was considerably affected by the kind and content of admixture. Dodoo-Arhin et al. [14] evaluated the impact of using BR from the region of Awaso in Ghana, calcined at 800 °C, in the properties of pavements produced with microconcrete of Portland cement concluding that up to 5% of substitution of PC there was not any loss in the mechanical strength or water absorption. Krivenko et al. [15] developed some alkali-activated concretes using a large amount of bauxite residue, pointing out for the formation of C-S-H, klinoferrosilite ($FaSiO_3$) and lawsonite, ($CaAl_2[Si_2O_7](OH)_2.H_2O$). The authors evaluated the mechanical strength, and leaching of heavy-metals and radiative elements, concluding that the components are following the standardized specifications for application in roads. Romano et al. [16] showed the impact of using bauxite residue in microconcrete of Portland cement and did a comparison with other kinds of ordinary supplementary cementitious materials, concluding that this practice is technically viable. Pontikes and Angelopoulos [17] presented a review of some applications of bauxite residue in association with Portland cement, providing a critical point of view of the research conducted in the last 40 years. In this paper, the authors pointed out that the main barrier for the transition from the laboratory scale to the industry is the economic aspect.

This is a fact, and even these days, the cost of disposal is between 4 and 12 dollars per ton, and this is part of the difficulty in the search for a viable solution for this huge residue generation [18].

However, for the construction of these deposits, it is necessary to manage large areas, affecting considerably the local fauna and flora [5], [10], [19], [20]. Additionally, there is always the possibility of an environmental catastrophe, such as that occurred in Hungary, October 2010, causing a state of emergency of 3 cities around the lake [11].

Evans [21] did another review, considering the storage and disposal of bauxite residue in the 19th century, discussing the changes in the environmental aspects. Some successful remediation and rehabilitation trends in Jamaica have been described, as well as proposed uses for BR. The survey indicates the considerable number of patents and technically feasible proposals for the use of BR, but that only about 4 million tons are used productively. Therefore, the author discusses the main barriers and why they are not used on a large scale, even with proven technical feasibility. Besides, it is mentioned that the use in association with cement or cementitious components, the raw material for steelmaking, landfill closure, soil improvement, and road construction, are the most promising alternatives.

According to some authors, the high alkalinity is the critical factor restricting complete utilization of bauxite residues, whilst the application of alkaline regulation agents is costly and difficult to apply widely [1], [11], [17].

It was also observed that one of the biggest problems is that BR shows a considerable chemical, mineralogical and physical variation from site to site, and a suitable solution for one collected waste cannot be adequate for another one [8], [18]. For instance, monitoring did by Garcia [22] indicates that iron content in the residue can vary from 20 to 60%, aluminum content from 10 to 58%, silica from 3 to 65%, and sodium from 0.4 to 15%, impacting considerably on the mineralogical phases.

Additionally, the strongly alkaline nature of bauxite residue and its ions leaching potential ability, are other drawbacks that need to be considered for most valorization routes [7]. So, as the large variability of BR can make difficult to implement of a single solution, in this first step of the study of this material the main goal is to evaluate the impact of the kind and content of different bauxite residues on rheological properties and chemical reactions of cement, a stage that impacts considerably on the microstructural development of cementitious materials.

MATERIALS AND EXPERIMENTAL PROGRAM

The purest Brazilian Portland cement was the binder choose to develop this work. It is referred to as a CPV according to the Brazilian standard [23]. Bauxite residues studied are from three different sites described as NE-BR - São Luís - MA, SE-BR1 - Poços de Caldas (MG), and SE-BR2 - Aluminio (SP), obtained from the Bayer process of aluminum production in plants from Northeast (NE) or Southeast (SE) regions. As the residues were received wet and in clods, it was necessary a prior preparation: drying at 105°C for 24 hours, grinding in a mill, and sieving with a 106-micron mesh sieve.

Characterization

X-ray fluorescence (FRX), in PANalytical equipment, model Minipal Cement, and X-ray diffraction (XRD) in a PANalytical X'PERT-MPD, were used to determine the chemical and mineralogical composition of each raw material, respectively, following the procedures reported by Romano et al. [12], and the thermal decomposition was quantified using a Netzsch thermobalance, model STA409EP [24].

The particle size distribution was measured on a laser granulometer, Helos (Sympatec) [25], the specific surface area was determined by N2 adsorption at 77K in a Belsorp Max equipment [12], the real density was determined by gas He pycnometry in Quantachrome equipment, MVP 5DC, while the pozzolanic index was defined by applying the method described in the NBR 15895/10 - Pozzolanic materials - Modified Chapelle method. The images of scanning electron microscopy (SEM) were obtained using a Quanta 600FEG instrument.

Preparation of the pastes

Pastes were produced maintaining the water-to-solid ratio of 0.50, using a composition with pure cement (i.e., for reference) and 9 more compositions with partial replacement, in weight, of 5, 10, and 20% of cement by the bauxite residues. Table 1 illustrates the evaluated compositions, indicating the nomenclatures used for each one.

Table 1 Compositions evaluated in the study.

Nomenclature	Portland cement	NE-BR	SE-BR1	SE-BR2
CPV	100	-	-	-
5NE-BR	95	5	-	-
10NE-BR	90	10	-	-
20NE-BR	80	20	-	-
5SE-BR1	95	-	5	-
10SE-BR1	90	-	10	-
20SE-BR1	80	-	20	-
5SE-BR2	95	-	-	5
10SE-BR2	90	-	-	10
20SE-BR2	80	-	-	20

NE – Brazilian northeast; SE – Brazilian southeast; BR – bauxite residue. The number described in the Nomenclature column indicates the percentage of Portland cement replacement by BR.

All dry components were blended and placed into a metal container. The water was added, and 30 seconds was allowed for the initial wetting of the particles. After that, mechanical dispersion was applied at a constant speed of 10,000 rpm for 90 seconds using a Cowles' impeller.

Isothermal calorimetry

The heat released during the hydration reaction of Portland cement was monitored for 48 hours in an isothermal calorimeter, TAM Air model, TA Instruments, following the procedure described by Romano et al. [24]. The stages of hydration reaction were discussed according to reported in the same work.

Oscillatory rheometry

Tests were performed in a Mars 60, Haake rheometer, using a parallel-plate type geometry. Samples were prepared following the procedure described in Fujii et al. [9], and all tests were performed at a temperature of 23 °C. Time sweep test was the procedure choose for the monitoring of gain of consistency over time, performed maintaining the strain at 10^{-4}, and frequency of 1 Hz for 6 hours.

The rheological evaluation is fundamental for the comprehension of the phenomena that can affect the stage of transportation, application, workability, and time stability. In this work, the changes promoted by BR addition were monitored using the time sweep test: the application of strain and frequency in the linear viscoelastic region (LVR) makes it possible to monitor the increase in the particle agglomeration forces without any external interference in the formed microstructure, i.e. without the microstructure breaking down. As a result, it was measured the gain on consistency over the time, represented by G', of each blended suspension.

RESULTS AND DISCUSSIONS

Materials characterization

Table 2 presents the chemical analysis of each material. The iron content in the waste NE-BR, 56%, was higher than for the other residues, 29.5% and 37.1%, respectively for SE-BR1 and SE-BR2. Due to this large amount found in the waste, some works are reported in literature trying to recover iron from the bauxite residue [26], [27], but the process is not yet economically viable, and the remaining waste (with a low amount of iron) is still discarded. Other works are purposed to understand the mechanisms of iron interaction with cementitious materials for predicting the service life and design of reinforced concrete structures [28].

The large amounts of aluminum and silica illustrate, respectively, the low efficiency of the Bayer process and the considerable amount of impurities in the bauxite ore. Kaußen and Friedrich [29], evaluated a way to recover Al from bauxite residue using dissolution in caustic soda at high pressure followed by thermal treatment, but even with an efficiency around 90%, the contamination with silica is still a problem, due to the complete dissolution of aluminum silicates.

The loss of ignition comprises the humidity, CO_2 from the decomposition of carbonates, and combined water from zeolites, goethite, and gibbsite dehydroxylation.

The ratio between aluminum, calcium, and silicon oxides obtained for these residues, illustrate that both are in accordance with the results presented by Romano et al. [12] in the ternary diagram of supplementary cementitious materials.

The SE-BR1 has higher alkalinity due to the higher amounts of Na_2O and K_2O content. This is an important characteristic to be observed because the alkalis content can limit the use of bauxite residue as a supplementary cementitious material.

The higher the amount of soluble ions, the higher the susceptibility to leaching if these elements do not participate in hydrated compounds formation.

As the hydration of Portland cement is governed by the dissolution/precipitation and by the equilibrium shifting, the soluble ions inserted in the blends replacing partially Portland cement by different kinds of bauxite residue directly affects the chemical reaction.

The soluble ions of each residue were quantified for this work mixing 10 g of residue in 100 ml of deionized water. This suspension was mixed for 30 minutes and then kept at rest for more 30 minutes. After this time, the water was separated from the powder by filtration and used in the determinations. For the determination of soluble ions, it was applied the recommendations of ASTM C114-18: *Standard Test Methods for Chemical Analysis of Hydraulic Cement*, and the Brazilian standard NBR 13810/1997: *Water – Determination of metals – Method determination of metals spectrometric method by flame absorption*.

Table 2 Chemical composition of Portland cement and bauxite residues.

Determinations	% (dry basis)			
	CPV	NE-BR	SE-BR1	SE-BR2
Calcium oxide (CaO)	60.8	0.72	2.76	4.58
Silicon oxide (SiO2)	19.2	10.0	16.6	12.8
Aluminum oxide (Al2O3)	4.94	11.5	18.7	16.5
Iron oxide (Fe2O3)	2.97	56.6	29.5	37.1
Sulfur oxide (SO3)	4.47	0.32	0.31	1.19
Magnesium oxide (MgO)	0.67	und	0.07	0.09
Sodium oxide (Na2O)	0.15	6.43	8.41	7.38
Potassium oxide (K2O)	0.70	0.32	2.21	0.42
Alkaline Eq. (%K2O x 0.658 + %Na2O)	0.61	6.64	9.86	7.18
Titanium oxide (TiO2)	0.26	2.91	4.96	3.64
Phosphorus oxide (P2O5)	0.27	0.06	0.50	0.55
Zirconium oxide (ZrO2)	-	0.47	0.74	0.28
Cromium oxide (Cr2O3)	-	0.09	0.03	0.09
Niobium oxide (Nb2O5)	-	0.02	0.22	0.02
Other oxides	1.70	0.06	1.29	0.24
Loss on ignition (LOI)	3.87	10.5	13.7	15.4

Results obtained are presented in Table 3, illustrating that the residues SE-BR2 and SE-BR1 presented a larger amount of soluble ions than NE-BR. This information is relevant because, as will be seeing later, the residues from SE Brazilian region influenced the chemical reaction more than NE.

Table 3 Soluble ions quantified mixing 10g of residue in 100ml of deionized water. Results are presented in mmol/kg of BR.

Ions	NE-BR	SE-BR1	SE-BR2
Na+	89.8	109.0	123.3
K+	0.88	1.76	0.88
AlO2-	7.94	2.27	3.40

Figure 1 presents the XRD curves for bauxite residues and Table 4 presents the mineralogical composition of the three samples.

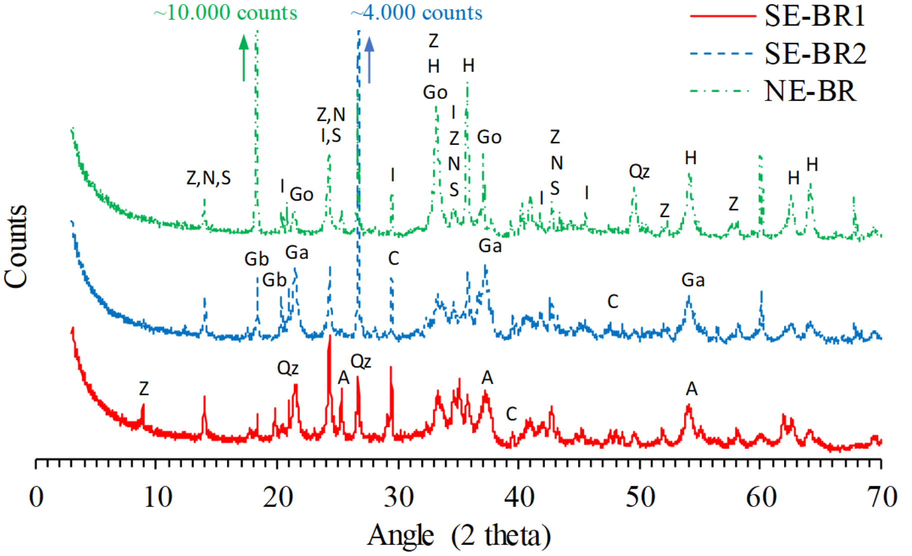

Figure 1. X-ray diffractograms of bauxite residues.

Table 4. Mineralogical phase, molecular formula, and consulted the file number of the phases found in the bauxite residues.

Mineralogical phase	Molecular formula	Consulted file	Main peaks (°)
Zeolite (Z)	1.08Na2O·Al2O3·1.68SiO2·1.8H2O	00-031-1271	24.2*, 13.9, 8.97
Sodium aluminum silicate nitrate (N)	Na7.9(Al6Si6O24)·(NO2)0.9·(NO3)1.2	01-082-1080	24.3*, 14.0, 34.6
Illite (I)	K2Al4Si8O24	96-901-3720	24.4*, 29.1, 35.0
Sodalite (S)	Na8Al6Si6O24Cl2	96-900-3327	24.3*, 13.9, 34.7
Hematite (H)	Fe2O3	00-013-0534	33.3*, 54.2, 35.7
Goethite (Go)	FeO(OH)	96-900-3080	21.6*, 37.2, 33,7
Gibbsite (Gb)	Al(OH)3	96-101-1082	18.3*, 20.3, 20.6
Quartz (Qz)	SiO2	96-500-0036	26.6*, 50.1, 20.9
Calcite (C)	CaCO3	01-072-1652	29.5*, 48.6, 47.7
Anatase (A)	TiO2	96-900-8214	25.3*, 37.8, 53.9

* 100% of the intensity

The three main peaks of each mineralogical phase are illustrated, being the gibbsite, goethite, and hematite the most important phases. Sodalite, due to the bauxite ore digestion with caustic soda, a zeolite, and a sodium aluminum silicate nitrate phases were also observed in all residues. The considerable amount of potassium quantified by X-ray fluorescence was detected as illite, mainly in the SE-BR1.

The CPV cement XRD diffractogram (not shown) indicated the main clinker phases, gypsum, and a small content of syngenite.

Figure 2 shows the DTG results, confirming that between 30 and 150°C there is the moisture evaporation; around 200°C there is a peak referred to the loss of zeolitic water; from 210 to 295°C the loss of water, related to the conversion of gibbsite in g-alumina; between 295 and 420°C the transformation of goethite to hematite; around 520°C there is an indication of diaspore decomposition, and from 550°C to 700°C related to calcite decomposition.

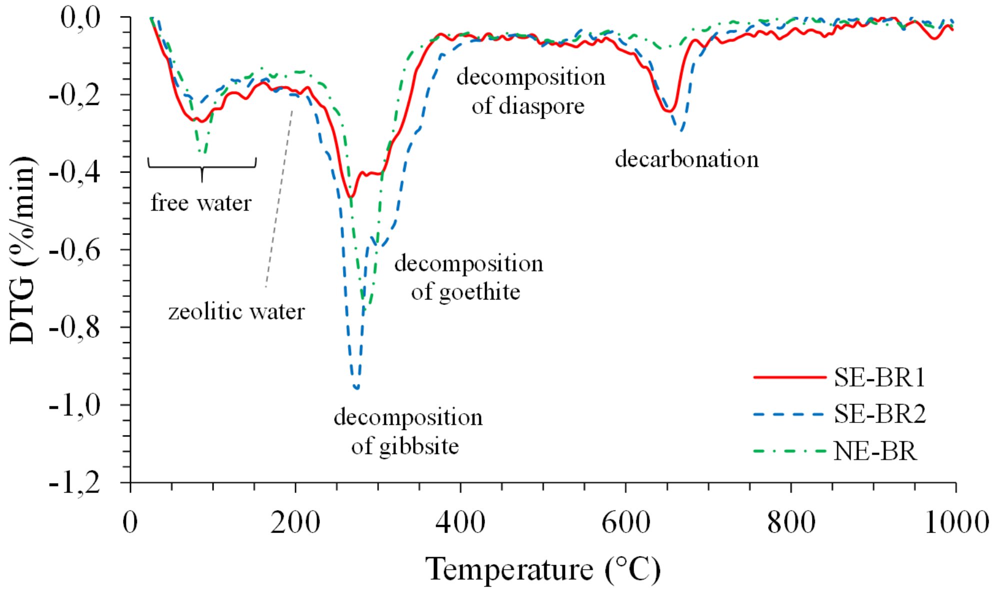

Figure 2 Derivative of mass loss (DTG results) of bauxite residues.

The lower decomposition referred to goethite and gibbsite in the sample SE-BR1 is convergent with the results of chemical analysis when was observed lower amount of iron and aluminum than in the other residues. This information will be relevant for the explanations about the chemical reaction of blended Portland cement with this residue, presented later. In the same way, the calcium content detected by FRX had a direct correlation with the carbonates quantified by thermogravimetric analysis (TGA).

Figure 3 illustrates the particle size distribution of each material and Table 5 presents d_{10}, d_{50}, and d_{90}, specific surface areas (SSA), and real densities. The high amount of larger particles in NE-BR can explain, in part, the sensible displacement of TGA-curve between 210 and 380°C, difficulting the evaluation of Al and Fe phases by thermal analysis due to the overlap of both decomposition phenomena.

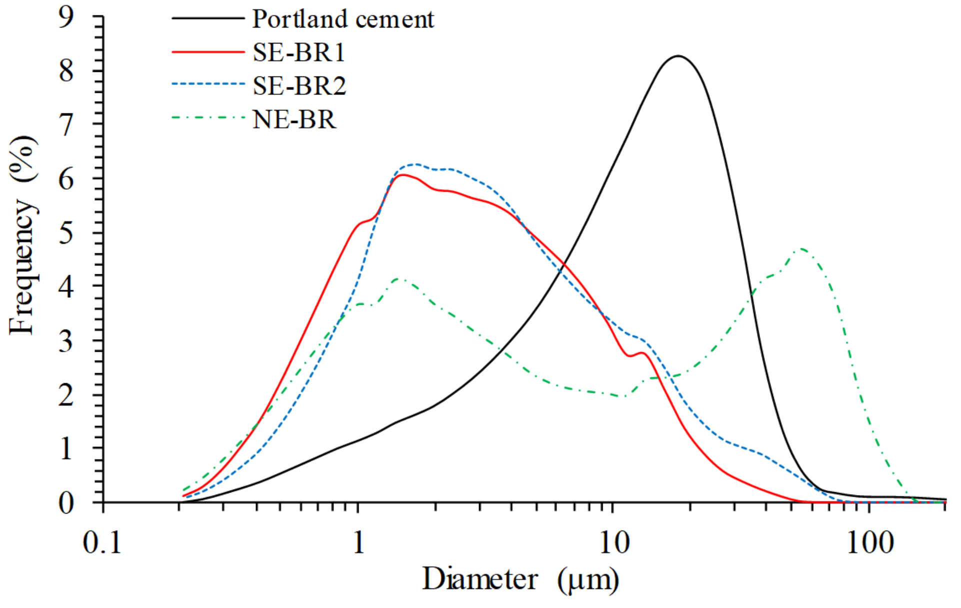

Figure 3 Particle size distribution of cement and bauxite residues.

Table 5 Real densities, specific surface area (SSA), d10, d50, and d90 of each material.

	Portland cement	NE-BR	SE-BR1	SE-BR2
d_{10} (mm)	5.90	0.65	0.60	0.75
d_{50} (mm)	21.8	5.60	2.35	2.80
d_{90} (mm)	58.3	56.0	11.0	14.0
SSA (m^2/g), BET	1.29	8.85	16.6	13.5
Real Density (g/cm^3)	3.10	3.28	2.96	2.98

Samples of SE-BR present similar particle size extension and real density, but the sample NE-BR has coarse particles and higher density, probably in function of the large amount of iron, difficulting the ground. The SSA of three residues is at least 8 times higher than Portland cement, which affects directly the chemical reaction and development of microstructure during the hardening step: the higher the SSA, the higher the water demand to moisten the particles and start the flow.

A common doubt about the characteristics of bauxite residue is its potential to be considered as a pozzolan. Pozzolans are materials consisting of silica and alumina which, in the presence of water, combine with calcium hydroxide resulting in water-stable compounds with binding properties. However, the three BR evaluated in this work did not present pozzolanic activity according to the requisites of Brazilian standard, i.e. the $Ca(OH)_2$ consumption was lower than 436 mg per grams of each BR.

For illustration, Figures 4 to 6 present the SEM images, highlighting some different particles found in the three bauxite residues, and the energy-dispersive X-ray spectroscopy analysis (EDS) confirming the presence of Fe, Al, Si, Ti and Na as the main elements; it was also observed the presence of Zr, Mg, Mn, Ca and K in low proportion. However, the semi-quantitative evaluation is not being presented due to some concerns about the inaccuracy of this method for this purpose.

NE-BR

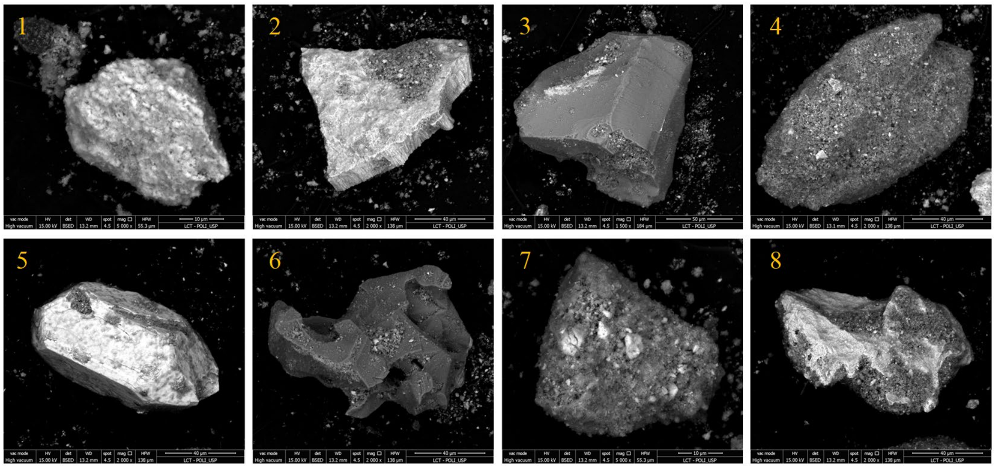

Figure 4 SEM images of NE-BR. EDS illustrates the presence of: 1 - Fe, Al, Si; 2 - Fe; 3 - Ca, Si, Al, Mg; 4 and 7 - Fe, Al, Si, Na, Ti; 5 – Zr, Si, Al, Fe, Na; 6 - Si; 8 - Al, Si, Na

SE-BR1

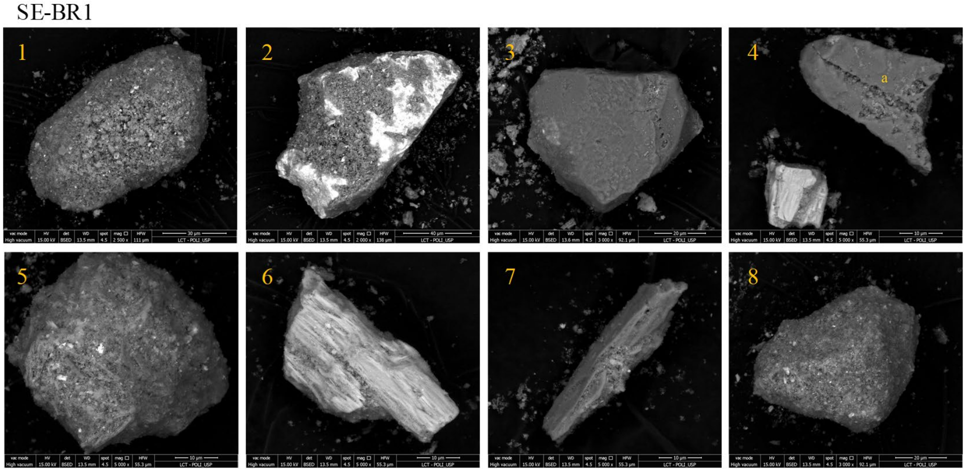

Figure 5. SEM images of SE-BR1. EDS illustrates the presence of: 1 and 8 - Al, Si, Na; 2 – Zr, Si, Fe; 3 - Si; 4a – Si; 5 – Al, Si, Fe, Na; 6 – Fe, Al, Na, Ti; 7 – Al, Si, K.

SE-BR2

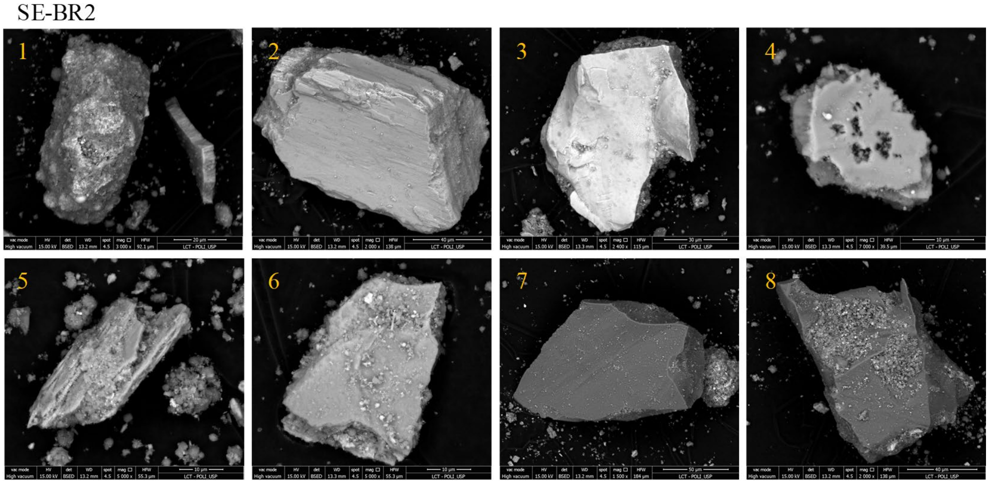

Figure 6. SEM images of SE-BR2. EDS illustrates the presence of: 1 – Al; Fe; Si, Na, Ti; 2 – Al; Fe; 3. Ti, Fe, Mn; 4 – Al, Fe; 5 – Al, Fe, Si, Na; 6 – Al, Fe; 7 and 8 – Si.

Monitoring the hardening stage of pastes

Cement hydration reaction

Figure 7 shows the heat flow released during the hydration of CPV blended with different BR content: (a) NE-BR, (b) SE-BR1, and (c) SE-BR2. The heat released was normalized according to cement content. Even with the changes promoted using different BRs up to 24h of monitoring, in this work the main goal was evaluating the very early age of development of microstructure combining the results of chemical reaction and rheometry. So, the cumulative heat during the first 5 hours is illustrated on the right in Figure 7, showing the chemical contribution to the hardening process, at a very early age of cement hydration reaction. In this stage, all compositions with BR presented a delay of heat released, but it was more intense using the SE-BR1.

It is worth to be mention that the wetting period was excluded from this illustration due to the inaccuracy of the method applied in this work and the combined evaluations presented later (rheology vs calorimetry) will be performed using these data.

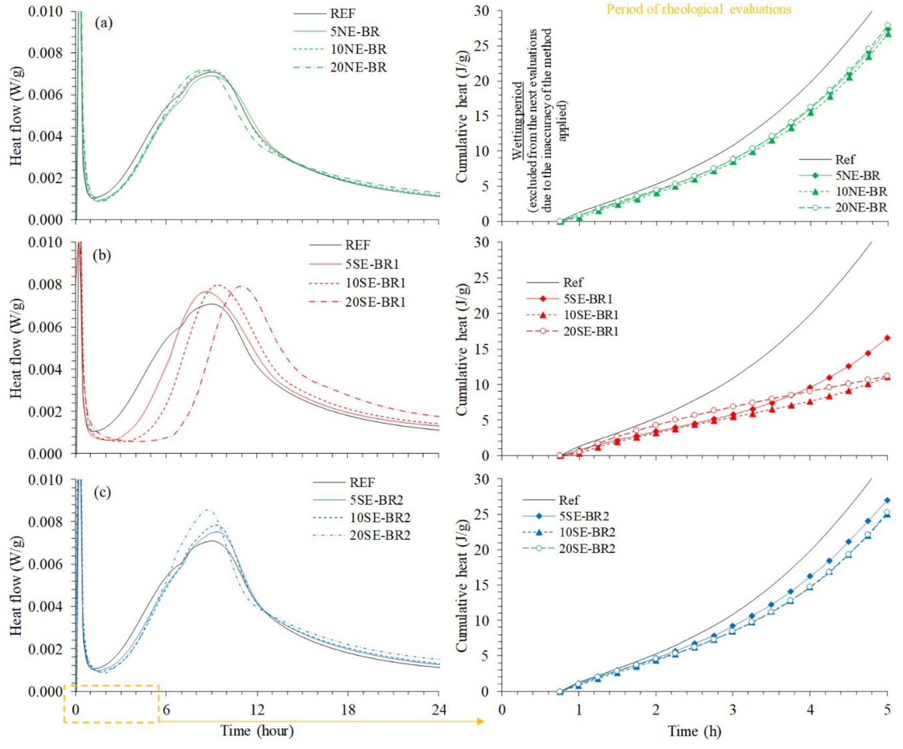

Figure 7 Heat flow released during the hydration reaction of Portland cement blended with different BR types and content. In (a) is presented the results for NE-BR, in (b) for SE-BR1, and (c) SE-BR2. On the right are presented the cumulative heat up to 5 hours of evaluation, the period of rheological evaluations. It was excluded the heat released during the wetting period due to the inaccuracy of the method applied in this work for this period.

The use of mineral additions affects the dilution of clinker phases and the nucleation [11], [12], so changes on the heat released represents the impact of different kind and content of bauxite residue addition.

The use of bauxite residue in association with Portland cement makes the hydration reaction increasingly complex: the presence of soluble aluminates in contact with Ca^{2+}-ions from Portland cement, produces calcium aluminates, and it can accentuate or cause a delay in the hydration reaction, depending on the concentration of dissociated aluminates from bauxite residue [19], [24], [30]–[38]. Because of this, it was not observed in this work, a tendency in the function of the kind and content of bauxite residue [12], [39]–[41].

There is a consensus in the literature that the presence of aluminates, in excess, causes a delay in the nucleation of C-S-H, because the precipitated containing Al-ions does not work as a nucleation seed [24], [42]. Additionally, during the AFt formation, the Al-ions are quickly consumed, due to the dissolution of alkaline sulfates of cement. There also is an inhibitory effect, even at lower concentrations, which can affect the dissolution during the early hydration of C_3S.

Converging with what was reported by Nicoleau et al. [41] using other materials, the kind and content of bauxite residue used replacing the Portland cement influenced considerably the formation of Si-O-Al bonds, affecting the induction period.

In the same way, there is no convergence about the Na^+-ion solubilized from the bauxite residues used in this work: it was observed the most impacting delay in the chemical reaction of compositions blended with SE-BR1, but it was quantified an intermediary value comparing with the other BRs.

Changes in the induction period were higher using the substitution by SE-BR1. Scrivener et al. [43] using the geochemical theory of dissolution, suggest the growing of disorganized C-S-H on the original grains and finishing the induction stage even at Ca^{2+} undersaturation.

Applying the concept presented by Romano et al. [12] the monitoring of heat flow in the acceleration period showed that the nucleation effect of powder was negligible using NE-BR, due to a large amount of coarse particles, but considerable in the compositions with SE-BR1 and SE-BR2. During this period there is a dynamic equilibrium, and removing the ions from the solution by precipitation of hydrated compounds, the under-saturation of alite will increase, causing an increase in the dissolution rate up to the replacement of ions in solution [12]. In this way, using different kinds and contents of bauxite residue, it was observed distinct dissolution rates.

During the deceleration stage, there is a considerable decrease in the available surface for the growth of hydrated products, so they start to impinge. In this way, the calcium silicate hydrate formation and portlandite are occurring slowly [12]. At that stage, the presence of the larger amount of aluminates inserted using bauxite residue affects the formation of ettringite (AFt) and conversion in monosulfoaluminate (AFm) [24].

Gain on consistency over time

Figure 8 represents the impact of using bauxite residue collected from the different sites in Brazil in the gain on consistency over the time (G') of blended Portland cement.

The storage modulus, G', express the elastic response of material during the transition from fluid to elastic behavior in the consolidation. At the oscillatory test, part of the applied strain (at a controlled frequency) is dissipated by the energy dissipation mechanisms in the bulk of cement paste, and another part is stored in the material: higher G' denotes more solid-like property. So, during the time sweep test, G' was monitored under a quasi-static condition, indicating the development of the suspension stiffening when at rest and that can be related to the applied or molded material.

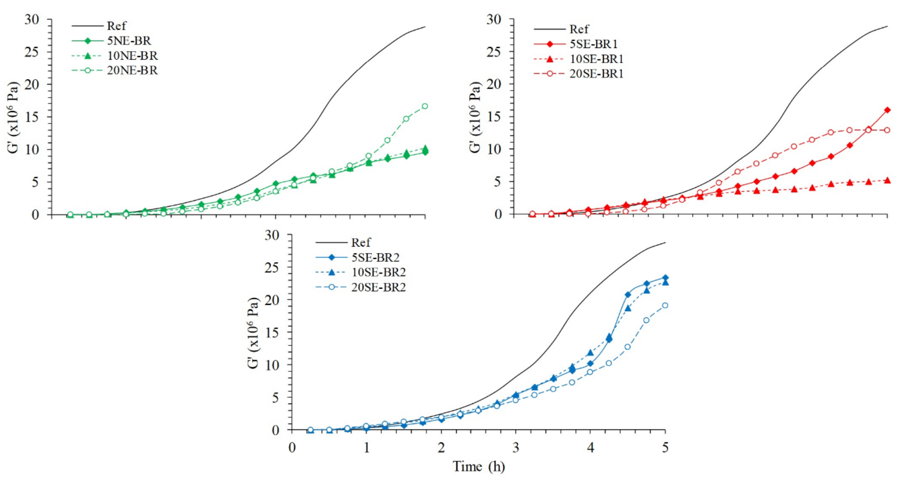

Figure 8 Gain on the consistency of blended pastes. From top to bottom are presented the results for NE-BR, SE-BR1, and SE-BR2, respectively.

For the compositions with NE-BR the impact of residue content is negligible up to 4 hours of monitoring, and after this time only in the composition with the highest amount of BR presented an accentuated growth in G', showing the increase in the particle agglomeration.

For the other compositions, a similar behavior was observed up to 2.5 hours of monitoring, independently of kind of bauxite residue. However, after this time, the gain on consistency promoted by the SE-BR2 was more accentuated than by the SE-BR1 and close to the reference paste.

These alterations in viscoelastic behavior were irreversible due to the hydration reactions of the cement. Thus, an understanding of the chemical influence related to this stage of fluid-to-solid transition is important for the comprehension of how those changes occurred.

Combined evaluation: G' vs cumulative heat

A combined evaluation of the results obtained in the different tests can provide a clearer notion of the cause-effect relationship in the hardening process of the cementitious suspensions evaluated as a function of the type and content of bauxite residue. It was possible to visualize that the kinetics of agglomeration and the kinetics of chemical reactions are phenomena that occur in parallel and are directly related.

Figure 9 shows the physicochemical contribution to the hardening stage of each suspension. In (a) is presented the results for NE-BR, in (b) for SE-BR1, and (c) SE-BR2.

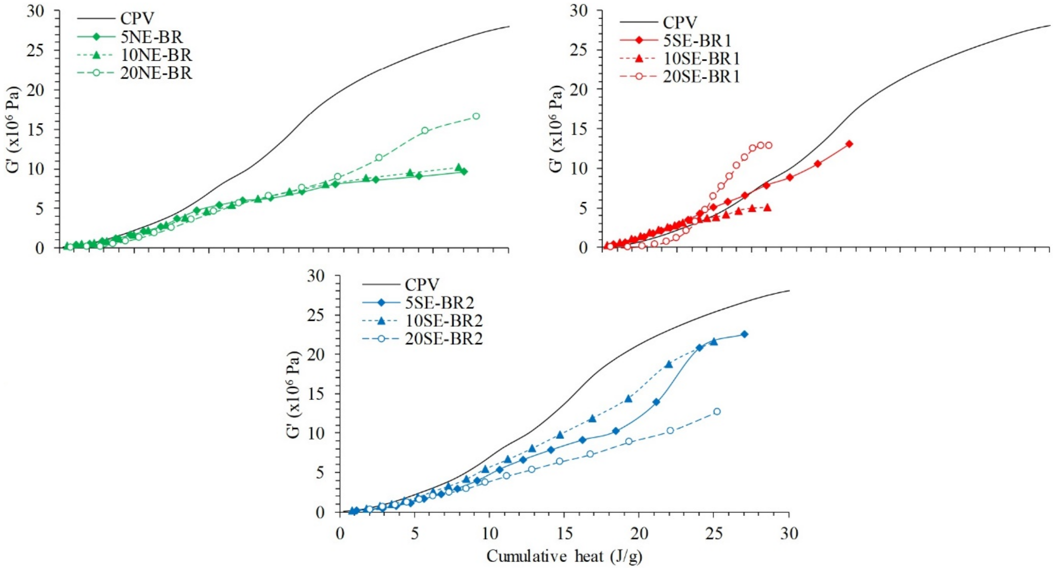

Figure 9 **M**onitoring the hardening stage combining the results of oscillatory rheometry and isothermal calorimetry. In above is presented the results for NE-BR, in the middle for SE-BR1 and below for SE-BR2.

In summary, using bauxite residues of these three distinct sites, different developments of microstructure were observed. In the compositions with NE-BR, the use of residue had a negligible influence on the cement hydration and on the gain on consistency over time. The only difference was observed in the composition 20NE-BR after 4 hours of monitoring the G'. On the other hand, the most impacting influence of the SE-BR1 was in the chemical reaction, causing a considerable delay for the development of hydrated compounds, but the gain on consistency was also affected by the content of residue. In the compositions with partial replacement of Portland cement by 5 and 10% of SE-BR1, the hardening stage followed the same pattern of physicochemical changes that were observed for the reference paste at least up to 2 hours of monitoring. However, for the composition SE-20BR1, the changes in G' value were very slow at the beginning of hardening, but from 2.5 hours of monitoring the physical contribution had more impact on the development of microstructure.

This is an important observation because in this composition was quantified the highest delay in the chemical reaction, confirming that the discussion of the hardening process must be done correlating both parameters.

This behavior reveals an abrupt rise in the dominance of the agglomeration forces due to the cement hydration evolution, thus indicating the minimum amount reaction requested to change the balance to surface attractive forces in the system. More specifically, the ionic strength and the particle specific surface area are increased due to the formation of cement hydrated compounds, thus increasing these agglomeration forces.

Finally, even with the clear impact of using SE-BR2 (kind and content) during the development of the hardening stage, the difference with the reference paste was the lowest compared with the other residues.

CONCLUSION

The proper replacement of Portland cement by bauxite residue depends, as in the case of other mineral additions, on the correct evaluation of the resulting rheological properties after the addition. These properties depend on the different physical characteristics of the particles concerning the cement.

Converging with some studies reported in the literature, it can be said that in this work, the hardening stage of the cementitious material was not only related to the chemical reaction, but also to the surface forces raised with the hydration reaction and with the changes in the liquid phase: even with the impact of bauxite residue, the chemical reaction was fundamental but insufficient for the gain on the consistency of the suspensions.

The Brazilian Northeast residue (NE-BR) was the only one that presented a negligible impact on the Portland cement chemical reaction (up to 10% of substitution), independently of the content used. However, the microstructural hardening was lower than for the reference suspension (prepared using only Portland cement).

For the other suspensions, even with the lower rigidification comparing with the Portland cement, the changes promoted using different contents of bauxite residue were negligible up to 2.5 hours of monitoring: although after this time, the differences of G' over time were more intense in the compositions with SE-BR1.

On the other hand, both residues from the Brazilian Southeast have had an impact on the development of the chemical reaction of cement: causing a delay due to the presence of a high amount of soluble sodium and aluminates (SE-BR1) or accentuate the nucleation effect (SE-BR2).

So, the correct comprehension of the phenomena that occur during the hardening of cementitious materials, i.e. from viscous fluid to elastic solid behavior, is extremely important for the development of eco-friendly cement composition, with better and more durable properties.

The analysis of the changes occurred during the hardening is not insignificant since several physicochemical phenomena take place at the same time and always change the cement microstructure. This means that for studies with other types of cement associated with other kinds of content of bauxite residue the trends could not be the same as those observed in this work.

ACKNOWLEDGMENTS

The authors wish to thank the Alcoa Foundation, the Brazilian Aluminium Company, the Fundação de Amparo à Pesquisa do Estado de São Paulo (Research Grant 2012/19262-2) and the Conselho Nacional de Desenvolvimento Científico e Tecnológico (Research Grant - 155357/2016-6) for the support during the development of this research.

REFERENCES

[1] S. Xue et al., "Industrial wastes applications for alkalinity regulation in bauxite residue: a comprehensive review," *J. Cent. South Univ.*, vol. 26, no. 2, pp. 268–288, 2019.

[2] D. J. Cooling, P. S. Hay, and L. Guilfoyle, “Carbonation of bauxite residue,” in *Proc. 6th Int. Alumina Qual. Workshop*, Brisbane, 2002, pp. 185–190.

[3] Y. Pontikes, P. Nikolopoulos, and G. N. Angelopoulos, "Thermal behaviour of clay mixtures with bauxite residue for the production of heavy-clay ceramics," *J. Eur. Ceram. Soc.*, vol. 27, no. 2-3, pp. 1645–1649, 2007., http://dx.doi.org/10.1016/j.jeurceramsoc.2006.05.067.

[4] M. Gräfe, G. Power, and C. Klauber, "Bauxite residue issues: III. Alkalinity and associated chemistry," *Hydrometallurgy*, vol. 108, no. 1-2, pp. 60–79, 2011.

[5] C. Klauber, M. Gräfe, and G. Power, "Bauxite residue issues: II. options for residue utilization," *Hydrometallurgy*, vol. 108, no. 1-2, pp. 11–32, 2011., http://dx.doi.org/10.1016/j.hydromet.2011.02.007.

[6] R. C. O. Romano, *Avaliação das Interações Físico-Químicas entre Resíduo de Bauxita e Cimento Portland*. São Paulo: Universidade de São Paulo, 2016.

[7] L. Arnout, T. Hertel, M. Liard, D. Lootens, and Y. Pontikes, “Use of bauxite residue slurry as single activator in a hybrid binder system,” in *Proc. 35th Conf. Exhib. ICSOBA – Bauxite Alumina Alum. Ind. Eur. New Glob. Dev., ICSOBA*, Hamburg, 2017, pp. 519–528.

[8] R. C. O. Romano, H. M. Bernardo, D. A. Niza, J. A. F. S. Mesquita, M. A. Cincotto, and R. G. Pileggi, *Evaluation of the Hardened State Properties of Zero-Cement Mortars Produced Using Bauxite Residue as an Activator to Ground Blast Furnace Slag*. Athens: An Serbruyns, 2018, pp. 293–300.

[9] A. L. Fujii, D. dos Reis Torres, R. C. de Oliveira Romano, M. A. Cincotto, and R. G. Pileggi, "Impact of superplasticizer on the hardening of slag Portland cement blended with red mud," *Constr. Build. Mater.*, vol. 101, pp. 432–439, 2015., http://dx.doi.org/10.1016/j.conbuildmat.2015.10.057.

[10] C. C. Liberato, R. C. O. Romano, M. Montini, J. B. Gallo, D. Gouvea, and R. G. Pileggi, "Efeito da calcinação do resíduo de bauxita nas características reológicas e no estado endurecido de suspensões com cimento Portland," *CEP*, vol. 5424, pp. 970, 2013.

[11] R. C. O. Romano, C. C. Liberato, M. Montini, J. B. Gallo, M. A. Cincotto, and R. G. Pileggi, "Evaluation of transition from fluid to elastic solid of cementitious pastes with bauxite residue using oscillation rheometry and isothermal calorimetry," *Appl. Rheol.*, vol. 23, pp. 9, 2013.

[12] R. C. O. Romano, H. M. Bernardo, M. H. Maciel, R. G. Pileggi, and M. A. Cincotto, "Using isothermal calorimetry, X-ray diffraction, thermogravimetry and FTIR to monitor the hydration reaction of Portland cements associated with red mud as a supplementary material," *J. Therm. Anal. Calorim.*, vol. 137, no. 6, pp. 1877–1890, 2019, http://dx.doi.org/10.1007/s10973-019-08095-x.

[13] A. L. Fujii, D. R. Torres, R. C. O. Romano, M. A. Cincotto, and R. G. Pileggi, "Impact of superplasticizer on the hardening of slag Portland cement blended with red mud," *Constr. Build. Mater.*, vol. 101, pp. 432–439, 2015.

[14] D. Dodoo-Arhin, R. A. Nuamah, B. Agyei-Tuffour, D. O. Obada, and A. Yaya, "Awaso bauxite red mud-cement based composites: characterisation for pavement applications," *Case Stud. Constr. Mater.*, vol. 7, pp. 45–55, 2017.

[15] P. Krivenko et al., "Development of alkali activated cements and concrete mixture design with high volumes of red mud," *Constr. Build. Mater.*, vol. 151, pp. 819–826, 2017.

[16] R. C. O. Romano et al., “Impact of using bauxite residue in microconcrete and comparison with other kind of supplementary cementitious material,” in *Proc. 35th Conf. Exhib. ICSOBA*, Hamburg, 2017, pp. 505–518.

[17] Y. Pontikes and G. N. Angelopoulos, "Bauxite residue in cement and cementitious applications: current status and a possible way forward," *Resour. Conserv. Recycling*, vol. 73, pp. 53–63, 2013.

[18] J. Roth and J. Falter, “Potential commercial processes for the utilization of bauxite residues,” in *Proc. 35th Conf. Exhib. ICSOBA – Bauxite Alumina Alum. Ind. Eur. New Glob. Dev., ICSOBA*, Hamburg, 2017, pp. 539–546.

[19] M. Singh, S. N. Upadhayay, and P. M. Prasad, "Preparation of special cements from red mud," *Waste Manag.*, vol. 16, no. 8, pp. 665–670, 1996.

[20] M. G. Sujana, R. S. Thakur, B. C. Acharya, S. N. Das, and S. B. Rao, *Effect of Calcination and Physico-Chemical Properties of Red Mud*. Washington: U.S. Department of Energy, 1996. [Online]. Available: https://www.osti.gov/biblio/371938

[21] K. Evans, "The history, challenges, and new developments in the management and use of bauxite residue," *J. Sustain. Metall.*, vol. 2, no. 4, pp. 316–331, 2016.

[22] M. S. Garcia, “Modificação do resíduo de bauxita gerado no processo Bayer por tratamento térmico,” M.S. thesis, Univ. São Paulo, São Paulo, 2012.

[23] Associação Brasileira de Normas Técnicas, *Cimento Portland – Requisitos*, ABNT NBR 16697, 2018.

[24] R. C. O. Romano, H. M. Bernardo, M. H. Maciel, R. G. Pileggi, and M. A. Cincotto, "Hydration of Portland cement with red mud as mineral addition," *J. Therm. Anal. Calorim.*, vol. 131, no. 3, pp. 2477–2490, 2018.

[25] R. A. Rojas-Ramírez, M. H. Maciel, R. C. de Oliveira Romano, R. G. Pileggi, and A. C. V. Coelho, "The impact of vermiculite residual fines in the rheological properties of cement pastes formulated with different waste contents," *Appl. Clay Sci.*, vol. 170, pp. 97–105, 2019.

[26] W. Liu, J. Yang, and B. Xiao, "Application of Bayer red mud for iron recovery and building material production from alumosilicate residues," *J. Hazard. Mater.*, vol. 161, no. 1, pp. 474–478, 2009.

[27] X. Wang, T. Sun, S. Wu, C. Chen, J. Kou, and C. Xu, "A novel utilization of Bayer red mud through co-reduction with a limonitic laterite ore to prepare ferronickel," *J. Clean. Prod.*, vol. 216, pp. 33–41, 2019.

[28] A. Mancini et al., "Fe(III) uptake by calcium silicate hydrates," *Appl. Geochem.*, vol. 113, pp. 104460, 2020.

[29] F. M. Kaußen and B. Friedrich, "Phase characterization and thermochemical simulation of (landfilled) bauxite residue (“red mud”) in different alkaline processes optimized for aluminum recovery," *Hydrometallurgy*, vol. 176, pp. 49–61, 2018.

[30] D. P. Bentz, "Modeling the influence of limestone filler on cement hydration using CEMHYD3D," *Cement Concr. Compos.*, vol. 28, no. 2, pp. 124–129, 2006.

[31] K. De Weerdt, M. B. Haha, G. Le Saout, K. O. Kjellsen, H. Justnes, and B. Lothenbach, "Hydration mechanisms of ternary Portland cements containing limestone powder and fly ash," *Cement Concr. Res.*, vol. 41, no. 3, pp. 279–291, 2011.

[32] J. Duchesne and M. A. Be´rube´, "Effect of supplementary cementing materials on the composition of cement hydration products," *Adv. Cement Base. Mater.*, vol. 2, no. 2, pp. 43–52, 1995.

[33] R. Snellings, G. Mertens, Ö. Cizer, and J. Elsen, "Early age hydration and pozzolanic reaction in natural zeolite blended cements: Reaction kinetics and products by in situ synchrotron X-ray powder diffraction," *Cement Concr. Res.*, vol. 40, no. 12, pp. 1704–1713, 2010.

[34] A. A. Elgalhud, R. K. Dhir, and G. Ghataora, "Limestone addition effects on concrete porosity," *Cement Concr. Compos.*, vol. 72, pp. 222–234, 2016.

[35] A. M. Ramezanianpour and R. D. Hooton, "A study on hydration, compressive strength, and porosity of Portland-limestone cement mixes containing SCMs," *Cement Concr. Compos.*, vol. 51, pp. 1–13, 2014.

[36] R. Kumar and B. Bhattacharjee, "Porosity, pore size distribution and in situ strength of concrete," *Cement Concr. Res.*, vol. 33, no. 1, pp. 155–164, 2003.

[37] P. E. Tsakiridis, S. Agatzini-Leonardou, and P. Oustadakis, "Red mud addition in the raw meal for the production of Portland cement clinker," *J. Hazard. Mater.*, vol. 116, no. 1-2, pp. 103–110, 2004.

[38] J. Zhang, E. A. Weissinger, S. Peethamparan, and G. W. Scherer, "Early hydration and setting of oil well cement," *Cement Concr. Res.*, vol. 40, no. 7, pp. 1023–1033, 2010.

[39] F. Begarin, S. Garrault, A. Nonat, and L. Nicoleau, "Hydration of alite containing aluminium," *Adv. Appl. Ceramics*, vol. 110, no. 3, pp. 127–130, 2011.

[40] A. Quennoz and K. L. Scrivener, "Interactions between alite and C3A-gypsum hydrations in model cements," *Cement Concr. Res.*, vol. 44, pp. 46–54, 2013.

[41] L. Nicoleau, E. Schreiner, and A. Nonat, "Ion-specific effects influencing the dissolution of tricalcium silicate," *Cement Concr. Res.*, vol. 59, pp. 118–138, 2014.

[42] S. Garrault, A. Nonat, Y. Sallier, and L. Nicoleau "On the Origin of the Dormant Period of Cement Hydration", in: *13th International Congress on the Chemistry of Cement (ICCC)*, Madrid, 2015.

[43] K. L. Scrivener, P. Juilland, and P. J. M. Monteiro "Advances in understanding hydration of Portland cement" *Cement Concr. Res.*, vol. 78, pp. 38–56, 2015. https://doi.org/10.1016/j.cemconres.2015.05.025.

Author contributions: RCOR: Study planning, supervision, funding acquisition, evaluation/analysis of the results, paper writing. JAFSM: Development of the practical work, data evaluation, support in the paper writing. HMB: Development of the practical work, data evaluation. DAN: Development of practical work. MHM: Evaluation/analysis of the results, support in the paper writing. MAC: Supervision, discussion of the results, revision of the paper. RGP: Study planning, supervision, funding acquisition, discussion of the results, revision of the paper.

Editors: Fernando Pelisser, José Luiz Antunes de Oliveira e Sousa, Guilherme Aris Parsekian.

IBRACON Structures and Materials Journal
Revista IBRACON de Estruturas e Materiais
ISSN 1983-4195 ismj.org

ORIGINAL ARTICLE

Proposition and analysis of strut and tie models for short corbels from techniques of topology optimization

Proposição e análise de modelos de bielas para consolos curtos a partir de técnicas de otimização topológica

Matheus Barbosa Moreira Cedrim[a]
Eduardo Nobre Lages[b]
Aline da Silva Ramos Barboza[b]

[a]Centro Universitário CESMAC – CESMAC, Maceió, AL, Brasil
[b]Universidade Federal de Alagoas – UFAL, Centro de Tecnologia, Programa de Pós-graduação em Engenharia Civil, Maceió, AL, Brasil

Received 23 January 2020
Accepted 10 July 2020

Abstract: Reinforced concrete short corbels are components characterized to represent typical conditions of geometrical and static discontinuity. In general, the classical bending theory is not valid for their design. With the strut and tie method, a model of a self-balanced truss, a strategy of representation of the principal stress flow appears as a representation of the trajectories of the main stresses in these components. Within the context of obtaining the strut and tie models, topology optimization is an indicated technique for an automated process. Combined with a numerical analysis based on finite elements, the SIMP (Solid Isotropic Material with Penalization) method formulation, which is defined with the criterion of minimum strain energy restricted by the volumetric fraction, is used for the development of the models with the ABAQUS® v. 6.14.1 software. Therefore, with the material distribution posterior to the optimization and the validation based on normative codes, it is demonstrated that the tool is effective in the development of strut and tie models.

Keywords: corbels, topology optimization, SIMP.

Resumo: Os consolos curtos de concreto armado são componentes caracterizados por representarem situações típicas de descontinuidade geométrica e estática. Para o seu dimensionamento, em geral, não é válida a teoria clássica da flexão. Com o método das bielas, um modelo de treliça autoequilibrada surge como uma representação das trajetórias de tensões principais nesses componentes. No contexto de obtenção dos modelos de bielas, a otimização topológica é uma técnica indicada para um processo automatizado. Combinado com uma análise numérica em elementos finitos, a formulação do método SIMP (Solid Isotropic Material with Penalization), que é definida com o critério da mínima energia de deformação com restrição de volume, é utilizada para a definição dos modelos com o software ABAQUS® v. 6.14.1. Assim, com a distribuição de material após a otimização e a validação feita a partir de recomendações normativas, mostra-se que a ferramenta é eficaz no auxílio no desenvolvimento de modelos de bielas.

Palavras-chave: consolos, otimização topológica, SIMP.

How to cite: M. B. M. Cedrim, E. N. Lages, and A. S. R. Barboza, "Proposition and analysis of strut and tie models for short corbels from techniques of topology optimization," *Rev. IBRACON Estrut. Mater.*, vol. 14, no. 2, e14212, 2021, https://doi.org/10.1590/S1983-41952021000200012

1 INTRODUCTION

In most of the one-dimensional bent elements in structural concrete, the design is based on the Euler-Bernoulli hypothesis, in which the cross-section, which is initially plane, remains plane, and results in a linear distribution of the specific longitudinal strains along the height of the bent element. For cases of special elements that contain discontinuity

Corresponding author: Matheus Barbosa Moreira Cedrim. E-mail: matheuscedrim@hotmail.com
Financial support: National Council for Research and Development (CNPq).
Conflict of interest: Nothing to declare.

regions, the strain distribution in the cross-section is not linear, which causes the structural problem to become more complex.

Among the elements used in precast structures, short corbels, dapped-beams, and pedestal walls are mentioned in Brazilian code NBR 9062 [1] as elements that are featured as discontinuity regions in the structural system and, for this reason, analyzed using the strut and tie model. With this methodology, it is possible to evaluate the structural behavior by an idealized truss, as shown in Figure 1 [2].

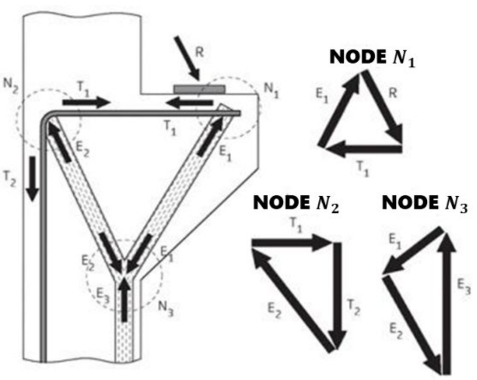

Figure 1. Static scheme of a strut and tie model for a short corbel.

To obtain the strut and tie model, it is common to make use of numerical methods to understand the structural behavior of special elements. Currently, the codes which consider the concrete structure design, for example, NBR 6118 [3], already suggest the use of the Finite Element Method (FEM) for the visualization of the load path by principal stress trajectories.

To help in the correct positioning of the struts in the inner side of the structure, Liang et al. [4] proposed using structural optimization techniques, which allow the positioning of the bar elements over the principal stress flow found in the linear elastic analysis.

Pantoja [5] also used these techniques to automatize the topological models, besides considering the aspects related to obtaining the failure probability by a reliability analysis.

Through evolutionary methods, Liang [6], Almeida et al. [7], Guerra [8], Guerra and Greco [9] used tools based on criteria for removing elements, represented by the quantities of stiffness contribution. Thus, based on the observation that if the element is no longer necessary to the structure, its contribution to the stiffness will progressively decrease, and this will reflect on attenuation in a constitutive matrix, as if it were in a damage process.

Once there is not only one specific approach in the solution for obtaining the strut and tie model, the development of new applications is a relevant factor. Besides this, there are different paths for its definition, the design codes for reinforced concrete structures NBR 6118 [3], ACI 318 [10], and Eurocode 2 [11] do not use the approach of topology optimization as a scheme for obtaining these models.

To help in choosing the truss model that better represents the structural behavior, the topology optimization technique, which consists of the optimized material distribution inside a previously established project domain, is presented as a promising alternative for this function.

It should be noted that the optimized topologies are balanced systems; however, no strength control is checked in the nodes and the other elements with the optimization algorithm. This procedure only produces preliminary patterns, and the entire design and checking of strut, ties, and nodal regions are the job of the engineer.

These analyses, based on appropriate volumetric fractions for the interpretation of structural behavior, assist the development of strut and tie models in a discerning manner, since the mathematical foundation is used to maximize the stiffness.

2 THEORETICAL REFERENCE

Corbels are structural elements that need different strategies of design, due to the evidenced discontinuity in the stress flow of the structural system.

2.1 Design models of short corbels

El Debs [2] conceptualizes that concrete corbels are characterized as structural elements that protrude from columns or walls to serve as a support for the other parts of the structure or for utilization loads.

The classification between short, very short, and long is related to distance “a”, measured from the action line of the applied load in the bearing pad to the external face of the column, with the effective depth “d”. According to NBR 6118 [3], the corbel is short if $d/2 \leq a \leq d$ and very short if $a < d/2$. In the case where $a > d$, the element should be analyzed as a cantilever beam.

Figure 2 [12] illustrates the discontinuity regions found in different corbels. In order to obtain a safe design for these elements, the boundary conditions of each problem should be considered individually. This way, each case will lead to a different conception of the strut and tie model.

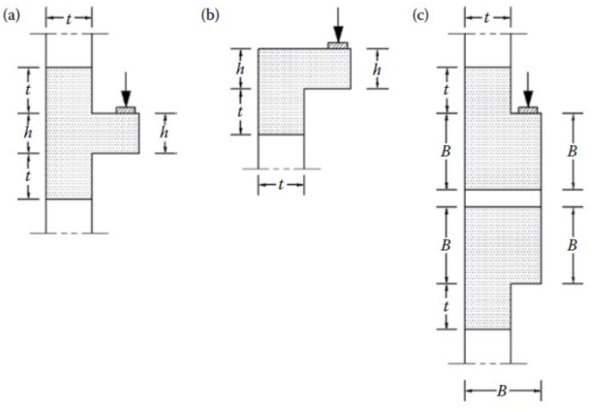

Figure 2. Discontinuity regions in corbels.

Through an analysis of strut and tie models, the behavior of a short corbel is idealized as a straight tie in the superior face, which, for constructive issues and ease of execution, does not necessarily follow the medium path of the tension stresses, once they are slightly inclined. To ensure the ductility of the elements, a secondary reinforcement is also placed, made up of horizontal stirrups.

The utilization of an integrated process for obtaining the strut and tie models through topology optimization is still an open issue. Liang [6] quotes that most of the topology optimization algorithms are still not developed for practical applications, and, are emphasized, mainly, on mathematical aspects. However, with the advance of computational development, a greater agility for the definition of structural projects is aimed.

Williams et al. [13] comment that the flexibility of the strut and tie models often causes uncertainties in engineers: there is no “correct” model for any particular structure. If the required principles to achieve a static solution based on the lower bound limit of the theory of plasticity are accomplished, the engineer is able to assure that the adopted model is safe.

2.2 Strut and tie models

Schlaich et al. [14] proposed that the strut and tie model may be adopted considering the stress flow in the structure, using the load path process. Once the stresses and their principal directions originated from the linear elastic analysis, the development of the model should represent these stresses in a region as well as possible.

Souza [15] relates that the representation of strut and tie generally is a function of the structure geometry and the acting forces in the contour. The model geometry can be usually obtained by analyzing the following aspects: types of load, angles between struts and ties, area of application of actions and reactions, number of reinforcement layers, and covering of reinforcements.

El-Metwally and Chen [12] conceptualize that the strut and tie model is a logical extension of the truss model proposed by Ritter and Mörsch. The greatest difference between these two methods is that the strut and tie model is a set of balanced loads, but it does not necessarily form a stable truss system. Therefore, it is a model that can be considered as a generalization of the truss analogy.

2.3 Considerations for obtaining the strut and tie models

In order to conceive a design model for corbels through a mathematical formulation, the topology optimization with the use of the Finite Element Method (FEM) is conceptually indicated for the conception of structural element projects. In this study, a formulation of topology optimization for linear elastic materials was adopted.

For Liang et al. [4], the consideration of elastic behavior for concrete, even in cracking situations, provides a clear understanding of the load transfer in reinforced concrete elements. As an indication to perform a strut and tie model, the obtained results through topological optimization of linear elastic structures should not be considered absolute; however, there are confirmations that these results are valid and checked by experimental analyses.

According to NBR 6118 [3], for the strut and tie model conception, it is possible to validate the application of the obtained results through analyses that consider linear elastic materials. This way, exceptionally, for the visualization of principal stress trajectories, the referred code allows the application of the finite element models with this simplification of analysis.

It is emphasized that for the technical reference NBR 6118 [3], the reinforcement design should not be limited only to the internal loads or stresses obtained through this analysis, but also that the necessary minimum and maximum quantities should be respected, demanded by the structural concrete theory, to assure the ductility of the elements.

Schlaich et al. [14] propose that the model geometry is based on elastic stress fields and the design follows the theory of plasticity. With this, from a practical point of view, it is possible to treat the ultimate limit state and serviceability limit state in the cracked situation as a unique model for both.

It is worth emphasizing that the serviceability limit state verification is a polemical theme since its consideration is implicit in the strut and tie model. This way, the displacement evaluation of the service loads requires that the adopted model estimate the stiffness of the elements in such a manner as to give an equivalent response to the real displacement of the structure.

2.4 Numerical modeling

The structural optimization process consists in obtaining a better performance project, which is evaluated through a defined objective function by a set of variables that describe the system, known as design variables. With the formulation of the method, the design variables defined in the problem are the relative densities related to the finite elements or the nodes of the mesh, such as the example in Figure 3 [16].

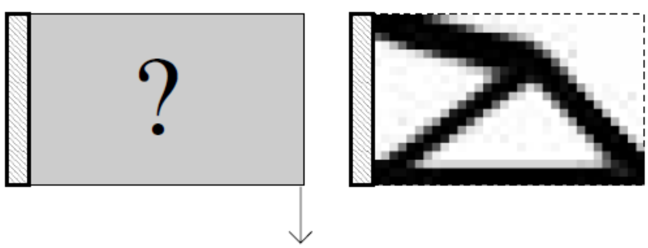

Figure 3. Structural optimization problem

The numerical method based on finite elements most known is the SIMP method, which was developed in the 1980s. The term SIMP means Solid Isotropic Material with Penalization [17].

The objective of the problem of the minimization of compliance or maximization of stiffness can be understood as an iterative process that seeks a better distribution of the design variables in the defined mesh.

A pioneer work on the application of the method is the publication of Sigmund [16], which presents a computational implementation of a 99-line code in MATLAB®, which shows its efficiency for educational applications of topology optimization problems. The method formulation is given by:

$$\min c(\mathbf{x}) = \mathbf{U}^{\mathbf{T}}\mathbf{K}\mathbf{U} = \sum_{e=1}^{N} (x_e)^p\, \mathbf{u}_{\mathbf{e}}^{\mathbf{T}}\mathbf{k}_{\mathbf{e}}\mathbf{u}_{\mathbf{e}}$$

$$s.t.\ V(\mathbf{x}) = f\,V_0$$

$$0 < x_{min} \le x_e \le 1 \tag{1}$$

where **U** and **F** are the global displacement and force vectors, respectively, **K** is the global stiffness matrix, $\mathbf{u_e}$ and $\mathbf{k_e}$ are the element displacement vector and stiffness matrix, respectively, **x** is the vector of design variables (relative densities of elements), x_{min} is a vector of minimum relative densities, N is the number of elements used to discretize the design domain, p is the penalization power, V(**x**) and V_0 are the material volume and design domain volume, respectively, and f is the prescribed volume fraction.

Sigmund [16] mentions that the material properties are modeled as relative material densities raised to some power multiplied by the material properties of solid material. It was criticized for a while, once it was argued that no physical material exists with properties described by the power-law interpolation. However, it was proven that the power-law approach is physically permissible if simple conditions on the power are satisfied (e.g. $p \ge 3$ for Poisson's ratio equal to 1⁄3).

A minimum value to Young's modulus of an element is adopted to avoid the singularity problem of the structure's stiffness matrix during the process of resolution of the balance equations. A value of x_{min} approximately 0.001 is enough to avoid this problem [5].

In this paper, the ABAQUS® v. 6.14.1 software was used as a tool for obtaining optimized topologies. The optimization platform available in ABAQUS® is TOSCA, which provides powerful and fast solutions for structural optimization based on finite elements. The flowchart presented in Figure 4 demonstrates the configuration process and execution of optimization inside the platform in use [18].

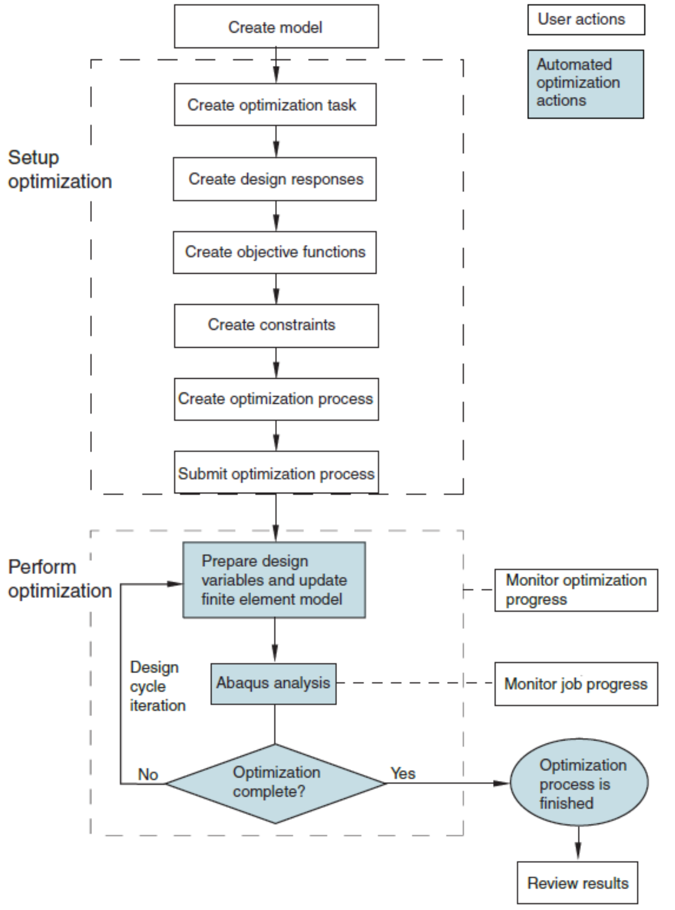

Figure 4. Flowchart of the optimization process.

The TOSCA Structure provides strategies for new concepts of projects that enable lighter, stiffer, and durable structures. The design development cycle may be directed to maximize or minimize any performance measure, making it possible for the engineer to discover new possibilities.

The nonlinear models, when validated, may contain the association of the elements that represent the reinforcement in a numerical analysis that modifies the behavior of the set. However, a bigger computational cost is demanded due to the cracking consideration during the optimization process, such as the high processing time for the three-dimensional elements, despite ABAQUS® providing a large number of design results for 3D elements, which can be interesting for the investigation of new optimized models, using, for example, von Mises stresses as constraints.

Once there is not a unique solution for the strut and tie model, different arrangements of bars may represent the same configuration to a given structural disposition. The presented flowchart in Figure 5 shows the adopted procedure. In this work, the optimized material distributions were interpreted as a preliminary pattern of the truss system.

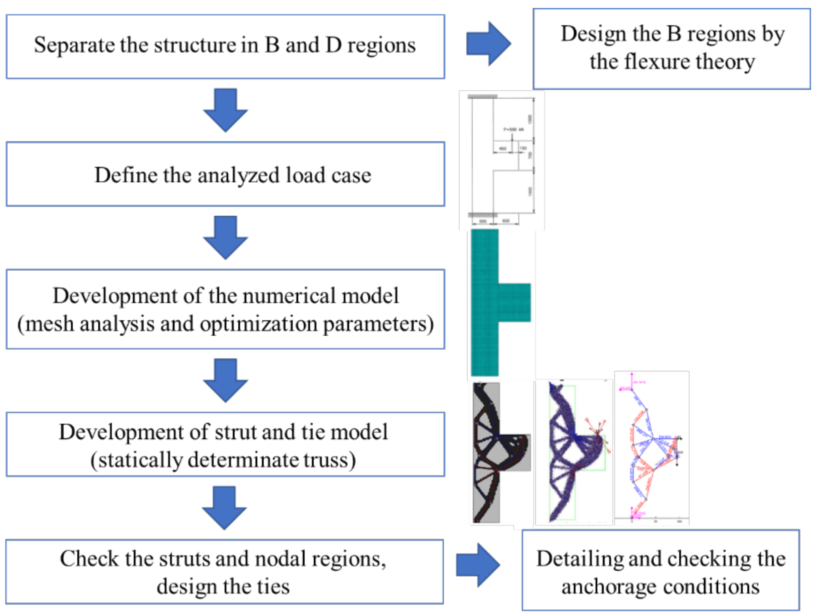

Figure 5. Design sequence with optimization assistance.

For the structural analysis of truss models, commercial software or free codes for computing the internal loads may be used. In this work, a computational code in MATLAB® language was developed, which calculates the axial loads and reaction forces, exclusively from nodal equilibrium equations. For this, to define the node positions, the connectivity of the bars, the prescribed nodal forces, and nodal supports were necessary.

Since there is no consensus of the ideal volume fraction for obtaining the strut and tie model, a critical transition analysis for low values of this fraction must be established. The smaller the volume fraction, harder is the task to interpret the optimized model as an articulated unidimensional model. The bar connection for each volume fraction must follow the closer one that was established for the end of the optimization process.

According to the design codes, the models must be stable, which means statically determinate. To solve this problem, the support conditions and formation law of trusses must be analyzed assuring that the balance is guaranteed.

3 RESULTS AND DISCUSSIONS

To obtain the strut and tie models, and use the methodology indicated in the design codes, an example of a rectangular corbel optimization available in the literature and a proposed example of a trapezoidal corbel are presented, with new models for design routines being developed.

3.1 Rectangular corbel

Liang et al. [4] proposed the rectangular corbel illustrated in Figure 6. The a/h ratio is 0.64. The load, considered punctual, is 500 kN. For the boundary condition considerations, the column presents restricted displacements in both ends. The compression strength of the concrete is f_{ck} = 32 MPa, the longitudinal elastic modulus is E = 28,567 MPa, and the Poisson ratio ν = 0.15, and CA-50 steel (characteristic yield stress f_{yk} = 500 MPa). The column and the corbel widths are presumed as b = 300 mm.

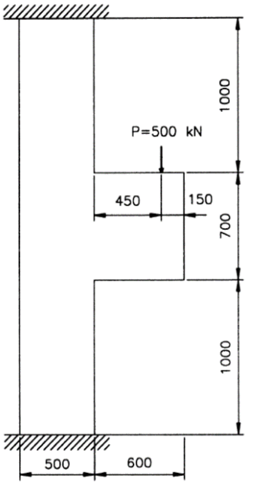

Figure 6. Rectangular corbel (dimensions in mm)

For modeling, the same element dimensions adopted in the work of Liang et al. were used [4]. A finite element mesh of approximately 25 mm for plane stress analysis of type CPS4 (quadrilateral element of 4 nodes with bilinear interpolation), 2,832 elements, and 2,985 nodes was considered.

Based on the proposed example, it is noted that the simplification for bidimensional analysis of corbels is indicated for a decrease of computational time, without damaging the interpretation of results. During the process of choosing the mesh, the elements of geometry and computational cost for solving the problem need to be taken into consideration. This way, for more complex problems, a sensitivity analysis of the mesh should be considered, mainly because the analysis via FEM, according to Sigmund [16], offers the possibility of numerical instabilities for the model that may be described in three categories: the checkerboard irregularities, mesh dependence and the problem of optimum location.

Concerning the mesh dependence, the more refined the mesh is in the reference domain, the more similar the structure will be to the predicted layout in the microstructure theory. The solutions` dependence to the chosen discretization leads to better or worse detailing and contour descriptions. To avoid this numerical instability, a sensibility filter adoption is needed. In the simulation using ABAQUS®, the filter criterion proposed by Sigmund [16] is adopted. The other instabilities were not evaluated in this work.

For the optimization process, it is considered that the load-applying region is not included since there is no removal of material in this region during the cycles of the project. To define the search direction of minimization, during the processing, the sensibility filter is automatically defined with r_{min} = 32.5 mm, and further information is listed in Table 1.

Table 1. Topology optimization parameters

Parameters of the SIMP method	**Value**
Minimum density (ρ_{min})	0.001
Maximum density (ρ_{max})	1
Maximum change of the density per cycle of project	0.25
Penalty factor (p)	3
Convergence criteria	**Value**
Maximum tolerance for the objective function	0.001
Maximum tolerance for the element density	0.005

The obtained optimized topologies when considering volume fractions of approximately 90%, 80%, 70%, 60%, 50%, 40%, 30%, 20%, and 10% of initial volume are presented in Figure 7. To reach the desired parameters, 15, 20, 34, 34, 35, 36, 37, 50 are necessary, respectively, as well as 42 cycles of the project.

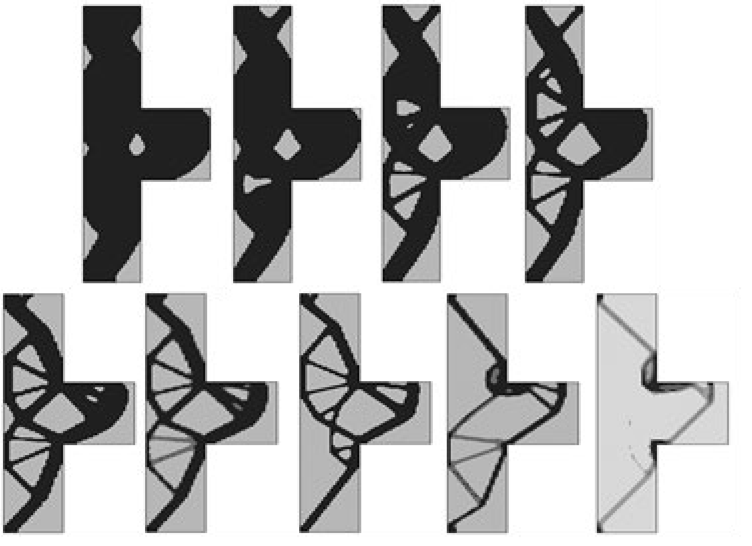

Figure 7. Optimized distribution of material, volume fractions of 90%, 80%, 70%, 60%, 50%, 40%, 30%, 20% and 10%, respectively.

When analyzing Figure 7, the definition of the two regions is carried out. The black region is the one that is considered in the optimization process as the optimized topology, and attends the minimization of the objective function and volume constraint. The grey region is characterized for minimum density (x_{min}), which avoids the singularity in the stiffness matrix.

In Figures 8 and 9 the principal stress trajectories are presented, with the optimized models f = 50% and f = 40%, respectively. The principal stresses of tension (a) and indicated in blue, and, in red, principal stresses of compression (b). It is verified, therefore, that there is a better visualization of the preliminary truss models.

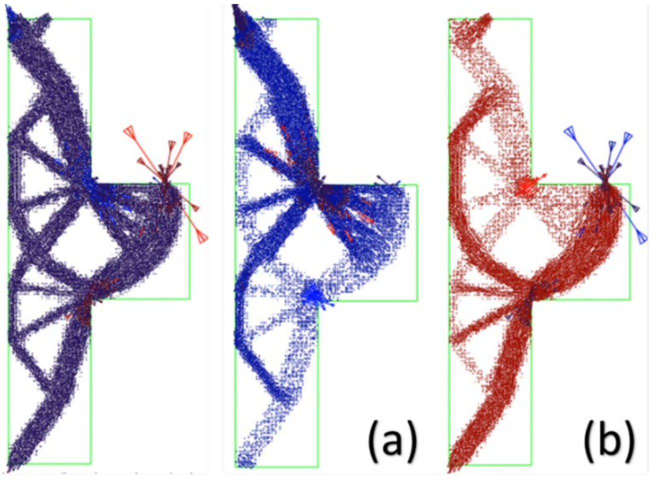

Figure 8. Principal stress trajectories for f = 50% (a: tension; b: compression)

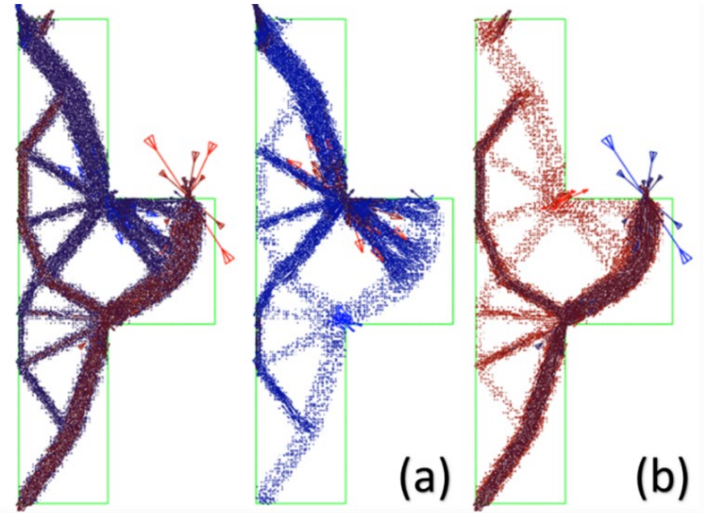

Figure 9. Principal stress trajectories for f = 40% (a: tension; b: compression)

The definition of the truss model, from the bidimensional composition of the material for the bar models, depends on the adopted criteria for each user to accomplish the specific filtering for each case. Therefore, procedures that make the use of the optimum model viable as a reference for building the truss system should be used.

As mentioned before, the topology optimization parameters influence the definition of the final result. The designation of adequate parameters allows a better understanding of the numerical analysis. This way, the emerging of the numerical instabilities is still a concern in the optimization procedure, but these problems can be solved with the adoption of some measures, such as the adequate mesh refinement and correct utilization of the convergence criteria.

In Figure 10, the suggested truss models are shown for the design according to the strut and tie model. The model in Figure 10a is based on the optimized topology found with f = 50%. The model in Figure 10b is based on the optimized topology found with f = 40%. The node coordinates are presented in Tables 2 and 3.

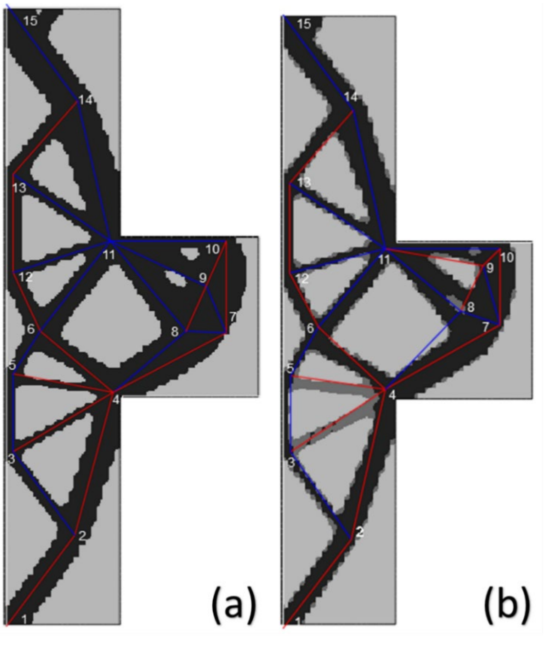

Figure 10. Suggested truss models for the rectangular corbel a) f = 50%; b) f = 40%

Table 2. Coordinates of truss model for f = 50%

Node	x (cm)	y (cm)
1	0.00	0.00
2	29.81	39.41
3	3.00	75.81
4	46.11	101.46
5	3.00	109.36
6	14.57	128.04
7	95.00	127.28
8	77.77	128.04
9	86.35	147.52
10	95.00	167.00
11	45.00	167.00
12	3.00	153.33
13	3.00	196.28
14	30.68	228.11
15	0.00	270.00

Table 3. Coordinates of truss model for f = 40%

Node	x (cm)	y (cm)
1	0.00	0.00
2	29.81	39.41
3	3.47	77.59
4	45.00	105.00
5	3.47	111.38
6	15.37	132.70
7	95.00	133.39
8	77.82	139.66
9	87.60	159.60
10	95.00	167.00
11	45.00	167.00
12	3.19	156.15
13	3.19	195.94
14	30.68	228.11
15	0.00	270.00

For the problem in the analysis, the strut strength according to each normative code are found in Table 4. Conservatively, the strut strength in CCT zones was adopted according to NBR 6118 [3]. For ACI 318 [10], it is considered that there is no transversal reinforcement. In the simplified model of Eurocode 2 [11], the value of the maximum stress in the nodal zone CCC was used as the strength parameter.

Table 4. Strut strength

Model	Strength (kN/m^2)
NBR 9062 [1]	14,350.63
ACI 318 [10]	16,320.00
Eurocode 2 [11]	15,812.27

In Figure 11 the internal loads for the two cases are presented. A horizontal load H_d = 0.16 V is also applied, following the technical code of NBR 9062 [1]. The positive loads (in blue) indicate tension, while the negative loads (in red) indicate compression. The detail of the loads in the bars for the models f = 50% (a) and f = 40% (b) in the corbel region are shown, and the steel reinforcement areas are found for the main tie, according to Table 5.

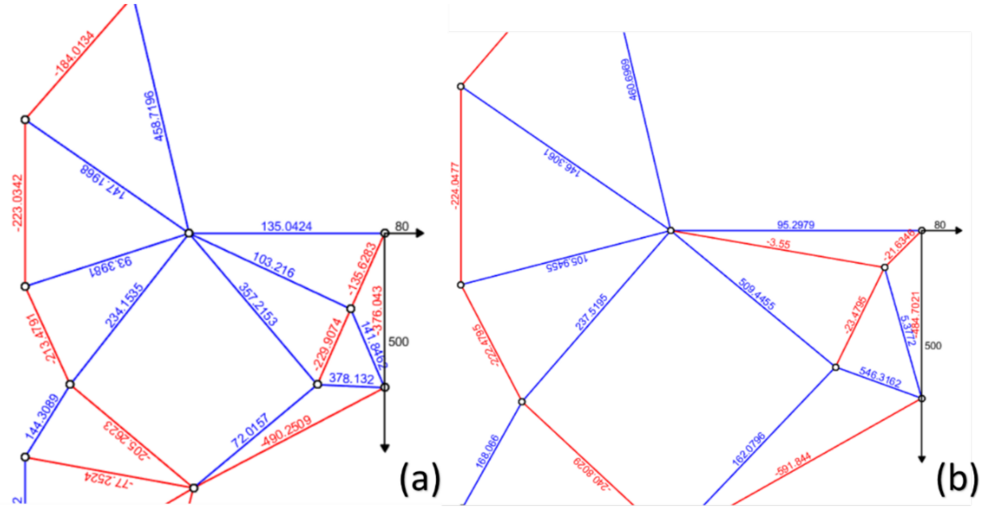

Figure 11. Load details in the rectangular corbel a) f = 50%; b) f = 40%

Table 5. Reinforcement areas of the main tie

Model	Steel area (cm²)
NBR 9062 [1]	10.95
PCI (2010) [19]	15.19
Eurocode 2 [11]	11.29

Despite containing a horizontal bar in the upper region of the corbel, suggesting that the main tie will be designed for this bar, the maximum load of tension in the two models with optimized topology occurred in an inclined bar, suggesting that the main reinforcement should also be inclined, which is not indicated for the building routine, due to the great probability of occurring a displacement of the reinforcement during the execution.

For the horizontal ties, in the models with f = 50% and f = 40% (bars 10-11), the steel reinforcement areas were 3.10 cm^2 and 2.19 cm^2, respectively. When analyzing the inclined ties (bars 11-14 and 7-8), the steel reinforcement areas were 10.55 cm^2 and 12.56 cm^2, respectively.

Considering the indication of Araújo [20], for the models of two bars, the computation of width of the strut depends on the bearing pad dimensions. Adapted for the case in analysis, for vertical struts, the width c_2 was determined for the models with optimized topologies, with the value of 20 cm.

In the model with f = 50%, the stress in the strut is 6,267.33 kN/m^2, and for the model with f = 40%, the stress in the strut is 8,078.3 kN/m^2. Despite the most loaded struts (bars 7-10) being located in the lower region of the corbel, it is highlighted that obtaining these widths was a difficult process.

For the models with optimized topologies, even with the lower strength, in this specific case the one in NBR 6118 [3], presented no concrete crushing, which indicates that the stress levels were safe.

The steel reinforcement areas of the inclined ties obtained through the models with optimized topologies resulted in a good approximation when compared to the design codes. Once each code has its particularity in the definition of the stress and safety factors, the applicability of the developed models through the connectivity of the materials could be verified.

3.2 Trapezoidal corbel

The trapezoidal corbel analyzed as an example was proposed by Silva [21], according to Figure 12. After the pre dimensioning suggested by the author, the adopted dimensions for analysis were a = 58 cm, d = 77 cm, h1 = 40 cm and a_2 = 8 cm. The a/d ratio was 0.75. The vertical load presented was characteristic. For the horizontal load, $H_d = 0.16\ F_d$ was considered.

For the computational analysis, the compression strength of the concrete of f_{ck} = 20 MPa was adopted, and the longitudinal elastic modulus was E_{cs} = 21,000 MPa, Poisson ratio v = 0.20 and steel CA-50 (characteristic yield stress f_{yk} = 500 MPa).

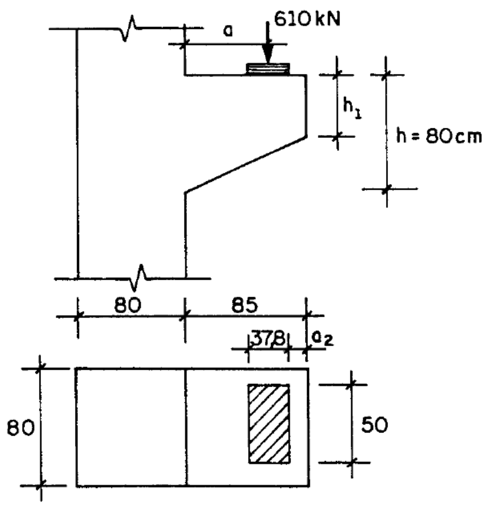

Figure 12. Trapezoidal corbel (dimensions in cm)

The boundary conditions for this corbel are shown in Figure 13, with the application of the vertical and horizontal loads distributed along the bearing pad and displacement restrictions in the bottom and on the top. The recommendation of El Debs [2] was considered in the modeling. Thus, the resultant loads were applied from a distance of 3/4 of the total length of the corbel (l_c). Therefore, the a/d ratio is 0.83.

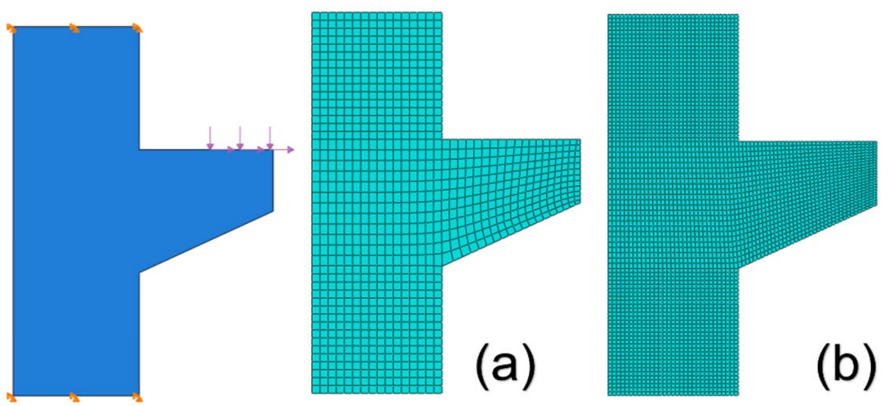

Figure 13. Boundary conditions and analyzed meshes a) dimension of 50 mm; b) dimension of 25 mm

In this example, the modeling with bi-dimensional finite elements was analyzed. A finite element mesh (a) with the approximate size of 50 mm was considered for plane stress analysis with the element type CPS4 (quadrilateral element of 4 nodes with bilinear interpolation). The model consists of 932 elements, and 1,012 nodes. Considering the same element formulation, the mesh (a) is refined to mesh (b), adopting the approximate mesh size of 25 mm, so the configuration is of 3,680 elements and 3,837 nodes.

Similar to the example of the rectangular corbel, it was considered that the load-applying region was not included in the optimization process since there was no removal of material in this contour. To reduce the mesh dependence, during the processing, the sensibility filter was automatically defined with r_{min} = 66.3 mm for mesh (a) and

r_{min} = 33.5 mm for mesh (b), and further information is listed in Table 1. In this analysis, the optimized topologies were defined for volume fractions below 50%, to reduce the amount of material, approximating the bidimensional model as a possible representation of the truss system.

For mesh (a), the obtained optimized topologies when considering volume fractions of approximately 50%, 40%, 30%, and 20% of the initial volume are presented in Figure 14. To reach the desired parameters, 27, 30, 31, and 34 cycles of project were necessary, respectively. However, for the comparison, the results of mesh (b) were also analyzed.

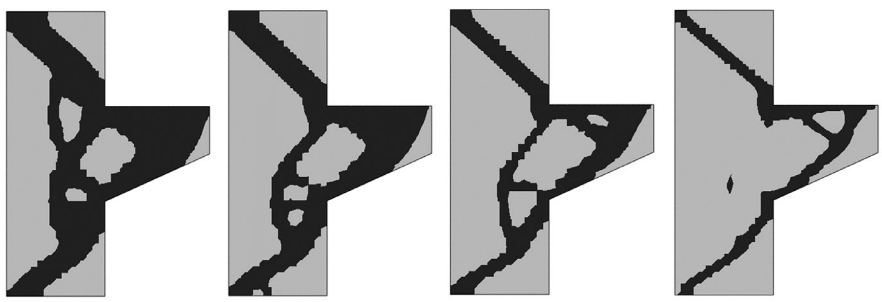

Figure 14. Optimized distribution of material for mesh a), volume fractions of 50%, 40%, 30% and 20%, respectively.

For mesh (b), the obtained optimized topologies when considering volume fractions of approximately 50%, 40%, 30%, and 20% of the initial volume are presented in Figure 15. To reach the desired parameters, 37, 36, 37, and 49 cycles of project were necessary, respectively. A better visualization of material distribution in this mesh was conducted, assisting in the process of conception of strut and tie model.

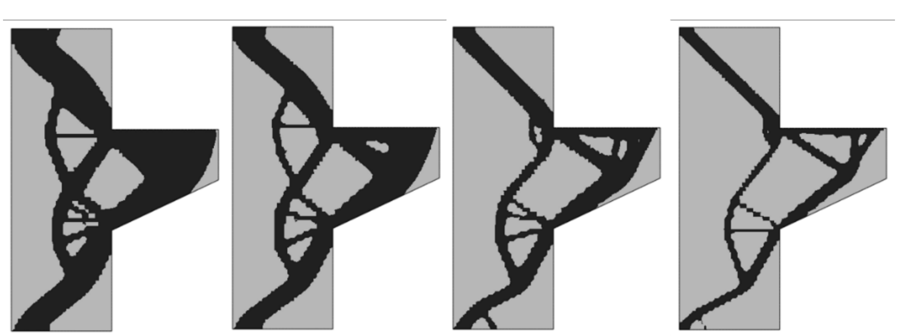

Figure 15. Optimized distribution of material for mesh b), volume fractions of 50%, 40%, 30% and 20%, respectively.

In Figures 16 and 17 the principal stress trajectories for mesh (b) are presented, with the optimized models f = 50% and f = 40%, respectively. The principal stresses of tension (a) are indicated in blue, and, in red, principal stresses of compression (b). With the identified regions, a truss model for the analysis of internal loads may be defined.

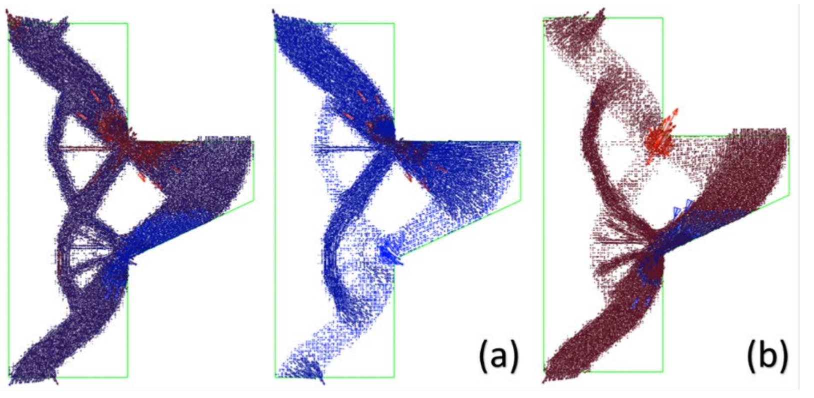

Figure 16. Principal stress trajectories for f = 50% (a: tension; b: compression)

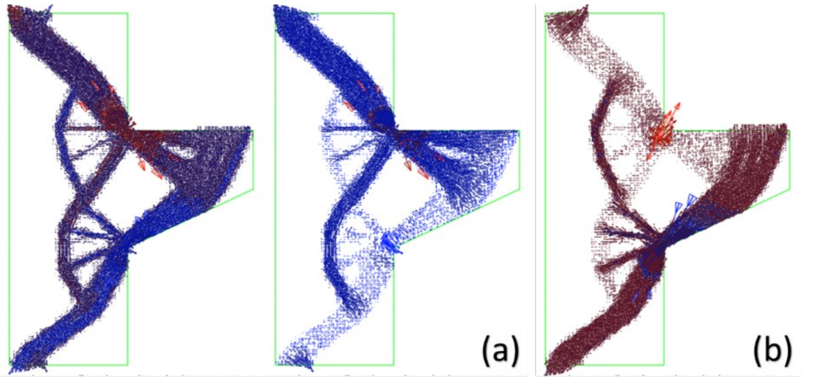

Figure 17. Principal stress trajectories for f = 40% (a: tension; b: compression)

Based on the optimized topologies obtained for mesh (b), in the different volume fractions f = 50% (Figure 18a) and f = 40% (Figure 18b), the connectivity of the resultant elements of the optimized models are presented, offering the indicative of truss models. The nodes coordinates are presented in Tables 6 and 7.

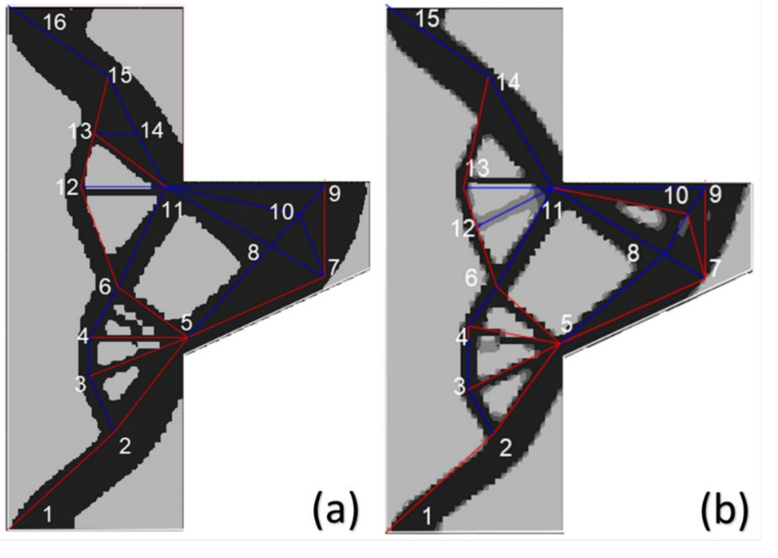

Figure 18. Suggested truss models for the trapezoidal corbel a) f = 50%; b) f = 40%

Table 6. Coordinates of truss model for f = 50%

Node	x (cm)	y (cm)
1	0.00	0.00
2	48.3	44.74
3	36.97	70.00
4	36.97	88.00
5	81.65	88.00
6	49.91	111.00
7	144.00	115.64
8	118.00	129.86
9	144.00	157.00
10	132.68	144.43
11	71.77	157.00
12	32.97	157.00
13	39.14	181.43
14	58.88	181.43
15	45.84	207.77
16	0.00	240.00

Table 7. Coordinates of truss model for f = 40%

Node	x (cm)	y (cm)
1	0.00	0.00
2	48.30	44.74
3	36.97	65.00
4	36.97	94.00
5	78.00	86.00
6	49.91	111.50
7	144.00	115.64
8	126.34	127.00
9	144.00	157.00
10	135.90	145.07
11	75.00	157.00
12	40.64	138.50
13	34.50	157.00
14	45.84	207.77
15	0.00	240.00

For the problem in the analysis, the strut strength according to each normative code is presented in Table 8. It is emphasized that the same criteria mentioned in the previous example was adopted for the calculated values.

Table 8. Strut strength

Model	Strength (kN/m^2)
NBR 9062 [1]	9,462.38
ACI 318 [10]	10,200.00
Eurocode 2 [11]	10,426.66

Figure 19 presents the internal loads for the two analyzed models. The positive loads (in blue) indicate tension, while the negative loads (in red) indicate compression. The detail of the loads in the bars for models f = 50% (a) and f = 40% (b) in the corbel region is shown, and the steel reinforcement area was found for the main tie, according to Table 9.

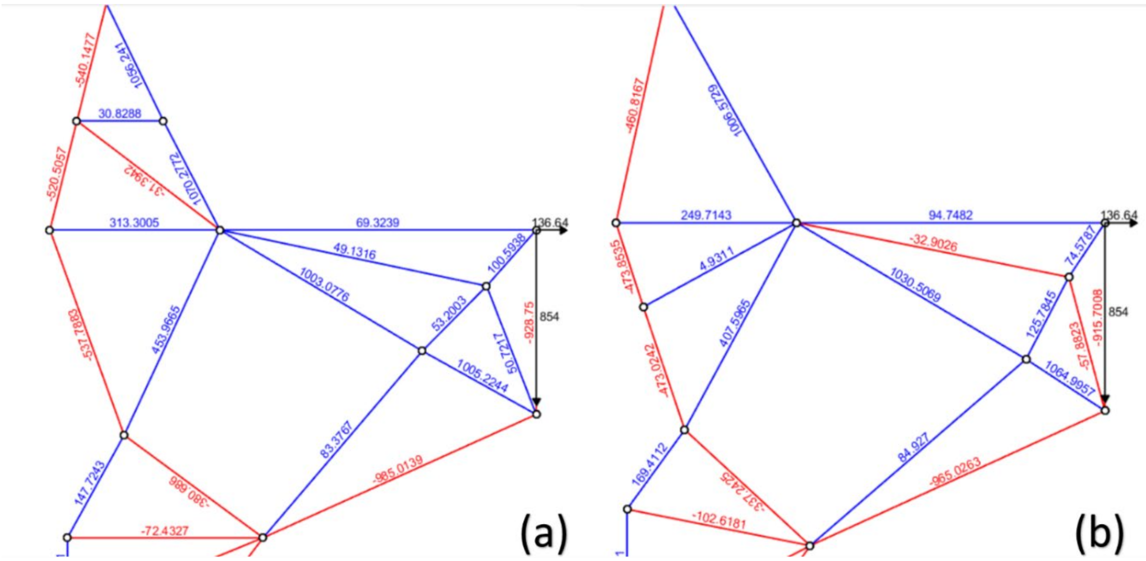

Figure 19. Load details in the trapezoidal corbel a) f = 50%; b) f = 40%

Table 9. Reinforcement areas of the main tie

Model	Steel area (cm²)
NBR 9062 [1]	21.43
PCI (2010) [19]	26.38
Eurocode 2 [11]	22.19

Similar to the example of the rectangular corbel, the main tie was designed according to the load located in an inclined bar, suggesting that the main reinforcement should also be inclined. This was not indicated for the building routine, due to the great probability of occurring a displacement of the reinforcement during the execution.

For the horizontal ties, in the models with f = 50% and f = 40% (bars 9-11), the steel reinforcement areas were 1.59 cm^2 and 2.18 cm^2, respectively. When analyzing the inclined ties (bars 11-14 and 7-8, in this order, for f = 50% and f = 40%), mentioned before, the steel reinforcement areas were 24.61 cm^2 and 24.50 cm^2, respectively.

Considering the indication of Araújo [20], for the two-strut models, the computation of the width of the strut depends on the bearing pad dimensions. For the vertical struts, in case in analysis, the width c_2 was determined equal to 38 cm for the models with optimized topologies the same as the width of the bearing pad.

In the model with f = 50%, the stress in the strut was 3,055.09 kN/m^2, and for the model with f = 40%, the stress in the strut was 3,012.17 kN/m^2. Despite the most loaded struts (bars 5-7) being located in the lower region of the corbel, it is highlighted that obtaining these widths was a difficult process.

For the models with optimized topologies, comparing with the lower strength, in this case, the one in NBR 6118 [3], they presented no concrete crushing, which indicates that the stress levels were safe.

In this new example, the steel reinforcement areas of the inclined ties obtained through the models with optimized topologies were coherent with the design codes. Since each model has its particularity in the methodology of analysis, it can be asserted that the developed models through the connectivity of the materials may be used as an assistance for design.

4 CONCLUSIONS

The fundamentals of the strut and tie model are directly related to the topology optimization problem of continuum structures. To maximize the stiffness and search for an optimized model, based on the criterion of minimum strain energy, the optimized topologies serve as assistance in the definition of representative truss models of the elements with geometrical and static discontinuities.

Even with a vast development in technical specifications, the research in the area of topology optimization, in general, does not emphasize the design of structural elements in discontinuity regions, focusing on just discussing the computational aspects. The task to interpret the result through the material distribution, as a strength mechanism through the truss bars, is still a challenge, because many parameters are involved in the process.

As a representation of preliminary truss models, the constraint in the optimization problem in which the volume fraction is about 40% to 50% was shown adequately as an indicative of initial analysis. Elevated fractions (above 50%) do not suppress the necessary amount of material for the visualization of the load path in the optimized model. Related to the mesh refinement, which depends on each analyzed geometry, in the presented cases, the results were satisfactory for the analysis in plane stress state with quadrilateral finite elements of edges of an approximate size of 25 mm.

The obtained results through topology optimization may be considered, in every case, as preliminary truss models. It should be considered that the proceeding is not conceived for the complete design. In general, the results should be validated by verified formulations in experimental analyses. To check the ductility criterion, it is necessary to verify if additional reinforcement will be necessary, in such a way as to assure that the model is agreeing with the lower bound theorem of the theory of plasticity.

For the development of optimized models, various aspects related to the project should be checked, such as the restraint factors of execution, financial availability, and specialized labor. A profound study and a larger structural sensibility, using the optimization tools will enable the engineer to develop bolder and cheaper projects.

ACKNOWLEDGEMENTS

The authors acknowledge the National Council for Research and Development (CNPq) for the financial support provided in this research and the Laboratory of Scientific Computing and Visualization (LCCV), from Technology Center (CTEC) at Federal University of Alagoas (UFAL).

REFERENCES

[1] Associação Brasileira de Normas Técnicas, *Projeto e Execução de Estruturas de Concreto Pré-Moldado*, NBR 9062, 2017.

[2] M. K. El Debs, *Concreto Pré-Moldado: Fundamentos e Aplicações*, 2. ed. São Paulo: Oficina de Textos, 2017.

[3] Associação Brasileira de Normas Técnicas, *Projeto de Estruturas de Concreto: Procedimento*, NBR 6118, 2014.

[4] Q. Q. Liang, Y. Xie, and G. P. Steven, "Topology optimization of strut-and-tie models in reinforced concrete structures using an evolutionary procedure," *ACI Struct. J.*, vol. 97, no. 2, pp. 322–330, 2000.

[5] J. C. Pantoja, "Geração automática via otimização topológica e avaliação de segurança de modelos de bielas e tirantes," Ph.D. dissertation, Pont. Univ. Cat. Rio de Janeiro, Rio de Janeiro, 2012.

[6] Q. Q. Liang, *Performance-Based Optimization of Structures: Theory and Applications*. London: Spon Press, 2004.

[7] V. S. Almeida, H. L. Simonetti, and L. Oliveira No., "Análise de modelos de bielas e tirantes para estruturas de concreto armado via uma técnica numérica," *Rev. IBRACON Estrut. Mater.*, vol. 6, no. 1, pp. 139–157, 2013.

[8] M. B. B. F. Guerra, "Modelos de concepção para estruturas em concreto armado com comportamento não linear obtidos pelo método de bielas e tirantes e otimização topológica," Ph.D. dissertation, Univ. Fed. Minas Gerais, Belo Horizonte, 2017.

[9] M. B. B. F. Guerra and M. Greco, "Modelos de concepção para estruturas de concreto armado com comportamento não linear obtidos pelo método de bielas e tirantes e otimização topológica," *Rev. Sul-Americana Eng. Estrut.*, vol. 14, no. 1, pp. 59–78, 2017.

[10] American Concrete Institute, *Building Code Requirements for Structural Concrete*, ACI 318-14, 2014.[11] European Committee for Standardization, *Eurocode 2: Design of Concrete Structures: General Rules and Rules for Buildings*, EN 1992-1-1, 2004.

[12] S. El-Metwally and W. F. Chen, *Structural Concrete: Strut-and-Tie Models for Unified Design*. Boca Raton: CRC Press, 2018.

[13] C. Williams, D. Deschenes, and O. Bayrak, *Strut-and-Tie Model Design Examples for Bridges: Final Report*. Texas: Texas Dep. Transportation, 2012.

[14] J. Schlaich, K. Schäfer, and M. Jennewein, "Toward a consistent design of structural concrete," *PCI J.*, vol. 32, no. 3, pp. 74–150, 1987.

[15] R. A. Souza, "Concreto estrutural: análise e dimensionamento de elementos com descontinuidades," Ph.D. dissertation, Esc. Politécnica, Univ. São Paulo, São Paulo, 2004.

[16] O. Sigmund, "A 99 line topology optimization code written in MatLab," *Struct. Multidiscipl. Optim.*, vol. 21, no. 2, pp. 120–127, 2001.

[17] M. P. Bendsøe and N. Kikuchi, "Generating optimal topologies in structural design using a homogenization method," *Comput. Methods Appl. Mech. Eng.*, vol. 71, no. 2, pp. 197–224, 1998.

[18] Simulia, *ABAQUS® User's Manual vol. 2*, 2014.

[19] Precast/Prestressed Concrete. *PCI Design Handbook: Precast and prestressed concrete*. 7 ed. Chicago, 2010.

[20] J. M. Araújo, *Curso de Concreto Armado: vol. 4*, 3. ed. Rio Grande: Dunas, 2010.

[21] R. C. Silva, “Concreto armado: aplicações de modelos de bielas e tirantes,” M.S. thesis, Esc. Eng. São Carlos, Univ. São Paulo, São Carlos, 1991.

Author contributions: M.B.M., Cedrim: conceptualization, methodology, analysis, writing; E.N., Lages and A.S.R., Barboza: conceptualization, methodology, analysis, writing, supervision.

Editors: Fernando Fonseca, José Luiz Antunes de Oliveira e Sousa, Guilherme Aris Parsekian.

IBRACON Structures and Materials Journal
Revista IBRACON de Estruturas e Materiais
ISSN 1983-4195 ismj.org

ORIGINAL ARTICLE

Assessment of low-cost wireless sensors for structural health monitoring applications

Avaliação de sensores sem fio de baixo custo para aplicações de monitoramento dinâmico estrutural

Emerson Toledo Júnior[a]
Alexandre Cury[a]
Jánes Landre Júnior[b]

[a]Universidade Federal de Juiz de Fora – UFJF, Programa de Pós-graduação em Engenharia Civil, Juiz de Fora, MG, Brasil
[b]Pontifícia Universidade Católica de Minas Gerais – PUC-MG, Departamento de Engenharia Mecânica, Belo Horizonte, MG, Brasil

Received 21 April 2020
Accepted 16 July 2020

Abstract: Structural Health Monitoring (SHM) programs play an essential task in the field of civil engineering, especially for assessing safety conditions involving large structures such as viaducts, bridges, stadiums, and tall buildings. In fact, some of these structures are monitored 24 hours a day, 7 days a week, to supply dynamic measurements that can be used for the identification of structural problems, e.g., presence of cracks, excessive vibration, damage, among others. SHM programs may provide automated assessment of structural health by processing vibration data obtained from sensors attached to the structure. Frequently, SHM uses wired systems, which are usually expensive due to the necessity of continuous maintenance and are not always suitable for sensing remote structures. Conversely, commercial wireless systems often demand high implementation costs. Hence, this paper proposes the use of a low-cost wireless sensing system based on the single board computer Raspberry Pi, which significantly reduces implementation expenses while keeping data's integrity. The wireless communication is performed in real-time through a local wireless network, responsible for sending and receiving vibration data. The proposed system is validated by comparing its results with a commercial wired system through a series of controlled experimental applications. The results suggest that the proposed system is suitable for civil SHM applications.

Keywords: structural health monitoring, wireless sensors, low-cost accelerometers.

Resumo: Os programas de Monitoramento Dinâmico Estrutural (SHM, em inglês) desempenham uma tarefa essencial na área da engenharia civil, especialmente para avaliar as condições de segurança que envolvem grandes estruturas, como viadutos, pontes, estádios e edifícios altos. De fato, algumas dessas estruturas são monitoradas 24 horas por dia, 7 dias por semana, com o objetivo de prover medições dinâmicas que possam ser usadas para a identificação de problemas estruturais como, por exemplo, presença de fissuras, vibração excessiva, danos, entre outros. Os programas de SHM podem fornecer uma avaliação automatizada da integridade estrutural, processando dados de vibração obtidos de sensores conectados à estrutura. Frequentemente, o SHM usa sistemas com fio que geralmente são caros devido à necessidade de manutenção contínua e nem sempre são adequados para utilização em estruturas de acesso difícil. Por outro lado, os sistemas sem fio comerciais geralmente exigem altos custos de implementação. Portanto, este artigo propõe o uso de um sistema de monitoramento sem fio de baixo custo baseado no computador de placa única Raspberry Pi que reduz significativamente as despesas de implementação, mantendo a integridade dos dados. A comunicação sem fio é realizada em tempo real através de uma rede local sem fio, responsável pelo envio e recebimento de dados de vibração. O sistema proposto é validado comparando seus resultados aos de um sistema comercial com fio a partir de uma série de aplicações experimentais controladas. Os resultados sugerem que o sistema proposto é adequado para aplicações de SHM em estruturas de engenharia civil.

Palavras-chave: monitoramento dinâmico estrutural, sensores em fio, acelerômetros de baixo custo.

How to cite: E. Toledo Júnior, A. Cury, and J. Landre Júnior, "Assessment of low-cost wireless sensors for structural health monitoring applications," *Rev. IBRACON Estrut. Mater.*, vol. 14, no. 2, e14213, 2021, https://doi.org/10.1590/S1983-41952021000200013

Corresponding author: Alexandre Cury. E-mail: alexandre.cury@ufjf.edu.br
Financial support: CNPq (Conselho Nacional de Desenvolvimento Científico e Tecnológico – Project number: 304329/2019-3); FAPEMIG (Fundação de Amparo à Pesquisa do Estado de Minas Gerais – Project number: PPM-00002-16/00001-18), CAPES (Coordenação de Aperfeiçoamento de Pessoal de Nível Superior – Finance Code 001), UFJF (Universidade Federal de Juiz de Fora) and PUC-MG (Pontifícia Universidade Catolica of Minas Gerais).
Conflict of interest: Nothing to declare.

1 INTRODUCTION

The assessment of vibration tests performed on structural systems has great practical importance for Civil Engineering. Several works published in the literature show different types of structural instrumentation schemes and data acquisition systems. These systems are often used as a tool for dynamic monitoring in structures of significant value, such as the Rio-Niterói Bridge [1] in Brazil, the Z24 Bridge [2] in Switzerland and the Millau Bridge [3] in France.

Numerous researches were carried out using long-term monitoring [4]–[6]. In fact, some structures are monitored 24 hours a day, 7 days a week, to supply dynamic measurements that can be used for the identification of structural problems, such as the presence of cracks [7], [8], excessive vibration [9]–[11], damage identification [12]–[15], among others. Furthermore, structural dynamic analyses allow performing a quite extensive structural evaluation concerning its reliability, vulnerability or even its life cycle [16].

Structural Health Monitoring (SHM) systems may provide automated assessments of structural health by processing data from sensors attached to the structure. SHM often uses wired systems, which are usually expensive due to the necessity of continuous maintenance and are not always suitable for sensing remote structures. Moreover, power and wiring constraints imposed by these systems can increase the acquisition costs of such datasets, impose significant setup delays, and limit the number and location of sensors due to costs and installation logistics. Thus, wireless sensor networks (WSNs) are a possible alternative for structural health monitoring systems, since they enable dense in situ sensing and simplify deployment of instrumentation [17], [18]. Nevertheless, wireless sensor networks should be wisely designed to contemplate important aspects, such as the connection range, i.e., how far is the sensor placed from the data processing unit. For short to mid-range distances, the engineer might opt for Wi-Fi protocols. For long distances, however, radio transmissions could be considered.

Due to their high installation costs, wired sensor networks are generally only feasible for long-term SHM applications. The significant cost reductions of using WSNs for SHM would enable their utilization in important public and private infrastructure and increase the use of applications such as short-term structural monitoring. Such systems could extend the lifespan of numerous structures by enabling earlier damage detection and eliminating the cost of routine inspections [19].

Table 1 gathers the most important comparative metrics for both wired and wireless sensor networks.

Table 1. Comparison of wired and wireless sensor networks (adapted from Noel et al. [19]).

Metric	Wired Sensor Networks	Wireless Sensor Networks
Cost	Very high, real world examples costing \$10,000 to \$25, 000	Low, each sensor node costing approximately \$500
Deployment Time	Very long, one real world example taking several days	Short, same real world example taking a half hour
Lifespan	Long, typically limited by hardware lifespan	Short, typically limited by node battery lifespan
Number of Sensors	Typically low due to sensor installation difficulty	Typically higher due to ease of sensor installation
Sensor Synchronicity	Very high due to wired connections.	Concern due to wireless connection.

The number of studies seeking the development of new sensors for the acquisition of dynamic data is growing continuously. In parallel, one observes the innovation regarding the use of wireless networks, proving better results when it comes to decreasing the presence of noise in signals while reducing maintenance costs. Particularly, WSNs start being used to facilitate data transmission. Wireless acquisition is advantageous for enabling instrumentation in inaccessible places, reducing installation and maintenance costs while expanding its use in situations where large wired systems are not feasible. WSNs have been historically powered by batteries and, as a result, the limiting factor in their overall lifespan has always been the battery lifetime. However, alternative solutions can be listed, such as the use of solar panels and the development of sensors that converted ambient vibrations into electromagnetic energy. Sazonov et al. [20] reported a field test in which the self-powered sensors were used on a rural highway. The sensors were shown to be self-powering even during periods of low traffic.

SHM makes use of different kinds of sensors to monitor structures: displacement sensors, strain-gages, and accelerometers, to name a few. In this paper, we focus on an accelerometer-based system. Accelerometers measure, as the name suggests, accelerations of the surface they are mounted on. From a structural engineering standpoint, accelerometers are characterized by several performance parameters: sensitivity, which denotes the smallest measurable acceleration and is expressed in g’s (gravitational acceleration); dynamic range, which denotes the range of accelerations that the device is capable of measuring and is also expressed in g’s; and noise, which is measured either as an RMS (root mean square) value, or is expressed as a function of the frequency of vibration [21].

Varanis et al. [22] proposed the analysis of mechanical vibrations in the time domain and frequency domain using the Arduino platform. The work has validated its use for educational purposes, and, in their work, they compared the experimental results with those obtained through numerical models using three applications: a cantilever beam, a simply supported beam and a fixed ended beam. The accelerometer used was the MPU-6050 and the results were enough for educational use considering its accuracy and low cost.

Abdelgawad and Yelamarthi [23] presented the importance of the Internet of Things concept for Structural Integrity Monitoring system based on the connectivity of sensors to the worldwide computer network. To this end, it proposes the use of a prototype based on Raspberry Pi 2 for the detection of damage in aluminum plates. The sensor used was not an accelerometer, but a pulse sensor to evaluate damage through the pulse-echo method. The proposed model was able to differentiate the presence of non-existence damage with 0% error, with 1.03% error in the location of the damage, and 8.43% error when measuring the damage. However, results of the proposed prototype were not compared to the conventional accelerometer counterpart.

Afsana et al. [24] proposed a wireless sensor network for detecting cracks in concrete structures. For this, they suggested the use of Raspberry Pi 3 Model B along with an unspecified vibration sensor. A relevant feature is the use of a GSM modem to perform the remote communication with the user, uploading the data on a web page. The work has no test results and is based on the indication of hardware for assembly of a prototype. A couple of works also pointed in this direction, such as Shachi and Manjunatha [25] and Chandankhede [26].

In this sense, this paper presents a study to explore the potentialities and verify the suitability of low-cost sensors as replacements to commercial wired accelerometers in specific testing scenarios. To this end, this paper details the design, programming, implementation, and evaluation of a low-cost wireless accelerometer based on a small single-board computer named Raspberry Pi. This platform significantly reduces implementation costs while keeping data's integrity. The wireless communication is performed in real-time through a local wireless network, responsible for sending and receiving data. To get acceleration data, two sensors are used in this work and are compared to evaluate the cost-effectiveness of each; these are the MPU-6050 and the MPU-9250. The proposed system is validated by comparing its results with a commercial wired system through benchmark experimental applications performed in laboratory.

2 DESIGN AND IMPLEMENTATION OF THE SYSTEM

In order to design a reliable and robust wireless accelerometer, certain minimum prerequisites are needed to fulfil an adequate sensing performance. The most important requirements are: sensor's autonomy, real-time data acquisition and transmission, low cost, and data's reliability.

Concerning sensor's autonomy, the choice of proper physical components plays a pivotal role. Thus, using modules with low-power consumption and a platform that supports the use of an external battery and sustainable energy systems are essential.

For a SHM system, the device must be able to receive orders from the remote user and send real-time data acquisition according to a given command. That means real-time data acquisition and transmission. Being low cost is the main purpose of this work, proposing an inexpensive wireless system. Thus, the physical components should be easy to buy, affordable as well as the controlling software should be preferably free.

Within this study, the synchronization is made using a broadcast command without addressing a specific IP. This means that a packet is received by all equipment almost simultaneously. Given the fact that all equipment is connected to a local network and care was taken to avoid interference from nearby networks, the latency reached was 1-2ms, which is not sufficient to significantly offset the frequency range proposed for the system.

For large-scaled applications, one could easily use GPS. However, it should be kept in mind that increasing the complexity of Wi-Fi networks, it would also increase the communications' latency. Thus, it would be possible to easily use a GPS module that has microsecond accuracy for remote synchronization. Such a procedure is already widely used for standalone sensors that require a high level of accuracy.

Data's reliability covers several factors such as noise, data loss, sensitivity, frequency range and duration of data acquisition. Noise can vary according to the accelerometer's resolution and to its way of acquiring data. However, it can also be influenced by how devices are connected to each other, especially the wiring. Data loss happens especially in wireless communication if the wireless accelerometers and the data acquisition module are not well synchronized or if there is an incompatibility between the devices. Sensitivity, frequency range and duration must be provided for each application so that the accelerometer is arranged to receive values in a frequency band. Thus, sampling frequency and time of acquisition are defined according to the sampling Nyquist-Shannon theorem. The proposed wireless system can be schematically represented as Figure 1 shows.

Figure 1. Wireless system schematics.

3 HARDWARE

The physical components are chosen to meet the aforementioned prerequisites. Their specifications should meet design specifications and must be compatible with each other. To assemble the wireless system proposed in this work, some components are used, including primarily the Raspberry Pi 3 Model B, followed by the sensors MPU-6050 and MPU-9050.

3.1 Raspberry Pi 3 Model B

Raspberry Pi is known as a single-board computer, being a complete computer built on a single circuit board, with microprocessor, memory, input/output (I/O) and other features required for a functional computer.

Raspberry Pi 3 Model B shown in Figure 2 is based on a Quad Core 1.2GHz Broadcom BCM2837 64bit and 1GB RAM. Its connectivity is made by cable with 10/100 Mbit/s Ethernet or wirelessly via BCM43438 wireless LAN and Bluetooth Low Energy (BLE) on board. The design of this model does not include non-volatile memory - such as a hard drive - but it has an SD card slot for data storage, which is a must for the proposed prototype.

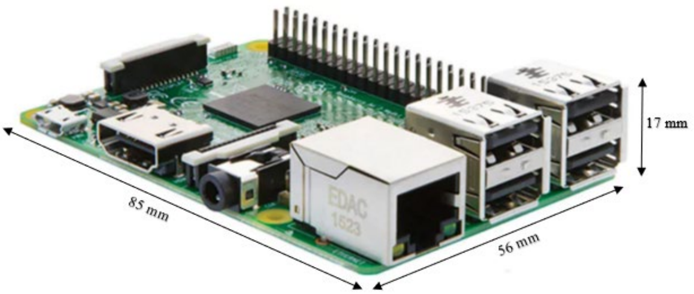

Figure 2. Raspberry Pi 3

3.2 MPU-6050

The InvenSense MPU-6050 sensor contains a MEMS accelerometer and a MEMS gyro on a single chip. It is very accurate since it contains 16-bit analog-to-digital conversion hardware for each channel. Therefore, it captures the x, y, and z directions at the same time. The sensor uses the I2C-bus to interface with Raspberry Pi. MPU-6050 was the first MotionTracking device designed for low-power, low-cost, and high-performance requirements for smartphones, tablets, and handheld sensors. All this in a device of dimensions 4 mm x 4 mm x 0.9 mm with prices ranging from around 6 to 8 US dollars.

The accelerometer is programmable by the user in several acceleration ranges, being able to be set on ± 2g, ± 4g, ± 8g and ± 16g. The MPU-6050 has an input voltage of 6-16V, a low-pass filter between 5-260Hz, and a data output rate between 4 to 1000 Hz. The prototype developed in this work uses the accelerometer sensor set on frequency range of ± 2g.

3.3 MPU-9250

The InvenSense MPU-9250 sensor is also a sensor containing a MEMS accelerometer and a MEMS gyro on a single chip. Its specifications are remarkably similar to the MPU-6050 previously mentioned, but with improvements that can be useful in structural monitoring.

From all improvements, three are highlighted: i) the promise of a 25% reduction in noise; ii) the increase of the sampling rate, to 4000 Hz (versus 1000 Hz of the MPU-6050); and iii) the data output rate is between 2.5 to 1000 Hz. This allows sampling in the 3 axes simultaneously at approximately 1300 Hz, while its predecessor was limited to approximately 300 Hz if the 3 axes were acquired at the same time.

According to the Nyquist-Shannon Theorem, a bandlimited continuous-time signal can be sampled and perfectly reconstructed from its samples if the waveform is sampled over twice as fast as its highest frequency component. Thus, for the case of the MPU-6050, it would be possible to properly sample a signal containing frequencies up to 150 Hz, whereas for the MPU-9250 such value would increase to 1300 Hz.

For common civil structures, which are the main focus of this paper, both would be appropriate for use. However, it is very important to have vibration signals sampled with adequate time and frequency resolutions (i.e., more data samples within a time window), since this would allow a better representation of the structure's dynamic behavior, yielding better post-processing of the data (e.g. modal identification, filtering, input to damage detection techniques, etc.).

4 SOFTWARE

The choice of suitable software to program and control the prototype is extremely important, since one of the most important points of the prototype is to efficiently perform the communication between the remote user and the accelerometer. In addition, considering a low-cost system, preference was given to free distribution and open source software. Concerning Raspberry Pi, it is still crucial to carefully choose the operating system, which will be decisive for the suitable functioning of the equipment according to the needs of the sensing system.

4.1 Raspbian Lite

Raspbian [27] is a free operating system based on Debian and optimized for Raspberry Pi hardware. The operating system is composed of a set of basic programs and utilities that allow the initialization and basic use of the device. Its reputation revolves around being a high-quality, stable, and scalable operating system. Being scalable indicates the ability of the system to increase its performance according to the increase of resources, for example, more powerful hardware.

Because Raspbian is an adaptation of Debian, there is a wide range of bibliography and documentation, as both have been extensively explored by users of various applications. The Raspbian operating system itself is offered through a graphical interface. The use of the graphical interface ends up generating a computational cost that does not generate return to the remote sensing system. Thus, it is interesting that the equipment has as priority only the acquisition and processing of the acceleration data.

From this comes the Raspbian Lite operating system, being a variation of the Raspbian system with the same functionalities, but without the graphical interface. All the configuration of the device, as well as its use and monitoring, is performed through the system terminal from command lines. With this, the prototype processor is relieved of graphic processing and can be used exclusively on its function as a sensor.

4.2 Putty

Putty [28] is an SSH communication client originally developed by Simon Tatham, an open source program that is currently developed and enhanced by a group of volunteers. Its utility is to be able to remotely access the terminal of any Raspberry Pi that is connected in the same Wi-Fi network as the user. That is, the user can reprogram any system sensor remotely, having access to the terminal of the coordinator of the accelerometer, in this case, the Raspberry Pi.

SSH is an acronym for Secure Shell which is a cryptographic network tool used in insecure networks to operate safely without data interception. The main use of this tool is the remote access of computers in a network, having access to their terminal.

4.3 WinSCP

WinSCP [29] is a software that is designed to be a free solution for file transfers using the FTP protocol and its variants, being a free award-winning software for file management. In the wireless sensing system, the accelerometers work remotely. This means that the computer does not have to be connected to the system during the test. Once automated, the system will run until the user asks to stop or set an end-of-trial parameter.

During the test, the accelerometers can instantly send their readings or save the dataset to their flash memory. Thus, WinSCP arises to enable the process of transferring files safely between the remote sensor and the user.

FTP is an acronym for File Transfer Protocol which is a standard network protocol used to transfer digital files between client and server on a computer network. This protocol is not considered secure purely. Thus, the variation used in this work is SFTP, which is the FTP protocol with SSH authentication explained previously.

To connect to the sensors and to recover the acceleration data, it suffices that the user is connected to the same Wi-Fi network and knows the IP address of the sensor. It is also possible to set a password authentication before full accessing Raspberry Pi.

5 EXPERIMENTAL APPLICATIONS

The effectiveness and robustness of the proposed wireless acquisition system is assessed through a series of experimental applications. The methodology relies on attaching three different accelerometers to two excitation modules. The first accelerometer is the CCLD 4507B, a commercial accelerometer with calibration certificate connected to a QuantumX MX1601B acquisition system; this setup represents a traditional wired instrumentation and is used as baseline for comparison. This assembly costs around 3000 US dollars.

The second accelerometer is the MPU-6050 connected to a Raspberry Pi 3 Model B, being a basic proposal of prototype using Raspberry Pi. The third accelerometer is the MPU-9250 connected to a Raspberry Pi 3 Model B, being a suggestion of improvement of the MPU-6050. Both assemblies cost around 30 US dollars.

The communication of the first accelerometer is entirely done through cables, whereas for the second and third accelerometers, data transmission is performed via local Wi-Fi network established in laboratory without connection to the Internet. All tests are performed at a constant acquisition rate of 600Hz, considering the Nyquist-Shannon theorem that limits the tested frequencies at 300Hz. Two sets of tests are performed separately using two different shakers.

The first testing setup consists in an experiment performed using an accelerometer calibrator. This equipment can generate a pure sinusoidal wave without harmonics in a frequency and amplitude predefined during its manufacture. The model PCB 394C06 operates at a frequency of 159.2Hz with a peak acceleration of 1.00g (9.81m/s^2). In this case, since there is a constancy of frequency and amplitude of acceleration, tests with three simultaneous accelerometers are not mandatory and thus, can be performed one after another, consecutively. Figure 3 shows the instrumentation scheme for these tests.

Figure 3. Testing setup (MPU-6050 attached to the calibrator).

The second testing setup consists in a modulated experiment using a ModalShop 2004E shaker. To modulate frequency and amplitude, a Keysight 33210A arbitrary waveform and function generator was used. The generator chosen is digital to offer greater control and stability to the system. In this process, the acceleration data are registered simultaneously for all three accelerometers and then compared. Figure 4 shows the instrumentation scheme for these tests.

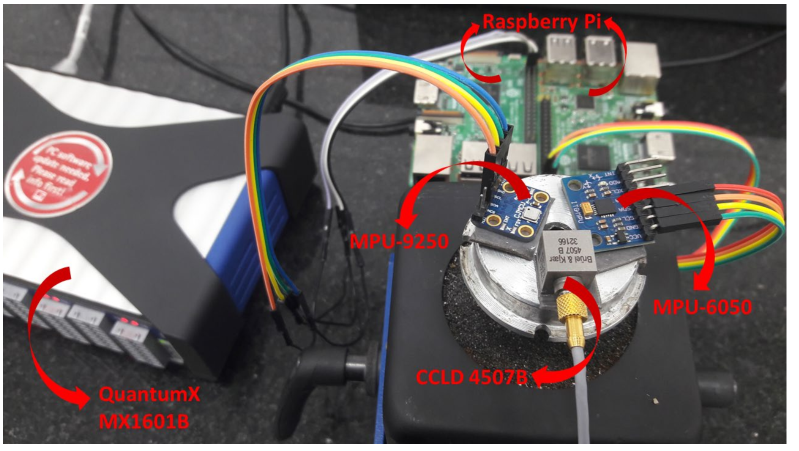

Figure 4. Testing setup (three accelerometers attached to the shaker).

5.1 Prototype Implementation

The process starts with the setup of a local Wi-Fi network, choosing the best channel to avoid interference during wireless communication.

Then, Raspbian Lite operating system is installed in the Raspberry PI module, setting the configuration for automatic connection to the local network with access password and the enabling of the SSH and I2C interfaces. Thus, tools such as I2C Tools and Python SMBUS are installed, followed by the algorithm that controls the data acquisition process, e.g. sampling rate, beginning of test, end of test, method of internal storage, data transferring and so on.

In this methodology, the start parameter of each experimental test is a command sent by a computer to all the equipment connected to the same network. After receiving this command, all prototypes start registering the readings at 600 Hz, with the end of the test being its duration (set to 90 seconds). Data is stored in the memory card in txt format.

Acquired data can be internally post-processed by the prototype using the Raspberry Pi's processing capability. However, this work is mainly interested in analyzing the data without any internal treatment. Thus, the txt files are stored until the user remotely accesses them and downloads them. Files are identified by their start acquisition date and time, with an accuracy of seconds. Figure 5 schematizes the entire instrumentation process.

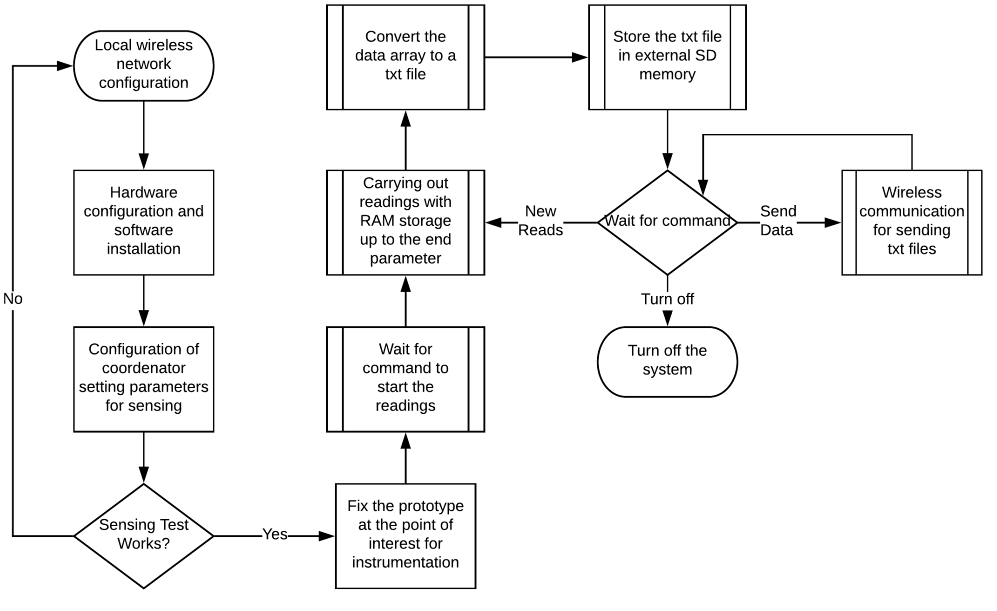

Figure 5. Flowchart of the prototype's implementation

5.2 Zero-G output tests

The zero-g output tests were performed comparing the response of the three accelerometers placed on a flat surface at rest without any vibration, as a way of assessing internal noise. Figure 6 depicts a part of such tests.

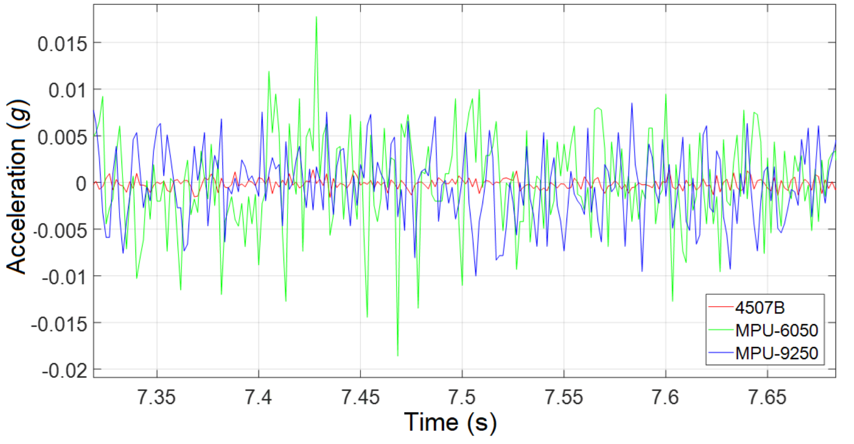

Figure 6. Comparison of the responses registered by the accelerometers at rest.

These results represent a limitation of the proposed system concerning vibration tests that generally occur under very low acceleration amplitudes (ambient excitation). However, this drawback is circumvented in frequency domain analyses, where the low cost sensors present very good results compared to the commercial accelerometer (further discussion is provided in section 5.3).

To better compare the influence of internal noise of each accelerometer, a statistical analysis is now proposed. When analyzing the noise range of the three accelerometers, 5% of the readings that are too far away from the mean values – outliers – are removed to avoid measurements that do not represent the usual behavior of the accelerometers. Thus, the 95% of the retained readings represent a range of noise that the accelerometer shows without external vibration. These acceleration ranges are shown in Table 2.

Table 2. Comparison of noise bands.

	Zero-G output (g)		
	Negative peak	**Positive peak**	**Average range**
4507B	-0,0014	0,0013	±0,00135
MPU-6050	-0,0105	0,0100	±0,01025
MPU-9250	-0,0095	0,0095	±0,00950

According to Table 2, the noise band for the MPU-6050 is 759% larger than the 4507B's counterpart, while the MPU-9250 is 704% larger. Thus, there is a noise reduction of 7.3% from the MPU-9250 to its predecessor.

Even though the percentage differences are substantial, the absolute differences may be insignificant depending on the desired application for the sensors. If the application requires a sensitivity of 0.001g, the commercial accelerometer would be the most recommended. On the other hand, applications that allow an uncertainty of 0.01g in the measurements, both MPU-6050 and MPU-9250 could meet the requirements of resting noise at a much lower cost.

The noise at rest does not actually represent the total existing reading error when the structure is in acceleration, but rather from which minimum acceleration of the structure it is possible to differentiate what is real structural acceleration to what is resting noise.

5.3 Frequency domain analyses

In the frequency domain, the interest is in determining the precision and accuracy of the results obtained by the prototypes when compared to the commercial accelerometer.

To this end, the first analysis is performed using the universal calibrator. This equipment guarantees an excitation frequency equal to 159,2 Hz. The second analysis utilizes the ModalShop 2004E shaker of modulated frequency and amplitude.

Figure 7 shows the frequency responses of the three accelerometers using the universal calibrator. For all cases, the natural frequency is exactly identified at 159.2 Hz. The difference in the peak values in the y axis reflects the divergences in the time domain, which will be discussed in the next section. Other identified frequencies indicated by the arrows were found only by the MPU-6050 and MPU-9250, with amplitudes proportional to the noise detected in the signals. Such spurious frequencies are not representative, given the discrepancy of their amplitudes in relation to main frequencies.

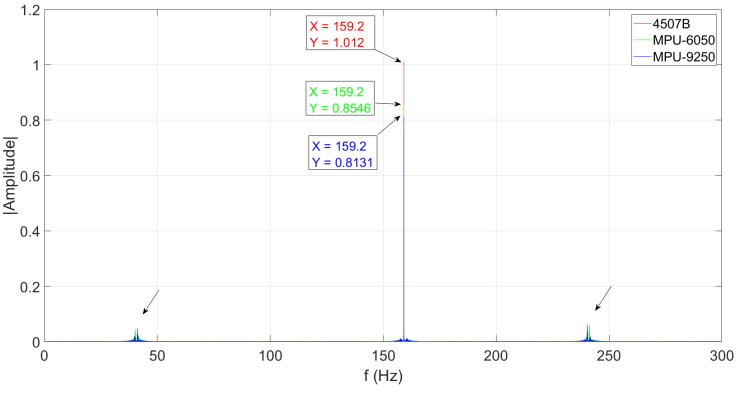

Figure 7. Responses in the frequency domain using the universal calibrator at 159,2 Hz/1,0g.

Figure 8 shows the results in the frequency domain for the tests carried out at 2.5Hz / 0,02g. This represents the 'worst' scenario for the prototypes since it has the lowest signal-to-noise ratio. For this case, all frequencies identified by the 4507B were also detected by the other two low cost accelerometers. It is interesting to note the tendency to find multiple frequencies from 2.5 Hz to the 95 Hz frequency, except for a few that were not detected by any of the three accelerometers.

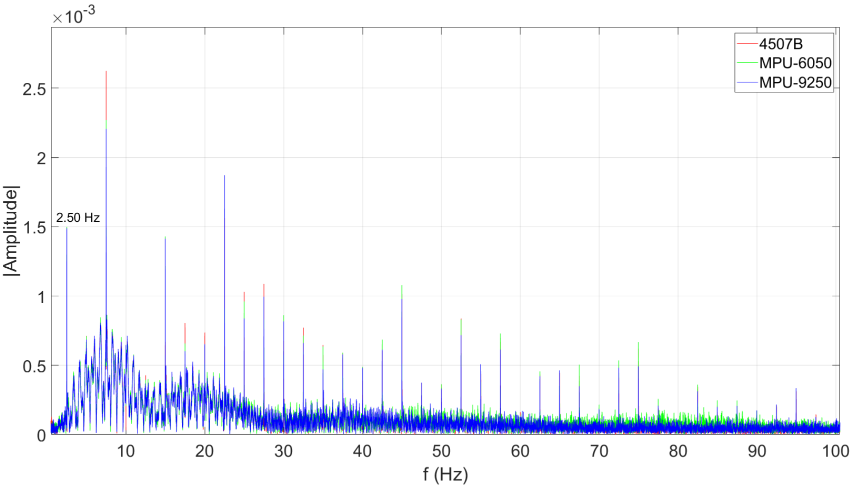

Figure 8. Responses in the frequency domain using the modulated shaker at 2,5 Hz / 0,02g.

For the frequency of 20 Hz, the most unfavorable situation is the acceleration amplitude of 0.2 g (see Figure 9). Again, the prototypes presented very satisfactory results.

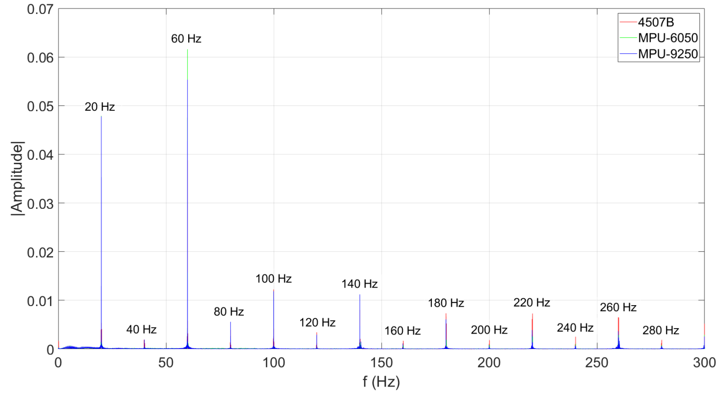

Figure 9. Responses in the frequency domain using the modulated shaker at 20 Hz/0,2g.

The accuracy, precision and reliability of the results obtained by the prototypes allow validating their operation in the frequency domain within the frequencies and amplitudes tested.

5.4 Time domain analyses

The main consequence of high internal noise levels lies mostly in the time domain. Therefore, quantifying the prototype's divergences from the commercial accelerometer is crucial for assessing their potential to accurately represent structural vibration. Hence, quantifying such errors allows establishing confidence acceleration intervals for the prototypes. While within these confidence intervals, the prototypes can be used in structural diagnostics established from temporal data, such as the criterion of maximum acceleration in a structure.

The first testing setup uses the universal accelerometer calibrator. The acceleration amplitude of 1,0 g without harmonic frequencies is guaranteed by certification, being the only test with a pure sinusoidal behavior. Results for the three accelerometers are shown in Figure 10.

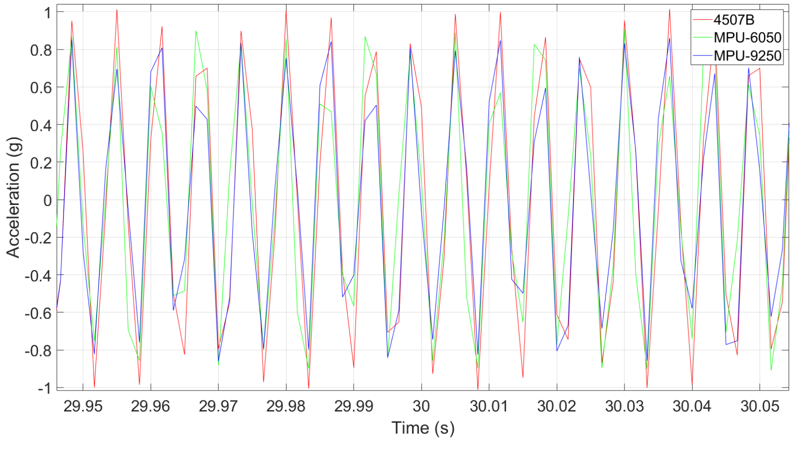

Figure 10. Responses using the universal calibrator at 159,2 Hz/1,0g.

By observing Figure 10, both MPU-6050 and MPU-9250 were able to reasonably represent the behavior of the vibration in the time domain when compared to the 4507B. Nonetheless, since the sampling rate is 600 Hz and the excitation frequency is 159.2 Hz, the acceleration peaks in the readings often do not match the accelerator peaks of the calibrator. Table 3 shows the maximum and minimum accelerations found for each accelerometer.

Table 3. Absolute acceleration peaks using the calibrator.

	Acceleration (g)		
	Negative peak	**Positive peak**	**Average range**
4507B	-1,0279	1,0191	±1,0235
MPU-6050	-0,9717	0,9600	±0,9658
MPU-9250	-0,8671	0,8717	±0,8694

The maximum acceleration values are important to realize that the 4507B, which has the lowest noise level, obtained a higher acceleration range value based on the maximum readings. Therefore, it is necessary to establish a multiplication factor for the prototype accelerometers, just as the 4507B has a calibration constant in its certificate.

The multiplication factor is evaluated by firstly identifying the positions in the time in which the dominant frequency reaches its maximum acceleration and then by extracting its respective acceleration peaks.

For the universal calibrator, the multiplication factor's evaluation becomes simpler because the signal has only one frequency. In the modulated shaker, however, it is necessary to use a frequency filter to obtain the time location where the maximum acceleration for the dominant frequency is, and then return to the raw signal to obtain the acceleration at that instant of time, since the frequency filters change the signal amplitude. Next, a filter is created to remove outliers. Thus, 5% of the most distant readings from the mean value are removed, i.e. 2.5% of the lowest readings and 2.5% of the highest readings.

With the average of the maximum values already filtered, all accelerometers are then compared. Note that for each set of experiments, new multiplication factors must be evaluated. Tables 4 and 5 show the average values (and respective standard-deviations) of the multiplication factors for the tests performed. Tests were repeated five times for each combination 'acceleration band' x 'frequency'.

Table 4. Multiplication Factors for the MPU-6050 (average and standard-deviation values).

		Acceleration band						
		0,02 g	**0,05 g**	**0,1 g**	**0,2 g**	**0,5 g**	**1 g**	**1,5 g**
Frequencies	2,5 Hz	0,8991 (0,0179)	0,9427 (0,0049)	1,0021 (0,0107)	1,1077 (0,0291)	1,0925 (0,0029)	1,0738 (0,0028)	X
	5 Hz	X	0,9149 (0,0074)	0,9519 (0,0096)	0,9791 (0,0083)	1,0800 (0,0070)	1,0509 (0,0102)	1,0119 (0,0175)
	10 Hz	X	0,9640 (0,0171)	1,0225 (0,0012)	1,0646 (0,0138)	1,0180 (0,0205)	1,0254 (0,0133)	1,0404 (0,0029)
	20 Hz	X	X	X	1,0846 (0,0106)	1,0771 (0,035)	1,0610 (0,0113)	1,0366 (0,0083)
	49 Hz	X	X	X	X	1,0877 (0,0082)	1,0768 (0,0035)	1,0280 (0,0098)
	95 Hz	X	X	X	X	X	1,1538 (0,0109)	1,1165 (0,0116)
	159,2Hz	X	X	X	X	X	1,1361 (0,0213)	X

Table 5. Multiplication Factors for the MPU-6050 (average and standard-deviation values).

		Acceleration band						
		0,02 g	**0,05 g**	**0,1 g**	**0,2 g**	**0,5 g**	**1 g**	**1,5 g**
Frequencies	2,5 Hz	0,8801 (0,0200)	0,9487 (0,0013)	0,9912 (0,0112)	1,0842 (0,0079)	1,0906 (0,0013)	1,0813 (0,0036)	X
	5 Hz	X	0,9035 (0,0071)	1,0380 (0,0253)	1,0245 (0,0133)	1,0386 (0,0018)	1,0558 (0,0055)	1,0587 (0,0123)
	10 Hz	X	1,0287 (0,0135)	1,0799 (0,0166)	1,0569 (0,0233)	1,0486 (0,0048)	1,0582 (0,0104)	1,0281 (0,0237)
	20 Hz	X	X	X	1,0839 (0,0145)	1,0304 (0,0086)	1,0368 (0,0122)	1,0436 (0,0168)
	49 Hz	X	X	X	X	1,0781 (0,0136)	1,0854 (0,0126)	1,0482 (0,0128)
	95 Hz	X	X	X	X	X	1,2006 (0,0066)	1,1614 (0,0178)
	159,2Hz	X	X	X	X	X	1,1980 (0,0117)	X

Figure 11 depicts the responses at 2.5 Hz/0.02g (low signal-to-noise ratio) for all accelerometers in the time domain after applying the multiplication factors. A general good agreement can be seen among the accelerometers' outputs.

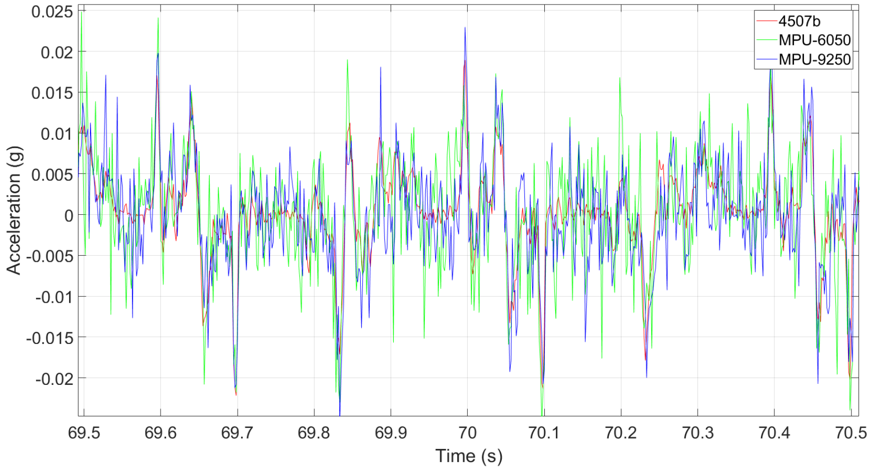

Figure 11. Responses in the time domain using the modulated shaker at 2,5 Hz/0,02g.

Figure 12 shows the 2.5 Hz/1g test responses with a high signal-to-noise ratio, where it is possible to observe the vibration behaviors on a scale where the noise is visually imperceptible for the three accelerometers.

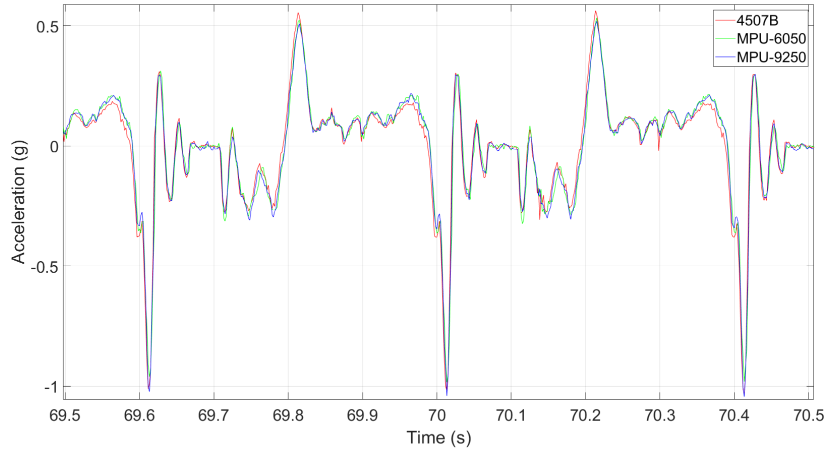

Figure 12. Responses in the time domain using the modulated shaker at 2,5 Hz/1g.

In summary, from the results obtained, considering a frequency range of 2.5 Hz to 49 Hz, it is safe to stipulate a margin of error of 10% between the measurements of the prototypes and the commercial accelerometer. If the frequency range is between 2.5 Hz and 159.2 Hz, such a margin increases to 20%. These are estimates for the reading errors of the MPU-6050 and MPU-9250 sensors, not including design safety factors, which must be added after considering the margin of error of the accelerometers. If the structural applications allow the margin of error presented in this work and are within the frequency range stipulated for the allowed error, then it is possible to use the MPU-6050 or MPU-9250.

Consequently, the main performance loss of the MPU-6050 (and the MPU-9250) happens in the time domain. Prototype accelerometers are not intended to achieve high-frequency performance, such as the 4507B that works up to 6 kHz with a 10% margin of error. In this study, it was possible to verify the reliability of the sensors for frequency bands compatible mainly with those found in SHM of civil engineering structures, such as buildings and bridges.

Finally, it is important to emphasize that the multiplication factors yield values that would best fit the signals' trend and not measurement-to-measurement values, which would be very difficult to achieve and not so useful, since in a structural health monitoring system, for example, numerical analyses would treat such peaks as outliers.

6 FINAL REMARKS AND CONCLUSIONS

This paper proposed a low-cost wireless accelerometer for dynamic structural monitoring based on a single-board Raspberry Pi computer. The entire planning, coding, execution, and evaluation process was carried out with the objective of reducing implementation costs while maintaining data's integrity. The main idea of this paper was to present a raw comparison between low cost and commercial accelerometers and show how close, in terms of performance and reliability, the former could get to the latter.

To assess the prototypes performance, several experimental applications were performed using controlled excitations. Firstly, the noise of the sensors at rest were evaluated. Both low-cost sensors presented higher noise values compared to the commercial accelerometer. Thus, for applications where readings are in the range of 0.001g, prototypes are not indicated. However, for accelerations above 0.01g, the use of the prototypes becomes viable. Moreover, it is important to keep in mind that no type of signal processing or conditioning (such as filtering, amplification, attenuation, among others) was performed during the acquisition process for both MPUs. If that were the case, such discrepancies would be largely reduced.

When it comes to frequency domain analyses, the prototypes presented remarkably similar performance compared to the commercial accelerometer for the tested frequency range between 2.5Hz and 159.2Hz.

Finally, in the time domain, the prototypes presented their largest differences compared to the commercial accelerometer. This happened since the sensors used in the prototypes do not have a calibration constant, such as the 4507B. However, by evaluating specific multiplication factors, those differences have significantly decreased.

In summary, the proposed prototypes could represent a potential low-cost replacement of conventional monitoring cabled systems or commercial wireless sensors for SHM applications. When it comes to field testing in real large-scale structures, it is imperative to carry out preliminary tests to assess suitable multiplication factors - according to frequency and acceleration ranges - so that the results will represent the structure's behavior properly.

As for further developments, the authors are working on fully wireless sensors using small solar panels as sources of energy and the remote synchronization of several sensors. Moreover, a special focus is being given to embedded data compression techniques along with filtering procedures. Finally, the proposed prototypes will be tested in real civil structures in the near future in applications concerning modal tracking and structural damage identification.

ACKNOWLEDGEMENTS

The authors would like to thank CAPES (Coordenação de Aperfeiçoamento de Pessoal de Nível Superior – Finance Code 001), CNPq (Conselho Nacional de Desenvolvimento Científico e Tecnológico - Finance Code 304329/2019-3), FAPEMIG (Fundação de Amparo à Pesquisa do Estado de Minas Gerais – Finance Codes PPM-00002-16 / 00001-18), UFJF (Universidade Federal de Juiz de Fora) and PUC-MG (Pontificia Universidade Catolica of Minas Gerais) for the financial support.

REFERENCES

[1] R. Battista and M. Pfeil, "Reduction of vortex-induced oscillations of Rio-Niterói Bridge by dynamic control devices," *J. Wind Eng. Ind. Aerodyn.*, vol. 84, no. 3, pp. 273–288, 2000, http://dx.doi.org/10.1016/S0167-6105(99)00108-7.

[2] J. Maeck and G. De Roeck, "Description of Z24 benchmark," *Mech. Syst. Signal Process.*, vol. 17, no. 1, pp. 127–131, 2003, http://dx.doi.org/10.1006/mssp.2002.1548.

[3] E. Cachot, T. Vayssade, M. Virlogeux, H. Lancon, Z. Hajar, and C. Servant, "The Millau Viaduct: ten years of structural monitoring," *Struct. Eng. Int.*, vol. 25, no. 4, pp. 375–380, 2015, http://dx.doi.org/10.2749/101686615X14355644770776.

[4] S. Soyoz and M. Q. Feng, "Long-term monitoring and identification of bridge structural parameters," *Comput. Aided Civ. Infrastruct. Eng.*, vol. 24, no. 2, pp. 82–92, 2009, http://dx.doi.org/10.1111/j.1467-8667.2008.00572.x.

[5] A. J. Cardini and J. T. DeWolf, "Long-term structural health monitoring of a multi-girder steel composite bridge using strain data," *Struct. Health Monit.*, vol. 8, no. 1, pp. 47–58, 2009, http://dx.doi.org/10.1177/1475921708094789.

[6] R. Cardoso, A. Cury, and F. Barbosa, "A robust methodology for modal parameters estimation applied to SHM," *Mech. Syst. Signal Process.*, vol. 95, pp. 24–41, 2017, http://dx.doi.org/10.1016/j.ymssp.2017.03.021.

[7] Z. R. Lu and S. S. Law, "Dynamic condition assessment of a cracked beam with the composite element model," *Mech. Syst. Signal Process.*, vol. 23, no. 2, pp. 415–431, 2009, http://dx.doi.org/10.1016/j.ymssp.2008.02.009.

[8] G. D. Ercolani, D. H. Felix, and N. F. Ortega, "Crack detection in prestressed concrete structures by measuring their natural frequencies," *J. Civ. Struct. Health Monit.*, vol. 8, no. 4, pp. 661–671, 2018, http://dx.doi.org/10.1007/s13349-018-0295-2.

[9] I. Z. Mat Darus and M. O. Tokhi, "Soft computing-based active vibration control of a flexible structure," *Eng. Appl. Artif. Intell.*, vol. 18, no. 1, pp. 93–114, 2005, http://dx.doi.org/10.1016/j.engappai.2004.08.017.

[10] L. Qiusheng, H. Yinghou, Z. Kang, H. Xuliang, H. Yuncheng, and S. Zhenru, "Structural health monitoring for a 600m high skyscraper," *Struct. Des. Tall Spec. Build.*, vol. 27, no. 12, 2018, http://dx.doi.org/10.1002/tal.1490.

[11] D. Ribeiro, J. Leite, N. Pinto, and R. Calçada, "Continuous monitoring of the dynamic behaviour of a high-rise telecommunications tower," *Struct. Des. Tall Spec. Build.*, vol. 28, no. 11, pp. e1621, 2019., http://dx.doi.org/10.1002/tal.1621.

[12] A. Cury, C. C. H. Borges, and F. S. Barbosa, "A two-step technique for damage assessment using numerical and experimental vibration data," *Struct. Health Monit.*, vol. 10, no. 4, pp. 417–428, 2010, http://dx.doi.org/10.1177/1475921710379513.

[13] R. P. Finotti, A. A. Cury, and F. S. Barbosa, "An SHM approach using machine learning and statistical indicators extracted from raw dynamic measurements," *Lat. Am. J. Solids Struct.*, vol. 16, no. 2, pp. e165, 2019, http://dx.doi.org/10.1590/1679-78254942.

[14] R. Cardoso, A. Cury, and F. Barbosa, "Automated real-time damage detection strategy using raw dynamic measurements," *Eng. Struct.*, vol. 196, 2019, http://dx.doi.org/10.1016/j.engstruct.2019.109364.

[15] L. Melo, D. Ribeiro, R. Calçada, and T. Bittencourt, "Validation of a vertical train–track–bridge dynamic interaction model based on limited experimental data," *Struct. Infrastruct. Eng.*, vol. 16, no. 1, pp. 181–201, 2020, http://dx.doi.org/10.1080/15732479.2019.1605394.

[16] M. A. Torres and S. E. Ruiz, "Structural reliability evaluation considering capacity degradation over time," *Eng. Struct.*, vol. 29, no. 9, pp. 2183–2192, 2007., http://dx.doi.org/10.1016/j.engstruct.2006.11.014.

[17] S. A. Sindhu and C. A. Nirrmala, "Structural health monitoring using wireless sensor network," *Int. J. Emerg. Technol. Comput. Sci. Electron.*, vol. 13, no. 4, pp. 319–322, 2015.

[18] S. Pandey, M. Haider, and N. Uddin, "Design and implementation of a low-cost wireless platform for remote bridge health monitoring," *Int. J. Emerg. Technol. Adv. Eng.*, vol. 6, no. 6, pp. 57–62, 2016.

[19] A. B. Noel, A. Abdaoui, T. Elfouly, M. H. Ahmed, A. Badawy, and M. Shehata, "Structural health monitoring using wireless sensor networks: a comprehensive survey," *IEEE Comm. Surv. and Tutor.*, vol. 19, no. 3, pp. 1403–1423, 2016, http://dx.doi.org/10.1109/COMST.2017.2691551.

[20] E. Sazonov, Haodong Li, D. Curry, and P. Pillay, "Self-powered sensors for monitoring of highway bridges," *IEEE Sens. J.*, vol. 9, no. 11, pp. 1422–1429, 2009, http://dx.doi.org/10.1109/JSEN.2009.2019333.

[21] N. Xu et al., “A wireless sensor network for structural monitoring,” in *Proc. 2nd Int. Conf. Embed. Netw. Sensor Syst., SenSys ’04*, 2004, pp. 13-24, http://dx.doi.org/10.1145/1031495.1031498.

[22] M. Varanis, A. L. Silva, P. H. A. Brunetto, and R. F. Gregolin, "Instrumentation for mechanical vibrations analysis in the time domain and frequency domain using the Arduino platform," *Rev. Bras. Ensino Fis.*, vol. 38, no. 1, 2016, http://dx.doi.org/10.1590/S1806-11173812063.

[23] A. Abdelgawad and K. Yelamarthi, "Internet of Things (IoT) platform for structure health monitoring," *Wirel. Commun. Mob. Comput.*, vol. 2017, pp. 1–10, 2017, http://dx.doi.org/10.1155/2017/6560797.

[24] A. Afsana, S. Anbarasi, P. Deepa, R. Ghaveya, and D. Marugesan, "Wireless sensor network based crack detection on concrete bridges/buildings," *Int. J. Eng. Trends Technol.*, vol. 57, no. 2, pp. 54–58, 2018, http://dx.doi.org/10.14445/22315381/IJETT-V57P211.

[25] P. Shachi and S. Manjunatha, "Automatic bridge health monitoring system using wireless sensors," *Int. J. Sci. Res.*, vol. 6, no. 6, pp. 2472–2475, 2015.

[26] V. Chandankhede, "Health monitoring of highway bridges using wireless sensor networks," *Int. J. Adv. Res. Electron. Commun. Eng.*, vol. 6, no. 8, pp. 927–930, 2017.

[27] Raspbian. https://www.raspberrypi.org/documentation/raspbian/ (accessed Apr. 21, 2020).

[28] Putty. https://www.chiark.greenend.org.uk/~sgtatham/putty/docs.html (accessed Apr. 21, 2020).

[29] WinSCP. https://winscp.net/eng/docs/start (accessed Apr. 21, 2020).

Author contributions: ET: Conceptualization, Data curation, Formal analysis, Investigation, Methodology, Writing-original draft, Writing-review & editing. AC: Conceptualization, Data curation, Formal analysis, Funding acquisition, Investigation,
Methodology, Project administration, Supervision, Validation, Writing-review & editing. JL: Conceptualization, Data curation, Formal analysis, Funding acquisition, Investigation,
Methodology, Resources, Supervision.

Editors: Tulio Nogueira Bittencourt, José Luiz Antunes de Oliveira e Sousa, Guilherme Aris Parsekian.

Rev. IBRACON Estrut. Mater., vol. 14, no. 2, e14214, 2021

IBRACON Structures and Materials Journal
Revista IBRACON de Estruturas e Materiais
ISSN 1983-4195 ismj.org

ORIGINAL ARTICLE

Partial replacement of Portland cement with industrial glass waste in mortars

Substituição parcial de cimento Portland por resíduo moído de vidro industrial em argamassas

Raduan Krause Lopes[a]
Jayne Carlos Piovesan[b]
Bernardo Fonseca Tutikian[c]
Atilio Efrain Bica Grondona[c]

[a]Fundação Universidade Federal de Rondônia – UNIR, Departamento de Engenharia Civil, Porto Velho, RO, Brasil
[b]Centro Universitário São Lucas – UNISL, Porto Velho, RO, Brasil
[c]Universidade do Vale do Rio dos Sinos – UNISINOS, Programa de Pós-Graduação em Engenharia Civil, São Leopoldo, RS, Brasil.

Received 14 November 2019
Accepted 29 June 2020

Abstract: The necessity to reduce the consumption of cement in cementitious composites is a worldwide concern and the partial replacement of cement with industrial waste has gathered considerable interest. One type of industrial waste is glass, which is rich in amorphous silica but can present problems with its use due to the alkali-silica reaction (ASR). The objective of this study was to analyze the compressive strengths of mortars using ground glass residue (GLR). Milling times of 16 h and 32 h were conducted and GLR tested in cement substitutions of 10 w.t.%, 15 w.t.% and 20 w.t.%. A statistical analysis was performed to verify which factors affected mortar strength. The mitigating effect of GLR in ASR was also tested. Results showed that milling time did not affect resistance significantly but w.t.% substitution did. The substitution of 20 w.t.% proved to provide the best result as it was statistically equal to the standard mixture.

Keywords: ground glass residue (GLR), mortar, pozzolanic activity, alkali-silica reaction (ASR).

Resumo: A busca pela redução do consumo de cimento em compósitos cimentícios se mostra uma preocupação mundial, e a substituição parcial do cimento por resíduos industriais tem ganhado impulsão. Um desses materiais é o vidro, material rico em sílica amorfa, mas que pode apresentar problemas em sua utilização, devido à reação álcali sílica (RAS). O objetivo da pesquisa foi analisar as resistências à compressão de argamassas com uso de resíduo moído de vidro (RMV). Foram testados dois tempos de moagem para RMV, 16 e 32 horas, bem como percentuais de 10, 15 e 20% de substituição em massa de cimento por RMV. Uma análise estatística foi realizada para verificar quais fatores interferiam na resistência das argamassas. O efeito mitigador do RMV também foi testado quanto à RAS. Os resultados mostraram que o tempo de moagem não foi significativo para resistência, mas os percentuais de substituição foram. O percentual de 20% mostrou-se o melhor, uma vez que foi estatisticamente igual ao traço padrão.

Palavras-chave: resíduo moído de vidro (RMV), argamassa, atividade pozolânica, reação álcali sílica (RAS).

How to cite: R. K. Lopes, J. C. Piovesan, B. F. Tutikian, and A. E. B. Grondona, "Partial replacement of Portland cement with industrial glass waste in mortars," *Rev. IBRACON Estrut. Mater.*, vol. 14, no. 2, e14214, 2021, https://doi.org/10.1590/S1983-41952021000200014

1 INTRODUCTION

Currently, one of the greatest challenges in construction is to merge material performance with reductions in environmental impact and cost of production. According to Higuchi [1], the environmental impact of concrete and mortar production are enormous, especially with respect to Portland cement and the environmental impact of its

Corresponding author: Bernardo Fonseca Tutikian. E-mail: bftutikian@unisinos.br
Financial support: None.
Conflict of interest: Nothing to declare.

production. Cement remains one of the main materials needed in construction and its production also consumes a significant amount of energy and contributes greatly to carbon dioxide emissions [2].

More recently, the environmental impacts of construction have been acknowledged and studies regarding sustainability have come to the forefront of this area. Much of this work has been focused in reducting in the quantity of cement used. To this end, Sales et al. [3] noted that cement substitution with solid residues has been used as an alternative. Several studies have been conducted to improve the performance, durability, physical and chemical properties, hydration and microstructure of mixtures mortar and concrete that incorporate residues [2].

Glass, as noted by Gómez-Soberón et al. [4], is a different type of recyclable material available in great quantities to supply the demand for substitute construction materials. Glass itself is also a solid residue with several environmental impacts: it is non-biodegradable so it permanently occupies landfills and associated pollution can be pervasive in the air, water and soil [2], [4]. A possible solution would be the use of glass in concrete and mortar mixtures since it has chemical composition and phases similar to traditional supplementary cementitious materials (SCMs) [5]. Higuchi [1] noted that the chemical composition and reactivity of glass as a SCM can improve chemical stability, water resistance and durability of concrete. However, other studies noted that the size of glass particle has an effect in concrete and mortar mixtures. Better results were obtained with glass residue particles in the microscale range [1], [4]–[6] and smaller particles have better activation and pozzolanic behavior [3], [7].

Special considerations must be taken so that an alkali silica reaction (ASR) does not occur when glass residue is incorporated in mortar and concrete mixtures. As noted by Azevedo et al. [8], glass and cement are chemically incompatible. Alkaloids present in Portland cement and vitreous silica react under humidity to form an ASR. This reaction can be reduced with the use of cements with low alkali content or which contains materials that inhibit or minimize the reaction, such as pozzolans and slag. Yet, other studies reported that glass residue used as supplemental cementitious material (SCM) or fine aggregate in concrete and mortar do not undergo ASR if the residue particles are of a size below 100 μm [8]–[9].

With these in mind, the objective of this study was to evaluate the partial substitution of Portland cement with ground glass residue (GLR) in mortars. Milling time and w.t.% substitution were tested with respect to inhibiting effects on ASR and compression strength.

2 MATERIALS AND METHODOLOGY

2.1 Materials

Portland cement CP II Z – 32 was used in mortar mixing ratios of. The average particle size of cement was measured with laser granulometry in order to ascertain the proper level of substitution with GLR. This work was performed in the Mineral Analysis Laboratory (LAMIN) of CPRM at Manaus/AM with a Malvern Mastersizer laser particle analyzer. Additionally, a thermogravimetric analysis was conducted to verify potential physiochemical changes in cement samples. This allowed the determination of decomposition reactions occurring in substances with respect to variations in mass and gradual temperature increases. This part of the work was conducted at the Physiochemical Test Laboratory at FT/UFAM with a TA Instrument thermal analysis system model SDT Q600. The cement sample of approximately 12 mg was subjected to a heating rate of 10 °C/min until a final temperature of 950 °C with an N 5.0 gas flow of 30 ml/min in an uncovered 90 μl aluminum crucible.

Chemical composition of cement was obtained through X-ray fluorescence (XRF) with a PANalytical spectrometer model EPSILON 3 XL in the Physiochemical Test Laboratory at FT/UFAM. Knowledge of the exact chemical composition of cement is paramount in identifying compounds that affect the hydration process and strength of the cementitious matrix. The crystallographic formations were obtained from X-ray diffraction (XRD) with a Brucker model D2 PHASER diffractometer in the Nanomaterial Characterization and Synthesis Laboratory (LSCN) at IFAM. Local tap water and a polycarboxylate-based 3rd generation superplasticizer with characteristics shown in Table 1 were also used.

Table 1. Polycarboxylates-vased plasticizer additive characteristics

Type	Chemical base	Aspect	Color	pH	Density (g/cm^3)	Solid %
3rd generation superplasticizer	Polycarboxylate ether (PCE)	Liquid	Murky white	5 to 7	1.066	28.50 – 31.50

Sand was taken from the Jamari river and the fine aggregate obtained from it has the characteristics shown in Table 2. Specific mass and apparent specific mass were 2.67 kg/dm^3 and 1.45 kg/dm^3, respectively. These values and the measured fineness modulus were similar to other works [1], [2]. Powdered material present was within the 3 w.t.% to 5 w.t.% recommended margin specified in NBR NM 46:2003 [12]. Organic impurities were also within the limits set by the color scale of NBR NM 49:2001 [13]. Clay and fracturing material were at the 1.5 w.t.% limit of use set in NBR 7218:2010 [15].

Table 2. Fine aggregate characterization.

Test	Norm	Units	Results
Specific mass	NBR NM 52:2009 [10]	kg/dm^3	2.67
Apparent specific mass	NBR NM 45:2006 [11]	kg/dm^3	1.45
Powdered material %	NBR NM 46:2003 [12]	%	4.70
Organic impurities	NBR NM 49:2001 [13]	ppm	300
Fineness modulus	NBR NM 248:2003 [14]	-	2.69
Maximum diameter	NBR NM 248:2003 [14]	mm	2.40
Clay and fracturing material %	NBR 7218:2010 [15]	%	1.50

These results showed that the fine aggregate of this study was suitable for mortar use. The granulometric distribution of fine aggregate was determined in accordance with NBR NM 258:2003 [14]. Results, shown in Figure 1, present a good distribution within optimal limits, according to NBR 7211:2009 [16].

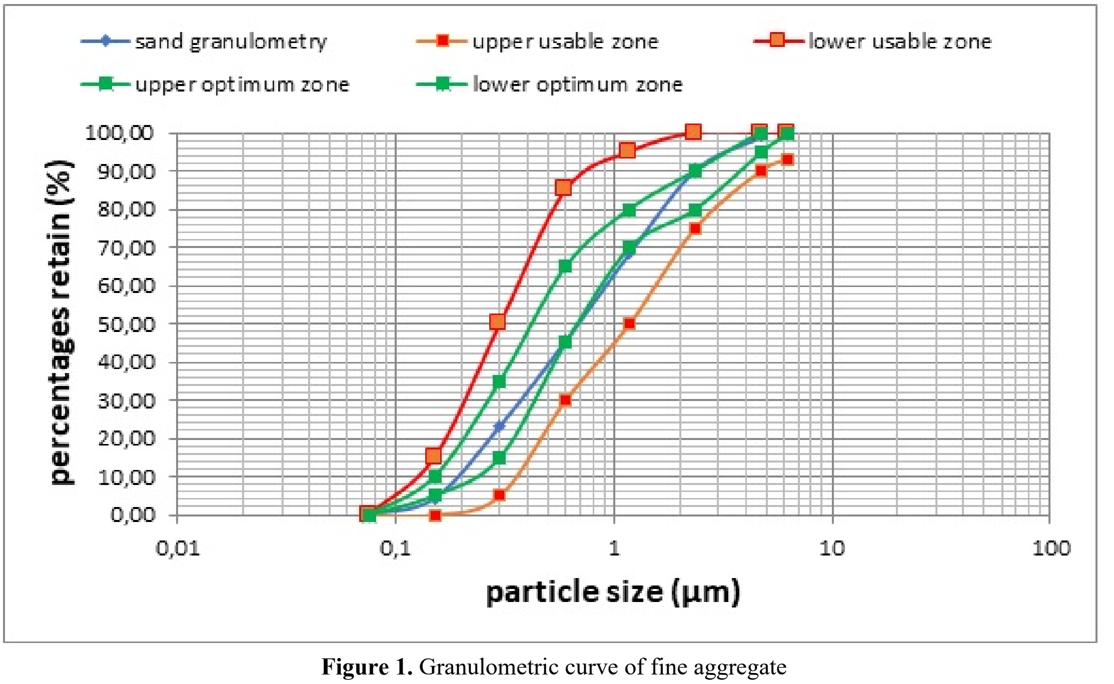

Figure 1. Granulometric curve of fine aggregate

2.2 Methodology

2.2.1 Ground glass residue (GLR) acquisition, preparation and characterization

Glass residue was acquired from Guaporé Indústria e Comércio de Vidros Ltda. from the east side of Porto Velho – RO. The supplier is responsible for supplying 70% of commercial glass in the state of Rondônia. The residue is produced from the cutting and polishing processes of commercial glass which is performed with water cooling. Glass dust and water are collected in troughs and deposited in decanting tanks. Water is reused while glass is collected in plastic bags and sent to landfills. Glass residue in paste form was collected for this study, dried in the laboratory at 105 °C for 24 h, disentangled and sifted through a 600 µm sieve. The dried material was placed in a mill with 30 ceramic balls: 7 of them with diameters of 10 cm and 23 with diameters of 5 cm. Two milling times were used: 16 h and 32 h which were selected based on GRL preparation procedures of Sousa Neto [17].

The milling efficiency was verified with laser granulometry. Chemical composition and crystallographic formations of GLR were analyzed with XRF and XRD, respectively. These same procedures were also applied to confirm the properties of Portland cement CP II-Z-32.

2.2.2 Fresh and cured mortar evaluation

Samples of mortar bars were produced to verify the mitigation of the alkali-silica reaction with a mixing ratio of 1:2.25:0.47 in mass with cement substituted with GLR in proportions of 10 w.t.%, 20 w.t.%, 30 w.t.% and 40 w.t.%. These large levels were selected to increase the effect of the substitution and to accentuate the effect of the milling times (16 and 32 hours). Portland cement CP V-ARI was purposely used in the mortar due to its high alkali content. The potential mitigation of ASR was evaluated following the procedures of Part 5 of NBR 15577:2018 [18]. An accelerated mortar test was conducted with samples immersed in a sodium hydroxide solution and heated to 80 °C, which causes expansion. Depending on the degree of expansion, the material could be considered as a having a mitigating effect on ASR. Expansion measurements were taken after the 3rd day and further readings were taken after 16 days and 30 days. Complementary studies were conducted on the pozzolanic potential of GLR: chemical analysis following NBR 12653:2014 [19] and physical analysis following NBR 5752:2014 [20].

Further test samples were produced based on Paiva [21]. A reference test control mixing ratio of 1:2:0.4 in mass was produced for compression resistance tests at 7 days and 28 days of curing. For these samples, GLR substitution was of 10 w.t.%, 15 w.t.% and 20 w.t.%. These values were selected based on results of other studies that noted that a 20 w.t.% to 25 w.t.% were ideal. Samples were further classified in accordance to GLR milling times of 16 h and 32 h (A = 16h and B = 32h). These samples incorporated a superplasticizer additive to maintain a minimum initial consistency of 200 mm. Consistency measurements followed the procedures of NBR 13276:2016 [22]. The composition and mixing ratio of these test samples are shown in Table 3.

Table 3. Mixing ratios of samples tested.

Ratio/Test Sample	TC	T10A	T10B	T15A	T15B	T20A	T20B
	Quantity of Material (kg/m^3)						
Cement	544.12	489.71	489.71	462.50	462.50	435.30	435.30
Glass	0.00	54.41	54.41	81.62	81.62	108.82	108.82
Sand	1088.24	1088.24	1088.24	1088.24	1088.24	1088.24	1088.24
Water	217.65	217.65	217.65	217.65	217.65	217.65	217.65
Plasticizer	0.54	0.65	0.65	0.76	0.76	0.87	0.87
water/cementitious material ratio	0.40	0.40	0.40	0.40	0.40	0.40	0.40

All test samples were produced in a Motomil 120-liter mechanical mixer. Five cylindrical test bodies measuring 5 cm x 10 cm were produced for each mixing ratio. Concrete was poured in two layers with 15 strokes of manual compacting each layer. Samples were demolded after 24 h and submerged in a water tank until rupturing. Mechanical grinding was used to smooth out the surfaces of the test samples.

Compression strength tests were conducted in an Instrom apparatus model EMIC 23-100 in the Structural and Mechanical Tests Laboratory (LAEEM) of the Civil Engineering department of UNIR. The load velocity was of 0.45 MPa/s as recommended by NBR 5739:2018 [21].

Axial compression strength results were validated with a 2 x 3 statistical model (2 ground times and 3 w.t.% substitution values) and the additional test control sample. An ANOVA analysis was performed with Assistant 7.7 commercial software and the averages were compared in Tukey tests ($P \leq 0.05$).

3 RESULTS AND DISCUSSION

3.1 GLR characterization

Following 16 h and 32 h milling times, the granulometric distribution of GLR samples was analyzed with a laser particle analyzer. Figure 2 presents granulometry results for both grounds alongside Portland cement CP II-Z-32.

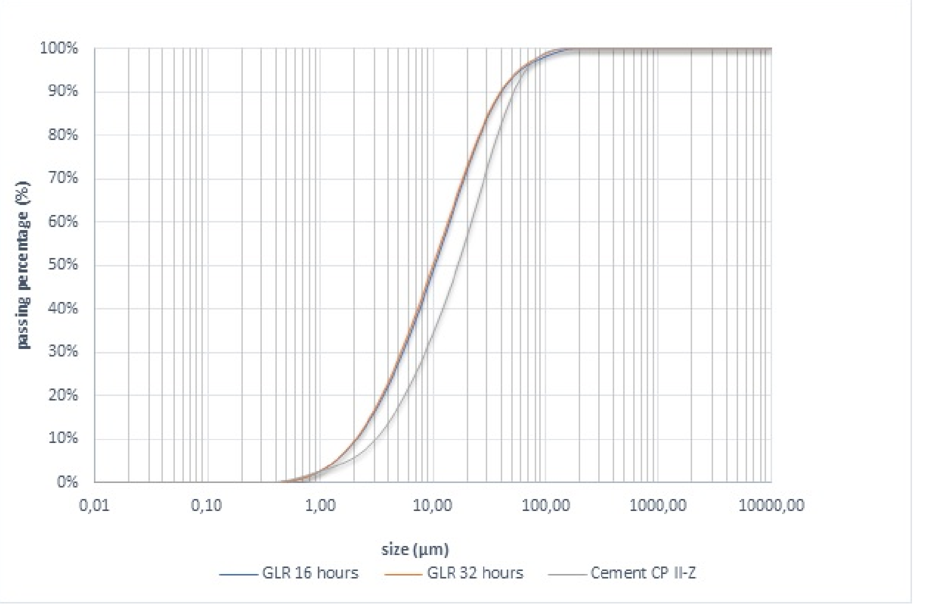

Figure 2. Granulometric distribution of both types of GLR milling and Portland cement CP II-Z

Results show that there were no significant differences in particle size between the milling times of 16 h and 32 h. This attests both to the efficiency of the 16-hour ground as well as the limits of the equipment to further reduce particle size. More specifically, sizes D(90), D(50) and D(10) after 16 h were of 40.38 µm, 10.44 µm and 2.11 µm, respectively. In comparison, the corresponding 32 h sizes were of 39.65 µm, 10.04 µm and 2.08 µm, respectively. The average D(50) of cement particles was 16.67 µm and since GLR particles were smaller than cement, they should have a filler effect and cause improved compaction of the mixture.

Table 4 presents the GLR chemical composition obtained from XRF. It can be seen that the GLR was classified as soda-lime glass containing sodium and calcium. The 74.07 w.t.% silica content pointed a pozzolanic potential. As noted in NBR 12653:2014 [19], a material may be classified as pozzolanic if the sum of SiO2 + Al2O3 + Fe2O is greater than 70 w.t.%.

Table 4. Chemical composition of GLR and Portland cement CP II-Z-32

Chemical compond	Ground glass residue – GLR (w.t.%)	Portland cement CP II-Z-32 (w.t.%)
SiO_2 – silicon dioxide	74.07	22.94
CaO – calcium oxicde	13.27	57.61
Na_2O – sodium oxide	7.94	-
MgO – magnesium oxide	1.93	3.99
Al_2O_3 – aluminum oxide	0.99	5.60
Fe_2O_3 – iron oxide	0.66	3.99
P_2O_5 – phosphorous pentoxide	0.49	0.37
K_2O – potassium oxide	0.35	1.68

The amorphous nature of the silica was checked with XRD and the results are shown in Figure 3. As expected, there is no change in the amorphous nature with respect to milling time since this process does not occur at high temperatures which could re-arrange the crystallographic structure. As such, there were no observed diffracted peaks of elements and there was a large halo between 20° and 35°.

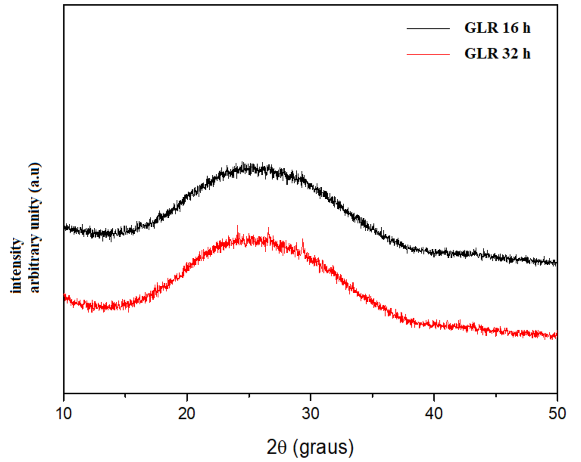

Figure 3. Comparison of XRD of GLR for 16 h and 32 h milling time

Pozzolanic activity was evaluated physically in accordance with NBR 5752:2014 [20]. As stated in the norm, a pozzolanic activity index (PAI) of over 90% must be attained for the material to be considered a pozzolan. In this study, GLR attained PAIs of 103.3% and 98.5% for milling times of 16 h and 32 h, respectively – more than sufficient to establish pozzolanic properties which were later confirmed from chemical tests.

3.2 Cement characterization

Figure 4 presents XRD results for Portland cement CP II-Z-32. Diffractogram peaks identified primarily calcium silicate, silicon oxide, calcium carbonate and magnesium oxide, which are all common to Portland cement. The full chemical composition of the cement is presented in Table 4.

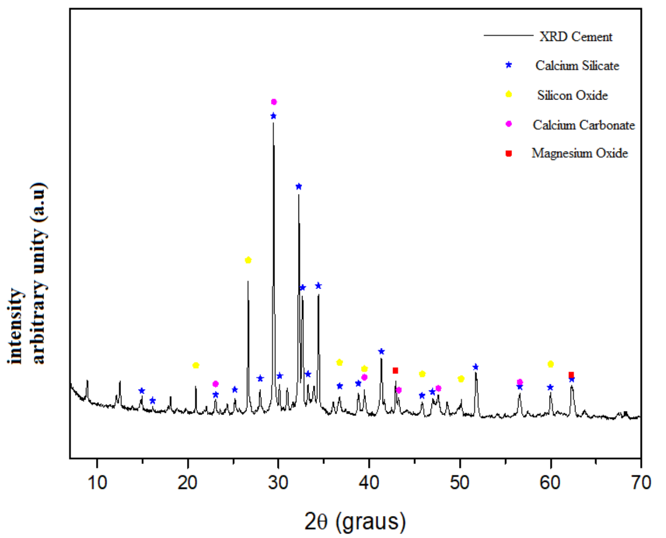

Figure 4. XRD of Portland cement CPII–Z–32

Cement thermogravimetric results are presented in Figure 5. In the figure, the derivative thermogravimetric curve (DTF) is shown as a red line. The first observed peak occurred at temperatures of less than 200 °C and was related to interstitial water in the cement. The second peak, observed between 400 °C and 500 °C, demonstrated the decomposition of a small portion of Portlandite. The third peak, between 600 °C and 800 °C, was related to the decomposition of calcium carbonate and presented the largest loss in mass of the cement sample. The calcinated mass at the end of the test was of approximately 5 w.t.% which was similar to the manufacturer's specifications of 5.69 w.t.% due to heat.

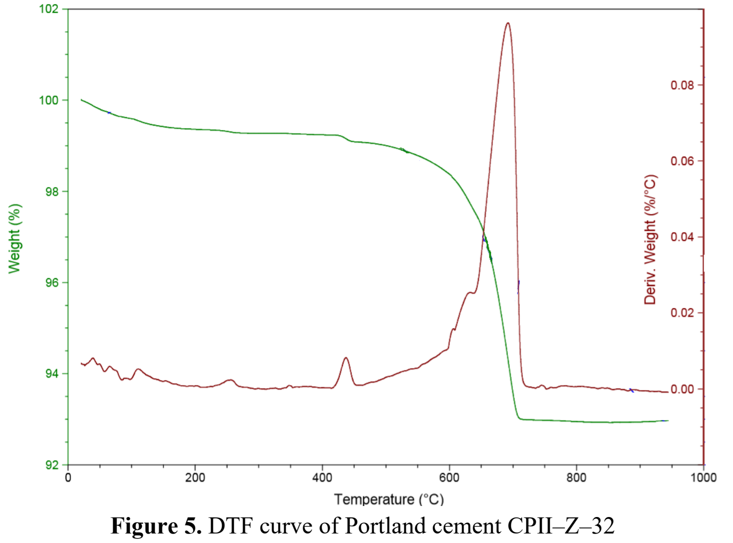

Figure 5. DTF curve of Portland cement CPII–Z–32

3.2 Alkali-silica reaction tests

Figure 6 presents the results of expansion tests conducted in accordance with NBR 15577:2018-5 [18] for samples with 10 w.t.%, 20 w.t.%, 30 w.t.% and 40 w.t.% GLR substitution for both 16 h and 32 h milling times. According to NBR 15577:2018-1 [23], mortar bars samples should not have expansions larger than 0.19% at 30 days and, as seen in the figure, all samples remained below this threshold. Milling time also did not affect the result which was expected since laser granulometry showed that both cases presented similarly-sized particles.

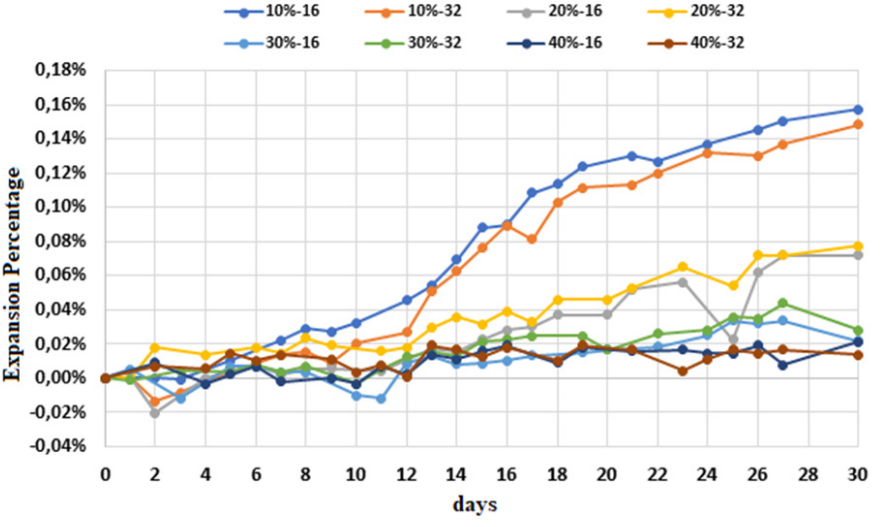

Figure 6. Mortar bars sample expansion with respect to GLR substitution

Further, as seen in Figure 6, expansion decreased as GLR replacement increased. This was to be expected since, with increasing substitution, the alkali content of the mixture decreased. Also, as noted in other studies, GLR with particle sizes of less than 100 µm inhibit alkali-silica reactions (ASR) [24], [17], [19], [25]–[26]. Following this trend, expansions further decreased as substitution increased from 10 w.t.% all the way to 40 w.t.%. It should be noted that the expansion test in NBR 15577:2018-4 [27] used a control mixture of only CP V cement for comparison purposes with regards to any ASR potential.

3.2 Axial compression strength of mortars

Compression strength and spread tests of mortar samples were measured at 7 days and 28 days of curing. Results are presented in Table 5 and shown graphically in Figure 7. It can be noted that compression strength increased for all samples with increasing time.

Table 5. Results of compression strength and spread tests of mortars

Mixture	Compression resistance and standard deviation (MPa)		Spread (mm)
	7 days	28 days	
TC	25.61 ± 3.32	27.95 ± 4.35	200
T10A	21.60 ± 0.90	24.76 ± 2.97	241
T10B	21.21 ± 1.15	21.76 ± 2.60	246
T15A	18.84 ± 1.23	23.73 ± 1.92	241
T15B	17.25 ± 1.04	21.16 ± 4.13	245
T20A	18.28 ± 1.31	25.78 ± 2.54	259
T20B	16.33 ± 1.03	22.95 ± 3.02	225

Overall, the test control sample (TC) achieved the highest compression strength but, at 28 days, the difference between the substitution samples and test control sample narrowed. This was a consequence of the pozzolanic effect of GLR which produced a substantial gain in strength over time. This effect was observed in other studies such as Ribeiro [28] and Paiva [21], which also measured significant gains in mortars after 7 days and 28 days. Spread tests noted that all samples exceeded the established initial limit of 200 mm but the samples with GLR substitution had larger spreads than the test control sample.

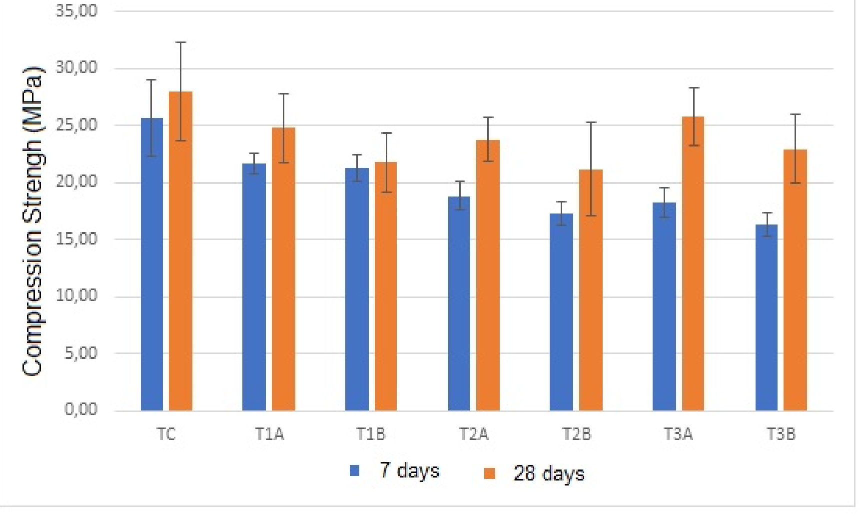

Figure 7. Compression strength of samples at 7 days and 28 days

Further analysis was conducted with ANOVA on Assistant 7.7 commercial software. Factors analyzed were ground time (f1) and w.t.% GLR substitution (f2) to determine their statistical differences in compression strength tests.

Table 6 shows the factorial analysis of compression strength for the 7 day case. It can be seen that ground time (factor 1 - f1) as well as w.t.% substitution (factor 2 - f2) affected resistance significantly.

Table 6. Factor analysis of compression strength at 7 days

VF	DOF	SM	SA	F
Factor 1 (f1)	1	12.84456	12.84456	4.8517
Factor 2 (f2)	2	95.42349	47.71174	18.0218
Interaction f1 x f2	2	3.33525	1.66762	0.6299
Factor x Test Control	1	191.67808	191.67808	72.4012
Treatment	6	303.28138	50.5469	5.74840
Residual	28	74.12844	2.64744	
Total	34	377.40982		
Factor 1 (f1) – GLR ground time of 16 h and 32 h; Factor 2 (f2) – GLR substitution of cement in 10 w.t.%, 15 w.t.% and 20 w.t.%.				
VF – variation factor; DOF – degrees of freedom; SM – squares sum; SA – squared average; F – F-test statistic.				

A Tukey test ($P \leq 0.05$) performed on strength data at 7 days led to several observations. Factor 1 presented significant differences as shown in Table 7, with milling time producing differences with respect to the test control sample. But between the milling times of 16 h and 32 h there were no significant differences.

Table 7. Tukey test of GLR milling time at 7 days

Multiple Comparisons				
Level	**Center**	**Lower Limit**	**Upper Limit**	**P-value**
16 - 0	-6.033333333	-8.982922991	-3.083743676	5.35652×10^{-5}
32 - 0	-7.342	-10.29158966	-4.392410343	2.28147×10^{-6}
32 - 16	-1.308666667	-3.394341515	0.777008182	0.285355015

This was to be expected since laser granulometry showed little difference in the particle sizes between both milling times. Factor 2 also displayed statistical difference as shown in Table 8. All substitution mixtures presented statistically different resistances from the test control sample. Mixtures of 15 w.t.% and 20 w.t.% substitution also presented differences with respect to the 10 w.t.% sample but no significant differences were observed between 15 w.t.% and 20 w.t.% samples.

Table 8. Tukey test of GLR substitution at 7 days

Multiple Comparisons				
Levels	**Center**	**Lower Limit**	**Upper Limit**	**P-value**
0.1 - 0	-4.202	-6.73925933	-1.66474067	0.000503383
0.15 - 0	-7.56	-10.09725933	-5.02274067	2.30941×10^{-8}
0.2 - 0	-8.301	-10.83825933	-5.76374067	2.98239×10^{-9}
0.15 - 0.1	-3.358	-5.429663568	-1.286336432	0.000657038
0.2 - 0.1	-4.099	-6.170663568	-2.027336432	4.23709×10^{-5}
0.2 - 0.15	-0.741	-2.812663568	1.330663568	0.766864077

The same factor analysis was conducted at 28 days. Table 9 presents ANOVA results with factor 1 and factor 2 having significant impacts.

Table 9. Factor analysis of compression strength at 28 days

VF	DOF	SM	SA	F
Factor 1 (f1)	1	58.8	58.8	5.8154
Factor 2 (f2)	2	18.48971	9.24485	0.9143
Interaction f1 x f2	2	0.23192	0.11596	0.0115
Factor x Test Control	1	90.34432	90.34432	8.9352
Treatment	6	303.28138	50.5469	2.767
Residual	28	74.12844	2.64744	
Total	34	377.40982		
Factor 1 (f1) – GLR ground time of 16 h and 32 h; Factor 2 (f2) – GLR substitution of cement in 10 w.t.%, 15 w.t.% and 20 w.t.%.				
VF – variation factor; DOF – degrees of freedom; SM – squares sum; SA – squared average; F – F-test statistic.				

The Tukey test (P≤0.05) of factor 1 shown in Table 10 presents a statistical difference between the 16 h milling time and test control sample but no further significant differences with the other cases. The Tukey test (P≤0.05) of factor 2 shown in Table 11 presented statistical differences between the test control sample and 10 w.t.% and 15 w.t.% GLR substitution samples. However no significant differences were observed between the test control sample and the 20 w.t.% GLR substitution sample. No significant differences were also noted in between the various substitution samples.

Table 10. Tukey Test of GLR milling time at 28 days

Multiple Comparisons				
Levels	**Center**	**Lower Limio**	**Upper Limit**	**P-value**
16 - 0	-3.191333333	-7.088629343	0.705962676	0.125567274
32 - 0	-5.991333333	-9.888629343	-2.094037324	0.001835111
32 - 16	-2.8	-5.555804437	-0.044195563	0.045817363

Table 11. Tukey Test of GLR substitution at 28 days

Multiple Comparisons				
Levels	**Center**	**Lower Limit**	**Upper Limit**	**P-value**
0.1 - 0	-4.686	-9.624613052	0.252613052	0.067853009
0.15 - 0	-5.502	-10.44061305	-0.563386948	0.024373398
0.2 - 0	-3.586	-8.524613052	1.352613052	0.220773465
0.15 - 0.1	-0.816	-4.848360671	3.216360671	0.946059845
0.2 - 0.1	1.1	-2.932360671	5.132360671	0.880013391
0.2 - 0.15	1.916	-2.116360671	5.948360671	0.576250688

Results showed that, at 28 days, milling time was no longer a relevant factor in compression strength – its effect having already occurred at the 7 day point. However, GLR substitutions were relevant both for the 7 day and 28 day periods. The pozzolanic activity of GLR resulted in increases in strength with respect to increasing w.t.% substitution.

The sample with the largest substitution (20 w.t.%) had strength statistically equal to the test control sample. Similar gains in strength due to pozzolanic activity have been observed by Paiva [21] and Ribeiro [28].

4 CONCLUSIONS

Ground glass residue (GLR) substitution of Portland cement was demonstrated as a viable alternative, especially since GLR has pozzolanic characteristics. Pozzolanic activity was proven chemically and physically and its use was deemed safe with regards to possible alkali-silica reactions.

Parameters of milling time and w.t.% substitution of cement with GLR were analyzed with respect to compression strength at 7 days and 28 days of curing. In all samples, strength increased with respect to curing period but the 20 w.t.% substitution sample obtained the most expressive gains.

Statistical analysis was performed to confirm which factors affected compression strength the most. Results showed that milling times of 16 h and 32 h were not significant factors while w.t.% GLR substitution was responsible for observed effects. In particular, 20 w.t.% GLR substitution showed no statistical difference in compression strength with respect to the test control sample.

ACKNOWLEDGEMENTS

The authors express their gratitude to FT/UFAM and IFAM for conducting experimental tests and LAEEM/UNIR for providing laboratory space and technical support.

REFERENCES

[1] A. M. D. Higuchi, “Estudo do desempenho do resíduo de vidro moído como material cimentício suplementar para aplicação em concreto autoadensável de alto desempenho,” M.S. thesis, 2018.

[2] H. A. Abdel-Rahman, M. M. Younes, and M. M. Khattab, "Effect of waste glass content on the physico-chemical and mechanical properties of styrene acrylic ester blended cement mortar composites," *Polym. Compos.*, vol. 39, no. 4, pp. 987–996, 2018.

[3] R. B. C. Sales, F. A. Sales, E. P. Figueiredo, W. J. Santos, N. D. S. Mohallem, and M. T. P. Aguilar, "Durability of mortar made with fine glass powdered particles. Hindawi," *Adv. Mater. Sci. Eng.*, vol. 2017, pp. 1–9, 2017.

[4] J. M. Gómez-Soberón, F. G. Cabrera-Covarrubias, J. L. Almaral-Sánchez, and M. C. Gómez-Soberón, "Fresh-state properties of mortars with recycled glass aggregates: global unification of behavior. Hindawi," *Adv. Mater. Sci. Eng.*, vol. 2018, pp. 1–11, 2018.

[5] N. A. Soliman and A. Tagnit-Hamou, "Partial substitution of silica fume with fine glass powder in UHPC: Filling the micro gap," *Constr. Build. Mater.*, vol. 139, pp. 374–383, 2017. [[Q2: Q2]]

[6] D. Patel, R. P. Tiwari, R. Shrivastava, and R. K. Yadav, "Effective utilization of waste glass powder as the substitution of cement in making paste and mortar," *Constr. Build. Mater.*, vol. 199, pp. 406–415, 2019.

[7] J. Kim, C. Yi, and G. Zi, "Waste glass sludge as a partial cement replacement in mortar," *Constr. Build. Mater.*, vol. 75, pp. 242–246, 2015.

[8] A. R. G. Azevedo, J. Alexandre, E. B. Zanelato, and M. T. Marvila, "Influence of incorporation of glass waste on the rheological properties of adhesive mortar," *Constr. Build. Mater.*, vol. 148, pp. 359–368, 2017.

[9] R. Oliveira, J. Brito, and R. Veiga, "Reduction of the cement content in rendering mortars with fine glass aggregates," *J. Clean. Prod.*, vol. 95, pp. 75–88, 2015.

[10] Associação Brasileira de Normas Técnicas, *Agregado Miúdo - Determinação de Massa Específica e Massa Específica Aparente*, NBR NM 52, 2009.

[11] Associação Brasileira de Normas Técnicas, *Agregados – Determinação da Massa Unitária e do Volume de Vazios*, NBR NM 45, 2006.

[12] Associação Brasileira de Normas Técnicas, *Agregados – Determinação do Material Fino que Passa Através da Peneira 75 Micrometro, por Lavagem*, NBR NM 46, 2003.

[13] Associação Brasileira de Normas Técnicas, *Agregado Miúdo – Determinação de Impurezas Orgânicas*, NBR NM 49, 2001.

[14] Associação Brasileira de Normas Técnicas, *Agregados – Determinação da Composição Granulométrica*, NBR NM 248, 2003.

[15] Associação Brasileira de Normas Técnicas, *Agregados – Determinação do Teor de Argila em Torrões e Materiais Friáveis*, NBR 7218, 2010.

[16] Associação Brasileira de Normas Técnicas, *Agregados para Concreto – Especificação*, NBR 7211, 2009.

[17] L. M. Sousa No., “Utilização de resíduo de vidro moído como adição mineral para a produção de concreto autoadensável e de alto desempenho,” M.S. thesis, Univ. Fed. Amazonas, 2014.

[18] Associação Brasileira de Normas Técnicas, *Agregados – Reatividade Álcali-Agregado – Parte 5: Determinação da Mitigação da Expansão em Barras de Argamassa Pelo Método Acelerado*, NBR 15577-5, 2018.

[19] Associação Brasileira de Normas Técnicas, *Materiais Pozolânicos – Requisitos*, NBR 12653, 2014.

[20] Associação Brasileira de Normas Técnicas, *Materiais Pozolânicos – Determinação do Índice de Desempenho com Cimento Portland aos 28 Dias*, NBR 5752, 2014.

[21] O. A. Paiva, "Resíduo Industrial de vidro moído em argamassa de cimento Portland," M.S. thesis, Univ. Fed. Amazonas, 2009.

[22] Associação Brasileira de Normas Técnicas, *Argamassa para Assentamento e Revestimento de Paredes e Tetos - Determinação do Índice de Consistência*, NBR 13276, 2016.

[23] Associação Brasileira de Normas Técnicas, *Agregados – Reatividade Álcali-Agregado – Parte 1: Guia para Avaliação da Reatividade Potencial e Medidas Preventivas para Uso de Agregados em Concreto*, NBR 15577-1, 2018.

[24] A. Khmiri, M. Chaabouni, and B. Samet, "Chemical behaviour of ground waste glass when used as partial cement replacement in mortars," *Constr. Build. Mater.*, vol. 44, pp. 74–80, 2013.

[25] Y. Shao, T. Lefort, S. Moras, and D. Rodriguez, "Studies on concrete containing ground waste glass," *Cement Concr. Res.*, vol. 30, no. 1, pp. 91–100, 2000.

[26] R.-U.-D. Nassar and P. Soroushian, "Strength and durability of recycled aggregate concrete containing milled glass as partial replacement for cement," *Constr. Build. Mater.*, vol. 29, pp. 368–377, 2012.

[27] Associação Brasileira de Normas Técnicas, *Agregados – Reatividade Álcali-Agregado – Parte 4: Determinação da Expansão em Barras de Argamassa Pelo Método Acelerado* – NBR 15577-4, 2018.

[28] A. O. Ribeiro, "Estudo de resíduo de lapidação de vidro para a incorporação em argamassas de cimento Portland," M.S. thesis, Univ. Fed. Uberlândia, Uberlândia, 2015.

[29] V. Corinaldesi, G. Gnappi, G. Moriconi, and A. Montenero, "Reuse of ground waste glass as aggregate for mortars," *Waste Manag.*, vol. 25, no. 2, pp. 197–201, 2005.

Author contributions: RKL: conceptualization, supervision, writing, data curation, formal analysis, methodology; JCP: conceptualization, writing; BFT: conceptualization, supervision, writing, data curation, formal analysis, methodology; AEBG: data curation, formal analysis.

Editors: Edgar Bacarji, José Luiz Antunes de Oliveira e Sousa, Guilherme Aris Parsekian.

IBRACON Structures and Materials Journal
Revista IBRACON de Estruturas e Materiais
ISSN 1983-4195 ismj.org

ORIGINAL ARTICLE

Study on the compatibilization of hierarchical models for tunnel design

Estudo para a compatibilização de modelos hierárquicos no projeto de túneis

Bruno Szpigel Dzialoszynski[a]
Fernando Rebouças Stucchi[a]

[a]Universidade de São Paulo – USP, Escola Politécnica, Departamento de Engenharia de Estruturas e Geotécnica, São Paulo, SP, Brasil

Received 02 February 2020
Accepted 07 July 2020

Abstract: This work presents a study on the compatibilization of the lining load results between continuous ground mass and bedded beam models for tunnel design, through the calibration of the loads imposed to the bedded beam models. A review on compatibilization premises and the computation of "ideal" compatibilization loads, which yield identical results between model hierarchies is presented. A case study was developed, illustrating that even with significant simplification of the calibrated loads, if they bear magnitude and distribution that resembles those of the "ideal" compatibilization load, reasonable compatibility, potentially better than that of usual generic imposed loads, may be obtained. Motivated by this observation, a parametric study on the magnitude and distribution of the "ideal" compatibilization load was performed, yielding conclusions that foresee the estimation of simplified compatibilization loads directly from the physical problem definition.

Keywords: tunnels, hierarchical modeling, numerical modeling.

Resumo: Esse trabalho apresenta um estudo acerca da compatibilização dos esforços solicitantes no revestimento entre modelos de maciço contínuo e de anel sobre apoios para o projeto de túneis, a partir da calibração de carregamentos impostos aos modelos de anel sobre apoios. Uma revisão das premissas de compatibilização e do cálculo de carregamentos de compatibilização "ideal", que levam a resultados idênticos entre hierarquias de modelos é apresentada. Um estudo de caso foi desenvolvido, ilustrando que mesmo com significativa simplificação dos carregamentos calibrados, se eles possuírem magnitude e distribuição que remetam às do carregamento de compatibilização "ideal", compatibilidade razoável, e potencialmente melhor que aquela obtida com carregamentos impostos usais genéricos, pode ser obtida. Motivada por tal observação, uma análise paramétrica da magnitude e distribuição do carregamento de compatibilização "ideal" foi efetuada, resultando conclusões que anteveem a estimativa de carregamentos de compatibilização simplificados diretamente da definição do problema físico.

Palavras-chave: túneis, modelagem hierárquica, modelagem numérica.

How to cite: B. S. Dzialoszynski and F. R. Stucchi, "Study on the compatibilization of hierarchical models for tunnel design," *Rev. IBRACON Estrut. Mater.*, vol. 14, no. 2, e14215, 2021, https://doi.org/10.1590/S1983-41952021000200015

1. INTRODUCTION

Duddeck [1] formalized a conceptual sequence of the basic routine structural engineering activities involved in the analysis and design process of a structure. Most of said activities necessarily imply a simplification and idealization of reality, with the definition of mathematical models to assess relevant physical phenomena within the design process. Two main model type groups are highlighted, Research Models and Technical Models. In summary, Research Models aim at representing as many physical phenomena with as much accuracy as possible. Technical Models strive to cover the essential physical phenomena with adequate accuracy to allow for design with adequate safety and performance

Corresponding author: Bruno Szpigel Dzialoszynski. E-mail: bruno.dzialoszynski@gmail.com
Financial support: None.
Conflict of interest: Nothing to declare.

with the lowest possible cost and effort. However, the formulation of adequate Technical Models requires the use of sound Research Models.

These reflections closely dialogue with Bucalem and Bathe's [2] definition of hierarchical modelling. A same set of physical phenomena may be represented by a series of hierarchical models, where increasing hierarchy leads to increasing amount and accuracy of physical phenomena representation, but also to greater modelling effort.

Due to the multitude, complexity and interdisciplinarity of physical phenomena involved in tunnel analysis, hierarchical modelling and various model hierarchies and methods are relevant within the design practice. The International Tunneling Association [3] lists 4 groups of models/methods for the structural design of tunnels, namely: continuum models; bedded-beam models; empirical approaches; and the observational method.

The continuum models may allow for the potential representation of complex physical phenomena, but also lead to greater effort / complexity in input data estimation / postulation and output data interpretation. Thus, it is common and may be advantageous in the design practice to apply the lower hierarchy bedded beam models together with the higher hierarchy continuum models, either for quick estimates, model validation, and, in some cases, direct application after calibration [4].

This paper follows up on Dzialoszynski and Stucchi [5] with an investigation of the potential result compatibilization between continuum models – henceforth referred to as hierarchy H1 models – and bedded-beam models – henceforth referred to as hierarchy H2 models. Specifically, the calibration of simplified hierarchy H2 model imposed loads based on the "ideal" compatibilization load (as defined in Dzialoszynski and Stucchi [5]) are analyzed, with a parametric study of the "ideal' compatibilization load in relation to the variation of reference hierarchy H1 model's parameters and hypotheses.

2. COMPATIBILIZATION OF RESULTS BETWEEN MODEL HIERARCHIES

Illustrating the common parallel application of model hierarchies in the tunnel design practice routine, many authors, like Duddeck [1], Duddeck and Erdmann [6], Van der Poel et al. [7], Prado and Waimberg [4], Vu et al. [8] and Dzialoszynski and Stucchi [5] have compared the application and results of different model hierarchies when representing the same physical problems.

Dzialoszynski and Stucchi [5] compared model hierarchies H1 and H2 from a conceptual standpoint, establishing basic premises for the potential result compatibilization of model hierarchies. In summary:

- The main difference between model hierarchies is their respective representation of the ground mass and the associated consequences to the manifestation soil structure-interaction.
- It is clear that the intended result compatibilization must refer to results that are common to both model hierarchies. Thus, model hierarchy result compatibilization shall refer to computed beam loads and displacements.
- Compatibilization refers herein to the calibration of input parameters of model hierarchies which lead to similar results. Due to the nature of the respective model inputs, compatibilization shall be achieved through the calibration and estimation of model hierarchy H2 input parameters, rather than model hierarchy H1 input parameters.
- From a conceptual standpoint, perfect and generalized compatibilization would imply that all the complex behaviors of the deformable solid ground mass of hierarchy H1 were fully translated at the soil-structure interface through the links / "springs" and loads imposed to model hierarchy H2. Thus, in practice, compatibilization should only be viable in an approximate, case-by-case basis (that is, for each type of problem, compatibilization rules may vary).

Under these premises, model inputs may be calibrated to achieve result compatibilization between models.

2.1. "Ideal" compatibilization load

One of the hierarchy-H2 models main advantages is its simplicity, and it is usually desirable that its imposed loads and links / "springs" have a rather simplified definition. Nonetheless, for the investigation on the postulation of simplified compatibilization loads, it is interesting to know the exact value of "ideal" compatibilization loads that yield identical results for analogous models in both hierarchies, despite of its potential complexity.

Dzialoszynski and Stucchi [5] formalized and validated a practical procedure for computing "ideal" compatibilization loads within the Finite Elements Method (FEM). The procedure may be easily implemented in usual available FEM applications.

In summary, the application of the procedure presumes:

- A given physical problem is defined and solved through a hierarchy H1 model, for which the results are considered to be known beforehand in all nodes and calculation stages.
- The definition of the hierarchy H1 model implies the definition of a beam / plate type element finite elements mesh for the lining, as well as a nodal force vector due to self-weight applied to the lining, f_n^w.
- Links / "springs" must be postulated to the hierarchy H2 model. The definition is arbitrary, and the procedure will yield "ideal" compatibilization loads regardless of the quality of the hypotheses. However, the compatibilization loads shall be more intuitive / representative for better link / "spring" hypotheses.

Under these premises, the procedure yields a nodal force vector due to the ground mass[1], f_n^s, which leads to identical displacement and beam load results between model hierarchies if imposed to a hierarchy H2 model with: analogous finite mesh to that of the reference H1 model; the same implied nodal forces due to self-weight, f_n^w; and the arbitrarily defined links / "springs". A nodal force vector due to links / "springs", f_n^l, will also indirectly be calculated.

Of course, the procedure implies that the results for the hierarchy H1 model are already known, so the "ideal" compatibilization loads thusly computed have little direct practical application. However, the "ideal" compatibilization loads can be used to investigate patterns and trends for the calibration of simplified compatibilization loads, as presented in the sections hereafter.

2.2. Simplified load calibration through the "ideal" compatibilization load

The "ideal" compatibilization load may be used to calibrate simplified imposed loads for hierarchy H2 models. Hierarchy H2 model imposed loads may be represented with vertical and horizontal components. As illustrated by Blom [9], they are usually defined as distributed loads applied to the tunnel area projected to a plane perpendicular to the respective load component direction. Loads shall be defined in such manner in this paper, and the calibration of loads from the "ideal" compatibilization nodal forces imply their distribution in the abovementioned projected areas.

Dzialoszynski and Stucchi [5] presented a case study evaluating the beam load result compatibility between analogous hierarchy H1 and H2 two-dimensional models. In the case study, the imposition of a load calibrated from the "ideal" compatibilization load yielded beam load results with a significantly better compatibility than the imposition of usual loads from the bibliography / design practice.

Of course, various simplified compatibilization loads may be calibrated from the same "ideal" compatibilization nodal forces, depending on their degree of complexity. It is expected that increasing complexity leads to more compatible results, whereas decreasing complexity leads to simpler load definition.

Under these premises, consider the same hypotheses as those of the abovementioned case study (see Dzialoszynski and Stucchi [5] for details) with a single stage excavation calculation sequence (excavation and support application are modelled as simultaneous, in a simplified manner) and both normal and tangential hierarchy H2 links / "springs".

Two imposed loads were calibrated by "fitting" from the "ideal" compatibilization load:

- Imposed load C-A was simplified form the "ideal" compatibilization load, but no restriction for its degree of complexity was imposed.
- Imposed load C-B was also simplified form the "ideal" compatibilization load, but its distribution was imposed as bilinear, that is, substantially simplified.

Figure 1 illustrates the proposed loads. Only the modelled symmetrical part is represented.

---

[1] Corresponding to the "ideal" compatibilization load.

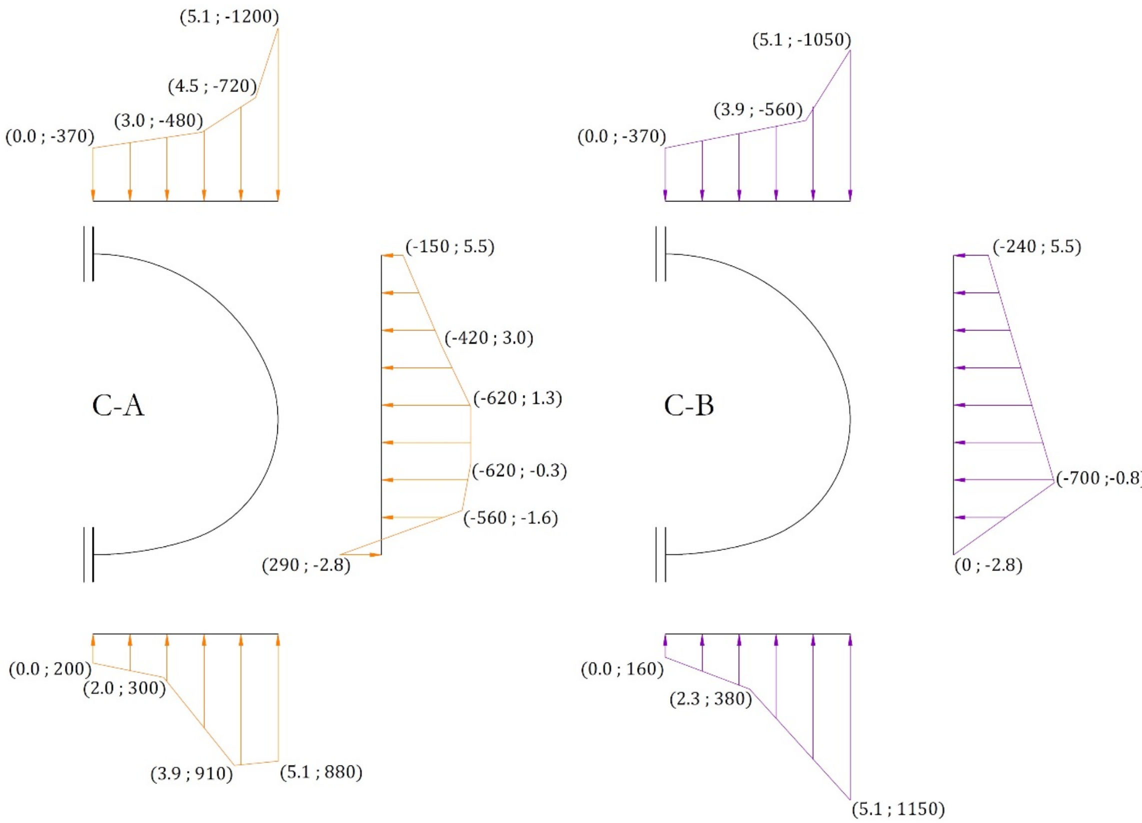

Figure 1. Loads calibrated from "ideal" compatibilization load proposed for comparison of compatibility with varying loading complexity.

Figures 2 and 3 show the axial force and bending moment beam load results for the hierarchy H2 model with the proposed loads, as well as for the reference hierarchy H1 model, for the sake of comparison. Results were plotted along the developed tunnel length of the modelled symmetrical part, s, starting from the base of the invert (see figures detail).

As illustrated by the figures, both proposed loads yielded results that are considerably compatible with those of the reference hierarchy H1 model, especially for the axial force, with practically identical maximum values, even for the greatly simplified load C-B. It should be highlighted that bending moments for the investigated problem were relatively low.

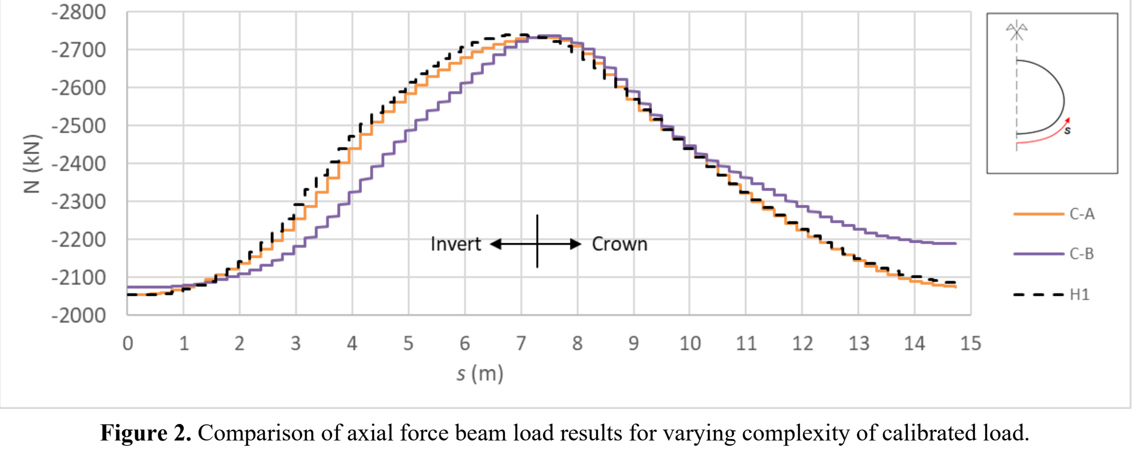

Figure 2. Comparison of axial force beam load results for varying complexity of calibrated load.

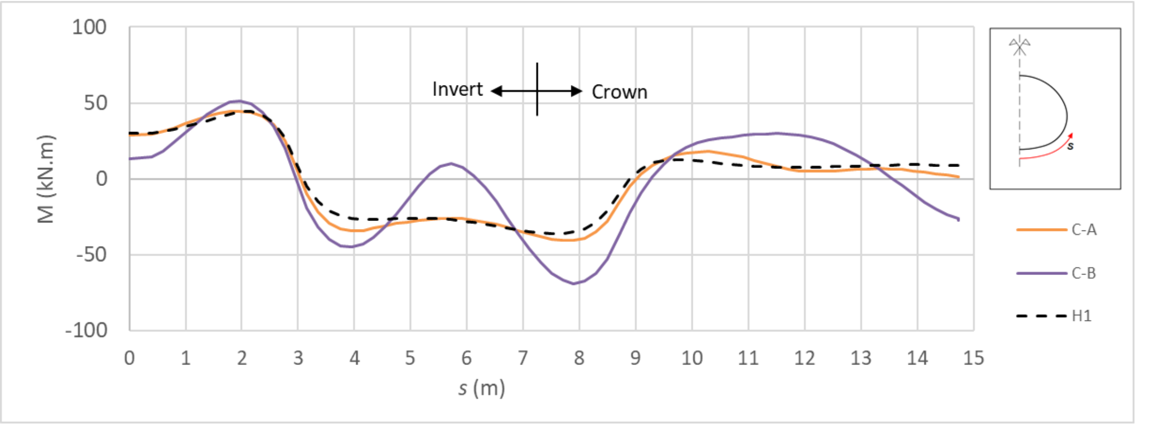

Figure 3. Comparison of bending moment beam load results for varying complexity of calibrated load.

Of course such comparison is not totally balanced, as the loads C-A and C-B are formulated specifically for the physical problem / tunnel being analyzed, and from the reference hierarchy H1 model results, which must be known beforehand. Usual imposed loads from bibliography and design practice are generically formulated, without any previous knowledge or necessary relation to the reference hierarchy H1 model results.

Naturally, the abovementioned observations refer to a single case study. Still, they may be seen at least as illustrative of the notion that even after great simplification, loads calibrated from the "ideal" compatibilization load can yield reasonable - and potentially better than usual generic imposed loads - result compatibility with the reference hierarchy H1 model.

That is, as long as the hierarchy H2 imposed load bears magnitude and distribution that adheres in a general manner to that of the "ideal" compatibilization load, the aforementioned reasonable result compatibility may be achieved between models.

However, there is an essential limitation to the practical application of "ideal" loads, as its computation requires solving beforehand the reference hierarchy H1 model, after which the practical significance of solving the analogous hierarchy H2 model is mostly lost. Such notion motivated the parametric study described hereafter, envisioning the estimation of compatibilization loads without the need of knowing beforehand the solution of the reference hierarchy H1 model.

It should be highlighted that the abovementioned discussion refers to result compatibility between models, and not necessarily between model and actual physical behavior. Even the hierarchy H1 models bear idealizations and simplifications that may lead to less accurate results. The "ideal" compatibilization loads essentially "inherit" those potential limitations. Of course, different hierarchy H1 models may be formulated to better represent physical behavior, with recalculation of the "ideal" compatibilization load.

3. "IDEAL" COMPATIBILIZATION LOAD PARAMETRIC STUDY HYPOTHESES

The conclusions from item 2.2 motivated a parametric study on the "ideal" compatibilization load response to the variation of hypotheses of the reference hierarchy H1 model, which reflect a variation on the definition of the physical problem. The present analysis focuses more directly on New Austrian Tunnelling Method (NATM) primary lining, but many conclusions apply broadly to tunnels in general.

The aim of the parametric study was to identify general patterns and trends in the magnitude and distribution of the "ideal" compatibilization load according to the hierarchy H1 model / physical problem definition. As concluded in item 2.2, as long as a hierarchy H2 model imposed load bears magnitude and distribution that generally resemble that of the "ideal" compatibilization load, reasonable - and potentially better than usual generic imposed loads - result compatibility may be obtained, even if it is greatly simplified.

The present study investigates the abovementioned patterns through simple models, foreseeing the potential postulation of compatibilization loads directly from the physical problem definition, without the need to know beforehand the results from the hierarchy H1 model, as the "ideal" compatibilization load computation would require.

3.1. Basic premises and disclaimers

As explained in item 2.2, the present study aims at investigating compatibility between models, and not between model and actual physical behavior measured from instrumentation.

Due to the intrinsic idealizations, even within the hierarchy H1 models, sometimes less realistic results were obtained (for example, exaggerated invert heave when linear-elastic behavior is considered). Nonetheless, the hypotheses in the study are similar to usual design practice considerations, and thus, those less realistic results are part of the routine engineering design challenges.

Analogously, due to its diversity, the combinations of hypotheses from the parametric analysis include some simulations for which structural analysis indicated inadequate safety or performance of the tunnel. In actual design, the dimensioning would be duly adjusted. Still, those simulation were considered conceptually adequate, enriching the spectrum of evaluated hypotheses.

In summary, for each combination of model H1 hypotheses, henceforth referred to as scenarios, the following activities were performed:

- Solve the hierarchy H1 model defined with the postulated combination of the hypotheses.
- Compute the hierarchy H2 model's nodal components of the "ideal" compatibilization load due to the soil mass $\boldsymbol{f_n}^s$ through the procedure outlined in item 2.1. The computation is performed for a postulated link / "spring" hypothesis applied for all scenarios.
- Distribute and normalize the nodal forces $\boldsymbol{f_n}^s$ into the normalized "ideal" compatibilization load $\boldsymbol{q_n}^s$.

It must be acknowledged that the activity sequence presumes the postulation of the hierarchy H2 links / 'springs' through bibliography, with compatibilization achieved through the imposed load. Thus, the present study implies protagonism of the imposed load and its calibration for compatibility, despite acknowledged limitations of the link / "spring" hypotheses of the bibliography.

3.2. Modeling hypotheses

Both model hierarchies were defined and solved through the FEM applying the software Midas GTS NX. Models were two-dimensional under plane strain hypothesis and considered only the righthand side symmetrical part of the physical problem.

For both hierarchies, the lining was modelled with 2-nodded Bernoulli-Euler beam elements. For the tunnel lining, constitutive behavior was assumed as homogeneous, isotropic and linear elastic, i.e., plasticity, and its associated parameters – e.g. friction angle and cohesion – were considered only for ground materials. It is acknowledged that some scenarios yielded results that would lead to the yielding of the lining, but to maintain homogeneity and the intended degree of complexity of the parametric analysis, elastic behavior was considered even in these cases.

For hierarchy H1, ground was modelled with 3-noded triangular plane strain elements, with various material hypotheses, depending on the scenario. No interface elements were considered.

For hierarchy H2, links / "springs" were applied discretely in the nodes along the full tunnel perimeter. Links / "springs" in the normal direction were considered with linear-elastic behavior in compression and null reaction to tension. The compressive stiffness was considered for each material as recommended by Martinek and Winter [10] for tunnels with cover equal or higher to 3 times its diameter. It must be highlighted that for the present study the scenarios with cover of 1 equivalent diameter do not adhere to such hypothesis, but the link / "stiffness" was maintained nonetheless, to allow for homogeneity along the analyses. Tangential links / "springs" were considered as linear elastic with stiffness estimated according to Plizzari and Tiberti [11].

3.3. Basic structure of the scenarios

The varying scenario hypotheses combinations were applied over a common basic model structure, as illustrated in Figure 4. The figure illustrates some parameters that are varied for the parametric analysis and some parameters that are kept constant throughout.

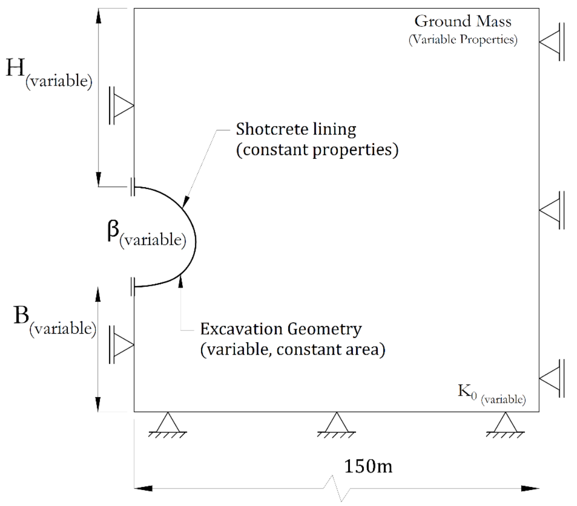

Figure 4. Basic hierarchy H1 model structure for the parametric analysis.

The basic structure reflects simple models, aiming at keeping the parametric analysis at a relatively low complexity level to allow better evaluation of fundamental physical behaviors.

A rectangular finite element mesh was considered, with horizontal ground surface and homogeneous stratigraphy. Mesh refinement was imposed such that the elements close to the tunnel lining had edges about 0,2m long, and the largest elements, close to the model boundary had edges about 1,0m long. This setup yielded result fields with acceptably smooth aspect and lower sensitivity to further refinements.

The external rightmost boundary of the finite elements mesh was considered at a distance where disturbances due to the modelled physical problem are negligible. The sole load applied to the model was self-weight, and the water table was considered to be below the lower boundary of the model.

The hierarchy H1 models were formulated as a common sequence of elastoplastic equilibrium calculations. Stage sequence was considered as:

- (E1) Initialization of the in-situ stress field prior to excavation through the K_0 procedure.
- (E2) Excavation of the full geometric section of the tunnel, with partial excavation stress relief on a fraction of $\omega = 1 - \beta, (0 \le \beta \le 1)$, with the excavation still unlined.
- (E3) Excavation stress relief of the remaining fraction of β with application of the full tunnel lining.

Figure 5 schematically illustrates the calculation sequence.

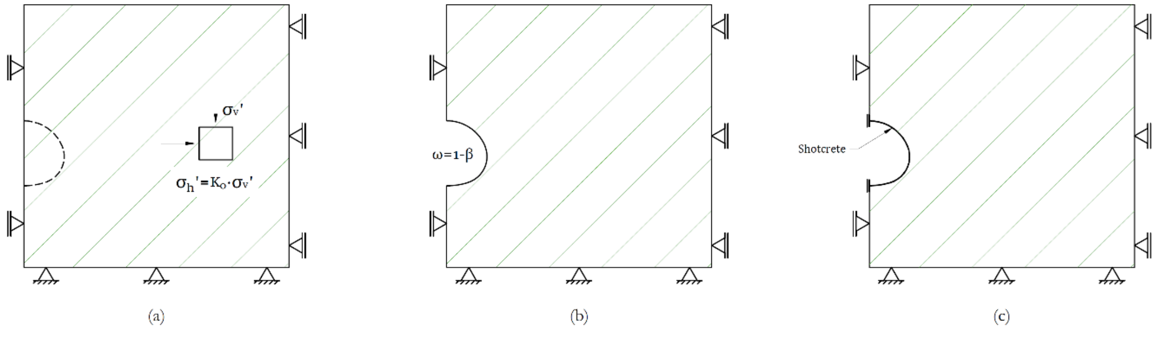

Figure 5. Calculation stages of hierarchy H1 model. (a) Stage (E1); (b) Stage (E2); (c) Stage (E3).

It must be highlighted that the proposed calculation sequence represents a significant simplification of the NATM excavation sequence and its tridimensional aspects. Nonetheless, the tridimensional effects of the lag between excavation and lining installation were considered in a simplified manner analogously to the β-method (Schikora and Fink[2], apud Plaxis [12]), allowing for the consideration and investigation of the basic associated physical behaviors.

Tunnel support was considered as a uniform 0.25m thick shotcrete layer applied along the full tunnel perimeter. As previously described, linear-elastic behavior was considered for the lining, with unit weight of 25kN/m^3, Young's modulus of 25GPa and Poisson's ratio of 0.25.

4. "IDEAL" COMPATIBILIZATION LOAD PARAMETRIC STUDY SCENARIOS

The hypotheses combined to form the evaluated scenarios are described in this section.

4.1. Tunnel geometry

Three tunnel geometries reflecting different types of tunnels were evaluated, as illustrated in Figure 6, from left to right, geometries G1, G2 and G3. All geometries bear the same area / equivalent diameter, seeking to normalize the excavated mass and, to a certain degree, the net stress relief.

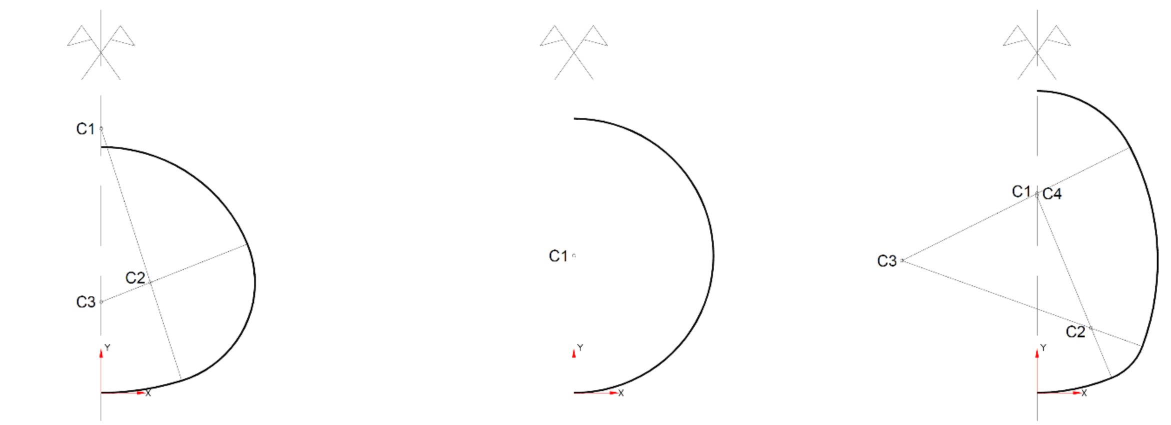

POINT	X	Y	R
C1	0.00	8.96	8.96
C2	1.64	3.74	3.49
C3	0.00	3.08	5.26

POINT	X	Y	R
C1	0.00	4.65	4.65

POINT	X	Y	R
C1	0.00	6.66	6.66
C2	1.79	2.20	1.83
C3	-4.50	4.48	8.52
C4	0.00	6.76	3.48

Figure 6. Tunnel geometries considered in the parametric analysis.

4.2. Tunnel cover

Three cover dimensions were evaluated (classification according to Chapman et al. [13]), namely: low cover, measuring 1 equivalent diameter; medium cover, measuring 3 equivalent diameters, and high cover, measuring 8 equivalent diameters.

4.3. Distance between invert bottom and model bottom

Three dimensions of the vertical distance between the bottom of the invert and the bottom of the model were considered, measuring 1, 2 and 5 equivalent diameters.

[2] K. Schikora and T. Fink, "Berechnungsmethoden moderner, bergmännischer Bauweisen beim UBahn-Bau," *Bauingenieur*, vol. 57, pp. 193–198, 1982.

4.4. In situ stress state prior to excavation

Under the basic structure of the scenarios, the in-situ stress state is fully defined through tunnel cover and the coefficient of horizontal stress K_0 , which was considered in the values of 0.5, 0.8 and 1.5. For specific cases, the value of 0.3 was also considered.

4.5. Unlined stress relief fraction

The unlined stress relief fraction ω may be defined with relation to the lined stress relief fraction, β. The value of β was evaluated as 0.25, 0.5 and 1.

4.6. Soil mass materials

For a given constitutive model, material behavior is given through a series of independent parameters. However, to maintain the degree of complexity and scenario count intended for the present study, parametric analysis was performed varying full sets of material parameters, rather than varying material parameters individually. Parameter sets were stipulated to be coherent to usual geomaterials – according to common practice and technical publications, such as FHWA [14] - and with mutual compatibility (e.g. materials with higher Young's Modulus are more resistant, etc.).

A total of 5 possible geomaterials mA, mB, mC, mD1 and mD2 were considered. In each scenario a single isotropic material is applied homogeneously to the full ground mass. Self-weight was considered constant throughout the materials so that the initial in situ stress state was independent of the material.

Materials mA and mC were modelled as linear elastic perfectly plastic with a Mohr-Coulomb yielding criterion. Material mB was considered as linear-elastic, seeking to represent a material with the same constitutive laws as mA and mC but with strength high enough to prevent any yielding. Table 1 illustrates the parameters for materials mA, mB and mC.

Materials mA, mB and mC were formulated to investigate different materials under the same constitutive model representation. It must be acknowledged that the considered constitutive laws are a great simplification of the actual geomaterial physical behavior, but as the applied hypotheses are relatively common in design practice, they are considered pertinent to the present study.

To evaluate said limitations, some scenarios applied materials mD1 and mD2, which considered the modified Cam Clay constitutive model [15]. Despite some limitations regarding quantitative representativity, this constitutive model reproduces various additional geomaterial behaviors. Materials mD1 and mD2 were considered with the same parameters except for the hardening parameter hypothesis as summarized in Table 2. For usual soil mechanics equivalent parameters, mD1 and mD2 would have C_c of 0.1, C_r of 0.01 and a friction angle of 30°.

Table 1. Parameters for materials mA, mB and mC.

Material	Unit weight	Young's modulus	Poisson's ratio	Cohesion	Friction angle	Dilatancy angle
	γ	E	υ	c'	ϕ'	ψ
	kN/m3	MPa		kPa	º	º
mA	20	100	0.3	75	22	0
mB	20	1000	0.3	-	-	-
mC	20	20	0.3	0	30	0

Table 2. Parameters for materials mD1 and mD2.

Material	Unit weight	Poisson's ratio	Initial void ratio	Stiffness parameter 1	Stiffness parameter 2	Critical state line slope	Over Cons. Ratio
	γ kN/m3	υ	e_0	λ	κ	M	OCR
mD1	20	0.3	0.5	0.04342	0.00434	1.2	1.1
mD2	20	0.3	0.5	0.04342	0.00434	1.2	6

4.7. Scenario summary

A total of 93 scenarios were analyzed. Scenarios were named according to their hypothesis combination as [Tunnel geometry]-[Cover]-[Distance from base of invert to base of model]-[K_0 value]-[β value]-[Ground mass material]. This scenario labeling system is applied to refer to scenarios henceforth in this paper.

Scenario analysis and global result inspection was performed individually, rather than with an automated routine. To make such approach feasible, the scenarios do not contemplate all possible combinations between the postulated hypotheses, and only the 93 combinations were selected and analyzed.

5. "IDEAL" COMPATIBILIZATION LOAD PARAMETRIC STUDY RESULTS

The 93 scenarios were divided into subgroups to evaluate the effects of the variation of each parameter regarding the "ideal" compatibilization loads, which are the focus of the study. Other outputs were also evaluated to interpret the physical meaning of the patters observed for the "ideal" compatibilization loads.

To allow interpretation with the usual design practice form of hierarchy H2 models' imposed load [9], the "ideal" compatibilization loads were decomposed in horizontal and vertical components and distributed along the projected lining area perpendicular to the direction of the respective component direction.

Additionally, to allow better comparison, loads were normalized by the pre-excavation in situ stress in the respective direction. Regarding this hypothesis, it is crucial to highlight that the normalization factor varies for each position – due to varying cover – and each direction – due to the K_0 coefficient.

Translating the abovementioned hypotheses mathematically, the horizontal component of the normalized "ideal" compatibilization load in a given node / position i, denoted by $\left[q_n{}^s\right]_{x,i}$ may be calculated by (Equation 1):

$$\left[q_n{}^s\right]_{x,i} = \frac{\left[f_n{}^s\right]_{x,i}}{\frac{|y_i - y_{i-1}|}{2} + \frac{|y_{i+1} - y_i|}{2}} * \frac{1}{(y_{terr} - y_i) * \gamma * K_0} \tag{1}$$

Where $i+1$ and $i-1$ denote the nodes adjacent to node i, $\left[f_n{}^s\right]_{x,i}$ is the horizontal component of the "ideal" compatibilization nodal force in node / position i; y_j is the vertical coordinate of an arbitrary node j; γ is the unit weight of the homogeneous hierarchy H1 ground mass; and y_{terr} is the vertical coordinate of horizontal ground surface.

Analogously, the vertical component of the normalized "ideal" compatibilization load in a given node / position i, denoted by $\left[q_n{}^s\right]_{y,i}$ may be calculated by (Equation 2):

$$\left[q_n{}^s\right]_{y,i} = \frac{\left[f_n{}^s\right]_{y,i}}{\frac{|x_i - x_{i-1}|}{2} + \frac{|x_{i+1} - x_i|}{2}} * \frac{1}{(y_{terr} - y_i) * \gamma} \tag{2}$$

Where x_j is the horizontal coordinate of an arbitrary node j.

Near the edges of the respective projected area "spans", the projected area magnitude is close to zero. Thus, even low nodal forces may yield high distributed loads, tending to highlight small disturbances from the numerical approximation. These potential high values are not considered representative or relevant for the actual load applied to the lining, because the area where these distributed loads are applied is practically null (i.e. these high values near the edges are usually not observed for actual the nodal forces). These values shall be nonetheless presented, for the sake of transparency, but result plot scale shall prioritize the representative / relevant results.

5.1. Variation of tunnel cover

The effects of tunnel cover variation on the normalized “ideal” compatibilization load were assessed based on the comparison of 27 scenarios. The normalized “ideal” compatibilization loads for 18 of those scenarios are presented in Figure 7 for illustration.

In summary it could be observed that:

- On the one hand, an “arching” effect is observed due to normalized values practically always lower than 1. On the other hand, cover variation usually did not lead to great / generalized variation in magnitude or distribution of the normalized “ideal” compatibilization loads. This behavior could be attributed to limitations of the constitutive model applied, and similar observations are also made in other publications, such as Hejazi et al. [16] or Chakeri and Unver [17].
- Usually slightly higher values were observed for normalized vertical loads applied to the crown and slightly lower in the invert for the higher cover scenarios.
- Plastification tends to cause local disturbances in the normalized load distribution. When the plastification pattern significantly shifts with cover, a trend of increase of normalized magnitude and homogenization of distribution is observed as elastoplasticity increases.
- Ascending / “floating” movements of the lining seem to be related to significant variations in normalized magnitude and distribution of the “ideal” compatibilization load, mainly for vertical loads applied to the crown. This occurs for low cover scenarios, especially for the vertically elongated geometry G3 and lower relative groundmass stiffness, as illustrated in Figure 8. These movements lead to compressive reaction in the normal hierarchy H2 links / “springs” in the crown, with otherwise null values for tension.

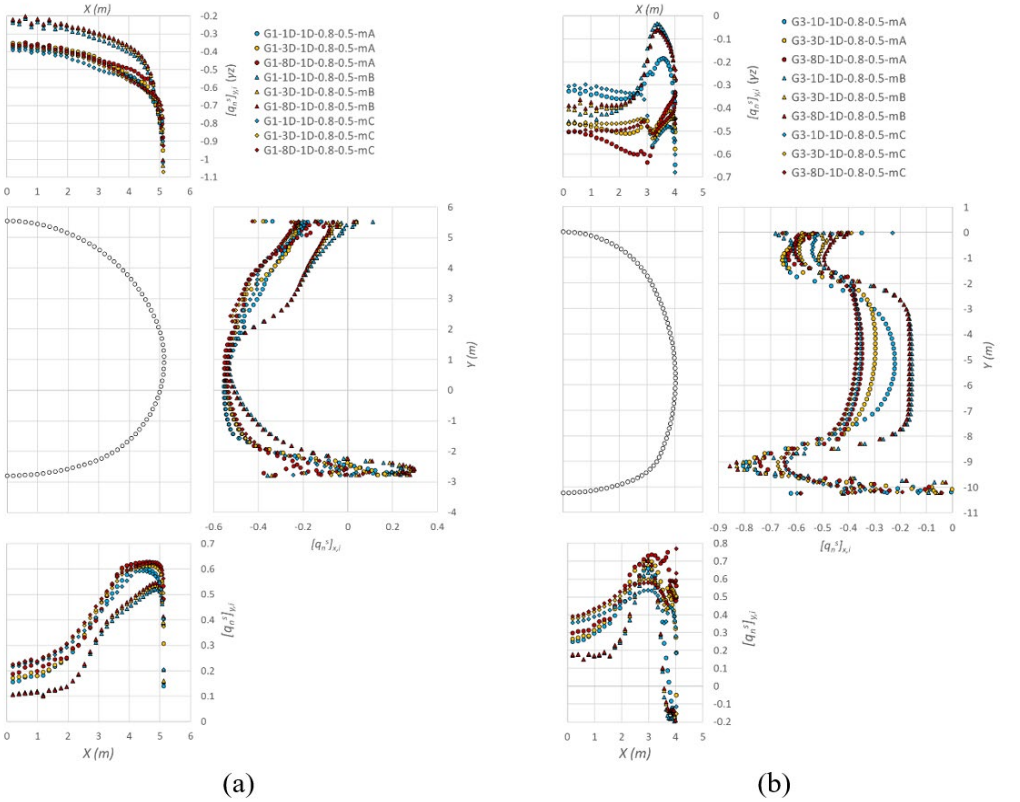

Figure 7. Normalized “ideal” compatibilization load for scenarios: (a) varying cover and materials in geometry G1; (b) varying cover and materials in geometry G3.

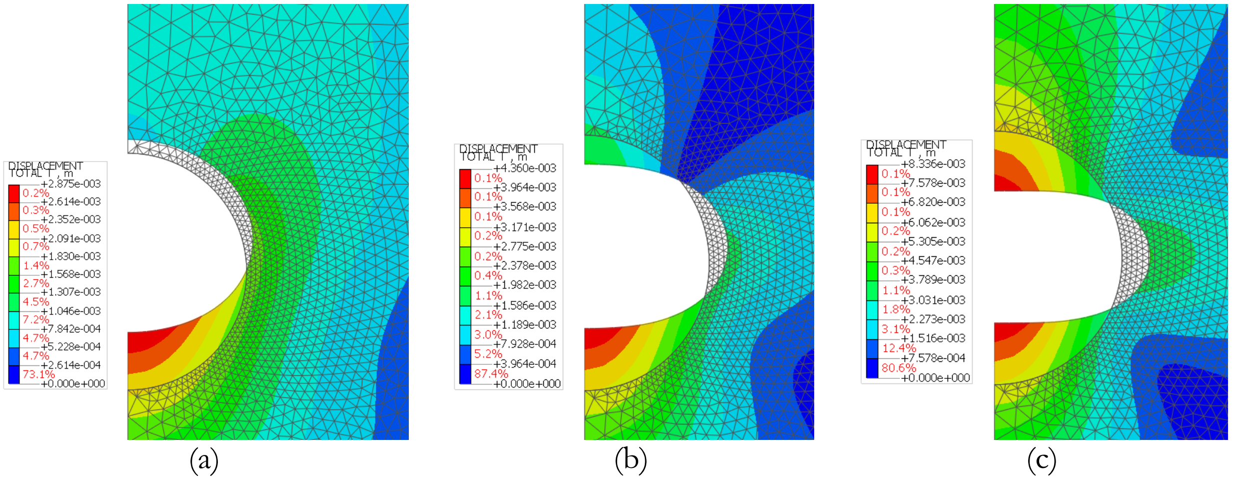

Figure 8. Variation of displacements in calculation stage (E3) (lined displacements) for scenarios varying cover in material with lower stiffness. (a) low cover; (b) medium cover; (c) high cover.

Regarding these "ascending" movements, it is considered that they may be exaggerated due to limitations of the applied constitutive models, and thus, the associated variation of the "ideal" compatibilization load may also not be representative of actual physical behavior.

5.2. Variation of soil mass materials

The effects of soil mass material variation on the normalized "ideal" compatibilization load were also assessed based on the comparison of 27 scenarios. The normalized "ideal" compatibilization loads for 18 of those scenarios are presented in Figure 7 for illustration.

It could be observed that:

- The evaluation was performed based on a limited amount of simulations, and with a rather simple constitutive model. Thus, conclusion must be considered in the light of this limitations. The observation regarding the applied constitutive model shall be explored in item 5.6.
- Relatively trivial observations were verified: higher ground stiffness usually leads to lower normalized loads and lower ground strength leads to more plastification, which cause higher normalized magnitude and more homogeneous distribution.
- The effects of the "ascending" movements of the lining crown described in item 5.1 were once again observed.

5.3. Variation of tunnel geometry and in situ stress state prior to excavation

As described hereafter, it was noticed that the way in which the shape of the tunnel influences the general distribution of normalized "ideal" compatibilization loads bears a relationship with the proportion between horizontal and vertical in situ stresses prior to excavation, quantified by K_0. The parameters were thus analyzed together in this section, based on 51 scenarios.

Figure 7a shows various results for scenarios with geometry G1. It may be compared to Figure 7b which shows results for analogous scenarios with geometry G3, respectively, to illustrate the effects of the variation of tunnel geometry. Figure 9a presents results for a collection of scenarios that illustrate the effects of the variation of K_0.

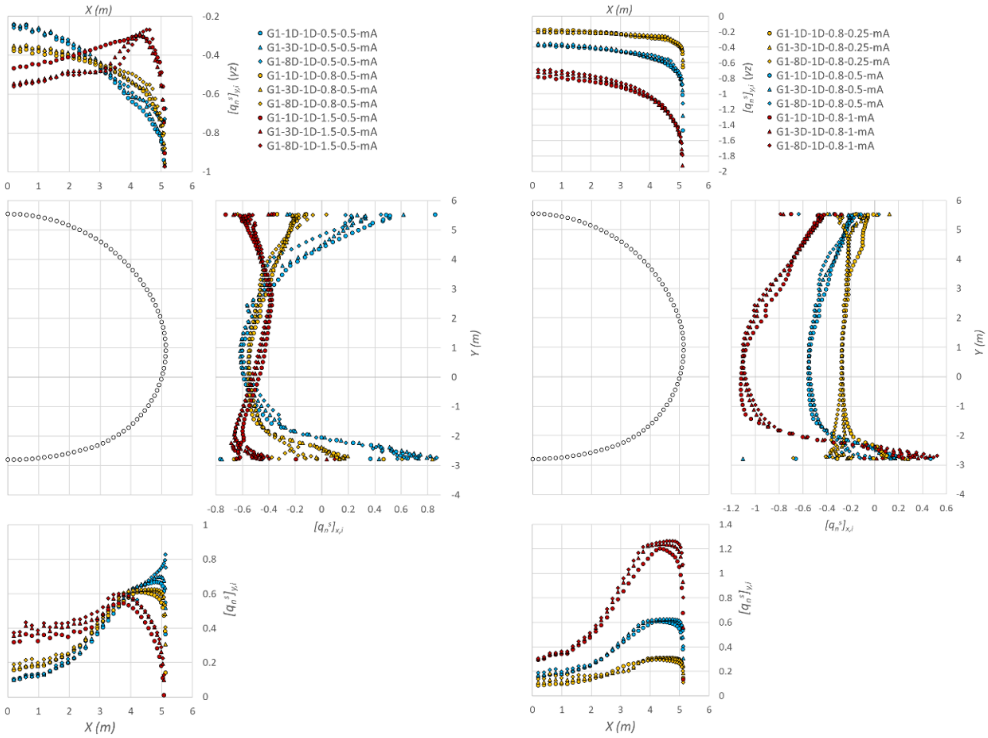

(a) (b)

Figure 9. Normalized "ideal" compatibilization load for scenarios varying: (a) cover and K_0 in geometry G1; (b) cover and β for geometry G1.

Regarding the normalized vertical loads applied to the crown:

- For the horizontally elongated geometry[3] normalized loads tend to concentrate in the edge of the "span"[4], with reduction in the direction towards the symmetry axis. Contrarily, for the vertically elongated geometry[5] normalized loads tend to concentrate "midspan"[6].
- Analogous behavior was observed for the variation of K_0, where higher values led to the tendency of normalized loads being concentrated "midspan" and lower values led to the tendency of normalized loads concentrating in the edge of the "span".

Regarding the normalized horizontal loads applied to the side of the tunnel:

- For the horizontally elongated geometry normalized loads tend to concentrate "midspan"[7], with reduction in the direction towards the edges. Contrarily, for the vertically elongated geometry normalized loads tend to concentrate near the edges of the "span"[8].
- Analogous behavior was observed for the variation of K_0, where higher values led to the tendency of normalized loads being concentrated in the edge of the "span" and lower values led to the tendency of normalized loads concentrating "midspan".

Regarding the normalized vertical loads applied to the invert:

[3] That is, the horizontal axis is longer than the vertical.
[4] That is, the outer edge of the area projection where the load is applied.
[5] That is, the horizontal axis is shorter than the vertical.
[6] That is, the symmetry axis of the area projection where the load is applied.
[7] That is, close to the middle of the height of the area projection where the load is applied.
[8] That is, the top and bottom of the area projection where the load is applied.

- In practically all scenarios lower normalized loads are observed "midspan"[9] and increase as the edge of the "span"[10] approaches.
- Still, trends like those observed for the vertical loads applied to the crown were observed. Higher K_0 led to higher values "midspan" and vice versa.

It must also be highlighted that variations of the arc radius along tunnel perimeter led to variation of the normalized load magnitude and distribution, especially when the transition is abrupt.

The analogy between behavior due to geometry elongation and K_0 is backed up by the physical interpretation that rotating by 90º the section of an oval tunnel that is very far from the model's boundaries would yield the same result as rotating the pre-excavation *in situ* stress field (lining self-weight neglected, ground self-weight proportionally adjusted). For the modelled scenarios, this correspondence is not exact, but the fundamental physical behavior still applies.

Under these premises, and despite specific differences regarding magnitude and trend intensity, as well as limited exception cases, two general distribution patterns were identified for the normalized "ideal" compatibilization loads:

- General distribution pattern I: vertical normalized loads applied to the crown concentrate in the edge of the "span"; horizontal normalized loads applied to the side of the tunnel concentrate "midspan".
- General distribution pattern II: vertical normalized loads applied to the crown concentrate "midspan"; horizontal normalized loads applied to the side of the tunnel concentrate in the edges of the "span".

For both patterns the normalized vertical loads applied to the invert concentrate in the edge of the "span", with varying intensity.

It was observed that the definition of the normalized load distribution pattern bears a relationship with the geometry – which may be quantified in a simplified manner by the section's aspect ratio[11] - and the initial *in situ* stress state - quantified by K_0 – as illustrated in Figure 10. General pattern I is observed for lower aspect ratios and lower K_0, and General pattern II is observed for higher aspect ratios and higher K_0.

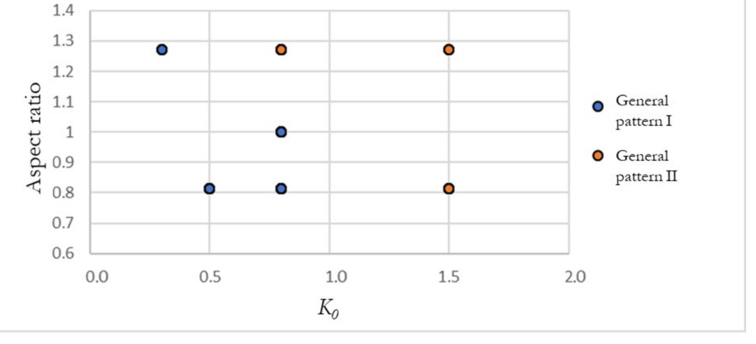

Figure 10. Normalized load distribution pattern depending on section's aspect ratio and K_0 value.

The models also showed a relation between the distribution pattern and the variation of displacements during calculation stage (E3), as illustrated in Figure 11 with some typical results. It may be observed that General distribution pattern I is related to variation of displacements that lead to horizontal "flattening"[12] of the section. General distribution

[9] That is, the symmetry axis of the area projection where the load is applied.
[10] That is, the outer edge of the area projection where the load is applied.
[11] Largest vertical dimension divided by largest horizontal dimension.
[12] That is, the horizontal axis length increases and the vertical axis length decreases, or the horizontal axis length increases more than the vertical axis length, or the horizontal axis length decreases less than the vertical axis length.

pattern II is related to variation of displacements that lead to vertical "flattening"[13] of the section. These trends are coherent with those related to tunnel section aspect ratio and K_0 values, which may be associated as relative stiffness and loading in relation to the aforementioned displacement patterns.

In some scenarios the displacements are less characteristic of the postulated definitions. Consistently, the general distribution patterns of the normalized loads are also somewhat less characteristic.

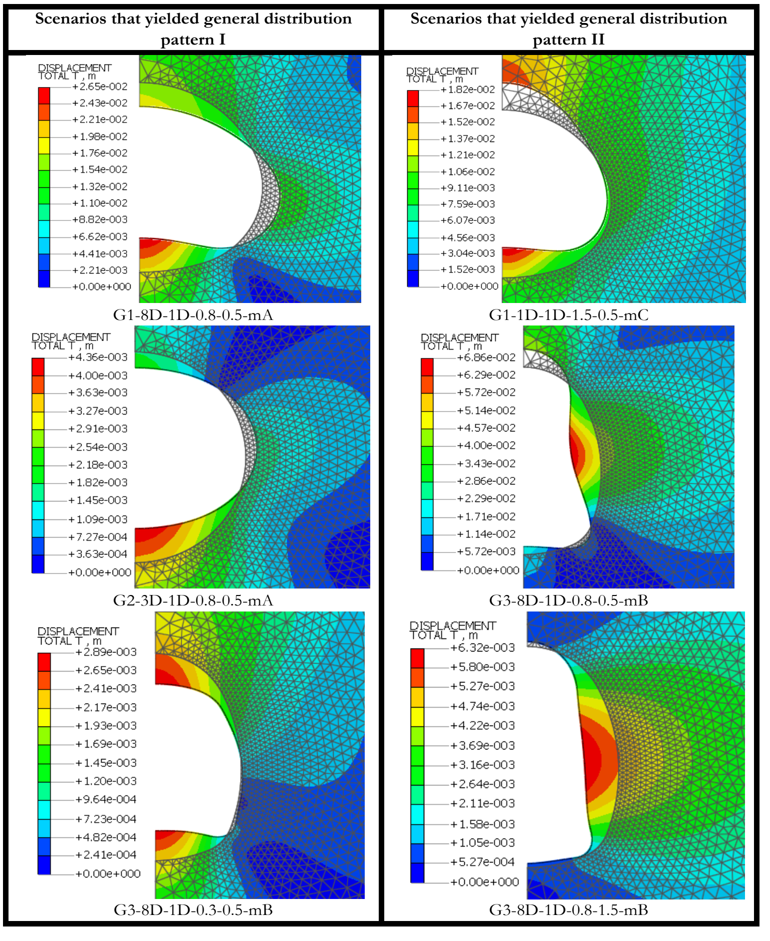

Figure 11. Variation of displacements in calculation stage (E3) in relation to normalized load general distribution patterns.

5.4. Variation of unlined stress relief fraction

The effects of the β value on the normalized "ideal" compatibilization load were assessed based on the comparison of 27 scenarios. The normalized "ideal" compatibilization loads for 9 of those scenarios are presented in Figure 9b for illustration.

In summary, it was observed that:

- The variation of β leads to a variation, from a general standpoint, of the same proportion of the normalized magnitude of the "ideal" compatibilization loads. The distribution pattern of the normalized loads does not vary greatly in most cases.

[13] That is, the vertical axis length increases and the horizontal axis length decreases, or the vertical axis length increases more than the horizontal axis length, or the vertical axis length decreases less than the horizontal axis length.

- Such trend, however, is not exact. Deviations from this behavior are as great as the variation of the plastification pattern within the ground mass as β varies. Major variations on the plastification pattern in the ground mass led to shifts in the normalized load distribution for specific cases.
- Nonetheless, despite the effects of plasticity, a general trend of proportionality between normalized magnitudes and β could be observed in most cases.

Thus, the value of β bears major importance in the normalized magnitude of the compatibilization loads. On the other hand, it has minor influence in the distribution of the normalized loads, except when severe variation of the plastification pattern of the ground mass is implicated.

5.5. Variation of distance between invert bottom and model bottom

The effects of the distance between the bottom of the invert and the bottom of the model on the normalized "ideal" compatibilization load were assessed based on the comparison of 27 scenarios. The normalized "ideal" compatibilization loads for 9 of those scenarios are presented in Figure 12a for illustration.

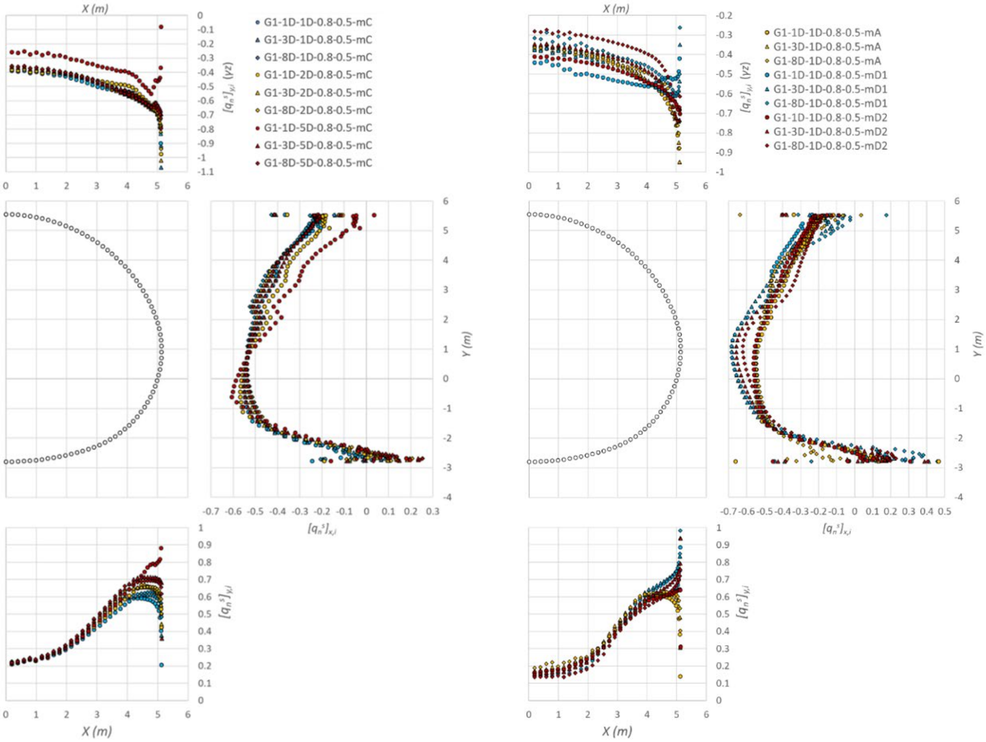

(a) (b)

Figure 12. Normalized "ideal" compatibilization load for scenarios varying: (a) the distance between invert bottom and model bottom for geometry G1; (b) constitutive models for geometry G1.

It could be observed that:

- In comparison to the other evaluated hypotheses and parameters, the variation of the distance between the bottom of the invert and the bottom of the model showed generally a smaller importance regarding effects on magnitude and distribution of the normalized loads.
- The proportion of the effects on the normalized magnitude is low in relation to the increase in distance required to cause it. That is, higher distance variations are required to cause substantial effects in the normalized load magnitudes.

- Examples of such effects are an increase in the normalized magnitudes of the vertical loads applied close to the outer part of the invert, as well as a smaller variation of the normalized horizontal loads.
- The effects are more prominent in low cover scenarios. A significant effect was noticed for the scenarios with highest distance from invert bottom to model bottom and lowest cover, with materials mA and mC. The effect may be attributed to the previously discussed "ascending" movement of the lining.

5.6. Variation of the constitutive model selected for soil mass representation

To evaluate the influence of the constitutive model applied to represent the ground mass, scenarios with material mA – represented with a linear elastic perfectly plastic model – were compared to analogous scenarios with materials mD1 and mD2 – represented by the modified Cam Clay model.

The three materials had their parameters estimated with reference to relatively hard clays, aiming at comparing the variation of material representation, rather than the variation of the material itself.

For this analysis 9 scenarios were considered. The normalized "ideal" compatibilization loads for these scenarios are presented in Figure 12b for illustration.

The limited number of evaluated scenarios must be acknowledged, highlighting that constitutive model comparison was performed for very particular conditions. Nonetheless, for the considered scenarios, it may be observed that:

- The effects of cover variation on the normalized loads are much more pronounced for the modified Cam Clay model. This observation is coherent with the different hypotheses of the constitutive models.
- Thus, the observations from item 5.1, regarding the lower effect of cover variation on the normalized loads for scenarios applying linear elastic perfectly plastic models with Mohr Coulomb yielding criterion are not necessarily valid for more complex constitutive laws.
- The hardening parameter, defined in the evaluated scenarios by the OCR, had a significant effect on the normalized loads.
- Even with limited number of scenarios evaluated, a higher complexity on the trends of normalized "ideal" compatibilization loads in relation to hierarchy H1 input parameter variation is foreseen, with maximum normalized loads for intermediary values of input parameters.

Nonetheless, the general distribution pattern of the normalized "ideal" compatibilization loads was generally similar along the scenarios, even with the variation of the constitutive model. As previously discussed in item 5.3, the evaluated scenarios showed that this pattern bears an important relationship with tunnel geometry and *in situ* stress states.

6. CONCLUSIONS AND FUTURE WORK

Within the context of tunnel modeling and lining analysis and design, this paper presented a study on the potential compatibilization of the beam load results between continuous ground mass models and bedded beam models, through the calibration of the loads imposed to the bedded beam model. The study follows up on previous work by Dzialoszynski and Stucchi [5], and is based on a procedure to compute "ideal" compatibilization loads, as presented and defined in the aforementioned previous publication.

A case study presented in this paper indicated that distributed loads calibrated from the "ideal" compatibilization load yielded beam loads that had reasonable and better compatibility with the reference continuous ground mass model than those obtained when usual generic loads from the bibliography / practice are applied. This compatibilization was achieved even when a significant simplification (bi-linear distribution) was imposed to the calibrated load. Despite the fact that the observations refer to a single case study, it at least illustrates that as long as the load imposed to the bedded beam model bears general magnitude and distribution that resembles those of the "ideal" compatibilization load, the aforementioned reasonably compatible results may be obtained.

However, an essential limitation – which is not imposed to the usual generic loads from the bibliography / practice – applies to the "ideal" compatibilization load, as its computation requires knowing beforehand the results of the reference continuous ground mass model.

Motivated by such observation, and foreseeing the potential estimation of compatibilization loads directly from the physical problem definition - and without the need of knowing beforehand the results of the reference continuous ground mass model - a parametric study was performed and presented in this paper. The study was performed to investigate the effects of the variation of the reference continuous ground mass model inputs on the general magnitude and distribution of the “ideal” compatibilization loads. The study applied a simple model structure to assess fundamental physical behaviors through the individual formulation, processing and interpretation of 93 simulation scenarios.

Qualitative / semi-quantitative trends and patterns were observed, which may serve as the basis for future work aiming at quantitative conclusions for the direct estimation of simplified compatibilization loads. Such future work would likely require a significant amount of model and result processing, probably involving routines for automated model definition and processing, as well as results processing and correlation, for example analogously to what Kung et al. [18] presented for retaining walls.

7. REFERENCES

[1] H. Duddeck, “Codes need different structural design models than research work,” in *Fundamental Developments in Design Models – Contributions to a Joint Meeting Organized by Commission II (Structural Analysis) and Commission IV (Members Design)*, International Federation for Structural Concrete, Ed., Lausanne: FIB, 1986, pp. 243–263.

[2] M. Bucalem and K. Bathe, *The Mechanics of Solids and Structures-Hierarchical Modeling and the Finite Element Solution*, 1st ed. Berlin, Germany: Springer Science & Business Media, 2011.

[3] International Tunneling and Underground Space Association, "Guidelines for the design of tunnels," *Tunn. Undergr. Space Technol.*, vol. 3, no. 3, pp. 237–249, Jul-Sep 1988, http://dx.doi.org/10.1016/0886-7798(88)90050-8.

[4] F. Prado and M. Waimberg, "A modelagem numérica da interação solo-estrutura," *Concreto Construcoes*, vol. 84, pp. 83–88, Oct-Dec 2016. Accessed: Jan. 1, 2020. [Online]. Available: http://ibracon.org.br/Site_revista/Concreto_Construcoes/ebook/edicao84/files/assets/basic-html/page1.html

[5] B. S. Dzialoszynski and F. F. Stucchi, "Contribution to hierarchical modeling in tunnel design practice," *Ibracon Struct. Mater. J.*, vol. 12, no. 5, pp. 1205–1219, 2019, http://dx.doi.org/10.1590/s1983-41952019000500012.

[6] H. Duddeck and J. Erdmann, “Structural design models for tunnels,” in *Tunneling 82*, 1982.

[7] J. Van der Poel, H. Hergarden, and H. Dekker, “Soil loads acting on shield tunnels: comparison between bedded beam model and finite element calculations,” in *Tunneling. A Decade of Progress – Geodelft 1995-2005*, A. Bezuijen and H. Van Lottum, Ed., London, United Kingdom: CRC Press, 2006, pp. 145-200.

[8] M. Vu, W. Broere, and J. Bosch, "Structural analysis for shallow tunnels in soft soils," *Int. J. Geomech.*, vol. 17, no. 8, pp. 1–10, 2017. Accessed: Jan. 1, 2020. [Online]. Available: https://ascelibrary.org/doi/10.1061/%28ASCE%29GM.1943-5622.0000866

[9] C. B. Blom, “Design philosophy of concrete linings for tunnels in soft soils,” Ph.D. dissertation, Civ. Eng. Dep., Delft Univ. Technol., Delft, 2002.

[10] K. Matinek and V. Winter, *Tunnelbeu Unter Tage – Erlaeuterungen Zu Den Normen, Richtlinien Und Regeln*, 1st ed. Wiesbaden, Germany: Bahverlag GmbH, 1987.

[11] G. Plizzari and G. Tiberti, "Steel fibers as reinforcement for precast tunnel segments," *Tunn. Undergr. Space Technol.*, vol. 21, no. 3-4, pp. 438–439, 2006, http://dx.doi.org/10.1016/j.tust.2005.12.079.

[12] Plaxis, *Plaxis Material Models Manual.* Netherlands: Plaxis bv., 2019.

[13] D. Chapman, N. Metje, and A. Stark, *Introduction to Tunnel Construction*, 2nd ed. Boca Raton, Florida, USA: CRC Press, 2018.

[14] U.S. Department of Transportation Federal Highway Administration, *Soils and Foundations – Reference Manual, vol. I*, 4th ed. Washington, DC, USA: FHWA, 2006.

[15] J. Burland and K. Roscoe, “On the generalized stress strain behaviour of 'wet' clay,” in *Engineering Plasticity*. Cambridge: Cambridge University Press, 1968, pp. 535–609.

[16] Y. Hejazi, D. Dias, and R. Kastner, "Impact of constitutive models on the numerical analysis of underground constructions," *Acta Geotech.*, vol. 3, no. 4, pp. 251–258, Mar 2008, http://dx.doi.org/10.1007/s11440-008-0056-1.

[17] H. Chakeri and B. Unver, "A new equation for estimating the maximum surface settlement above tunnels excavated in soft ground," *Environ. Earth Sci.*, vol. 71, no. 7, pp. 3195–3210, Aug 2014, http://dx.doi.org/10.1007/s12665-013-2707-2.

[18] G. T. C. Kung, E. C. L. Hsiao, M. Schuster, and C. H. Juang, "A neural network approach to estimating deflection of diaphragm walls caused by excavation in clays," *Comput. Geotech.*, vol. 34, no. 5, pp. 385–396, Sep 2007, http://dx.doi.org/10.1016/j.compgeo.2007.05.007.

Author contributions: BDS: methodology, numerical analysis, result analysis and evaluation, writing. FRS: methodology, result evaluation, supervision.

Editors: Mauricio de Pina Ferreira, José Luiz Antunes de Oliveira e Sousa, Guilherme Aris Parsekian.